Readout and control of molecules for electric dipole moment searches



Anno Touwen

Readout and control of molecules for electric dipole moment searches

Cover - In a symmetric experiment the difference between signals from a molecular beam traversing a parallel or antiparallel electric and magnetic field can be attributed to the charge conjugation-parity violating electric dipole moment.



university of groningen



Nikhef

The work in this thesis has been carried out at the Van Swinderen Institute for Particle Physics and Gravity of the University of Groningen. This work is done as part of the NL-eEDM consortium which receives funding (EEDM-166) from the Dutch Research Council (NWO). This work originates as part of the research programme of the Foundation for Fundamental Research on Matter (FOM), and falls as of 1 April 2017, under the responsibility of Netherlands Foundation of Scientific Research Institutes (NWO-I), which is part of the Dutch Research Council (NWO).

Cover design: Anno Touwen
Printed by: Gildeprint

university of groningen

Readout and control of molecules for electric dipole moment searches

PhD thesis

to obtain the degree of PhD at the
University of Groningen
on the authority of the
Rector Magnificus Prof. J.M.A. Scherpen
and in accordance with
the decision by the College of Deans.

This thesis will be defended in public on

Tuesday 22 October 2024 at 12.45 hours

by

Anno Paul Touwen

born on 11 June 1995
in Nieuwerkerk aan den IJssel

Supervisors
Prof. H.L. Bethlem
Prof. S. Hoekstra

Assessment Committee
Prof. J. Even
Prof. M. P. Decowski
Prof. G. Meijer

Contents

1 Introduction **1**
- 1.1 Discrete symmetries . . . 2
- 1.2 Electric dipole moments . . . 2
- 1.3 The NL-eEDM experiment . . . 5
- 1.4 Thesis outline and relation to other work . . . 7

2 Spin-precession method for electric dipole moment searches **9**
- 2.1 Optical method approach to phase evolution measurement . . . 10
- 2.2 Analytic model . . . 13
- 2.3 Signal and contrast . . . 18

3 Data acquisition and control **21**
- 3.1 Data collection approach . . . 22
- 3.2 Data acquisition . . . 24
- 3.3 Control . . . 33
- 3.4 Interference fringe for opposite field orientations . . . 39
- 3.5 Conclusion and outlook . . . 41

4 Traveling-wave Stark decelerator and hexapole lens **43**
- 4.1 Stark effect for SrF and BaF . . . 44
- 4.2 Hexapole lens . . . 47
- 4.3 Traveling-wave Stark decelerator . . . 49
- 4.4 Phase-space acceptance . . . 53
- 4.5 Filling of the phase-space acceptance . . . 63
- 4.6 Conclusion and outlook . . . 69

5 Deceleration of strontium fluoride **73**
- 5.1 Introduction . . . 74
- 5.2 Experimental setup . . . 75
- 5.3 Source reliability and ease of maintenance . . . 76
- 5.4 Data collection and control system . . . 79
- 5.5 Intensity increase using a hexapole lens . . . 85
- 5.6 Improvement to the deceleration of SrF . . . 88
- 5.7 Conclusion and outlook . . . 91

6 Guiding and deceleration of barium fluoride **93**
- 6.1 Setup changes for transition to BaF . . . 94
- 6.2 Characterisation of the molecular beam . . . 98
- 6.3 Guiding at different voltage amplitudes . . . 103
- 6.4 Hexapole lens . . . 105

6.5 Camera imaging of molecular beam . . . 106
6.6 First deceleration of BaF . . . 108
6.7 Outlook . . . 111

7 Electrostatic hexapole lens 113
7.1 Introduction . . . 114
7.2 The force on barium fluoride in an electrostatic multipole lens . . . 115
7.3 Design of the hexapole lens . . . 117
7.4 Methods . . . 119
7.5 Spectra with and without hexapole lens . . . 123
7.6 Molecular beam widths and intensities . . . 124
7.7 Beam deflection and alignment . . . 128
7.8 Conclusions and outlook . . . 129

8 Summary and outlook 133
8.1 Summary . . . 133
8.2 Discussion and outlook . . . 135

9 Nederlandse samenvattingen 141
9.1 Niet-deskundigen samenvatting . . . 141
9.2 Wetenschappelijke samenvatting . . . 148

Acknowledgements 151

List of Publications 154

A Molecular structure and labeling 156
A.1 State labeling . . . 156
A.2 Transitions and branches . . . 158

B (Re)booting the DAQ system - Full manual 159

C Data Acquisition channels 175

D Electric field configurations 179
D.1 Radial multipole field . . . 179
D.2 Traveling-wave Stark decelerator field . . . 182

Bibliography 187



1

Introduction

The Standard Model of particle physics describes matter and the interactions thereof in three of the four fundamental forces of nature, referred to as the electromagnetic, weak and strong interaction. This theoretical framework, based around a $SU(3)_C \times SU(2)_L \times U(1)_Y$ gauge symmetry [1–3] has proven to be highly successful in describing observed interactions and predicting the existence of fundamental particles. All of the predicted particles have been experimentally confirmed, including the weak interaction mediating W and Z bosons [4], strong interaction mediating gluons [5] and the Higgs boson [6] responsible for the mass of fundamental particles via spontaneous symmetry breaking [7]. Fermionic matter particles have also been predicted and observed, both in the leptonic sector, such as the tau [8] and the tau neutrino [9], and in the hadronic section with the charm [10, 11], bottom [12] and top quarks [13, 14].

Despite its successes, the Standard Model is not a complete theory, which from the theoretical point of view is obvious from the absence of the fourth fundamental force of nature, gravity. Additionally, there are cosmological observations that pose questions which are not answered by the Standard Model, for example on the nature of dark matter and dark energy. These open questions led to the proposal of a large variety of model extensions beyond the Standard Model, such as Grand Unified Theories [15–18] that include the Standard Model gauge symmetry in a larger symmetry group, supersymmetric theories [19] introducing a symmetry between fermions and bosons, and theories with extensions of the Higgs sector [20].

A model-independent approach to these extensions of the Standard Model is based on effective field theory. Here the Standard Model is considered as a low-energy effective field theory of some (unknown) fundamental theory, that manifests itself at higher energy scales. In this bottom-up procedure, no assumptions on the structure of this fundamental theory are necessary as all extensions are studied simultaneously by an expansion in mass-dimension of the possible interaction terms [21, 22]. Interactions of mass-dimension $d > 4$ are introduced with effective coupling strengths that contain a dimensionless coupling constant c_i and the

The chapter image shows an illustration of the symmetry breaking as can be probed by a precision measurement on composite system such as a molecule.

energy scale of new physics Λ as c_i/Λ^{d-4} [23]. These interactions are strongly suppressed at the electroweak energy scale at which the Standard Model has proven to be successful. Nevertheless, these beyond the Standard Model interactions can be probed with experiments at a lower energy scale, where they show up as corrections to observables which in the Standard Model are extremely small, or zero.

1.1. Discrete symmetries

In addition to the continuous gauge symmetries discussed above and the spacetime symmetries described by the Lorentz invariance, the Standard Model has been observed to largely follow some discrete symmetries as well. In particular charge conjugation (C), relating particles to their corresponding antiparticles, parity (P), corresponding to the flipping of the spatial coordinates, and time-reversal (T), meaning the inversion of the time coordinate, or combinations thereof are considered. According to the CPT theorem, any locally Lorentz invariant quantum field theory, such as the Standard Model, must be invariant under the combination of all three of these operations. No violation of either the Lorentz symmetry or the CPT theorem have been observed [24].

The theorem does however allow breaking of symmetry corresponding to a subcombination of operations. And indeed CP violation has been experimentally observed, for the first time in the decay of neutral kaons [25]. The Standard Model permits CP violation in two sectors. Firstly, CP violation occurs in the electroweak interaction, parameterized by a complex phase in the CKM matrix [26, 27], which describes the mixing between the mass and flavour eigenstates of quarks. Secondly, CP violation is also permitted in the strong interaction, parameterized by the QCD vacuum angle $\bar{\theta}$ [28, 29]. The latter has not been observed in experiments and is restricted to $\bar{\theta} < 10^{-10}$ by the limit on the neutron electric dipole moment [30, 31]. This restriction, which can be considered unnatural, is one of the open questions of the Standard Model and is known as the strong CP problem.

Cosmological observations, in the form of a large asymmetry between the amount of matter and antimatter in the universe, provide another motivation to look for CP violation. One of the requirements for explaining this asymmetry is the violation of CP symmetry [32]. The CP violation in the Standard Model is insufficient to account for the large asymmetry found in cosmological observations.

1.2. Electric dipole moments

A powerful probe for CP violation comes in the form of the (permanent) electric dipole moment (EDM). The coupling of a system with total angular momentum $\mathbf{F}$ to an external magnetic ($\mathbf{B}$) and electric ($\mathbf{E}$) field is described by the non-relativistic Hamiltonian,

$$H^{E,B} = -\mu \mathbf{F} \cdot \mathbf{B} - D^{\not{P},\not{T}} \mathbf{F} \cdot \mathbf{E}, \tag{1.1}$$

where μ and $D^{\not{P},\not{T}}$ are the magnetic and electric dipole moment of the system respectively. As the magnetic field and spin are even under parity transformation and odd under time-reversal, while the electric field is odd under parity and even under time-reversal, it follows

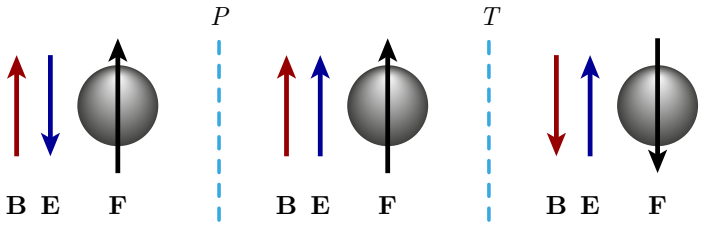

***Figure 1.1** | Parity (P) and time reversal (T) transformations of the total angular momentum* $\mathbf{F}$*, magnetic field* $\boldsymbol{B}$ *and electric field* $\mathbf{E}$*. Here a generic sphere is used as it holds for any system. In particular, in this work a barium monofluoride molecule is considered.*

that,

$$PH^{B}P^{-1} = -\mu(+\mathbf{F})\cdot(+\mathbf{B}) = H^{B}, \qquad PH^{E}P^{-1} = -D^{\not P,\not T}(+\mathbf{F})\cdot(-\mathbf{E}) = -H^{E}, \tag{1.2}$$

$$TH^{B}T^{-1} = -\mu(-\mathbf{F})\cdot(-\mathbf{B}) = H^{B}, \qquad TH^{E}T^{-1} = -D^{\not P,\not T}(-\mathbf{F})\cdot(+\mathbf{E}) = -H^{E}, \tag{1.3}$$

as illustrated in Figure 1.1. From the opposite transformation of the magnetic and electric field under parity (P) and time (T) reversal symmetry, it is clear that the magnetic dipole moment interaction is P and T conserving, while the electric dipole moment interaction is P,T violating, hence the labeling of the electric dipole moment by the symmetries it violates $D^{\not P,\not T}$. By the CPT theorem, T violation is equivalent to CP violation, making EDMs powerful probes of CP violation.
The electric dipole moment is probed in a double-differential measurement. The magnetic substates with $m_F = \pm 1$ of a state with total angular moment $F = 1$ experience opposite shifts in external fields. Following Equation 1.1, the energy difference between these substates for parallel and anti-parallel magnetic and electric fields is,

$$2\hbar\omega_{EB}(\hat{E} = \pm\hat{B}) = 2(\mu B \pm D^{\not P,\not T}E). \tag{1.4}$$

Hence, the difference between the shifts in the parallel and anti-parallel configuration provides a measure for the CP violating electric dipole moment,

$$D^{\not P,\not T} = \frac{\hbar\omega_{EB}(\hat{E} = +\hat{B}) - \hbar\omega_{EB}(\hat{E} = -\hat{B})}{2E}. \tag{1.5}$$

This generic probe of CP violation has been shown to be particularly sensitive to the electric dipole moment of the electron (eEDM) for heavy atoms or polar molecules containing heavy elements [33]. For a paramagnetic diatomic molecule, as studied in this work, the main sources of CP violation are expected to be due to the electron electric dipole moment (d_e) and the scalar-pseudoscalar electron-nucleon interaction (C_S). The EDM is therefore parameterised as,

$$D^{\not P,\not T} = -(d_e W_d + C_S W_S)\hbar|\Omega|P(E)/E, \tag{1.6}$$

where $|\Omega|$ is the projection of the electronic angular momentum on the internuclear axis, and $P(E)$ is the polarisation of the molecule in the electric field [34], which is between 0 and 1. The enhancement factors W_d, W_S are found from electronic structure calculations [34]. These

depend on the probed systems and will therefore enable distinction between the sources of CP violation once nonzero EDMs are observed for multiple systems. The enhancement factor for the electron electric dipole moment is often regarded as an effective electric field, as $E_{\text{eff}} = W_d \hbar |\Omega|$ carries the units of an electric field. Note that this effective parameter of the molecular EDM $D^{\hat{P},\hat{T}}$ works intuitively in the regime of linearly increasing polarisation $P(E) \propto E$, but starts decreasing with higher external electric fields as the polarisation saturates.

As the EDM is probed by measuring populations after a spin-precession measurement over an interaction time T, as described in chapter 2, the statistical sensitivity in the quantum projection limit is,

$$\sigma_{D^{\hat{P},T}} = \frac{\hbar}{2ET\sqrt{N}}, \tag{1.7}$$

where N is the number of contributing particles. Typically, the outcome from the search for a CP violating EDM is presented as a limit on a single source, being the electric dipole moment of a fundamental particle, in this case the electron. In this interpretation, the statistical uncertainty on the electron electric dipole moment becomes,

$$\sigma_{d_e} = \frac{1}{2W_d |\Omega| P(E) T\sqrt{N}}. \tag{1.8}$$

The quantum projection limit describes the sensitivity in the case of an ideal experiment, where each molecule emits one photon measured in the detector. In the case of a detector with efficiency ϵ and variable number of photons emitted per molecule, with mean $\bar{n}$ and standard deviation σ_n an excess noise factor F is derived in Boeschoten [23],

$$F = \frac{2}{\bar{n}}\left(\frac{1}{\epsilon} - 1\right) + \frac{2\sigma_n^2}{\bar{n}^2} + 1. \tag{1.9}$$

Assuming a Poisson distribution for the number of photons emitted per molecule, the standard deviation is given by $\sigma_n = \sqrt{\bar{n}}$. Background counts, which do not originate from the molecules, do further increase the excess noise factor. The excess noise factor from imperfections in detection is taken into account in the sensitivity estimate of the experiment by multiplying the statistical sensitivity in the quantum projection limit by $\sqrt{F}$.

Over the past decades there have been multiple experiments looking for CP violating interactions by probing the electron electric dipole moment using various atoms and molecules. As can be seen in Table 1.1, all results are consistent with zero, but the experiments are setting progressively more stringent limits, spanning multiple orders of magnitude.

The complex phase in the CKM matrix is the only observed source of CP violation in the Standard Model and can therefore be used to estimate the electron electric dipole moment. As this phase only appears in the EDM interaction through higher-order loop corrections that include all three quark generations, the Standard Model value is ten orders of magnitude below the current experimental limits [35],

$$d_e^{CKM} \simeq 5.8 \times 10^{-40}\ e\ \text{cm}. \tag{1.10}$$

In the near future, this value is out of reach for experiments. However, it has been shown that the Standard Model prediction for the scalar-pseudoscalar interaction is [36],

$$C_S^{CKM} \simeq 6.9 \times 10^{-16}. \tag{1.11}$$

***Table 1.1** | Most recent results of searches for the eEDM using various atoms and molecules, showing the value measured, the uncertainty and the upper limit found with 90% confidence level. Where statistical and systematic uncertainty are given, they are shown in this order. Also shown is the year at which these results were published, showing that both the upper limits and the value have reduced by several orders of magnitude over time. Table adapted from Marshall [37].*

System	Value and uncertainty d_e (e cm)	Upper limit d_e (e cm) at 90% confidence level	Year	Reference
Cs	$(-1.5 \pm 5.5_{\text{stat}} \pm 1.5_{\text{syst}}) \times 10^{-26}$	9.4×10^{-26}	1989	[38]
Tl	$(6.9 \pm 7.4) \times 10^{-28}$	1.6×10^{-27}	2002	[39]
YbF	$(-2.4 \pm 5.7_{\text{stat}} \pm 1.5_{\text{syst}}) \times 10^{-28}$	1.1×10^{-27}	2011	[40]
ThO	$(4.3 \pm 3.1_{\text{stat}} \pm 2.6_{\text{syst}}) \times 10^{-30}$	1.1×10^{-29}	2018	[41]
HfF^+	$(-1.3 \pm 2.0_{\text{stat}} \pm 0.6_{\text{syst}}) \times 10^{-30}$	4.1×10^{-30}	2023	[42]

This is equivalent to $d_e^{equiv} = C_S \frac{W_S}{W_d} \simeq 1.0 \times 10^{-35}$ e cm, five orders of magnitude below the current best experimental limit.
Extensions beyond the Standard Model may result in much larger values for d_e and C_S. Following the effective field theory approach, such interactions must be at least of mass-dimension six and are therefore strongly suppressed by the mass of the involved particles. In this way the mass scale M of these particles can be estimated [43],

$$d_e \simeq \sin\phi_{CPV} \left(\frac{1 \text{ TeV/c}^2}{M}\right)^2 \times 5.1 \times 10^{-27} \, e \text{ cm}. \tag{1.12}$$

For a CP violating phase $\sin\phi_{CPV} \sim 1$, this implies that the electron electric dipole moment limit of 10^{-30} e cm reached in current experiments corresponds to a sensitivity to beyond the Standard Model particles at a mass of 71 TeV/c^2, which is beyond the reach of direct searches using particle colliders.

1.3. The NL-*e*EDM experiment

In the NL-eEDM experiment [44], the electric dipole moment of barium monofluoride (^{138}Ba^{19}F) molecules in the $X^2\Sigma^+(v = 0, N = 0)$ ground state is measured. This molecule has a total nuclear spin $I = 1/2$, and one valence electron, and consequently a total electron spin of $S = 1/2$. The ground state has a hyperfine level with total angular momentum $F = 1$, which can be used to measure $D^{\vec{P},\vec{T}}$ as described in Equation 1.5. The projection of the electronic angular momentum on the internuclear axis for this ground state is $|\Omega| = 1/2$. The enhancement factors for this molecule have been calculated by Haase *et al.* [34] to be,

$$W_d = 3.13(12) \times 10^{24} \, \text{Hz}/(e \text{ cm}), \quad W_S = 8.29(12) \, \text{kHz}. \tag{1.13}$$

A typical polarisation factor for the molecules in the $N = 0$ ground state of $P(E) = 0.5$ can be reached at an experimentally feasible electric field strength of 10 kV/cm [34].

To reach a competitive sensitivity to the electron electric dipole moment, the use of a slow and intense molecular beam has been proposed. The aim is to combine a long precession time (T) and a large number of detected molecules (N), each boosting the statistical sensitivity of the experiment. The setup designed for this experiment is reviewed in Figure 1.2.
Following the estimates presented in the proposal by Aggarwal *et al.* [44], the detection of 7×10^5 molecules per shot at a repetition rate of 10 Hz should be feasible with this design. This corresponds to $N = 6 \times 10^{11}$ day^{-1}. Following Equation 1.8, at a precession time of 15 ms, this yields a statistical error in the quantum projection limit of,

$$\sigma_{d_e} = 5 \times 10^{-29}\ e\ \text{cm}\sqrt{\text{day}}, \tag{1.14}$$

using the same convention mentioned before to project this limit on the electron electric dipole moment. In the proposed detection scheme using an EMCCD camera with quantum efficiency of 0.5 and at a reasonable spatial collected fraction of 0.1, with 10^3 photons emitted per molecule, the excess noise factor is expected to be $\sqrt{F} = 1.02$, supporting the quantum projection limit estimate. Once appropriate systematic uncertainty is demonstrated, with this setup a sensitivity competitive with current experiments can be reached within a reasonable measurement time.

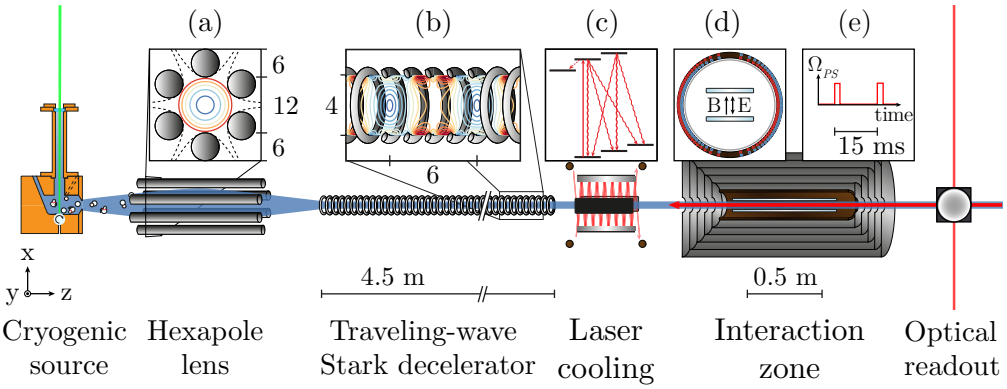

Figure 1.2 | *Proposed setup for the NL-eEDM experiment. A pulsed beam of molecules traverse the setup from left to right. Molecules are produced in a cryogenic buffer gas source, focused into the decelerator using a hexapole lens and longitudinally decelerated to a velocity of 30 m/s. In a transverse laser cooling section the molecular beam is collimated. The spin-precession measurement takes place over a 0.5 m long homogeneous-field region within the interaction zone. State-selective optical readout is performed by laser-induced fluorescence. The insets show: (a) Transverse electric field in the hexapole lens, (b) Electric field traps within the traveling-wave Stark decelerator, (c) Multiple vibrational levels that need to be addressed for laser cooling, (d) (anti) Parallel magnetic and electric fields generated by a double cosine coil and field plates, and (e) Phase evolution time between superposition pulses of 15 ms.*

1.4. Thesis outline and relation to other work

In this thesis I describe my contributions to the NL-eEDM experiment, which can be split into two parts: In the first half of this thesis, the development of the first generation spin-precession experiment of this collaboration is discussed. The main topic of my work was the data acquisition and control system, while working in close collaboration with fellow PhD students responsible for the characterisation of possible systematic effects, Boeschoten [23], a stable electric and magnetic field environment, Meijknecht [45], and manipulation and readout of molecules based on optical techniques, Marshall [37].
In the second half of this thesis, work is described on increasing the statistical sensitivity of a next generation of the experiment by developing a setup to produce an intense and slow molecular beam. This is done by using a traveling-wave Stark decelerator on a molecular beam produced in a cryogenic buffer gas source. The source used in this work has been developed by Esajas [46]. In parallel with this work, a similar source has been characterised and optimised by Mooij [47]. The decelerator has been developed and used previously by van den Berg [48], Meinema [49], Zapara [50], Aggarwal [51], and Mathavan [52].
This thesis is structured as follows:
Chapter 1 - has given a general introduction to the experiment and summarised the motivation for the research program.
Chapter 2 - provides an overview of the spin-precession measurement and describes the characteristics of the molecular signal, which is sensitive to the EDM, while it can also be used to reject many possible systematic biases.
Chapter 3 - demonstrates the structure of the data acquisition and control system that has been developed for the experiment. It discusses the devices used to measure both the signal from the molecules and many background parameters in parallel. In particular, the switching of the electric field direction has been characterised, which plays a central role in the EDM measurement.
Chapter 4 - reviews the operating principle of the traveling-wave Stark decelerator and hexapole lens. It describes the efficiency of the decelerator based on a study of the phase-space acceptance and how to improve the filling thereof by incorporating a hexapole lens between the source and the decelerator.
Chapter 5 - discusses the advances in the deceleration of heavy polar molecules using a traveling-wave Stark decelerator for strontium fluoride. The improvements to the setup are on source reliability, data acquisition, phase-space matching between source and decelerator, and the operation mode of the decelerator while molecules are leaving it.
Chapter 6 - shows the transition in the decelerator setup to barium fluoride, the molecule of choice for the NL-eEDM experiment. The molecular beam produced in the cryogenic source is characterised and the first results of Stark deceleration of BaF are demonstrated.
Chapter 7 - provides the details of the electrostatic lens used for focusing the molecular beam, produced in the cryogenic source, into the decelerator. The molecular beam is imaged on an EMCCD camera at the position where the molecules would enter the decelerator. The effect of the applied voltage on the measured intensity and size of the beam at the detection zone is discussed, and compared to simulations.
Chapter 8 - reviews the main conclusions of this work and discusses the implications on the future work of the NL-eEDM collaboration.

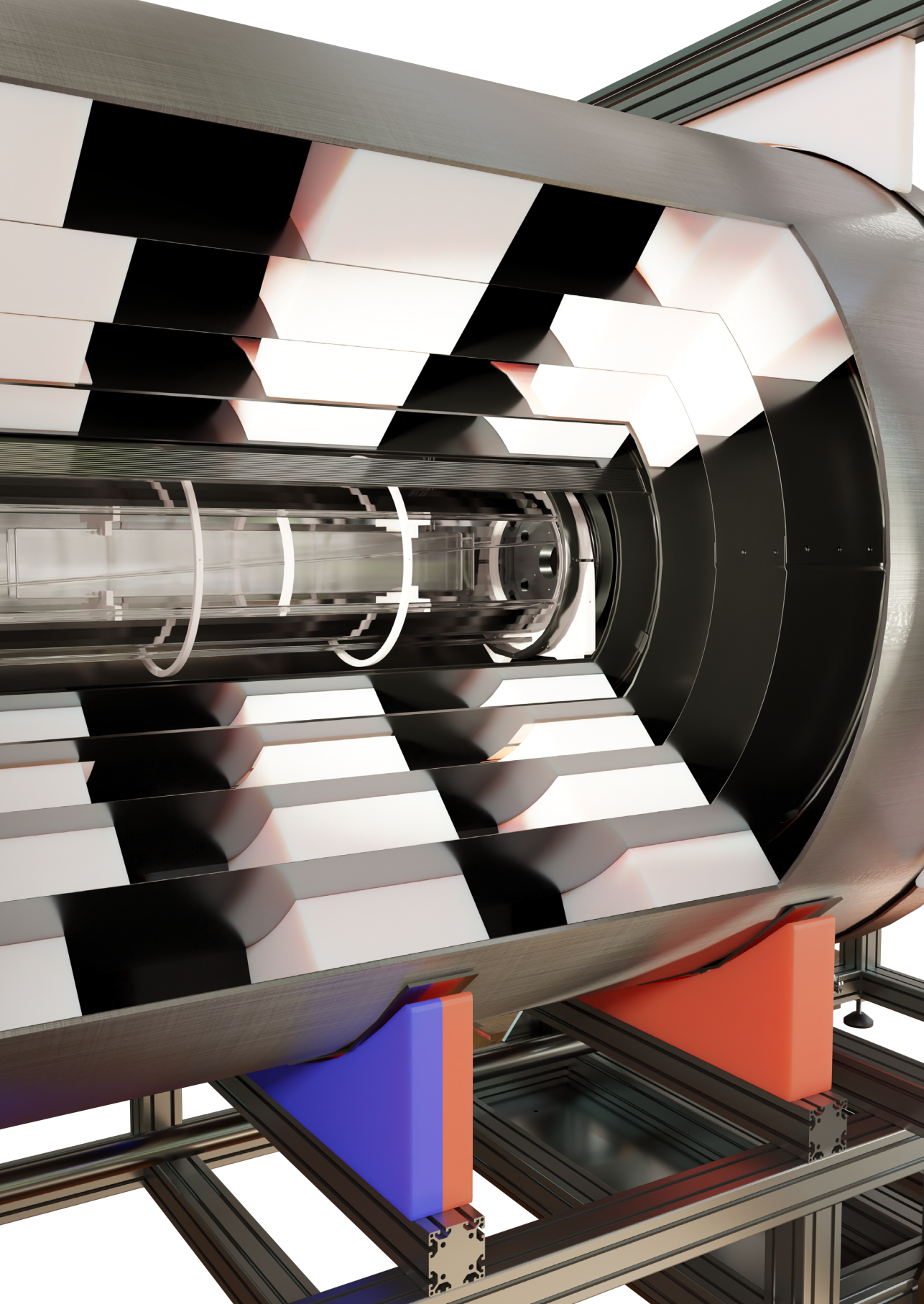

2

Spin-precession method for electric dipole moment searches

To perform a phase evolution experiment sensitive to the CP violating Electic Dipole Moment (EDM) a setup is needed which allows good control of both the state of the molecules on which the experiment is performed, and on the external field environment experienced by these molecules. In the NL-eEDM collaboration such a setup has been developed, nicknamed the *Fast beam* setup, based on a supersonic source producing a pulsed beam of barium monofluoride (BaF) molecules at a longitudinal velocity of 600 m/s. The phase evolution experiment takes place in an interaction zone of good external field control. At the core of this interaction zone are electric field plates with a length of 75 cm, allowing an interaction time on the order of 1 ms.
In this chapter the measurement approach for performing a phase evolution experiment is described, as presented in Boeschoten *et al.* [53]. An analytic description of the interference signal is given. The approach to derive this signal is similar to the one presented for a the eEDM experiment on YbF in Kara *et al.* [54], but adapted to the optical techniques in this experiment. In Boeschoten [23], the interference signal is described in a more accurate numerical approach using the Optical Bloch Equations, taking into account populations and coherences between the ground and excited states involved in this experiment. As the analytic solution can be fitted to the measured signal for data analysis, as will be shown in the next chapter and has been used in Boeschoten *et al.* [53], a review of the description and the necessary assumptions as presented in this chapter is considered valuable.

The chapter image shows the spin-precession region of well controlled magnetic and electric field environment, with partial removal of magnetic field shields and coils to show the inside.

2.1. Optical method approach to phase evolution measurement

To probe the EDM ($D^{\not P,\not T}$) a double-differential measurement is performed that probes the energy difference between hyperfine components of the $X^2\Sigma^+(v = 0, N = 0)$ ground state[1] with $F = 1, m_F = \pm 1$ (see Appendix A for a review of the labeling of states and transitions). The energy difference between these state in an external magnetic (B) and (anti-)parallel electric field (E) is,

$$\Delta W_{EB} = 2\hbar\omega_{EB} = 2(\mu B \pm D^{\not P,\not T} E), \tag{2.1}$$

following Equation 1.4. An overview of the involved states is shown in Figure 2.1. The energy difference is probed by the accumulated phase of a superpostion of these hyperfine components in traversing a region of homogeneous magnetic and electric fields. The (limit on the) EDM is deduced from the difference in accumulated phase in a configuration of parallel and anti-parallel magnetic and electric fields.

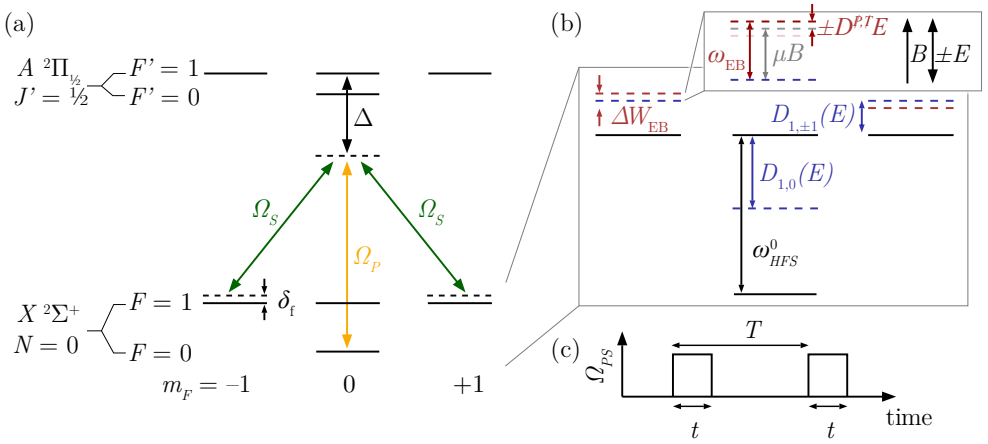

***Figure 2.1** | System description of states and laser pulses for the spin-precession experiment. a) Level scheme of ground and excited states as well as the components of the laser pulses (S and P) coupling these. b) Zoom-in on the ground states showing the shift in magnetic and electric fields. c) Pulse timing and two-photon Rabi frequency. Energy shifts are given as angular frequencies, omitting ħ for clarity. Adapted from Boeschoten* et al. *[53].*

The measurement sequence is graphically described in Figure 2.2, showing the source distribution (a), state preparation (b), phase evolution (c) and readout (d) in an ideal case of perfect state control. The experiment is based on a molecular pulse, which traverses the sequence based on its position in the setup. The laser pulses, counter-propagating to the

[1] Unless specified otherwise, only molecules in the lowest vibrational state ($v = 0$) are considered in this work. Molecules from excited vibrational states could be brought into states that contribute to the measurement by optical cycling, as will be done for the vibrational repumping during laser cooling and is planned as an upgrade.

molecular beam, that create and collapse the superposition state are timed to perform the phase evolution step in the field controlled region, with a timing scheme as illustrated in Figure 2.1c. In this section the relevant processes are summarised to give the background for the rest of the chapter.

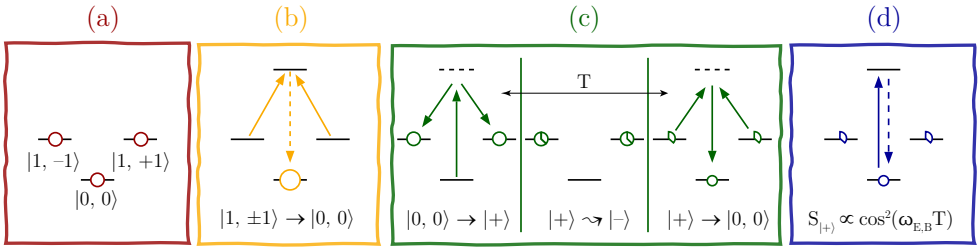

***Figure 2.2** | Basic principle of the measurement sequence. Molecules traverse the sequence from left to right, showing the source distribution (a), state preparation (b), phase evolution (c) and readout (d). Ground states in the $X^2\Sigma^+(N = 0)$ are labeled by $|F, m_F\rangle$ or the superposition thereof introduced in Equation 2.2.*

Source - Molecules are formed in a supersonic source which is described in Aggarwal *et al.* [55]. A mixture of sulfur hexafluoride and an argon carrier gas is released into vacuum using an Even-Lavie valve. The BaF molecules are formed in the reaction with barium from the ablation of a metal target with an Nd:YAG laser. A molecular pulse is produced at a typical repetition rate of 10 Hz used as a trigger for the experiment sequence. The molecular pulse has been shown to have an average longitudinal velocity of 610(4) m/s and relative velocity spread of 0.054(9) [55].

Optical pumping - Molecules in the beam are distributed over many rotational and vibrational states. To increase the number of molecules in the $X^2\Sigma^+(N = 0)$ state in which the experiment is performed, molecules from excited states are optically pumped to this state. By traversing a laser field resonant with a transition from $X^2\Sigma^+(N = 2)$ to $A^2\Pi_{1/2}(J = 1/2)$ and spontaneous emission more molecules are brought into states that take part in the measurement.

State preparation - By interaction with another laser field, molecules are pumped from the $X^2\Sigma^+(N = 0, F = 1)$ to $A^2\Pi_{1/2}(J = 1/2)$ to empty this ground state where the superposition is to be created, with a typical efficiency of 80%. The implementation of optical pumping, state preparation and many other optical methods used in this experiment are described in Marshall [37].

Interaction zone - Molecules enter the interaction zone of small, $O(10$ nT), and homogeneous, $O(10$ pT), magnetic field obtained by a five-layer μ-metal shield. The well controlled magnetic field is created using a double cosine coil that generates a magnetic field in the horizontal direction orthogonal to the propagation axis of the molecular beam. In the innermost shield an electric field, $O(10$ kV/cm), with homogeneity $\Delta E/E < 10^{-4}$, is generated by applying voltages on two indium-tin-oxide (ITO) coated plates of 75 cm length. The field

environment for the experiment is described in Meijknecht [45].

Superposition creation - A pulsed counter-propagating laser beam couples the $|F, m_F\rangle = |0,0\rangle$ state of the molecules via a two-photon transition to the $|+\rangle$ superposition of $|1,+1\rangle$ and $|1,-1\rangle$, defined as,

$$|+\rangle = \Big(|1,-1\rangle + |1,+1\rangle\Big)/\sqrt{2}, \quad |-\rangle = \Big(|1,-1\rangle - |1,+1\rangle\Big)/\sqrt{2}. \tag{2.2}$$

The $|-\rangle$ state is the orthogonal superposition reached by spin-precession in the interaction zone, but is dark to this light pulse as a result of the chosen polarisation. The process of creating the $|+\rangle$ superposition is crucial to the measurement and will be described in more detail in section 2.2. The optical implementation can be found in Marshall [37].
When the two-photon Rabi frequency Ω_{PS} and the pulse length t are set such that $\Omega_{PS}t = \pi$, all molecules in the $F = 0$ state are brought to the superposition in the previously emptied $F = 1$ state. This is referred to as a π-pulse.

Phase evolution - The superposition precesses under the influence of the magnetic field between the $|+\rangle$ and $|-\rangle$ configuration, with a possible contribution of the EDM. The velocity of the molecular beam and the dimensions of the electric field plates and homogeneous field region set the maximum precession period that can be achieved. For this experiment the interaction time T is typically 1 ms.
The phase build-up between the $|+\rangle$ and $|-\rangle$ superposition is,

$$|\psi(T)\rangle = \cos(\omega_{EB}T)\,|+\rangle - i\sin(\omega_{EB}T)\,|-\rangle\,. \tag{2.3}$$

The most sensitive point of the signal to phase differences (due to the EDM) is where,

$$\cos^2(\omega_{EB}T) = \sin^2(\omega_{EB}T) = 1/2. \tag{2.4}$$

As the contribution of the EDM is a small perturbation in the precession frequency $\omega_{EB} = (\mu B \pm D^{\mathcal{P},\mathcal{T}}E)/\hbar$, the most sensitive point is governed by the magnetic field, and occurs when,

$$\mu BT/\hbar = \pi/4 + k\pi, \quad k \in \mathbb{Z}. \tag{2.5}$$

Sensitive points for higher $|k|$ are increasingly impacted by field inhomogeneity. For $k = 0$ the magnetic field required for this experiment is $|B| \approx 8$ nT. For longer interaction times, reached with slower beams, the magnetic field has to be even smaller.

Superposition projection - Similar to the laser pulse for superposition creation, a second laser pulse interacts with the molecular beam at the end of the interaction zone, projecting the $|+\rangle$ superposition back to the $|F, m_F\rangle = |0,0\rangle$ state.

Readout - Molecules are detected by laser-induced fluorescence by traversal of an orthogonal laser beam which is set to excite molecules from either the $F = 0$ or the $F = 1$ substates of the $X^2\Sigma^+(N = 0)$ to $A^2\Pi_{3/2}(J = 1/2)$. The fluorescence of these molecules is detected on a photomultiplier tube (PMT) and provides the signal corresponding to the $|+\rangle$ or $|-\rangle$ superposition after phase evolution respectively.

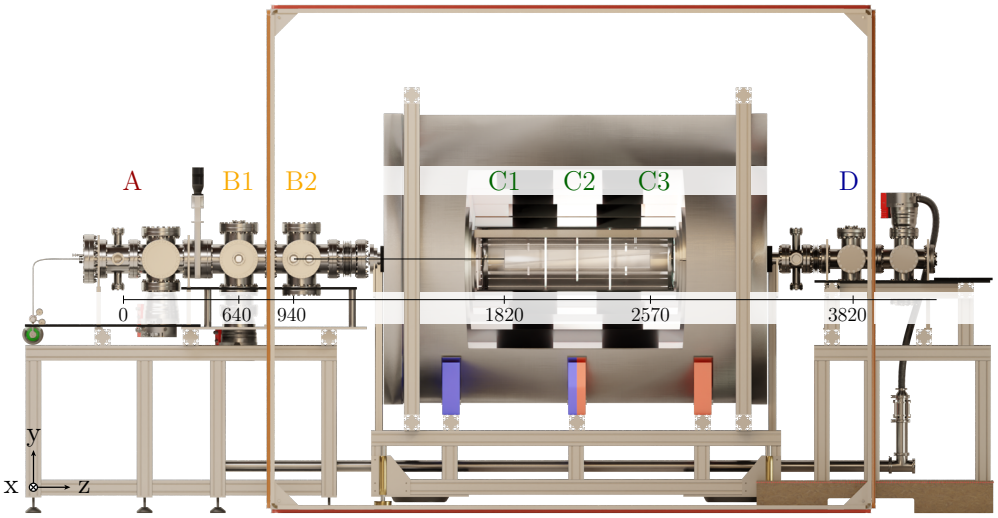

Figure 2.3 *| Schematic overview of the setup. Molecules traverse the setup from left to right. Optical and electronic elements are omitted for clarity. The opening in the side of the μ-metal shield and cosine coil is to show the inside where the glass tube vacuum chamber is, that houses the electric field plates. The rectangular frame around the interaction zone shows the three pairs of rectangular compensation coils described in Meijknecht [45]. The superposition creation and projection pulse is implemented as a counter-propagating laserbeam in this image traversing right to left. Distance from the source nozzle given in mm.*
The labeled sections are related to the experiment sequence described above as follows: (A) Source, (B1) Optical pumping, (B2) State preparation, (C) Interaction zone with (C1) Superposition creation (C2) Phase evolution (C3) Superposition projection, (D) Readout.

2.2. Analytic model

An analytical model will be discussed here to improve the understanding of the interference signal and its dependence on many experimental parameters. The approach is similar that of Kara *et al.* [54], which provides an analytic model for the EDM experiment on a molecular beam of YbF. As our experiment is based on optical instead of radio-frequency techniques a review is considered useful. A more complete description based on numerical diagonalisation of the Hamiltonian to describe the states in electric and magnetic fields and population dynamics in laser fields using optical Bloch equations can be found in Boeschoten [23].
In the analytical model, the state of the molecule is described based on a sequence of evolution operators corresponding to the elements of the spin-precession measurement procedure. The model describes the population in the main hyperfine components of the $X^2\Sigma^+(N=0)$ ground state partaking in the measurement. As the superposition is created and projected via a two-photon transition, one exited state, labeled $|e\rangle$, is also considered. The set of states considered in this model in the $|F, m_F\rangle$-basis is,

$$|\psi\rangle_{F,m_F} = \Big\{|0,0\rangle, |1,-1\rangle, |1,+1\rangle, |e\rangle\Big\}. \tag{2.6}$$

In a region with (anti-)parallel electric and magnetic field these are energy eigenstates and the Hamiltonian is diagonal,

$$H^0_{F,m_F} = \mathrm{diag}(-\hbar\omega_{00}, \hbar\omega_{EB}, -\hbar\omega_{EB}, \hbar\omega_e). \tag{2.7}$$

The zero point of energy is taken at the center between $|1,+1\rangle$ and $|1,-1\rangle$. The shift $\omega_{00} = \omega^0_{HFS} + D_{1,\pm1}(E)$ consists of the zero-field hyperfine splitting of the ground state and the tensor Stark shift, see Figure 2.1.

Superposition - As the polarisations of the light fields are chosen to couple to the superposition, it is useful to consider the superposition $|\pm\rangle$-basis for the coupling of the fields.

$$|\psi\rangle_\pm = \left\{|0,0\rangle, |+\rangle, |-\rangle, |e\rangle\right\}, \tag{2.8}$$

with the superposition states $|\pm\rangle$ defined in Equation 2.2. The superposition and $|F, m_F\rangle$-basis are therefore linked by the unitary transformation,

$$U = \begin{pmatrix} 1 & & & \\ & 1/\sqrt{2} & 1/\sqrt{2} & \\ & 1/\sqrt{2} & -1/\sqrt{2} & \\ & & & 1 \end{pmatrix}, \tag{2.9}$$

where $|\psi\rangle_\pm = U|\psi\rangle_{F,m_F}$. The zero elements are omitted for clarity. The Schrödinger equation, $i\hbar\frac{d}{dt}|\psi\rangle = H|\psi\rangle$, is invariant under any unitary transformations ($|\psi\rangle' = U|\psi\rangle, U^{-1} = U^\dagger$), where the transformation of the Hamiltonian is given by,

$$H' = UHU^{-1} - i\hbar U\frac{d}{dt}U^{-1}. \tag{2.10}$$

For this time-independent transformation, the last term is zero, but later on the general expression will be used.

Light fields - To make a two-photon transition, the light pulse consisting of light fields P and S are interacting with the molecules. Their polarisations are chosen to be orthogonal, such that P couples $|0,0\rangle$ and $|e\rangle$, while S couples $|+\rangle$ and $|e\rangle$, as illustrated in Figure 2.1. The Hamiltonian for the molecules coupled by these light fields is therefore,

$$H_\pm = \hbar\begin{pmatrix} -\omega_{00} & & & \Omega_P\cos(\omega_P t+\phi_P) \\ & & \omega_{EB} & \Omega_S\cos(\omega_S t+\phi_S) \\ & \omega_{EB} & & \\ \Omega_P\cos(\omega_P t+\phi_P) & \Omega_S\cos(\omega_S t+\phi_S) & & \omega_e \end{pmatrix}. \tag{2.11}$$

The angular frequencies of each laser beam P/S are $\omega_{P/S}$ and the phase offsets $\phi_{P/S}$. The Rabi frequencies $\Omega_P = -\langle x|\vec{\mu}_e|e\rangle\hat{e}_P E_P/\hbar$ and $\Omega_S = -\langle 0,0|\vec{\mu}_e|e\rangle\hat{e}_S E_S/\hbar$ are given by the dipole coupling of the states, their polarisation $\hat{e}_{P/S}$ and the intensities of the beams.

Rotating wave approximation - The explicit time dependence of the Hamiltonian can be shifted to the parameters describing the state of the molecule by transferring to a rotating frame. This is done by a unitary transformation with component $U_{ab} = \exp\big(i\xi_a(t)\big)\delta_{ab}$. Following the transformation of the Hamiltonian (Equation 2.10), the components of the Hamiltonian in the rotating frame become, $H'_{ab} = H_{ab}\exp\big(i(\xi_a - \xi_b)\big) - \hbar\delta_{ab}\, d\xi_a/dt$, where δ_{ab} is the Kronecker delta. After a transformation with the phases chosen as $\xi_1 = -\omega_{00}t, \xi_2 = \xi_3 = \xi_1 + \omega_P t + \phi_P - \omega_S t - \phi_S$ and $\xi_4 = \xi_1 + \omega_P t + \phi_P$, the Hamiltonian in the rotating frame is,

$$H'_{\pm} = \hbar\begin{pmatrix} & & & \frac{\Omega_P}{2}\big(1 + e^{-2i(\omega_P t+\phi_P)}\big) \\ & -\delta_f & \omega_{EB} & \frac{\Omega_S}{2}\big(1 + e^{-2i(\omega_S t+\phi_S)}\big) \\ & \omega_{EB} & -\delta_f & \\ \frac{\Omega_P}{2}\big(1 + e^{2i(\omega_P t+\phi_P)}\big) & \frac{\Omega_S}{2}\big(1 + e^{2i(\omega_S t+\phi_S)}\big) & & \Delta \end{pmatrix}. \quad (2.12)$$

At optical frequencies the terms $\exp\big(\pm 2i(\omega_{P/S}t + \phi_{P/S})\big)$ are rapidly oscillating and can be neglected following the rotating wave approximation. In this approximation the explicit time dependence of the Hamiltonian is removed in the rotating frame.
The detuning from the excited state $\Delta = \omega_{00} + \omega_e - \omega_P$ and two-photon detuning $\delta_f = \omega_P - \omega_S - \omega_{00} \equiv \omega_{PS} - \omega_{00}$ are illustrated in Figure 2.1.

Effective two-photon system - Consider the parametrization of the state vector in the rotating frame $|\psi\rangle'_{\pm} = (c'_1, c'_2, c'_3, c'_4)$. The Schrödinger equation with the Hamiltonian in the rotating wave approximation $H'_{\pm}$ provides,

$$\frac{dc'_4}{dt} = -i\frac{\Omega_P}{2}c'_1 - i\frac{\Omega_S}{2}c'_2 - i\Delta c'_4. \quad (2.13)$$

For large detuning $\Delta \gg \Omega_P, \Omega_S$ this produces a rapid oscillation in the excited state in which we are not interested, $c'_4(t) \approx \exp\big(-i\Delta t\big)c'_4(0)$. One can consider the average instead, where $d\bar{c}'_4/dt = 0$. The resulting solution of Equation 2.13 can be used to rewrite the rest of the system of equations to be corresponding to an effective three level Hamiltonian. This procedure is called adiabatic elimination [23]. After inversion of the unitary transformation back to the non-rotating $|\pm\rangle$-basis, now reduced to $|\psi\rangle_{\pm} = \Big\{|0,0\rangle, |+\rangle, |-\rangle\Big\}$, the effective Hamiltonian takes the form,

$$H^{\text{eff}}_{\pm} = \hbar\begin{pmatrix} -\omega_{00} - \frac{\Omega_P^2}{4\Delta} & -\frac{\Omega_P\Omega_S}{4\Delta}e^{i(\omega_{PS}t+\phi_{PS})} & \\ -\frac{\Omega_P\Omega_S}{4\Delta}e^{-i(\omega_{PS}t+\phi_{PS})} & -\frac{\Omega_S^2}{4\Delta} & \omega_{EB} \\ & \omega_{EB} & \end{pmatrix}. \quad (2.14)$$

It can be seen from this that there is an effective coupling between the state $|0,0\rangle$ and the superposition $|+\rangle$ with frequency $\omega_{PS} = \omega_P - \omega_S$, phase offset $\phi_{PS} = \phi_P - \phi_S$ and two-photon Rabi frequency $\Omega_{PS} = -\Omega_P\Omega_S/2\Delta$. Also the energy corresponding to the states $|0,0\rangle$ and $|+\rangle$ are shifted by $-\Omega_P^2/4\Delta, -\Omega_S^2/4\Delta$ respectively, knows as a light shift. The dark superposition $|-\rangle$ is not shifted.

Solving the system - Unfortunately, the effective three level system described by Equation 2.14 has no general analytic solution. In order to find the time evolution operator, the system is split in a two level and one level system instead. During the superposition pulses, the coupling between $|0,0\rangle$ and $|+\rangle$ by the light fields is dominant, while during the free phase evolution the coupling between $|+\rangle$ and $|-\rangle$ by the magnetic and electric field is crucial.
To find the solution to this system, the two regimes have to be considered separately, by setting the light fields to zero ($\Omega_P, \Omega_S = 0$) or by considering a region of zero magnetic and electric field ($\omega_{EB} = 0$). In these regimes, the system of differential equations following from the time dependent Schrödinger equation can be solved explicitly. With a significant amount of algebra, the solution can be found in terms of an initial state vector $|\psi(t_0)\rangle_\pm$, in the form of a time evolution operator, $|\psi(t_0+t)\rangle = \Pi(t_0,t)\,|\psi(t_0)\rangle$, that describes the evolution of the state from initial time t_0 after a period t.

Phase evolution - First consider the region of phase evolution, where spin-precession takes place due to the energy difference between the hyperfine substates in the presence of a magnetic and electric field. The region is traversed during a time $T-t$ between the light pulses, ($\Omega_P, \Omega_S = 0$). The time evolution operator over this period is,

$$\Pi_\pm^{EB}(t_0, T-t) = \begin{pmatrix} e^{i\omega_{00}(T-t)} & & \\ & \cos\left(\omega_{EB}(T-t)\right) & -i\sin\left(\omega_{EB}(T-t)\right) \\ & -i\sin\left(\omega_{EB}(T-t)\right) & \cos\left(\omega_{EB}(T-t)\right) \end{pmatrix}. \tag{2.15}$$

Superposition pulse - To find the evolution during the superposition pulses, the coupling due to the energy difference in a magnetic and electric field is neglected ($\omega_{EB} = 0$). Typical time scales and the validity of this description will be discussed later. In this regime, the time evolution operator over a light pulse starting at t_0 of length t is given by,

$$\Pi_\pm^{2p}(t_0,t) = \begin{pmatrix} \cos\left(\frac{Wt}{2}\right) - i\frac{\delta}{W}\sin\left(\frac{Wt}{2}\right) & -i\frac{\Omega_{PS}}{W}\sin\left(\frac{Wt}{2}\right)e^{i\tilde{\phi}_{PS}} & \\ -i\frac{\Omega_{PS}}{W}\sin\left(\frac{Wt}{2}\right)e^{-i(\tilde{\phi}_{PS}+\omega_{PS}t)} & \left[\cos\left(\frac{Wt}{2}\right) + i\frac{\delta}{W}\sin\left(\frac{Wt}{2}\right)\right]e^{-i\omega_{PS}t} & \\ & & e^{-i\omega_- t} \end{pmatrix}, \tag{2.16}$$

where the generalised Rabi frequency $W = \sqrt{\Omega_{PS}^2 + \delta^2}$ consists of the two-photon Rabi frequency and the light-shifted two-photon detuning $\delta = \omega_{PS} - \omega_{00} - \Omega_P^2/4\Delta + \Omega_S^2/4\Delta$. The phase $\tilde{\phi}_{PS} = \omega_{PS}t_0 + \phi_{PS}$ is the effective phase offset of the light fields at the start of the pulse. $\omega_- = \delta/2 - \Omega_S^2/4\Delta$ is introduced for short. From comparison to Kara *et al.* [54] the analogy to a radio frequency pulse is clear.

Interference fringe - To find the analytic expression for the interference fringe resulting from the experiment sequence the time evolution operators are applied consecutively. The final state of a molecule that has undergone an superposition creation pulse, phase evolution and a superposition collapse pulse as described by the experiment timing described in Figure 2.1c is,

$$\begin{aligned} |\psi(t_0+T+t)\rangle_\pm &= \Pi_\pm^{2p}(t_0+T,t)\Pi_\pm^{EB}(t_0+t,T-t)\Pi_\pm^{2p}(t_0,t)\,|\psi(t_0)\rangle_\pm\,, \\ &\equiv \Pi_\pm(t_0,T+t)\,|\psi(t_0)\rangle_\pm\,. \end{aligned} \tag{2.17}$$

The probability of finding a molecule that was in the $|F, m_F\rangle = |0,0\rangle$ state before the first pulse, in the same state after the second pulse can be calculated to be,

$$\begin{aligned} P_{F=0} &= |\langle 0,0|\,\Pi_{\pm}(t_0, T+t)\,|0,0\rangle|^2, \\ &= \left|\left[\cos\left(\frac{Wt}{2}\right) - i\frac{\delta}{W}\sin\left(\frac{Wt}{2}\right)\right]^2 - \frac{\Omega_{PS}^2}{W^2}\sin^2\left(\frac{Wt}{2}\right)e^{i\delta_f(T-t)}\cos(\phi_{EB})\right|^2. \end{aligned} \tag{2.18}$$

Here $\phi_{EB} = \omega_{EB}(T-t)$ corresponds to the EDM sensitive phase. The signal for detecting molecules in the $F = 0$ during detection is therefore proportional to this expression. As the model describes a closed system, the probability of finding a molecule in $F = 1$ is $P_{F=1} = 1 - |\langle 0,0|\,\Pi_{\pm}(t_0, T+t)\,|0,0\rangle|^2$.

Model validity - As with any model, there are a number of simplifications and assumptions made in this description of the interference signal. These have implications on the validity of the model, and are therefore discussed over the course of this derivation. A couple of related observations are summarised here.

Due to imperfections in the emptying of the $F = 1$ state before creating the superposition, an offset signal is present in the experiment, that limits the contrast. This will be discussed in the next section.

In Equation 2.18, the accumulated phase $\phi_{EB} = \omega_{EB}(T-t)$ includes possible signals due to the EDM. The interaction time in this equation is limited to the time between the pulses as the shift during the pulses is neglected. This is a good approximation for short pulse lengths, but for a more complete solution the optical Bloch equation (OBE) model in Boeschoten [23] has to be considered. In the experiment, the pulses are typically tens of microseconds long, to allow for state transfer close to π-pluses at intensities of hundreds of mW/cm for a beam diameter of a centimeter [37].

Another simplification in this model is in the excited state structure, which was simplified here to a single state, without consideration of the structure and field shifts thereof. Due to the large excited state detuning Δ, typically 1 GHz, the structure of these states is of limited importance.

Furthermore, the contributions from the $|1,0\rangle$ ground state are not considered in this model. This state plays a limited role due to the tensor Stark shift and choice of polarisation. In the OBE model [23] all eight substates in Figure 2.1 are taken into account.

In Kara *et al.* [54], an arbitrary phase difference Φ_{rf} between the pulses is considered. In the experiment described in this work the superposition pulses to create and project the superposition originate from the same laser. The phase decoherence between the pulses is expected to be minimal at the relevant timescale and this phase is neglected. An explicit phase difference could be added if needed.

As the molecular pulse is counter-propagating to the superposition laser pulses, the molecules experience a significant Doppler shift due to their velocity. However, as the frequency difference $\omega_P - \omega_S \approx \omega_{HFS}^0$ is small relative to the optical frequency, the Doppler shift of the two-photon frequency ω_{PS} is only of the order of 100 Hz, corresponding to a shift of several Hz between slow and fast molecules for a relative velocity spread of 0.054(9) [55]. The Doppler shift of the exited state detuning Δ does not cancel, and is approximately 700 MHz for mean longitudinal beam velocity of 610(4) m/s [55]. For a detuning of approximately

1 GHz this results in a difference of a few percent for over the velocity spread of molecular beam with corresponding difference in two-photon Rabi frequency [23].
In the model the electric and magnetic field are assumed to be (anti-)parallel, corresponding to the relative sign in ω_{EB}. The contribution of the phase due to orthogonal field components and the effect of the related motional magnetic field are discussed in Meijknecht [45].
The impact of the variation of many parameters, such as pulse timings, intensity variation and asymmetries in the pulse intensity between the pulses are investigated theoretically in Boeschoten [23] and experimentally in Marshall [37]. These model can be expanded to include these by differentiation of the parameters corresponding to each of the pulses.

2.3. Signal and contrast

The probability in Equation 2.18 can not be directly measured. In the experiment, photon pulses are counted related to the number of molecules in a specific state in the detection zone in section D of the setup, as labeled in Figure 7.4. Currently the signal from a single hyperfine substate, usually the $F = 1$, is measured, via the $X^2\Sigma^+(N = 0)$ to $A^2\Pi_{3/2}(J = 1/2)$ transition, but effort is put in an upgrade where the population in the $F = 0$ state is probed in the same shot. As the molecular signal is pulsed, the background signal is measured during a time window in the experiment sequence when no molecules are in the detection zone, as discussed in subsection 3.2.1. This background is subtracted in the analysis.
A major contribution to the variation in the number of molecules in the detection zone is due to the variations in the molecule production of the supersonic source. This is compensated for by normalisation to the signal measured in section B1, before the spin-precession [56]. Here the laser-induced fluorescence signal is probed on a PMT due to excitation on the $X^2\Sigma^+(N = 1)$ to $A^2\Pi_{3/2}(J = 5/2, 3/2)$ transitions [37].
Typically, this normalised signal ($S_{F=1}$) is measured for multiple effective two-photon frequencies around the resonance ($\delta = 0$), by varying the laser frequency of the P wave contribution to the interference pulses. Experimentally this is done with the help of an Acousto-optic modulator (AOM), scanning $\omega_P/2\pi$ over a range of a couple of kHz relative to the frequency $\omega_S/2\pi$, as discussed in subsection 3.2.5. A simulated spin-precession spectrum is shown in Figure 2.4, illustrating the expected pattern for typical experimental parameters. In this simulated spectrum the frequency offset can be subtracted easily to center the pattern at zero. As this resonance frequency is strongly dependent on the electric field, it will be used in subsection 3.3.2 to analyse the electric field conditions within the interaction zone.
The analytic description of the spin-precession spectrum in Equation 2.18 is fitted to the measured signal, with an amplitude a and offset b,

$$S_{F=1} = a \times P_{F=1} + b, \tag{2.19}$$

The amplitude is related to the number of molecules taking part in the measurement, the offset is due to the imperfect emptying of the $F = 1$ before the spin-precession sequence in the hyperfine pumping. In Figure 2.4 the signal is simulated for $a/b = 10$. The amplitude and offset are used to define a contrast C between 0 and 1, by $C = S_{F=1}/(a + 2b)$ [37], used on the vertical axis of the spin-precession spectra.
The analytic model will be used to analyse the electric field amplitude equivalence between the configuration with parallel and antiparallel electric field relative to the magnetic field in

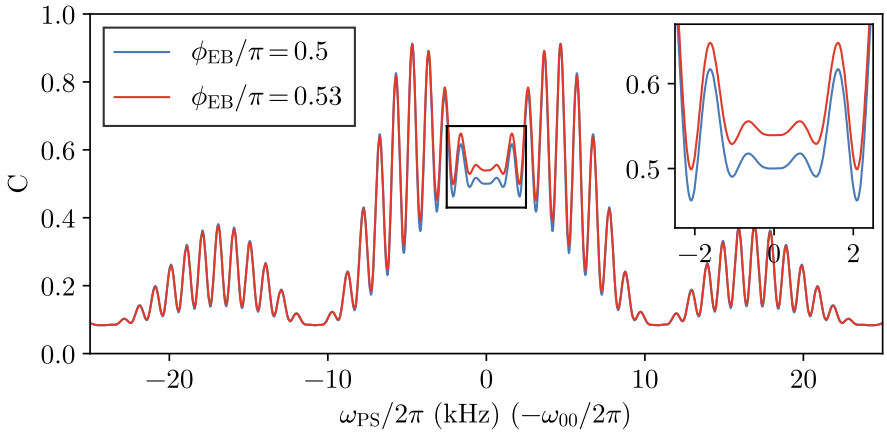

***Figure 2.4** | A simulated spectrum for molecules in the $F = 1$ at the end of the spin-precession sequence, based on the analytic model in Equation 2.18. The frequency is offset by $\omega_{00}/2\pi$, corresponding to the energy splitting of the $F = 0$ and $F = 1$. In this spectrum the pulse length is set to $t = 80\,\mu s$, the time between pulse beginnings $T = 1$ ms and $\Omega_{PS}t = \pi$. The (exaggerated) difference in phase ϕ_{EB} between blue and red shows the characteristics of an EDM signal, in the case where each would correspond to a opposite direction of electric relative to magnetic field.*

section 3.4. In Boeschoten *et al.* [53] the impact of the superposition pulse intensity and the electric field amplitude have been investigated and characterised based on a fit of the analytic model to the experimental data in which these were actively varied. In that work is has been shown that taking a signal over a variety of effective two-photon frequencies provides insights on the environment of the experiment, and the related systematic effects, with minimal loss of sensitivity to the electric dipole moment signal. The fit of the analytic model can be used to interpret the difference in accumulated phase ϕ_{EB} to set a limit on the electric dipole moment, while the match between the model and the data demonstrates the systematic uncertainty to many parameters.

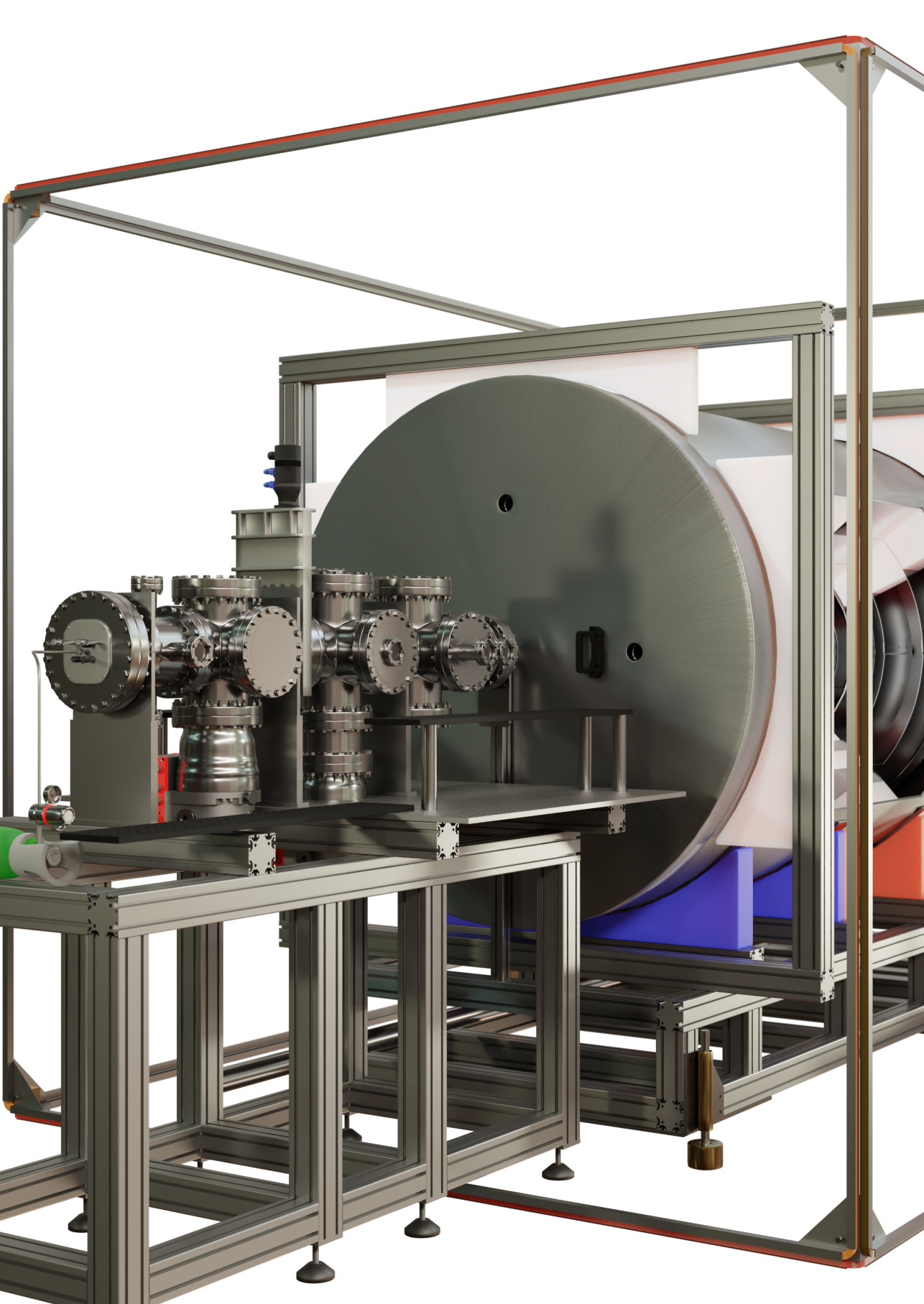

3

Data acquisition and control

The electron Electric Dipole Moment (EDM) measurement is a differential measurement between experiments with opposite contribution of the CP-violating term to the phase build-up due to the reversal of the electric field orientation relative to the magnetic field. The systematic sensitivity is based on the equivalence between the experiments except for this reversal of field orientations, which is pursued by stabilising the environment and operation conditions of the experiment. To validate this equivalence, many parameters are monitored besides the signal proportional to the EDM. In Boeschoten *et al.* [53] the strategy was discussed to use optical techniques to probe multiple parameters using the molecular signal with a limited reduction of EDM sensitivity, minimising the loss of measurement time spend on explicit background measurements.
In this chapter, the development of the setup for performing this symmetric experiment is discussed, with a focus on the data acquisition system (DAQ) developed for this experiment. The system is designed to monitor parameters which cannot be inferred directly from the molecular signal, as well as parameters used as cross reference for the parameters included in the signal. It follows the same shot-based structure as the rest of the experiment. Furthermore, the control system is discussed which is responsible for, among others, the field orientation reversal. The implementation of this introduced asymmetry is laid out in detail, the performance of the switching system is characterised and feasible timescales for the switching are investigated.

The chapter image shows the NL-eEDM measurement setup with molecular beam produced by a supersonic buffergas source.

3.1. Data collection approach

As described in chapter 2, the molecular signal which is to be used to deduce a limit on the electron Electric Dipole Moment depends on many parameters. A data acquisition system (DAQ) has been developed which monitors many of these parameters, either through auxiliary measurements or deduced from the molecular signal itself. Understanding the relations of the molecular signal to these experimental parameters plays a crucial role in validating the accuracy of the EDM measurement.

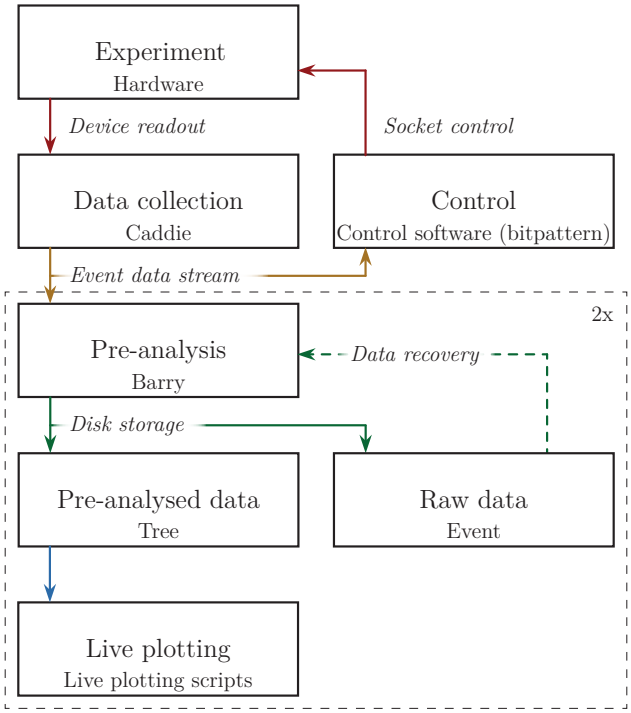

***Figure 3.1** | Data acquisition readout structure showing the modular nature of the (software) blocks and their communication interfaces. The processes in the dashed box are performed in two computers in parallel for redundancy and ease of operation of the experiment.*

The system is designed to be highly adaptable and expandable by its modular nature. A structure is setup with a network of independently operating readout devices that send data to a central real-time pre-analysis and storage location. Live plotting and experiment control are again performed by separate systems. These systems use the data stream as triggers for updating the plots and changing the state of the experiment. Apart from contributing to the robustness of the data collection system itself, this has also turned out to be important for running the experiment during its continuous development. The overall structure of the data acquisition system is illustrated in Figure 3.1.

The data collection is based on the Caddie [57] data acquisition software, which has been developed as a modular readout system suitable for setting up a network of devices, mostly in the Versa Module Eurocard bus, VMEbus. It has been expanded to include other devices in a compatible data collection framework described in more detail in section 3.2. The data is collected in full device readouts as structured streams of 32 bit words, called events. Over a local network the events are gathered at a central Caddie instance, which redistributes it to control devices as an update trigger and to the two parallel data processing instances as illustrated in Figure 3.1.

The event data is sent to a pre-analysis software package which we have developed for this experiment under the name Barry. This analyser saves the event data stream in its event structure as a raw data file. This raw data file can be used as a replacement for the Caddie data stream, to ensure any (pre-)analysis improvements can be used for previously taken datasets as well.

The Barry system also records the data from the events to buffers corresponding to the different data acquisition channels. Simple pre-processing operations, which may be done in real-time and on a shot level, are also performed in this system as discussed in the next sections. These buffers are then flushed to a file containing a ROOT [58] TTree data structure, referred to as the data-tree. Data saving is performed after analysis of each event corresponding to data from alcatraz-VME012, as this is the last device in the shot-synchronised readout sequence. In the data-tree, the data is structured per molecular shot for the synchronous data streams, and the best estimate thereof for the asynchronous data streams, by combining the latest events of each of the devices. The data is sorted in branches, containing leaves grouped by readout device. Each device readout comes with a timestamp. This timestamp is stored to the data as well, which is used to check the readout rate of these devices during analysis.

The pre-analysis device identification and processing parameters are based on a user interface accessible configuration file structure with embedded version control. This ensures the possibility to reconstruct the software state of previous measurements, as well as version control of the software itself. The user interface allows for ease of operation.

Live plotting scripts read the latest version of the data-tree as an input for the display. During measurement runs the experiment is monitored from the control room or remote access thereof, thereby not disturbing the data acquisition branch in the lab and the experiment itself. The data-tree is also used for data analysis afterwards. Here the parameters are read to buffers corresponding to the physics parameters, as listed in Appendix C and Figure 3.2.

The system is set up to be continuously running and recording the status of the experiment. Daily at 6 am local time, new raw and pre-analysed data files are started automatically. The typical data rate after file compression is about 1 GB per day. The data files are also backed-up daily on a Network Attached Storage (Synology DS918+). For analysing specific measurements and synchronisation to the logbook, an experiment tag (ExpPa0, ExpCn0) is stored in the data which is updated automatically every two hours, but can also be updated manually if needed, as will be discussed in subsection 3.2.6.

The system has been setup to be robust, automatic and user friendly to make it not just reliable now, but ready to be used for future experiments. The modular structure also ensures expandability with new software and hardware modules. Details of multiple components in the system are discussed in the next sections.

3.2. Data acquisition

The core of the data acquisition system is formed around two VMEbus systems located in the laserlab, where the optics systems are situated, and the Alcatraz-lab[1], where the molecular beam experiment takes place. Each of these VMEbus crates house a CPU arbiter (Men A19 VME) on which Caddie instances are running that gather data from the modules and send it over the local network to the centralised data acquisition PC.

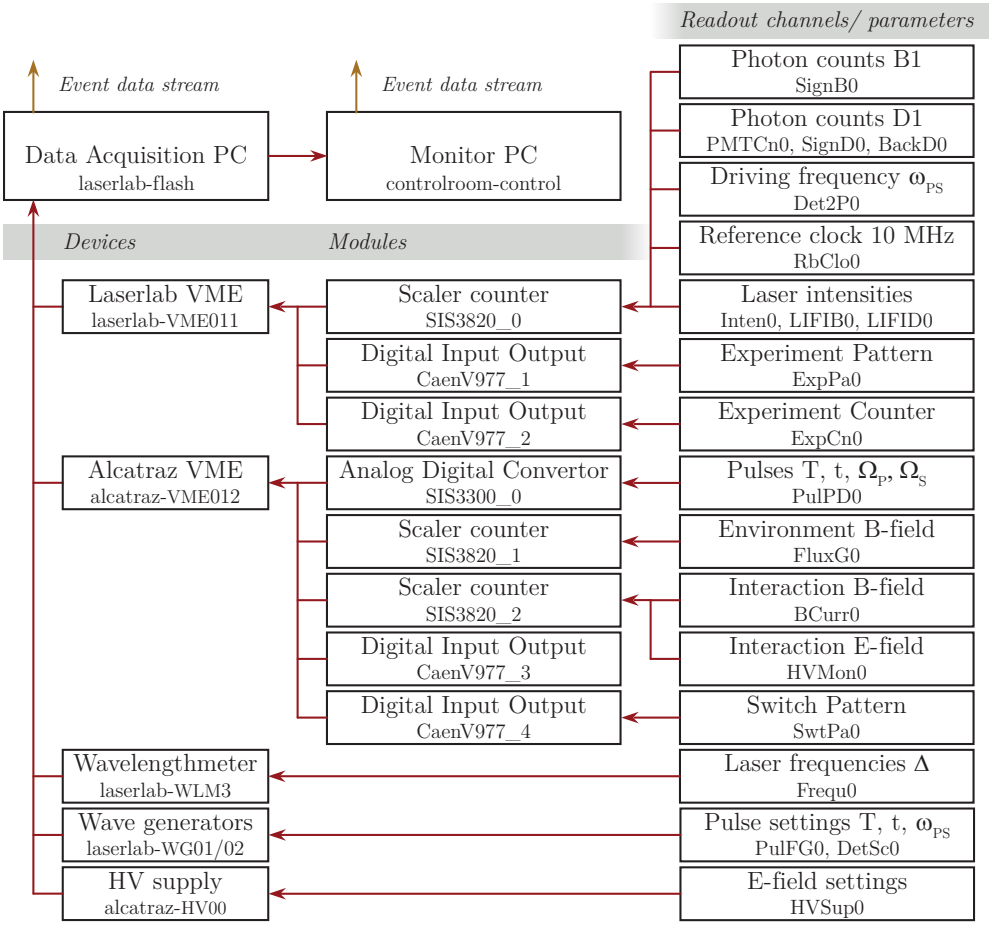

***Figure 3.2** | Structure of devices used in the data collection system, showing the function description and the device name in the network and pre-analysed data structure. For the VME crates the incorporated modules are listed. A summary of the readout channels is listed, next to their name in the analysis software. A full list is given in Appendix C.*

[1] In the meantime the setup has been moved to a new building and combined in a single lab, making this naming convention less obvious.

Figure 3.2 shows an overview of the network including all modules in the VME crates, and the relation to the measured channels and parameters. A full list of data acquisition channels is given in Appendix C. The rest of this section discusses how these devices are used to probe the listed physics parameters.

3.2.1. Trigger sequence and time synchronisation

Each molecular shot has the same general timing structure repeated at the repetition rate of the experiment (typically 10 Hz). The first couple of milliseconds involve the molecular pulse production and phase evolution measurement, after which the data acquisition readout is triggered and the overall experiment state is updated. An overview of this timing sequence is shown in Figure 3.3.

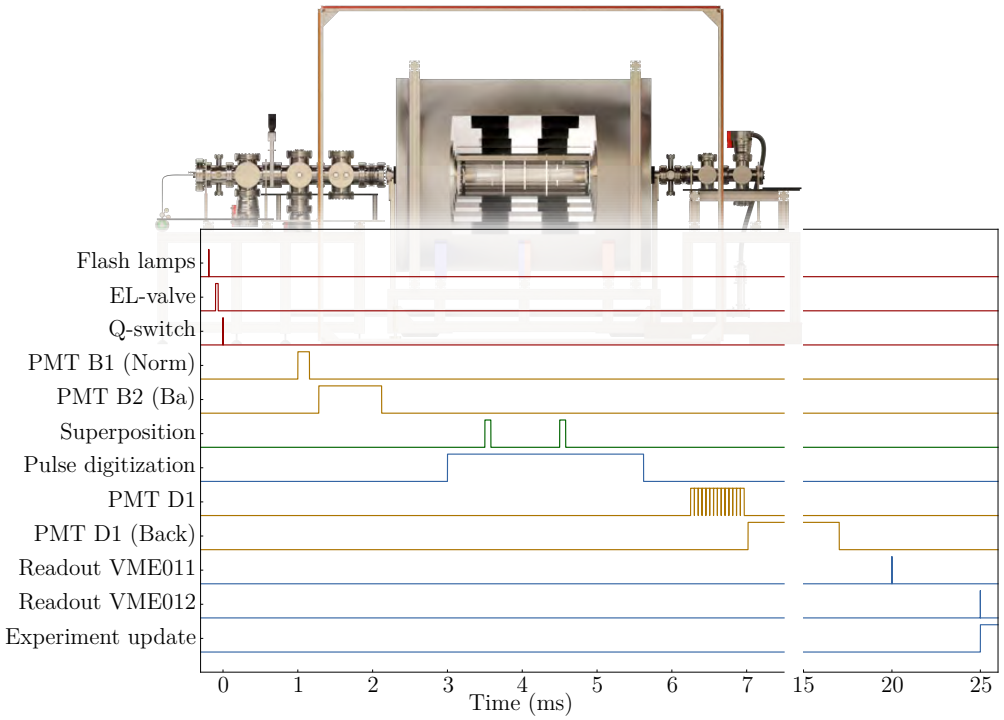

***Figure 3.3** | Time-sequence of a single molecular shot, relative to the Q-switch trigger. Source triggers are shown in red, photon signal time windows in yellow, superposition creation and collapse pulses in green and data acquisition and control blue. Where the rising edge is used as trigger in the time-sequence, the pulse is shown as a zero length pulse instead of showing the full pulse length to distinguish these from time windows. The image of the setup shown above the sequence illustrates the approximate position of molecules travelling at 600 m/s at the different time widows.*

The master trigger of the experiment is generated by a SRS trigger box (Stanford Research Systems DG535). This trigger box also generates the triggers for the ablation lasers flash lamp at -0.19 ms and the Q-switch, which defines the zero time of the experiment. Lastly, the box triggers the Even-Lavie valve [59] at -0.1 ms which is then opened for approximately 35 μs.
Fluorescence signal from BaF molecules and Ba atoms, collected on photomultiplier tubes (PMTs) located in section B1 and B2 in Figure 2.3, respectively, is used for normalisation of fluctuations in molecule production, as discussed in section 2.3, and as laser frequency reference [37]. The photon counting signals are gated using gate generators (U. Heidelberg G43) producing time windows starting at 1 ms and 1.28 ms, of 155 μs and 840 μs length for the BaF and Ba signal, respectively.
The timings of the superposition creation and collapse pulses are controlled from a waveform generator (Rigol DG4162). The pulse lengths and their relative timings are of importance to the phase measurement and are varied depending on the performed experiment. A typical start time of the first pulse $T_0 = 3.5$ ms, pulse length t = 80 μs and phase evolution time between the pulses T = 1 ms are shown in Figure 3.3. These parameters are controlled remotely by the control software and the settings are saved in the data on a second timescale, triggered digitally, asynchronously to the other data streams.
The fluorescence signal from the molecules recorded after the interaction zone is monitored using another PMT in section D1. It is gated with a sequence of 14 consecutive signal time windows of 51.2 μs starting at 6.25 ms after the experiment-trigger. The windows are generated using a digital sequencer (U. Heidelberg DL104) running at 255 ticks of the 5 MHz reference clock generated by a waveform generator (Rigol DG4162). Photon counts which do not originate from the molecular pulse are monitored in a background window starting at a delay from a dual gate generator (Caen V462) of 7 ms with a length of 10 ms, from another gate generator (U. Heidelberg G43). This window is significantly longer than the signal windows to improve the signal to noise ratio.
The readout of the data acquisition crates laserlab-VME011 and alcatraz-VME012 are triggered at 20 and 25 ms after the experiment-trigger, respectively, delayed by two dual gate generator modules (Caen V462) housed in the respective crates. The triggering of the readout is performed by digital IO modules (Caen V977) in each each crate. An event from alcatraz-VME012 triggers that all data buffers containing information from all devices in the data stream are flushed to the data-tree file.
A possible update of the experiment state is triggered digitally by an event from alcatraz-VME012 in the data stream, thus starting from 25 ms after the experiment-trigger. The experiment updates will be discussed in section 3.3.
The trigger box and all waveform generators are connected to the same 10 MHz Rubidium clock reference (Stanford Research Systems FS725) to ensure time synchronisation. The signal of this clock is also recorded by the data acquisition system.

3.2.2. Asynchronous data streams

In addition to the data that is collected for each shot in the trigger sequence, there are parts of the data stream which are not synchronised, as this is not feasible or necessary. The data is collected in the same shot-based structure in the data-tree, where for these devices the latest updated value is saved instead of the value of the latest shot. Typically, the asynchronous data stream devices are readout once a second. As the latest update time of each device is saved in the data-tree, the timeliness of the readout can be checked during analysis.

Wavelength meter - The lasers used in this experiment are locked to a wavelength meter (HighFinesse WS8-2) via an 8 channel Photonic Cristal Switch, cycling sequentially through all active channels. Every readout cycle the frequencies and feedback voltages for all active channels, as well as the internal temperature and pressure readouts are saved over the data stream.

Waveform generator - The settings of the waveform generator (Rigol DG4162, DG420) driving the Acousto-optic modulators (AOMs) that form the superposition creation and collapse pulses are of great importance for the performed experiment. As these settings are regularly changed for performing different measurements, it is important that the configuration is saved. The device can also be controlled remotely via the user interface, and as part of the switch-pattern, as will be described in section 3.3, to perform experiments like field maps by altering pulse timings and measurements at different detuning ranges. Triggered by the control software running on the data acquisition PC which is based on the computer time, the full settings of these devices is read out every second, as well as after each remote control update.

High voltage supply - A positive and negative high voltage supply (Iseg HPx 300 106) are used to set the electric field magnitude within the interaction zone. The field direction relative to the magnetic field is switched using a relay based switch box that will be described in subsection 3.3.2. With these supplies, DC voltages up to 30 kV can be supplied corresponding to a maximum electric field of 15 kV/cm for a field plate separation of 4 cm as used in this work. Currently the maximum feasible voltage is limited to approximately 10 kV by the relays in the switch box and the connection to the field plates. The supplies can be controlled remotely, as part of the switch-pattern, that will be described in section 3.3. The readout of the supplies is controlled by software running at the data acquisition PC at a typical rate of once per second. A readout is also performed after each remote control update. The readout includes the settings as well as a readout of the voltage and current measured by each supply. The readouts have turned out not to be representative of the voltage applied to field plates at short switching timescales. Therefore, monitoring voltages in the switch box are read out for every shot instead. The best measurement of the field as experienced by the molecules is by the signal from the molecules themselves as discussed in Boeschoten *et al.* [53].

3.2.3. Magnetic field monitoring

Flux gates (Stefan Mayer FLC3-70) are used, both for investigating the magnetic field environment during development of the setup, and for monitoring of the field outside of the magnetic shields during the measurement. Details on these measurements are provided in Meijknecht [45], here the data acquisition for these devices is summarised. The flux gates provide the magnetic field strength in three orthogonal directions in the form of three voltages relative to a reference voltage for each probe. The voltages are translated to frequencies using custom voltage-to-frequency convertor modules in a NIM crate, providing NIM pulses at a frequency,

$$f = A + V \times G \times B, \tag{3.1}$$

where V is the provided voltage in volts, G is the set gain factor of 10^n with $n = 0, 1, 2, 3$. The offset A and slope B are typically 100 kHz and 10 kHz, respectively. As the exact values are device specific, they need to be calibrated. Operated at a repetition rate of 10 Hz, the frequency provides the integrated voltage over a range of $V = \pm 10$ V/G as 0 to 2×10^5 counts, which corresponds to a dynamic range comparable to an 8 bit digitizer. The NIM pulses are registered on counter modules (Struck SIS3820) with a memory depth of 32 bit per channel. In this way the external field can be digitized over the range of the earth magnetic field of $O(70\ \mu\text{T})$ with a sensitivity of <1 nT.

During development, eight flux gates where used with readout channels distributed over the two counter modules in alcatraz-VME012. During later measurements the number of flux gates was reduced to two, one positioned before the interaction zone in B2 of Figure 2.3, and one after in D1, as this turned out to be sufficient to monitor the external field [45].

The best probe for the magnetic field experienced by the molecules, is provided by the molecules themselves, as the phase evolution signal strongly depends on this magnetic field as described by Equation 2.18 and shown in Meijknecht [45]. Nevertheless, a measure of the external field on a shot level timescale is helpful information on the environment in which the measurement is performed.

The magnetic field within the interaction zone is generated by a double cosine coil, as described in Meijknecht [45]. The current driving this coil is provided by a multichannel current source (DM Technologies MCS), which is also monitored on a shot level timescale in the data acquisition system.

3.2.4. Fluorescence detection

State sensitive detection of the atoms and molecules is performed by laser-induced fluorescence at multiple positions in the setup using photomultiplier tubes (PMT). The electric pulses resulting from detected photons are counted in time windows, as described for each detector in subsection 3.2.1 using a counter module (Struck SIS3820) in laserlab-VME011. The time windows are chosen around the expected arrival time of the molecular signal to reduce the accumulation time for background counts. For the detection behind the interaction zone, a background window is used to explicitly subtract background counts.

During the optical pumping in section B1 marked in Figure 2.3, fluorescence light from the BaF molecules driven by the excitation on the transition from $X^2\Sigma^+(v = 0, N = 2)$ to $A^2\Pi_{1/2}(v' = 0, J' = 1/2)$ is collected on a PMT (Hamamatsu H7421-50). This provides a

measure on the molecular flux and is used to normalise for shot-to-shot source fluctuations [56], as discussed in section 2.3.
At section B2, fluorescence from atomic barium is collected, to serve as another monitor on the source performance and to provide an absolute frequency reference during the measurement. Behind the interaction zone in section D of Figure 2.3, readout of the phase evolution measurement is performed by detecting on a PMT (Thorlabs PMT1001/M) the fluorescence light emitted by molecules excited on the $X^2\Sigma^+(v = 0, N = 0)$ to $A^2\Pi_{3/2}(v' = 0, J' = 1/2)$ transition, tuned to probe either the $F = 0$ or $F = 1$ hyperfine component of the groundstate. The pulse counting is done over a set of time windows as described in subsection 3.2.1, allowing analysis to be performed on parts of the molecular beam separately.

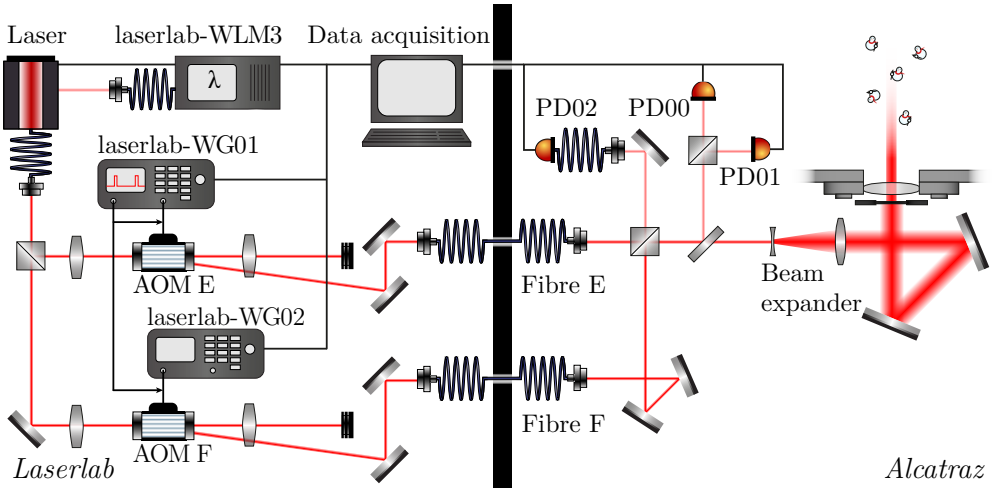

***Figure 3.4** | Overview of the optics for generating the superposition pulses. In the laserlab, light from a Ti:Sa laser is split and frequency shifted in AOMs E and F to create laser pulses at frequency difference ω_{PS}. In the Alcatraz-lab, the pulsed beams are recombined. The intensity distributed over different polarisation components is monitored on photo-diodes. The laser beam is expanded before it is sent into the setup counter-propagating the molecular beam. Figure adapted from Marshall [37].*

3.2.5. Superposition pulses

The spin-precession interference signal strongly depends on the timing and the intensity of the pulses that create and collapse the superposition. Therefore, these parameters are closely monitored. The timings are controlled by a waveform generator, named laserlab-WG01, as described in subsection 3.2.1. This timing signal gates the frequency shift signals (Minicircuits ZASWA-2), generated by the second channel of laserlab-WG01 (Rigol DG4162) and another waveform generator laserlab-WG02 (Rigol DG4202). These signals are sent to AOMs (IntraAction) producing the pulses labeled at the S and P-wave respectively in Figure 2.1. By driving AOM E and AOM F at a frequency of typically 100 MHz and 100 MHz + $\omega_{PS}/2\pi$, respectively, the frequency difference for driving the transition to and

from the superposition state is introduced. To probe the interference spectrum, this frequency difference is scanned by varying the driving frequency of AOM F.
For both waveform generators, the settings are saved to the data stream asynchronously, as discussed in subsection 3.2.2. An overview of the optics system is shown in Figure 3.4. For more information on the optical system see Marshall [37].
The laser pulse beams are transported from the laserlab to the experiment in the Alcatraz-lab over optical fibres. Here, the orthogonally polarised components S and P are overlapped with a polarising beam splitter. To monitor the polarization of the light coming from the fibres the polarization component opposite to the beam sent to interact with the molecules is measured on a photo-diode (Thorlabs FGA04). To monitor the resulting timing and intensity of the pulses experienced by the molecules, a fraction of the combined beam is split off and again split to the orthogonal polarisation components. Both components are monitored on separate photo-diodes (Thorlabs DET36A/M). All three photo-diodes are read out by a 5 V, 12 bit analog to digital convertor module (ADC, Struck SIS3300) in alcatraz-VME012, digitizing a time window starting at 3 ms after the experiment-trigger, of 2.621 ms length (see Figure 3.3) at a time resolution of 1.28 μs. This pulse monitoring is performed for each shot. A single shot pulse measurement is shown in Figure 3.5. The exponential rise and fall time is understood to originate from the photo-diode itself, the intensity profile of the light pulses themselves is expected to be sharper from the specified rise and fall times of these AOMs. As the spin-precession measurement depends on the time integral of the intensity, and in particular variations thereof, this rise time is not expected to be important.

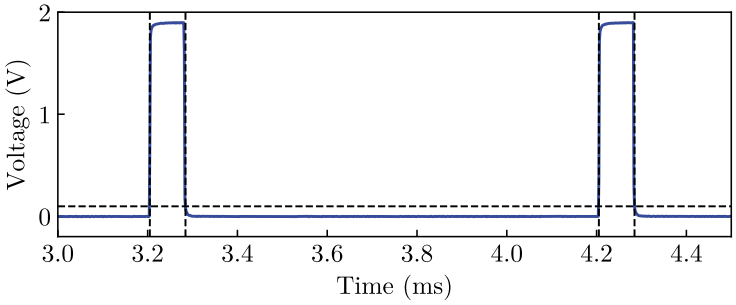

Figure 3.5 *| Single shot digitisation of a set of superposition creation and readout pulses. The horizontal dashed line shows the set threshold level for the pulse edges. In the pre-analysed data the integrated intensity, start time and pulse length of each pulse are stored.*

For the pre-analysed data, the digitized signal is translated to a pulse start, pulse length and integrated intensity for up to two pulses per channel. To do this, a background level is found by averaging over a background region set in the configuration. A pulse is detected when the signal rises above or falls below a threshold, set in the configuration.

3.2.6. Experiment state tagging

As the data acquisition system is running continuously, one needs to link a performed experiment to the corresponding dataset. This is done by setting an experiment bitpattern as the output of a set of three 16 bit Digital Input/Output modules (Caen V977), which is then also read to the data stream. The modules are software controlled over the local network via a user interface operated by the experimenter, or automatically, following a preset pattern. The first module identifies the Major and Minor category of the performed experiment that is used to label the content of each data block (ExpPa0). The second module is used as binary counter labeling each data block with an increasing experiment-count (ExpCn0). It is usually configured to increment by one every two hours of data taking for ease of selection during analysis, but can also be updated manually. This experiment-count value is referred to in the logbook to link the data.
A third module is used to control the experiment switch state of the experiment (SwtPa0). It is used to control the switch state of a device, either via the TTL pulse from each of the 16 output channels of the module, or via a broadcasting of the updated bitpattern over the local network to other digitally controlled devices. More details on this control will be given in section 3.3.

3.2.7. Data integrity

There are many aspects to ensuring the integrity of the data and the software used for analysing the experiment. This section summarises the most important concepts that have been implemented.
While running the experiment, real-time analysis and clear visual feedback are important to make sure the experiment is running as intended. We have developed real-time analysis scripts to show the relevant set of measurement channels to the experimenter. One important signal therein is the list of latest update times of data entries from all devices to ensure the completeness of the dataset.
To confirm the completeness of the dataset during the analysis, the update time of the entries are checked to the expected readout rate of the corresponding device. For the shot-based entries, this is the repetition rate of the experiment, typically 10 Hz. For the asynchronous data streams, the readout rates are typically at the 1 Hz level. Each readout of each device is accompanied by a timestamp, used for this check.
Data is saved in two structures. Firstly, raw data is saved in the event structure as generated by the Caddie [57] system, read directly from the hardware. Secondly, data is saved in the pre-analysed ROOT [58] tree structure used in the analysis scripts. This is to make sure any analysis can be restarted from the raw data. The raw data file can be used to generate a new tree file using the same software as used in real-time during the experiment.
To secure the data storage all data files are backed-up to a network attached storage (Synology DS918+) on the local network daily. When new data files are created automatically at 6 am, the data files of the previous day are closed, compressed and backed-up. It was checked that the raw data files do not to change during (de)compression using a MD5 checksum. The tree files are in their structure already compressed.

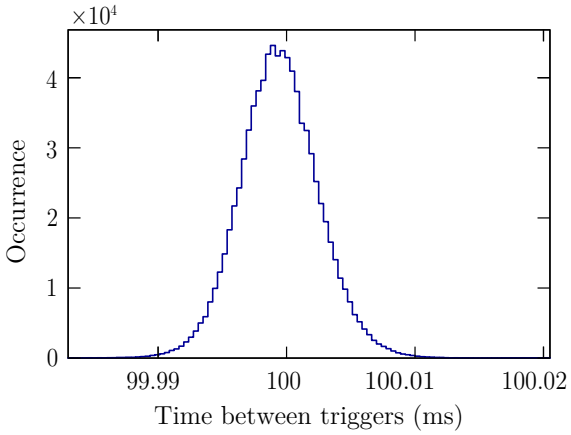

***Figure 3.6** | Variation in shot length according to readout rate of laserlab-VME011 over a 24 hour dataset, as measured compared to the 10 MHz reference clock. The variations show communication time variations over the VMEbus. Double registered shots would show as zero time between shots, while missed shots would show up at 200 ms. Neither are observed in this dataset.*

Data acquisition, control, simulation and analysis software is version controlled using the git system [60], initially hosted on a server at the university of Groningen, and later migrated to a Nikhef server.
To avoid irreproducible hard coding of data acquisition device infrastructure, configuration files are used. These configuration files can be edited and expanded upon using a user interface and are automatically saved with full configuration history and time stamping to enable backwards compatibility.
Most important for the data integrity of this experiment is the redundancy of information. The final measurement depends mostly on the molecular signal after phase evolution. This signal has been shown in Boeschoten *et al.* [53] to provide information on many physics parameters, such as the timings and intensities of the laser pulses and the electric and magnetic fields experienced by the molecules. Nevertheless, it is of great importance to cross reference the behaviour to channels measured in parallel in this data acquisition framework.

3.3. Control

Thus far, the readout system for the experiment has been discussed. In this section the control system is described, which sets the state of the experiment. Although closely related and connected to the data collection system, the control system is developed separately, following the modular structure of the full software infrastructure. The control system is running on the same PC as the data collection system (laserlab-flash).
The experiment state update by this control system is triggered by the readout of the last device in the synchronised data stream of each shot, 25 ms after ablation, as shown in Figure 3.3. The control software receives the event data stream over the local network in which it looks for an update from this specific device as an update trigger. It communicates possible changes to the control devices in the form of a 16 bit pattern.

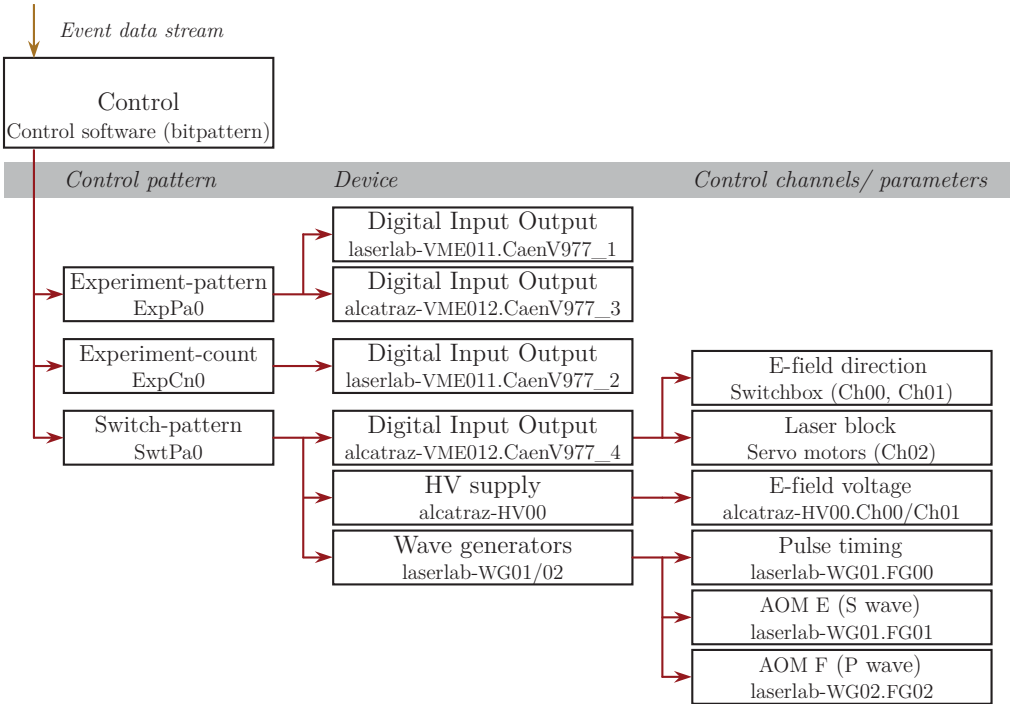

Figure 3.7 | *Structure of devices and communication interfaces used in the control system. The control software defines three 16 bit bitpatterns that encode the experiment type (Experiment-pattern), label the experiment index (Experiment-count) and set the state of control devices (Switch-pattern). All of these patterns are set to the outputs of Digital Input/Output modules (Caen V977) and thereby read to the data stream. The switch-pattern controls devices both via* TTL *signals from the module, and by communication of the pattern to the control software of the linked devices.*

These bitpatterns are set as the output of a Digital Input/Output modules (Caen V977), and are thereby read into the data stream. The experiment-pattern and experiment-count are used for tagging the state of the experiment, as discussed in subsection 3.2.6. The switch-pattern controls devices via TTL signals from the output channels of the module, such as the switch box that controls the electric field configuration, and motorised laser beam blockers. The bitpatten is also communicated over socket connections in the local network to the control software of other devices, specifically to the waveform generators that control the superposition pulses, and to the high voltage supplies that generates the electric field in the interaction zone. In the control software of these devices, the bitpattern is translated to corresponding configuration files which are then communicated to the devices themselves.
The change of the switch-pattern for consecutive shots is given by the switch-sequence. The switch-sequence is designed in the same user interface where the experiment tagging bitpatterns are controlled from. An example of a switch-sequence for a measurement of the interference fringe at different electric field configurations is illustrated in Figure 3.8. As the switch-sequence update is triggered by the readout within the shot time-sequence, it follows the repetition rate of the experiment. At a typical repetition rate of 10 Hz the switch-sequence is performed at ten switch-patterns per second, as used in this example.
A switch-sequence can be built up out of multiple blocks, to perform a sequence of different experiment consecutively. In this way, experiment sequences such as electric and magnetic field maps, described in chapter 5 of Meijknecht [45], can be automatised by performing interference fringe measurements for different superposition pulse timings. Also, reference measurements can be incorporated in longer data-taking sequences, if necessary. For the measurements presented in this work, trivial switch-sequences consisting of one block have been used.
Each switch-block has a corresponding experiment-pattern that describes the performed experiment, consisting of a major and minor category, as described in subsection 3.2.6. When the switch-pattern is updated as part of the switch-sequence, the corresponding experiment-pattern is also updated, providing real-time feedback on the experiment to the experimenter and serving as a reference during the analysis afterwards.

3.3.1. Superposition pulse

The waveform generators (Rigol 4000 series) used for generating the superposition pulses, as described in subsection 3.2.5, can be controlled remotely by the user, or via the switch-sequence. A readout and control program communicates via the local network to obtain, or set the setting of the waveform generators and sends the device settings regularly over the data collection network. The setting can also be read from, and written to, a settings file. When updated, the control program receives the bitpattern over a socket connection, following the switch-sequence. In the configuration file of the control program, it is set which setting file to apply for which state of the switch-pattern. If this is different from the setting currently set in the device, the relevant settings are updated.
For most experiments the waveform generator settings do not have to be switched. Scanning of the driving frequency of the superposition pulse is done using the scan functionality of the waveform generator itself. Both the shot trigger box and the waveform generator are connected to the same Rb reference clock, but the scan trigger is not synchronised to the shot time-sequence, as discussed in subsection 3.2.1.

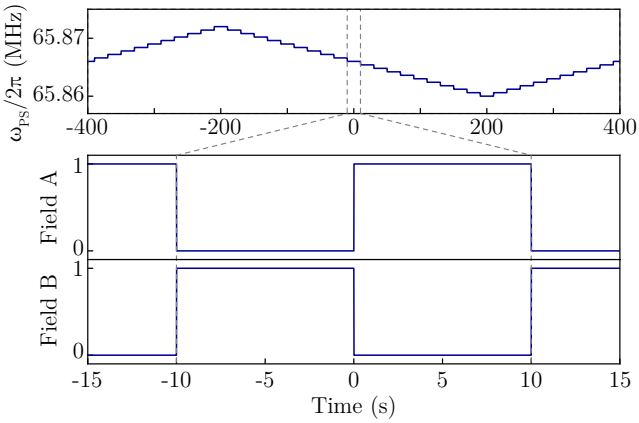

Figure 3.8 | *Example of a switch-sequence for switching between electric field configurations while scanning the superposition pulse frequency ω_{PS} to map out the interference fringe as described in Equation 2.18. The electric field configuration is controlled by the switch-pattern, alternating between Field A and Field B, corresponding to opposite electric field directions. The electric field direction is altered every 100th shot in this sequence, resulting at a 10 Hz repetition rate of the experiment in a period of 20 seconds. The settings for the waveform generators responsible for the superposition pulses are not altered in this switch-pattern. With these settings the frequency ω_{PS} is scanned by varying the frequency driving the AOMs over 12 kHz in 40 steps over a period of 800 seconds. This scan is not synchronised to the field direction switching, resulting in a possible timing offset between these.*

3.3.2. Electric field switching

The electric field in the interaction zone is created by applying a voltage to two indium-tin-oxide (ITO) coated glass plates, which are 10 cm tall, 75 cm long and placed 4 cm apart. The voltage is generated by two high voltage supplies (Iseg HPx 300 106) providing positive and negative voltages up to 30 kV. The supplies can be remotely controlled, as well as switched in the switch-sequence to perform experiments at different voltages, similar to the procedure for the waveform generators described in subsection 3.3.1. For typical testing experiments, the voltage was set to ±4 kV on each plate.
The direction of the electric field is switched by a home made switch box based on a set of HV relays (Meder HM12-1B69-150). The main circuit including the voltage monitor connections for both polarities (+, −) and field configurations (A, B) is shown in Figure 3.9. The configuration of the switch box is controlled by two TTL signals on Ch00 and Ch01 in the Digital Input/Output module set to the experiment switch-pattern. The four possible combinations of these control channels set the relay states as described in the truth table in Table 3.1. This is implemented by a micro controller (Microchip PIC16F628P). The *Field A* and *Field B* configuration correspond to opposite electric field directions, parallel or anti-parallel to the magnetic field. In the *Grounded* configuration both electric field plates are connected to ground. In the *Floating* configuration all relays are opened. This configuration is used for analysing the stability of the electric field and the corresponding leakage current.

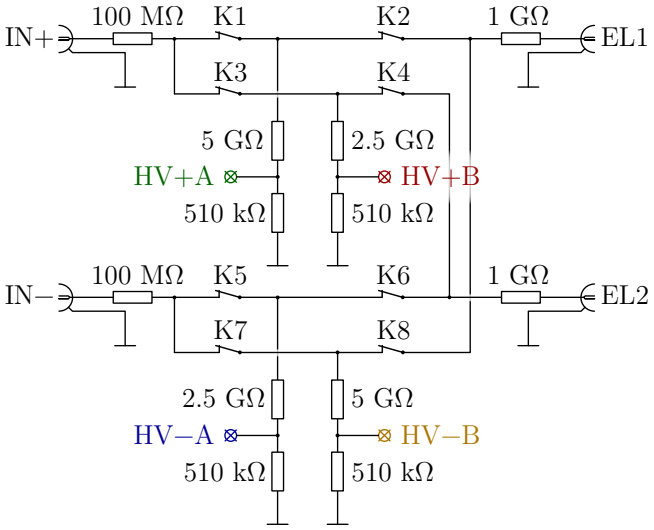

Figure 3.9 *| Main circuit of the home made high voltage switch box. The positive and negative HV supplies are connected to IN+ and IN- respectively. EL1 and EL2 are connected to the field plates. The circuit with the control channels Ch00 and Ch01 of the bitpattern that sets the state of the relays K1 to K8 following the truth table in Table 3.1 is not included in this figure for simplicity. HV+A and HV-B monitor the voltage applied to EL1 over a voltage divider, reducing it by a factor* 10^{-4}*. HV-A and HV+B monitor the voltage applied to EL2. Here the reduction factor is* 2×10^{-4}*, making the monitoring channels for both electrodes easily distinguishable.*

Table 3.1 *| Truth table used for translating each of the four possible combinations of the control channels Ch00 and Ch01 of the Switch-pattern to relay states resulting in the required field configurations. Here "1" and "0" correspond to the closed and open state of the relay, respectively.*

Configuration	Control		Relay state							
	Ch00	Ch01	K1	K2	K3	K4	K5	K6	K7	K8
Floating	0	0	0	0	0	0	0	0	0	0
Field A	1	0	0	0	1	1	1	1	0	0
Field B	0	1	1	1	0	0	0	0	1	1
Grounded	1	1	0	1	0	0	0	1	0	0

Field plate charging - To analyse the electric field switching behaviour of the setup, a switch-sequence is used that alternates between configurations *Field A* and *Field B* every 100th experiment-trigger, corresponding to a period of 20 seconds. The voltage at the monitoring points for field configuration A are shown in Figure 3.10, together with the relevant trigger and control channels.

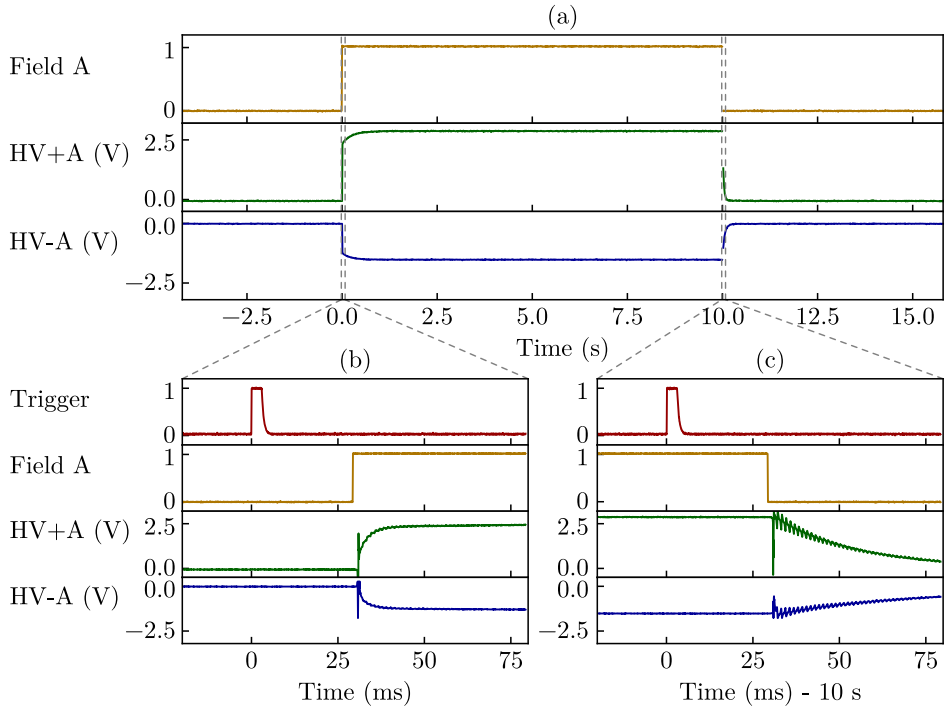

Figure 3.10 *| Monitor voltages showing the charging of the electric field plates to the Field A configuration. The channel Field A corresponds to the output state of the relevant control channels. HV±A show the voltage monitors as labelled in Figure 3.9. In (a) a full switch-sequence cycle of 20 s is shown. The charging time of the field plates equal to RC = 250(20) ms, can be seen here in the slow exponential tail of the HV±A voltage monitors. In (b) and (c) a zoom-in of 100 ms around the triggering of the field configuration change is shown, including the experiment-trigger.*

As shown in subsection 3.2.1, the experiment state is changed after the last device readout, 25 ms after the experiment-trigger. The state of the control channels, labelled in Figure 3.10 as *Field A*, updates 29 ms after this trigger. It can therefore be deduced that processing the switch-pattern takes approximately 4 ms. In the following ~2 ms the state of the relays is changed following the truth table in Table 3.1. Imperfect synchronisation between the different relays result in rapid changes in the monitor voltages.
When the relays are closed, the voltage monitors are charged with a RC-time of 2.8(1) ms as shown in Figure 3.10b. The slower exponential charging component with an RC-time of

250(20) ms, shown in Figure 3.10a, corresponds to the charging of the electric field plates in the interaction zone themselves.
The field plates are charged over a combined resistance of 1.1 GΩ. This large resistance is chosen to limit the current during (dis)charging of the field plates, which could magnetise the inner μ-metal shield layers and break the necessary low- and homogeneous magnetic field conditions necessary for this experiment. This does however result in the long RC-time discussed above.
It was found by disconnecting the cable at the high voltage feed-through into the vacuum chamber and at the switchbox itself, and comparing the charging times, that the system inside the vacuum and the connecting coaxial cable contribute about equally to the total capacitance of 230(20) pF.

Leakage current - To test for leakage currents, the electric field in the interaction zone is monitored using the molecules. The field plates are charged to ±4 kV, corresponding to an electric field of 2 kV/cm. After a charging time of 10 seconds, much longer than the RC-time measured for charging, the switch box is set to the *Floating* state where all relays are opened. In this state the electric field plates are isolated and the discharging is purely due to leakage currents.

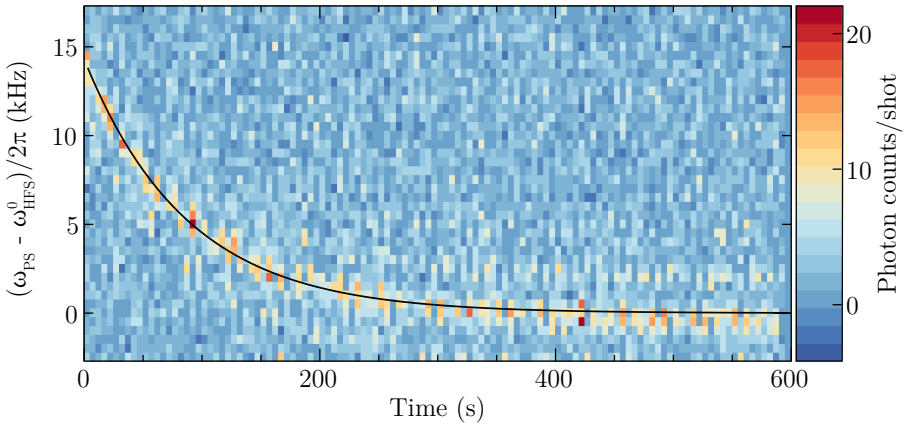

Figure 3.11 *| Signal from molecules in the $X^2\Sigma^+(v = 0, N = 0, F = 1)$ after pumping from the $N = 0, F = 0$. The two-photon resonance shifts due to the tensor Stark shift in the decaying electric field after opening the HV relays, demonstrating a leakage current. Time is relative to the opening of the relays. The driving frequency is offset by the zero field hyperfine splitting $\omega^0_{HFS}/2\pi$ of 65.85 MHz. The black line corresponds to an RC/2-time of 87 s, which corresponds to a leakage current of 11 nA.*

The electric field is probed by a single two-photon pulse of 500 μs, 3.5 ms after the experiment-trigger, counter-propagating the molecular pulse. The pulse transfers molecules from the $X^2\Sigma^+(v = 0, N = 0, F = 0)$ to the emptied $N = 0, F = 1, M_F = \pm 1$ superposition state, as also used in the spin-precession measurement. The driving frequency ω_{PS} of the laser pulse is

scanned over 20 kHz. The observed shift is due to the tensor Stark shift $D_{1,\pm1}(E)$, which enables the use of the molecules themselves as a probe for the electric field.
The tensor Stark shift $D_{1,\pm1}(E)$ is approximately quadratic for electric fields up to the applied field E_0 of 2 kV/cm [23]. The resonance frequency is therefore expected to decay following $\omega_{PS} - \omega^0_{HFS} = D_{1,\pm1}(E_0)\exp(-2t/RC)$, where C is the capacitance of the system after the relays, determined from the charging measurement to be 230(20) pF, and R is the resistance between the isolated field plates and ground. From the fit in Figure 3.11, it is found that RC/2 = 87 s, corresponding to a resistance of 7.6×10^2 GΩ.
For an applied voltage difference of 8.0 kV, the steady state leakage current is therefore 11 nA. Assuming the leakage current is flowing in the longitudinal direction over the 10 cm wide surface of the field plates[2], it would generate a magnetic field at the molecular beam axis of approximately 0.13 nT. As the orientation of this magnetic field switches with the direction of the electric field, it will not cancel out between both electric field configurations and may give rise to a false EDM. However, as the field is orthogonal to the direction of the electric field and thereby strongly suppressed [45, 61], the contribution to the systematic error on the EDM is $< \mathcal{O}(10^{-32}$ e cm) and not expected to become limiting in the near future.
The magnetic field due to the leakage currents has an effect analogous to the motional magnetic field, which originates from the traversal of the molecules through the electric field. The effect of the motional magnetic field is estimated significantly larger than the leakage current field found here, although still far below the EDM sensitivity of the current experiment [45].

3.4. Interference fringe for opposite field orientations

The systematic sensitivity to the EDM is given by the equivalence of the experiment for each of the opposite electric field configurations, *Field A* and *Field B*. In Figure 3.12, a measurement of the interference fringe is shown for the combined data, consisting of the sum of both configuration datasets, and for each of the configurations separately. The measurement is taken in blocks of 19 seconds for each field configuration. Data from the first 2 seconds after switching have been omitted because of the rapidly changing field strength. Data taken during the 5 seconds blocks of the switch-sequence in the *Grounded* configuration, meant for calibration and monitoring of systematic effects, was not included in this analysis. The data was averaged over a dataset of two hours, corresponding to approximately 2.8×10^4 molecular shots in each field direction.
To the combined dataset, the sum of both field configurations presented in the middle of Figure 3.12, the analytic description of the interference fringe in Equation 2.18 was fitted. In this fit the light shifts and explicit phase offset between the pulses $\Delta\phi_{PS}$ were both set to zero. The offset and amplitude were fitted and used to convert the normalised signal strength to contrast (C), following the procedure discussed in section 2.3.
The reduced chi-squared $\chi^2/\text{ndf} = 411/113 > 1$ illustrates the under fitting of the model function to the data. This is attributed to variation of the two-photon Rabi frequency Ω_{PS} during this measurement due to the instability of the laser intensity, which during this

[2]This assumption is taken as an extreme case used to provide an upper limit to the magnetic field as would be experienced by the molecules

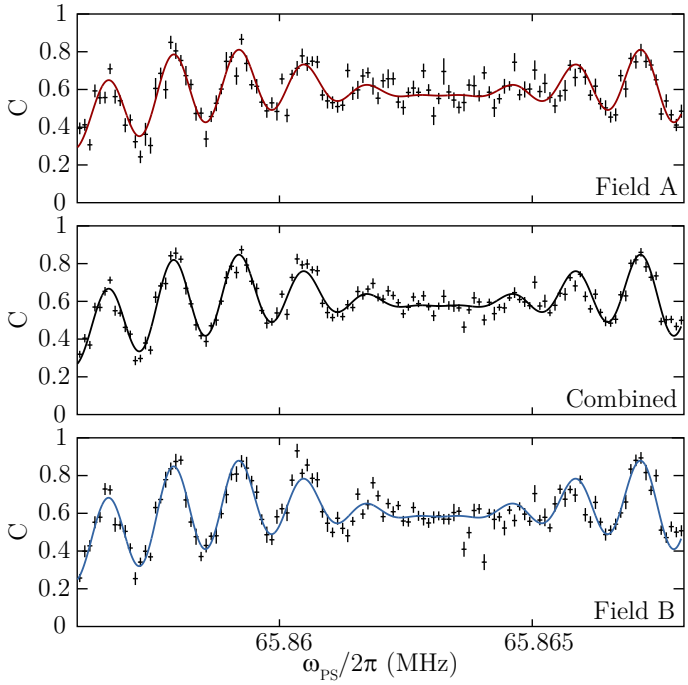

Figure 3.12 | *Interference fringe of molecules in the $X^2\Sigma^+(v = 0, N = 0, F = 1)$ after the spin-precession measurement for both field configurations Field A and Field B at an electric field of 2 kV/cm. The fitted line corresponds to the analytical model in Equation 2.18. The vertical axis has been converted to contrast (C) following the procedure discussed in section 2.3.*

measurement was not monitored accurately. In Boeschoten *et al.* [53] the impact of the variation of the laser intensity was investigated extensively. It was found there that the variation in laser intensity results in an effective smearing out of the interference fringes not included in this model.

The upper and lower panel of Figure 3.12 show the dataset decomposed into the different field configurations *Field A* and *Field B*, respectively. The fits with the interference fringe are shown in solid red and blue lines. Here, only the amplitude, offset and two-photon frequency offset ω_{00} have been fitted, taking the values from the combined fit for all other parameters. Particularly, a difference in the resonance frequency is of interest here, as it demonstrates an electric field amplitude asymmetry between the configurations.

For both fits, similar reduced chi-squared values were obtained to the value for the combined fit. This confirms the equivalence of the electric field amplitude between the configurations within the error deduced from the fit of 0.5 V/cm.

3.5. Conclusion and outlook

As shown here and in related work [23, 37, 45], a first generation NL-eEDM experiment has been built successfully, and is ready to be used for looking for EDM-like signals. This setup has been used to identify and characterise multiple systematic effects, which are well described by the analytic interference fringe pattern in Equation 2.18 and in even more detail in the optical Bloch equation description. A novel spin-precession method has been demonstrated in Boeschoten *et al.* [53] using all-optical techniques to probe the EDM while simultaneously probing many experimental and environmental parameters.
In this chapter the data acquisition and control system has been presented. During multi-day measurement runs the reliability of the system has been demonstrated. The modular design ensures both the robustness during current experiments, but also expandability for future experiments. A framework has been set up for the analysis of datasets to be taken by future generations, gathering statistics to warrant a competitive limit on the electron electric dipole moment.

In this chapter the analysis of the electric field experienced by molecules traversing the interaction zone has also been presented. In particular the charging time of the electric field plates has been investigated. In the design for the switching scheme, this charging time plays a significant role. As the measured RC-time of 250(20) ms is on the order of a couple of shot lengths, during the first shots after the field direction change the electric field will be changing significantly. Due to the tensor Stark shift $D_{1,\pm1}(E)$ the resonance for the superposition creation and readout pulses will be varying over this period, resulting in a significant shift of the interference pattern. For this reason the first shots after the switch have not been taken into consideration for Figure 3.12. This introduces an effective dead-time in the measurement sequence for each switch. To optimise the sensitivity of the experiment the switching rate has to be balanced to the stability of the other experiment parameters.
In this work, voltages applied to the field plates up to 4 kV have been used. With the distance between the field plates of 4 cm the resulting electric field in the interaction zone was up to 2 kV/cm. The setup has been tested up to voltages of 8 kV, the specified voltage limit for the HV relays used in the switchbox is 10 kV. The sensitivity to the electron electric dipole moment (Equation 1.8) significantly increases with electric field up to a field strength of approximately 10 kV/cm, as given by the polarisation of the molecule [34]. In the meanwhile, the distance between the electric field plates has been reduced to 2 cm to be able to reach these higher field strengths. To be able to handle higher voltages required to go to even higher fields without introducing strong leakage currents or field asymmetries, the design of the switchbox and field plate connections would have to be revised.

As a further upgrade to the sensitivity of the experiment, focus will be on increasing the number of molecules contributing to the measurement (N) and increasing the interaction time during spin-precession (T). This can be achieved by replacing the supersonic source used in this work by a cryogenic source, possibly combined with a traveling-wave Stark decelerator, as will be the main topic of the following chapters.



4

Traveling-wave Stark decelerator and hexapole lens

The statistical sensitivity of an electron electric dipole moment experiment can be improved by increasing the interaction time T and the number of molecules N taking part in the measurement. In the NL-eEDM experiment, this is proposed [44] to be done by interchanging the currently used supersonic source [55] by a combination of a cryogenic source [46] and traveling-wave Stark decelerator [62]. To improve the coupling between the latter two, an electrostatic hexapole lens is used.

In this chapter the operating principle of the traveling-wave Stark decelerator and the hexapole lens are discussed. Both are based on the Stark effect, which describes the energy shift of molecules in the presence of an electric field. The Stark shift for SrF and BaF molecules in the lowest rotational states of the $X^2\Sigma^+(v = 0)$ electronic and vibrational groundstate is described in section 4.1.

In section 4.2 and section 4.3 the electric field configurations of the hexapole lens and traveling-wave Stark decelerator are discussed, as well as how these are generated in the experiment. A mathematical treatment of both electric field configurations is given in Appendix D. There, the ideal cases are discussed and the approximation by the practical implementation are reviewed.

The efficiency of the decelerator in capturing and decelerating molecules is described by the phase-space acceptance of this device. In section 4.4 this phase-space acceptance is calculated based on separatrices in the effective potential given by the combination of the Stark shift and the electric field geometry, and based on trajectory simulations.

The phase-space distribution of these molecules from the cryogenic source, although large, does not fully fill the acceptance of the decelerator, especially due to the unavoidable free-flight distance between these. The filling of the phase-space acceptance is improved by placing a hexapole lens between the source and the decelerator, as discussed in section 4.5.

The chapter image shows decelerator modules with the eight rods and connected ring electrodes to which voltages are applied to form the electric field traps.

4.1. Stark effect for SrF and BaF

The electronic and vibrational ground state $X^2\Sigma^+(v = 0)$ is split by the rotational, spin-rotation and hyperfine interaction[1]. For illustration of the Stark effect an analytic treatment is considered first, where the fine and hyperfine structure are negated by setting the total electron spin S to zero, simplifying to a $X^1\Sigma$ system. The numerical solution to the full system will be considered at the end of this section.[2].
In the low field regime $E \ll B/\mu_e$, the rotational splitting, given by the Hamiltonian $H_R = B\,N^2$, predominates the Stark shift $H_S = -T^{(1)}(\mu_e)T^{(1)}(E)$. The energy shift due to the electric field can be derived using second-order perturbation theory, as shown in section 8.4.2 of Brown and Carrington [63], resulting in,

$$\Delta W_{lf}(E) = \begin{cases} -\dfrac{\mu_e^2 E^2}{6B} & \text{for } |N, M_N\rangle = |0, 0\rangle\,, \\ \dfrac{N(N+1) - 3M_N^2}{N(N+1)(2N-1)(2N+3)} \dfrac{\mu_e^2 E^2}{2B} & \text{otherwise.} \end{cases} \tag{4.1}$$

In the high field regime $E \gg B/\mu_e$, the molecule is fully polarised and the Stark shift is given by,

$$\Delta W_{hf}(E) = -\mu_e E, \tag{4.2}$$

which is the same for all rotational states. The measured values for the molecular constants used in these equations are summarised in Table 4.1.

Table 4.1 *| Mass, rotational constant and electric dipole moment for SrF and BaF in the electronic and vibrational ground state* $X^2\Sigma^+(v = 0)$.

Molecule	Mass (amu)	Rotational constant B/h (GHz)	Electric dipole moment μ_e (D)
$^{88}Sr^{19}F$	107	7.487536(7) [64]	3.4676(10) [65]
$^{138}Ba^{19}F$	157	6.47395465(11) [66]	3.1702(15) [67]

As no static electric field configurations exist with field maxima away from the electrodes that generate the field, molecules in high-field seeking states are always attracted to the electrodes, which is not useful for these experiments. Therefore, molecules in low-field seeking states are of interest for this work.
It can be seen from Equation 4.1 that, in the low field regime, the Stark shift for molecules with $M_N^2 < N(N+1)/3$ increases with increasing field strength. States following this requirement are therefore referred to as low-field seeking. Especially molecules in a state with $M_N = 0$ are used in this work, as for these the low-field seeking Stark shift is largest.

[1] The labeling of states, transitions and branches is reviewed in Appendix A.

[2] As the spin-rotation and hyperfine energy shifts are significantly smaller than the rotational and Stark shifts at the typical external field strength, the dynamics of the molecules can be largely described without taking (hyper)fine structure into account.

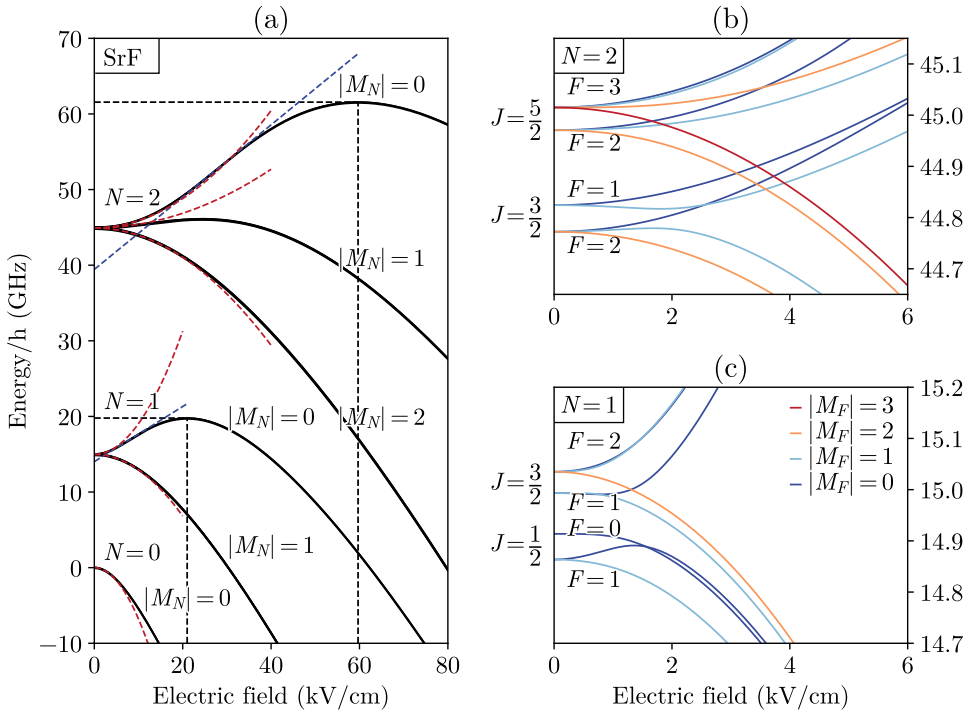

Figure 4.1 | *Stark effect in $^{88}Sr^{19}F$ for the lowest rotational states ($N \leq 2$) of $X^2\Sigma^+(v = 0)$ simulated in PGOPHER [68]. (a) The large field splitting into projection substates labeled by M_N with significant low-field seeking components for $N = 1, 2$, $M_N = 0$. The dashed black lines show the turning points where these low-field seeking components become high-field seeking. The values at which this happens are summarised in Table 4.2. The red dashed lines show the analytical Stark shift at low-fields, Equation 4.1. The blue dashed lines show a linear extrapolation for the maximum Stark shift. (b) and (c) Low-field zoom-in around the $N = 2$ and $N = 1$ states showing the hyperfine structure.*

Because all rotational states eventually become high-field seeking, for the initially low-field seeking states there must be a turning point field E_{tp} at which the Stark shift $W_{tp} = \Delta W(E_{tp})$ turns to decrease with increasing field strength.

To find the intermediate-field behaviour, where the turning point occurs, and to include the spin-rotation and hyperfine interactions the full Hamiltonian was diagonalised, using PGOPHER [68]. The results for $N \leq 2$ are shown for SrF in Figure 4.1 and for BaF in Figure 4.2. In the simulation, contributions of rotational states up to $N = 5$ are taken into account. The simulation for SrF is based on molecular constants summarised in Aggarwal [51]. The simulation for BaF is based on molecular constants from Ryslewicz *et al.* [66] and Ernst *et al.* [67] summarised in Mooij [47].

In the following discussion the Stark shift for SrF will be referenced, but as the structure is the same for BaF the same arguments hold for this molecule.

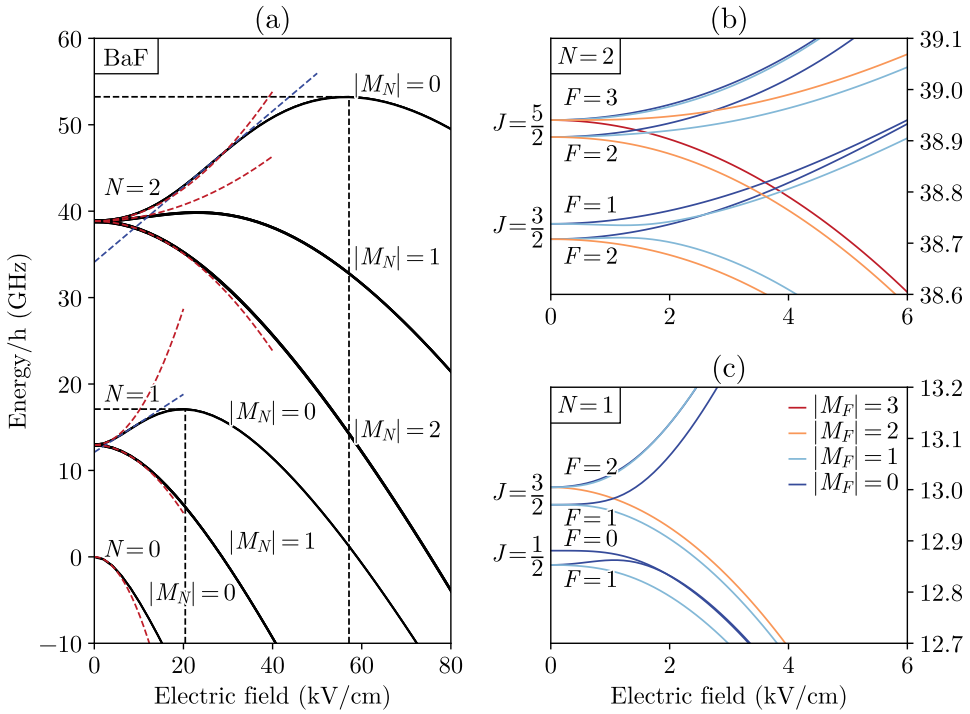

***Figure 4.2** | Stark effect in $^{138}Ba^{19}F$ for the lowest rotational states ($N \leq 2$) of $X^2\Sigma^+(v = 0)$. See caption of Figure 4.1 for details.*

From the Stark curves in Figure 4.1a, it can be seen that molecules in the $N = 1, M_N = 0$ states are most suitable for capturing with electric fields that can reasonably be achieved in the lab. For molecules in the $N = 2, M_N = 0$ a higher Stark shift within the low-field seeking regime can be achieved, but only by applying a significantly higher electric field, for which a voltage upgrade for the decelerator is necessary which is beyond the scope of this work, but is being implemented at the time of writing.
In Figure 4.1c the low field regime of the Stark shift is shown. In this regime the rotational quantum numbers N, M_N no longer correctly describe the grouping of states as the hyperfine interaction dominates over the Stark shift. It is shown how the $N = 1$ is split into hyperfine components, labeled by F, M_F of which 4 out of 12 are low-field seeking. In the state-selective detection this hyperfine structure is taken into account.

4.2. Hexapole lens

To transfer the diverging molecular beam coming from the source into the acceptance of the decelerator, an electrostatic hexapole lens has been designed and installed between these parts of the setup.
In previous experiments presented in Aggarwal *et al.* [62], there was a 370 mm gap between the cryogenic source and the decelerator to allow for separation of the source and decelerator chambers by a vacuum valve. Such a valve is necessary, as the source is heated up regularly and the target is replaced every few weeks. Breaking the vacuum of the decelerator chamber requires high voltage conditioning of the electrodes which typically takes many hours. The hexapole lens has been implemented to regain the losses due to the under filling of the transverse phase-space acceptance of the decelerator due to the divergence of the molecular beam over this necessary distance between the source and decelerator.
An ideal electrostatic lens of inner radius r_0 and with an applied voltage Φ_0 generates an electric field with amplitude,

$$E_{(n)}(r) = n\Phi_0 \frac{r^{n-1}}{r_0^n}, \tag{4.3}$$

as shown in Equation D.6. Here $n = 2$ corresponds to a quadrupole and $n = 3$ to a hexapole field. These radially increasing electric fields focus molecules in a low-field seeking state back towards the molecular beam axis.
To find the best suitable lens, a quadrupole and hexapole with inner diameter of 12 mm are compared, with a voltage applied such that the electric field at the electrodes is 20 kV/cm, close to the turning point field E_{tp} for SrF or BaF in the $X^2\Sigma^+(v = 0, N = 1, M_N = 0)$. The following discussion is based on SrF, but as the Stark shift is extremely similar the reasoning would hold the same for BaF, which was also considered during design.

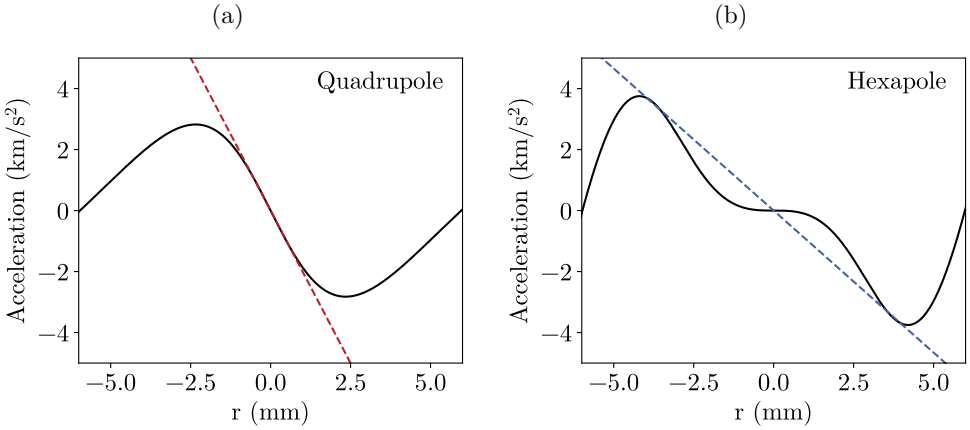

Figure 4.3 | *Radial acceleration for displacements for SrF in the $X^2\Sigma^+(v = 0, N = 1, M_N = 0)$, (a) within a quadrupole lens with an inner diameter of 12 mm and voltage magnitude of 6 kV, and (b) within a hexapole lens with an inner diameter of 12 mm and voltage magnitude of 4 kV. The red and blue dashed lines show the extrapolation for a quadratic or linear Stark shift, respectively, shown in Figure 4.1 in the same colors.*

In the low field regime the Stark shift for molecules in the low-field seeking state is quadratic, as described by Equation 4.1. In this regime a quadrupole lens with linearly increasing electric field in the radial direction, $E_{(2)}(r) = 2\Phi_0 r/r_0^2$, results in a radially harmonic potential experienced by the molecules. However, for larger displacements, into higher field strengths, the radial restoring force decreases, as shown in Figure 4.3a.
As the electric field within a hexapole lens increases quadratically in the radial direction, $E_{(3)}(r) = 3\Phi_0 r^2/r_0^3$, a radially harmonic potential occurs for a linear Stark shift. From Figure 4.1 it can be seen that the Stark shift of the low-field seeking states of SrF becomes close to linear in the intermediate field regime. The linear Stark shift is given by $W(E) = -\mu_{eff}E$, where the effective dipole moment $\mu_{eff} = -\partial W(E)/\partial E$. Here the maximum effective dipole moment is considered, illustrated in Figure 4.1a by the blue dashed line. In Figure 4.3b it can be seen that the restoring force for a hexapole lens is indeed larger than for a quadrupole lens for displacements into a larger field. However, the restoring force is smaller for smaller displacements.
Due to the particular shape of the Stark shift it is impossible to make a perfect electrostatic lens for these molecules. However, as it is the goal of this work to improve the projection of the source distribution into the phase-space acceptance of the decelerator, not to make a perfect image, installing a lens is still beneficial.

(a) (b)

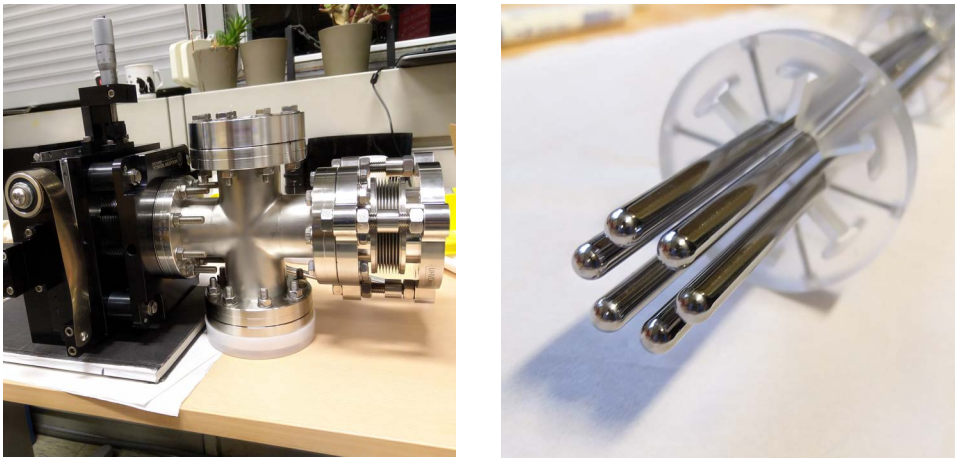

Figure 4.4 *| (a) Vacuum system for holding the hexapole lens using the XY-manipulator on the left and bellow on the right to fine-tune the alignment of the molecular beam from the source into the decelerator. (b) Hexapole lens with 12 mm inner diameter and 6 mm diameter cylindrical electrodes.*

Using trajectory simulations, it was confirmed that a hexapole lens would result in the largest improvement for SrF molecules in the $N = 1, M_N = 0$ low-field seeking state. The larger restoring force for molecules with a significant transverse velocity, thereby reaching higher field regions, outweighs the limited effect on molecules which have a low transverse velocity and therefore still fall within the acceptance of the decelerator. To better understand this, the phase-space acceptance of the decelerator will be investigated further in section 4.4.
The hexapole lens implemented in this experiment has an inner diameter of 12 mm and

consists of six cylindrical[3] rods of 6 mm diameter, to which a static voltage with alternating polarity is applied. A picture of the hexapole lens is shown in Figure 4.4b. The hexapole is mounted in a vacuum system with a bellow on either end. The bellow mounted on the source side is part of a XY-manipulator (Hositrad HMC1000), which is used to position the hexapole to optimise the alignment of the molecular beam from the source into the decelerator. Further characterisation of the hexapole lens is presented in chapter 7, based on imaging of the molecular beam for BaF on an EMCCD camera.

4.3. Traveling-wave Stark decelerator

For longitudinal deceleration of the molecular beam, a traveling-wave Stark decelerator is used. Its ring electrode geometry and applied voltage pattern result in three-dimensional traps for molecules in a low-field seeking state. By modulating the velocity of these traps the velocity of the molecules is changed. This particular decelerator has been show before to be able to bring SrF molecules from 190 m/s to complete standstill [62]. Many details on its development are described in van den Berg *et al.* [70, 71], and a more general overview of Stark decelerators is given in various papers [69, 72, 73]. The design of the decelerator used in this work is based on Meek *et al.* [74].
The field within the decelerator approximates the ideal decelerator field, which would be achieved by applying a periodic voltage in the longitudinal direction of a hollow tube electrode. In practice this is not feasible and a series of ring electrodes is used instead. Lessons that can be learned from this defining geometry and the quality of the approximation are reviewed in section D.2.
The decelerator consists of ring electrodes with an inner radius r_0 of 2 mm, made of 0.6 mm diameter tantalum wire. The rings are separated by 1.5 mm, heart to heart, and connected to eight rods. Every ninth ring is connected to the same rod and therefore has the same voltage applied. The decelerator consists of nine modules with 336 ring electrodes each, resulting in a total length of 4536 mm.
By applying a sinusoidal voltage to the electrodes consecutively numbered n,

$$V_n = V_0 \sin\left(-\phi(t) + \frac{2\pi n}{8}\right), \quad n = 0, 1, 2, ...7, \tag{4.4}$$

cylindrically symmetric three-dimensional traps are formed within the rings, with electric field minima at a separation of 6 mm. The shape of the electric field in this configuration is shown in Figure 4.5. The location of the field minima can be modulated by the phase,

$$\phi(t) = 2\pi \int_0^t f(\tau) d\tau, \tag{4.5}$$

referred to as the waveform. The waveform is set according to the motion of a synchronous molecule, which in the context of a traveling-wave decelerator can be understood as a

[3]The cylindrical shape of the electrodes results in a deformation of the electric field compared to the ideal multipole field. For radial displacements below the inner radius of the lens ($r < r_0$) this deformation is however minimal, as shown in section D.1, and this deformation is of minimal impact to this work. The distortion of the electric field is discussed in Meerakker *et at.* [69].

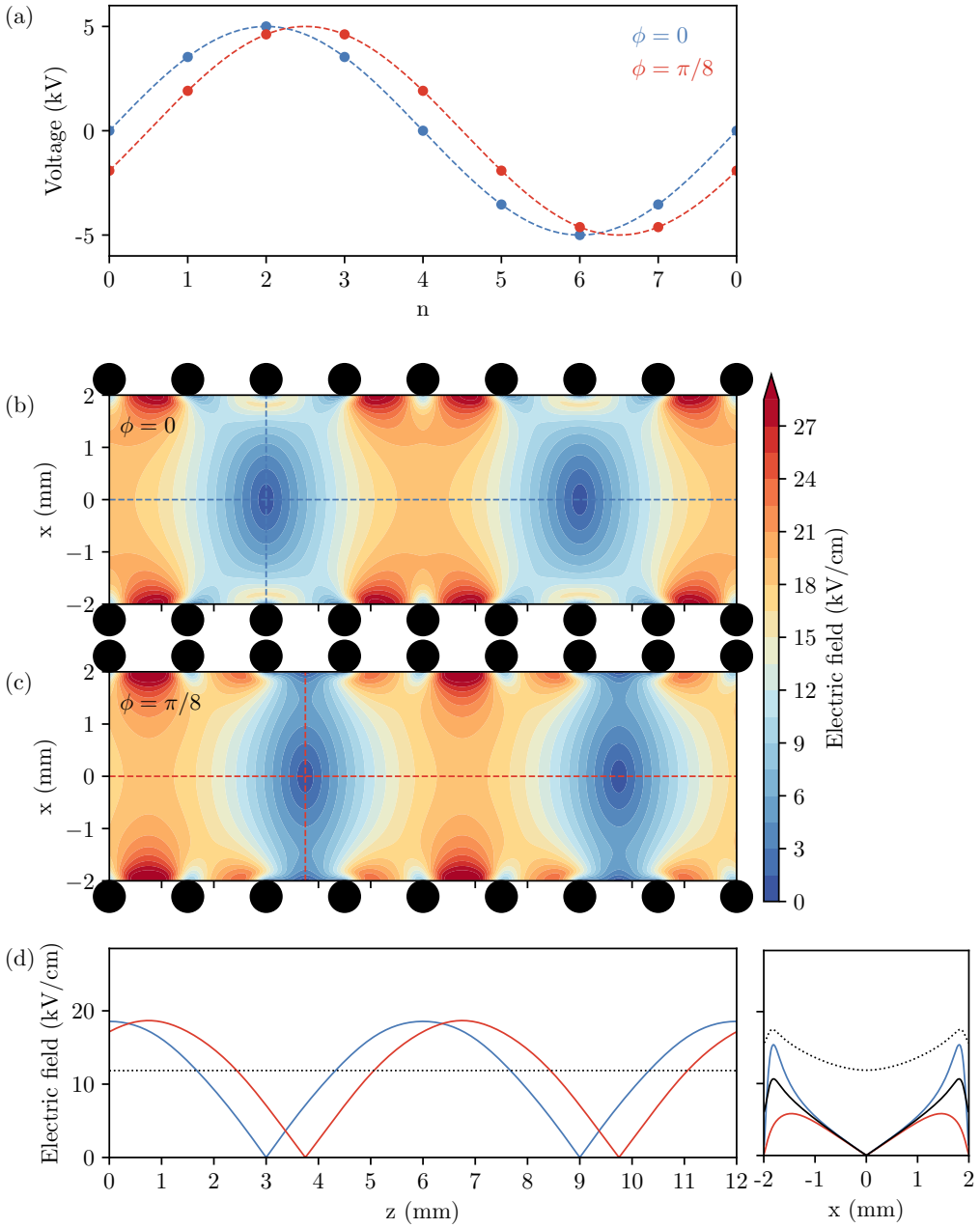

Figure 4.5 *| (a) The voltage applied to each electrode number (n), following Equation 4.4, for $\phi(t) = 0, \pi/8$. (b) and (c) The electric field within the decelerator along the longitudinal axis (z) and a transverse axis (x) for a voltage amplitude of V_0 = 5 kV at $\phi(t)$ = 0 and $\phi(t) = \pi/8$ respectively. The black circles spaced by 1.5 mm indicate the positions of the ring electrodes. (d) A longitudinal and transverse[4] field slice at positions marked in (b) and (c) by the dashed lines. The black dotted lines show the field average as experienced by non-trapped molecules. The solid black line shows the average transverse field experienced by a molecule in the trap.*

(hypothetical) molecule which has a fixed position relative to the moving traps. The frequency of the waveform is given by the velocity of this synchronous molecule $f(t) = v(t)/l$, where $l = 12$ mm is the distance between rings to which the same voltage is applied.
For a constant deceleration a the velocity of the synchronous molecule is given by,

$$v(t) = v_0 + at = v_i + a\left(t - \frac{d}{v_i}\right). \tag{4.6}$$

Here, the offset velocity v_0 is parameterised by the initial velocity of the synchronous molecule v_i and the distance d between the source exit and the entrance of the decelerator. As the decelerator works optimally for this synchronous molecule, v_i is usually chosen to be the mean longitudinal velocity of the molecules originating from the source. However, the initial velocity can be reduced to decrease the deceleration strength needed to decelerate to a fixed final velocity. In this case, the improved phase-space acceptance needs to be balanced to the reduced number of molecules at this initial velocity.
Typically, the waveform is started just before the synchronous molecule is at the start of the decelerator, i.e. $t = d/v_i$ after the synchronous molecule exits the source. To incorporate the waveform trigger in the timing sequence of the experiment, the time offset is adjusted to the time after ablation based on the maximum in the time-of-flight signal from the absorption measurement close to the source exit.

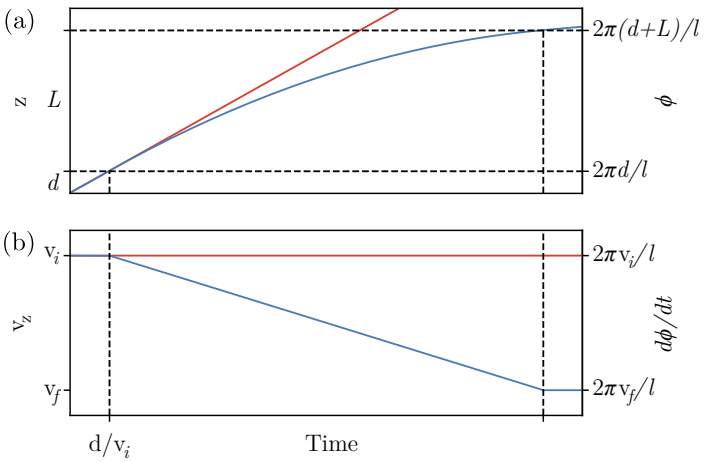

Figure 4.6 *| Motion of the synchronous molecule for AC guiding in red and constant deceleration in blue, and its relation to the phase of the waveform. (a) Longitudinal position and waveform phase, and (b) longitudinal velocity and waveform frequency over time.*

[4]The electric field shown here is simulated in COMSOL [75] by Muller [76] as part of the COLDSIM trajectory simulation package. In incorporating the electric field geometry into the simulation, the electric potential at the electrodes was smoothed incorrectly. This results in an underestimate of the electric field near the electrodes and corresponding transverse trap depth and corresponding phase-space acceptance.

Constant deceleration from initial velocity v_i to final velocity v_f over a distance L corresponds to a deceleration,

$$a = \frac{v_f^2 - v_i^2}{2L}. \tag{4.7}$$

The decelerator can also be used in an AC guiding mode where the deceleration $a = 0$ and molecules with longitudinal velocity matching the synchronous molecule are guided through the decelerator. In this mode the frequency of the waveform is constant with a corresponding phase, $\phi(t) = \frac{2\pi}{l} vt$. For a typical mean forward velocity of molecules emitted from the cryogenic source of 200 m/s, this corresponds to a frequency of 16.7 kHz.
Experimentally the waveform is generated at a sampling frequency of 10 MHz by an 8 channel arbitrary wave generator (AWG Acquitek DA8150) and amplified by custom high-voltage amplifiers (Trek Inc PD10039) with a gain of 1e3, specified to work for a sine-wave frequency of 30 kHz to DC, resulting in a maximum voltage amplitude of 5 kV.

4.3.1. DC guiding field

For characterisation of the molecular beam it is convenient to have access to an operation mode of the decelerator producing a strong molecular signal. For this a DC guiding mode is used in which the voltage on the electrodes is not varied over time and a static electric field is generated in the decelerator, providing transverse confinement without the longitudinal velocity acceptance restriction in AC guiding.
To minimise the electric field in the fluorescence detection area, the static waveform was designed with zero voltage applied to the last ring electrode, closest to the detection area,

$$V_n = V_0 \cos\left(\frac{\pi n}{2}\right), \quad n = 0, 1, 2, ...7, \tag{4.8}$$

with V_0 the voltage amplitude and n the electrode number. The halved longitudinal voltage period in this configuration relative to the deceleration waveform, results in a increased field trap aspect ratio[5] of 4/3 instead of 2/3 for the geometry of the electrodes used in this work. This results in an increase of the transverse to longitudinal trap depth, especially useful for the transverse confinement we are after here. The resulting electric field within the decelerator for a voltage amplitude V_0 of 2 kV is shown in Figure 4.7.
It was shown by Shyur *et al.* [77] that this electric field configuration is useful for deceleration, in the pulsed operation mode as an alternative to the traveling-wave operation mode. Here only the static alternative is considered, referred to as DC guiding.
Molecules traversing the decelerator in a DC guiding mode travel between the electric field minima at a rate much larger than the transverse oscillation rate. Consequently, their motion is predominately determined by the longitudinal field average, which is shown in the black dotted lines in Figure 4.7b. The corresponding Stark shift for BaF in the $N = 1, M_N = 0$ results in a transverse trap depth corresponding to a transverse velocity acceptance of v_x^{acc} of 3.68 m/s. In this work the decelerator is assumed to be operated in an AC guiding or deceleration mode unless stated otherwise.

[5] For some consideration on trap dimensions and aspect ratios and their impact on the phase-space acceptance of the decelerator see subsection D.2.2.

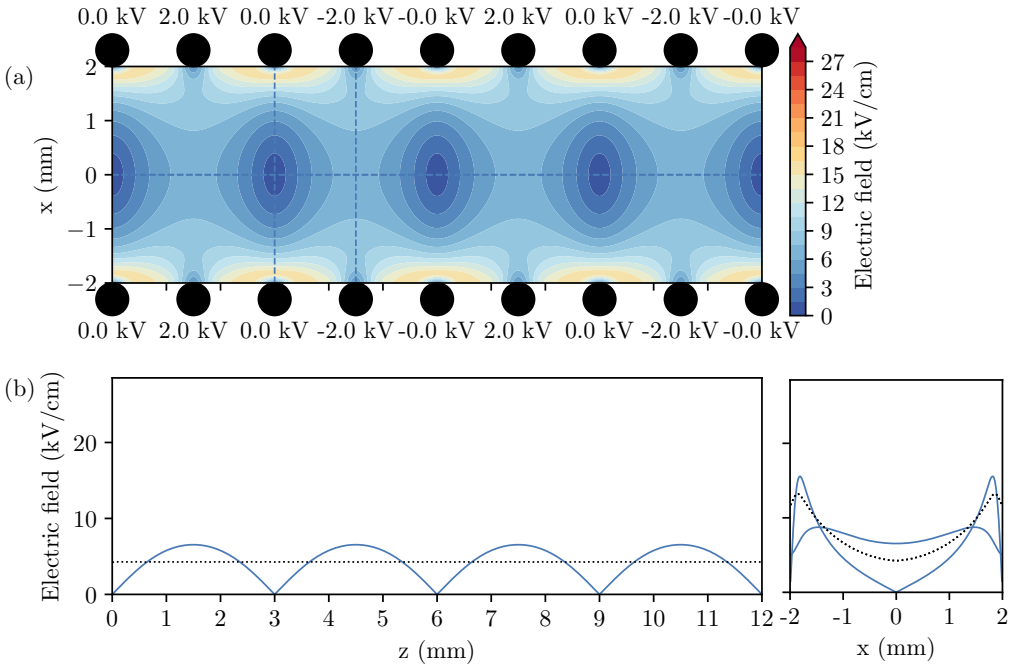

Figure 4.7 | *(a) The electric field within the decelerator when in* DC *guiding mode for a voltage amplitude of V_0 = 2 kV. The black circles indicate the positions of the ring electrodes labelled with their applied voltages. (b) Longitudinal and transverse field slice at positions marked in (a). The black dotted lines show the longitudinally average fields in each direction.*

4.4. Phase-space acceptance

The motion of molecules in the traveling-wave Stark decelerator is determined by the electric field experienced by these molecules and the resulting state dependent Stark shift, which combined provide an effective potential. This effective potential can be used to calculate the phase-space acceptance of the decelerator, describing the efficiency of the decelerator and how to optimise this. The larger the (filled) phase-space acceptance of the decelerator, the more molecules can be decelerated.
The maximum trap depth of any electrostatic trap for these molecules is given by the turning point in the Stark shift W_{tp}. The corresponding maximum capture velocity is,

$$v_{max} = \sqrt{\frac{2W_{tp}}{m}}, \tag{4.9}$$

where m is the molecular mass. This upper limit to the capture velocity is determined by the structure of the molecular state, independent of the trap shape. The trap depth and corresponding field strength obtained from the Stark shifts shown in Figure 4.1 and Figure 4.2 are summarised in Table 4.2.

Table 4.2 | *Turning point electric field strengths and corresponding Stark shifts and maximum capture velocities for lowest rotational states of SrF and BaF.*

Molecule	$\|N, M_N\rangle$	E_{tp} (kV/cm)	W_{tp} (GHz)[6]	v_{max} (m/s)
$^{88}Sr^{19}F$	$\|1,0\rangle$	21.0	4.83	6.01
	$\|2,0\rangle$	59.7	16.7	10.4
$^{138}Ba^{19}F$	$\|1,0\rangle$	20.4	4.14	4.59
	$\|2,0\rangle$	57.1	14.4	8.55

4.4.1. Effective potential

The maximum capture velocity v_{max} is fixed by molecular structure, but the phase-space acceptance is further restricted by the electric field within the decelerator. To quantify this phase-space acceptance the capture range of a single decelerator trap is considered.
The total phase-space volume A_0 of this trap is restricted by the decelerator geometry and maximum capture velocity to be within a sphere of radius v_{max}, and cylinder of length $l/2$ and radius r_0. In this section the fraction of this volume which is captured in the trap is investigated based on the effective potential.
From Figure 4.5, it can be seen that the shape of the electric field trap depends on its position relative to the ring electrodes. The extreme cases where the trap center is at the heart of a ring electrode ($\phi = 0$), and between two ring electrodes ($\phi = \pi/8$), are shown in the figure. As the velocity of molecules within the trap is low compared to the velocity of the trap center relative to the electrodes, the effective trap field is well described by the average over the trap center positions.
The potential energy of molecules in the trap is given by the Stark shift corresponding to the electric field at its position in the trap. During deceleration the effective potential is shifted by the deceleration strength a of the trap in the longitudinal direction. The effective potential is therefore,

$$W_{eff} = \Delta W\big(E(r,z)\big) - maz. \tag{4.10}$$

The effective potential for SrF molecules in the $N = 1, M_N = 0$ state is shown in the first column of Figure 4.8 for multiple deceleration strengths. The potentials have been offset such that the effective potential minimum is zero.
To find the acceptance, cuts through the effective trap minimum are plotted in the longitudinal and transverse direction. The cuts are shown for each of the deceleration strengths in Figure 4.8d, demonstrating the reduced longitudinal trap depth for increasing deceleration strength. Note that the position of the effective trap minimum shifts forward for increasing deceleration strength, corresponding to a displacement of the effective trap center from the electric field minimum. This illustrates the position of molecules on the potential slope during deceleration.

[6] In this work the energy shifts are typically given in frequency units, i.e. divided by Planck constant h. The relation to velocity is via the kinetic energy, as in Equation 4.9. The relation between different common trap depth units is 1 GHz = 0.03336 cm^{-1} = 47.99 mK.

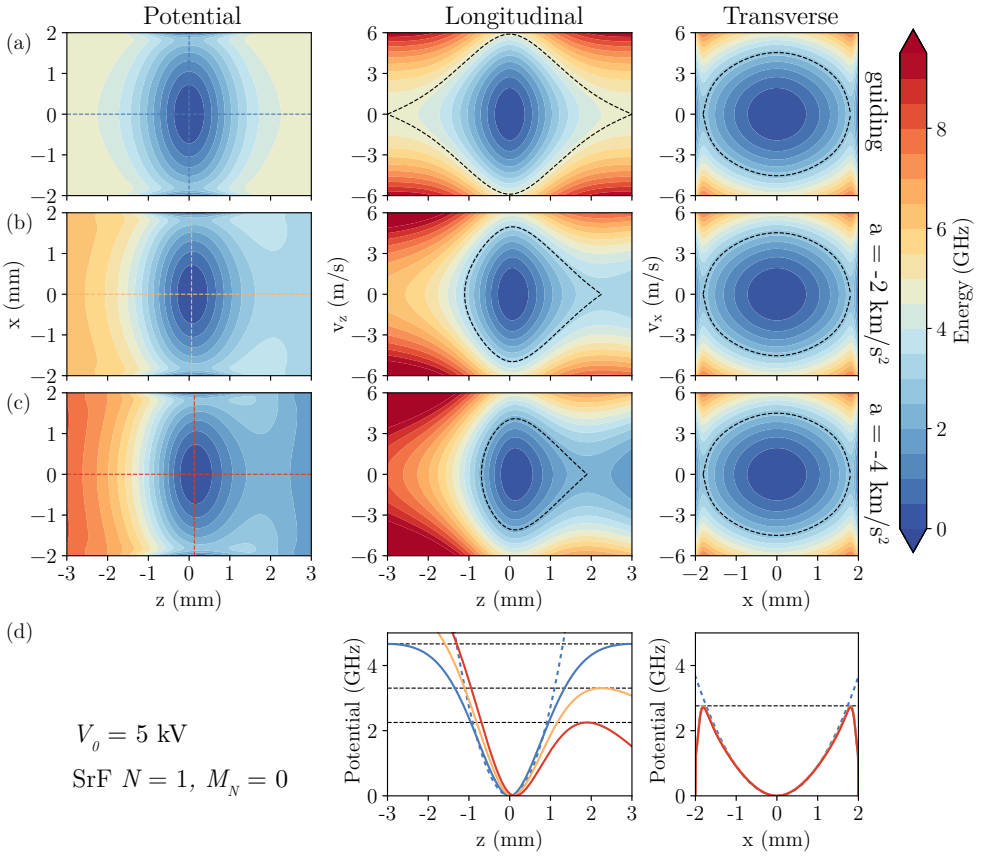

Figure 4.8 *| (left) Effective potential W_{eff} for SrF in $N = 1, M_N = 0$ in the decelerator at a voltage amplitude of 5 kV. The rows correspond to different operation modes of the decelerator, being (a) AC guiding (b) deceleration of a = -2 km/s² and (c) a = -4 km/s². The colored dashed lines show the effective potential minimum. The total energy is shown for (middle) longitudinal and (right) transverse displacement and velocity relative to the effective potential minimum. The black dashed lines indicate the separatrix, corresponding to the boundary of the trap. Row (d) shows a cut-through of the effective potential at the effective potential minimum for the deceleration of a = 0, -2 and -4 km/s² in blue, orange and red, respectively. Here the black dashed lines demonstrate the energy corresponding to the maximum trap depth. The blue dashed line shows the harmonic fit to the potential for AC guiding used to estimate the oscillation frequency within the trap.*

The effective potential for BaF molecules in the $N = 1, M_N = 0$ state is shown in the first column of Figure 4.9. The shape is similar to the effective potential for SrF, although the trap depth is slightly lower by the lower turning point shift W_{tp}. As a result of the higher mass, the reduction of the trap depth for deceleration is larger, reducing the efficiency of deceleration for BaF.

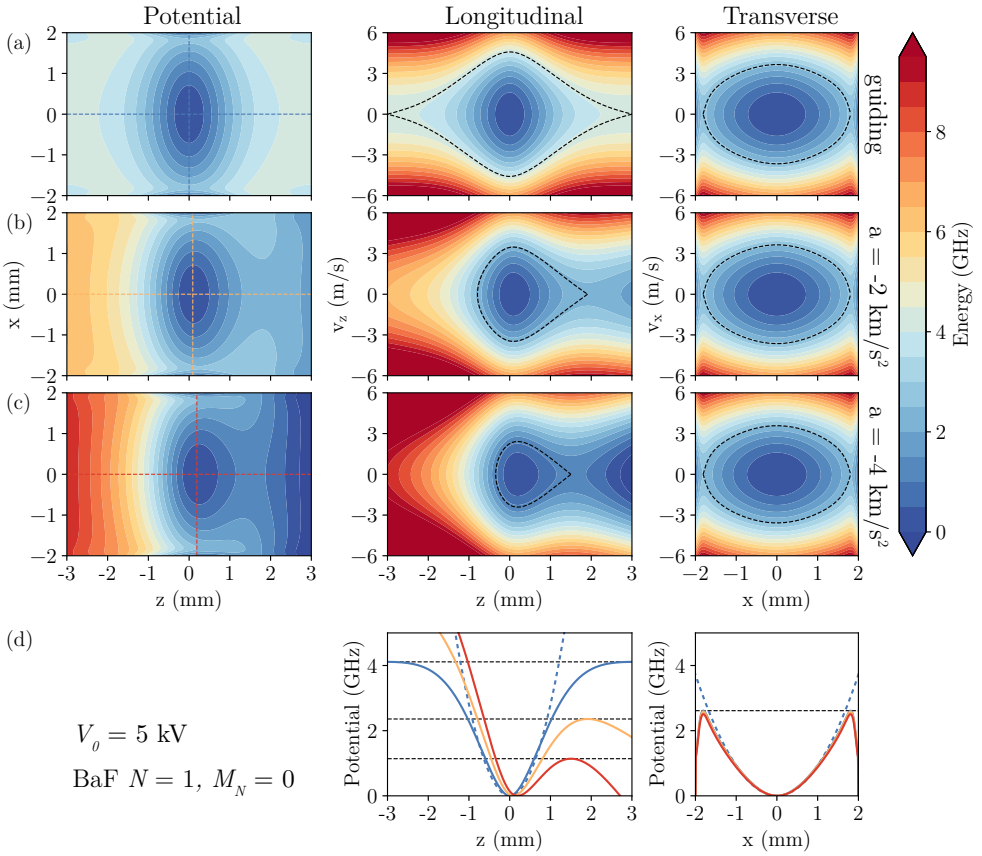

Figure 4.9 *| Effective potential and energy in one dimension for BaF in $N = 1, M_N = 0$ in the decelerator at a voltage amplitude of 5 kV. See caption of Figure 4.8 for details.*

4.4.2. One-dimensional phase-space acceptance

The phase-space acceptance in each direction for a singular trap in the decelerator is given by the phase-space area corresponding to a total energy below the effective trap depth in that direction, incorporating the trap center. From the conservation of energy, any molecule outside of this phase-space area will not be able to enter the trap, while all molecules within this are will stay in the trap. Therefore it provides a useful measure of the efficiency of the decelerator.

In general the full three-dimensional phase-space acceptance has to be considered, as there is a coupling between the different directions of motion for the molecules in the trap, as will be done in the next section. It turns out, however, that some important observations can be made on the limitations to the phase-space acceptance based on the one-dimensional treatment, which is therefore presented here first.

The total energy in each direction, given by the effective potential W_{eff} and kinetic energy,

is shown for a pair of the position and velocity coordinates in the longitudinal and a transverse direction in the middle and right column, respectively, of Figure 4.8 and Figure 4.9. Black dashed lines show the maximum trap depth corresponding to phase-space acceptance boundary of a single trap in this direction, referred to as the separatrix. The area enclosed by these lines provides the one-dimensional phase-space acceptance.

The velocity acceptance, corresponding to the maximum velocity an accepted molecule may have relative to the trap center, is summarised in Table 4.3. The longitudinal velocity acceptance v_z^{acc} strongly depends on the deceleration strength and is therefore given for guiding and a = -2, -4 km/s^2, separately.

The transverse velocity acceptance v_x^{acc} only depends on the position of the effective trap minimum relative to the electric field minimum. For the relatively low deceleration strength considered here, this displacement is minimal as can be seen in the bottom-right of Figure 4.8 and Figure 4.9 for a voltage amplitude of 5 kV. Therefore only the value for guiding is given in this table.

Note that all velocity acceptances are below the maximum capture velocity v_{max} for each of the states, as expected.

Table 4.3 *| Longitudinal (v_z^{acc}) and transverse (v_x^{acc}) accepted velocity for SrF and BaF molecules in the low-field seeking components of the lowest rotational states of SrF, for different voltage amplitudes applied to the decelerator (V_0). The longitudinal acceptance is given for different deceleration strengths a.*

Molecule	$\|N, M_N\rangle$	V_0 (kV)	v_z^{acc} (m/s) at			v_x^{acc} (m/s)
			guiding	a = -2 km/s^2	a = -4 km/s^2	
^{88}Sr^{19}F	$\|1,0\rangle$	3	4.75	3.46	2.07	3.12
	$\|1,0\rangle$	5	5.90	4.97	4.10	4.54
	$\|2,0\rangle$	5	5.12	3.95	2.72	2.68
	$\|2,0\rangle$	8	8.00	7.26	6.52	4.54
	$\|2,0\rangle$	10	9.42	8.79	8.16	5.74
^{138}Ba^{19}F	$\|1,0\rangle$	5	4.59	3.47	2.41	3.66
	$\|2,0\rangle$	5	4.20	2.76	1.10	2.23
	$\|2,0\rangle$	8	6.46	5.53	4.60	3.73
	$\|2,0\rangle$	10	7.51	6.72	5.94	4.70

From Figure 4.8, it can be seen that the longitudinal potential is not symmetrical around the effective trap center for deceleration. Nevertheless, the position acceptance can be considered, given by half the distance between the maximum position coordinates within the phase-space acceptance. Note that the position acceptance in the longitudinal direction is limited to half the spacing between two trap centers $l/2 = 3$ mm, and the transverse position acceptance is limited by the inner radius of the ring electrodes $r_0 = 2$ mm.

In Figure 4.10, the one-dimensional phase-space acceptance is shown for different voltage amplitudes applied to the decelerator and different deceleration strengths, for SrF molecules in $N = 1, M_N = 0$. Again, I will discuss SrF first, and the difference for BaF later.

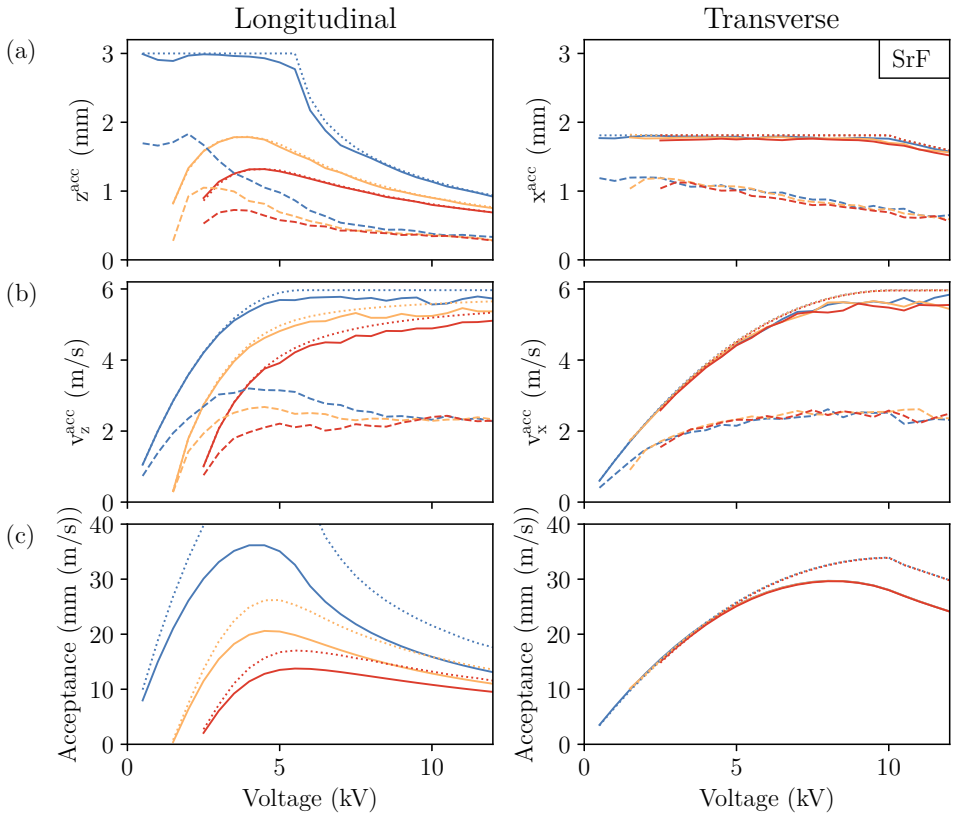

Figure 4.10 | *One-dimensional phase-space acceptance in a longitudinal and transverse direction for SrF in the $N = 1, M_N = 0$ state in a single trap of the decelerator and the voltage which is applied to it, for guiding (blue), deceleration at a = -2 km/s^2 (yellow) and -4 km/s^2 (red). In (a) and (b), the dotted lines are determined from the separatrix. The solid and dashed lines correspond to the maximum and HWHM of the accepted distribution from Monte-Carlo simulations. In (c) the dotted line corresponds to the harmonic approximation of the 1D acceptance. The solid line corresponds to the phase-space area enclosed by the separatrix.*

The dotted lines in Figure 4.10a show the maximum displacement radius, while the dotted lines in Figure 4.10b show the maximum velocity acceptance, determined from the separatrix. The continuous and dashed lines will be treated later, when discussing the three-dimensional acceptance.

A number of observations on the limitations to the phase-space acceptance of the decelerator are warranted. Firstly, consider the decelerator in a guiding mode, represented in blue. It can be seen in Figure 4.10b that the longitudinal velocity acceptance becomes equal to the maximum capture velocity at approximately 5 kV, for which the maximum electric field amplitude at the longitudinal axis becomes equal to the turning point field. As the transverse electric field maximum around the trap center is lower, the transverse velocity acceptance

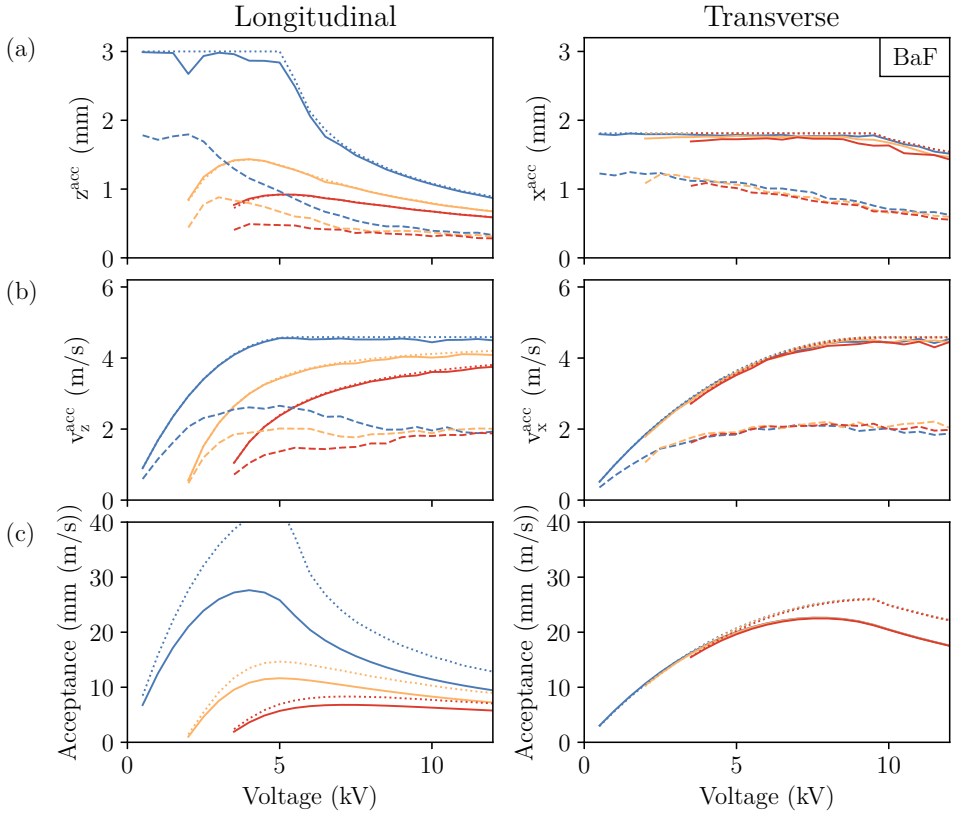

Figure 4.11 | *One-dimensional phase-space acceptance in a longitudinal and transverse direction for BaF in the $N = 1, M_N = 0$ state in a single trap of the decelerator and the voltage which is applied to it. See caption of Figure 4.10 for details.*

becomes equal to the maximum capture velocity at a higher voltage. For higher voltages it can be seen in Figure 4.10a that the effective trap size in either direction is reduced.
Secondly, considering deceleration, it can be seen from the overlapping of the acceptance dimensions for different deceleration, that the transverse acceptance is hardly effected by increasing deceleration, as was also observed previously.
The solid lines in Figure 4.10c show the one-dimensional phase-space acceptance calculated by the phase-space area enclosed by the separatrix. The dotted lines in this row of figures show the approximation to the phase-space acceptance for a harmonic potential, for which the phase-space contour is an ellipse of area $\pi q^{acc} v_q^{acc}$, where $q = z, x$ is the longitudinal or transverse coordinate, respectively.
In Figure 4.11, the one-dimensional phase-space acceptance is shown for BaF molecules in $N = 1, M_N = 0$. It follows the same trends as SrF, as expected from the similarities in the Stark shift. The higher mass of BaF does however result in a reduced velocity acceptance, also resulting in an overall reduction of the one-dimensional acceptance. Moreover, it results

in a stronger decrease in longitudinal acceptance with deceleration.

4.4.3. Three-dimensional phase-space acceptance

Thus far, the phase-space acceptance for each dimension has been considered separately. As however the Stark shift is given by the electric field amplitude, which can not be separated into different coordinates, the motion in the different directions is coupled.
The amount of coupling is not immediately obvious. For low deceleration strengths, the potential is approximately harmonic in all directions. In this case the contribution to the total energy from the motion in each dimension remains approximately constant over time and the coupling between the motion in different directions is weak. However, at further displacements from the trap center in the longitudinal direction, the effective potential deviates from being quadratic, resulting in a stronger coupling between oscillations of the molecule in each direction of the trap.

Two limiting cases can be considered. Firstly, a lower-bound is given by the phase-space volume corresponding to molecules in the trap with a total energy below the lowest of the trap depths in each direction. A molecule with this energy will never escape the trap, even if it is all brought into motion in this one direction. This lower-bound is shown in Figure 4.12 and Figure 4.13 for each deceleration strength by the lowest colored dashed lines.
The upper-bound to the phase-space acceptance is given by the phase-space volume corresponding to molecules in the trap with a total energy below the sum of the maximum trap depths in all three dimensions. Whatever the distribution over the motion in the different dimensions, a molecule with a higher energy will not be captured. This upper-bound is shown in Figure 4.12 and Figure 4.13 for each deceleration strength by the upper colored dashed lines. The shaded area between these upper and lower bounds shows the possibilities for the full three-dimensional phase-space acceptance.

Arguments based on the total energy and the dependence on each of the phase-space coordinates have brought us this far. A further description based on this argumentation does not seem to be possible. To estimate the three-dimensional phase-space acceptance for molecules in the decelerator, Monte-Carlo trajectory simulations are used, similar to the procedure presented in [50].
The simulation performed for this has been developed in our group, started by Muller [76] under the name COLDSIM. In this simulation the trajectories are calculated for individual molecules based numerical integration of the equations of motion. The force on the molecule is given by the electric field gradient and the Stark shift, as presented earlier. The electric potential geometry is simulated in COMSOL [75] based on a single ring to which a voltage is applied, within a sequence of grounded electrodes. In this way, the electric field can be calculated for any waveform based on the superposition principle. The Stark shift is simulated in PGOPHER [68], implemented as a 10th-degree polynomial fit. The simulation package is used to simulate full trajectories, but also time-of-flight profiles or phase-space distribution evolution, as are shown in this work.

To estimate the three-dimensional phase-space acceptance of a single trap, the trajectory is simulated for molecules with an initial uniform distribution over the phase-space

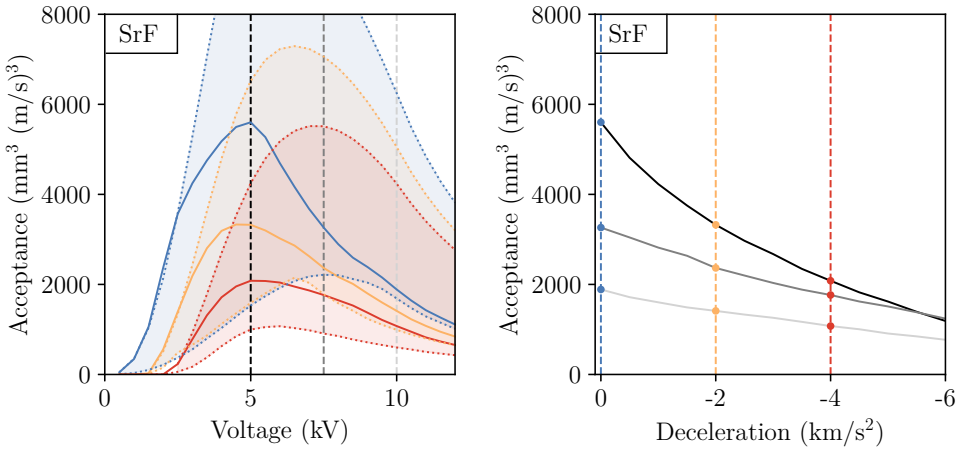

Figure 4.12 | *Three-dimensional phase-space acceptance for SrF in the $N = 1, M_N = 0$ state in a single trap of the decelerator. The acceptance is shown for guiding (blue), deceleration at a = -2 km/s^2 (yellow) and -4 km/s^2 (red), and for voltage amplitudes applied to the decelerator of 5 kV (black), 7.5 kV (grey) and 10 kV (light grey). The dotted lines corresponds to the upper and lower estimate for the acceptance based on the energy of the molecule in the trap.*

volume span by the maximum position and velocity acceptance in each direction. The fraction of molecules which are still within the trap after traversing the effective potential for 10 ms is considered to be accepted, and multiplied by the total probed phase-space volume to give the three-dimensional phase-space acceptance. This upper limit to the simulation time is chosen as it is of the same order as the molecules spend in the decelerator, and for typical voltages it corresponds to multiple oscillation periods around the trap center. The resulting three-dimensional phase-space acceptance is shown as a solid line in Figure 4.12 and Figure 4.13 for different voltages applied to the decelerator, in the cases of guiding, deceleration by -2 and -4 km/s^2. For voltage amplitudes of 5, 7.5 and 10 kV, the decrease of the phase-space acceptance with increasing deceleration strength is also shown.

With the initial phase-space distribution corresponding to the molecules captured in the three-dimensional trap the distribution over the different phase-space coordinates can now also be investigated. The maximum position and velocity acceptance coordinates have been confirmed by the Monte-Carlo simulation, taken to be the maximum of the accepted distribution, shown as the solid lines in rows (a) and (b) of Figure 4.10 and Figure 4.11. More interesting is the half width at half maximum of the distribution in each phase-space coordinate, as shown by the dashed lines in these figures. These are particularly interesting as they can be compared to the distributions found from the fit to the peaks in the time-of-flight profiles, corresponding to the individual traps in the decelerator.

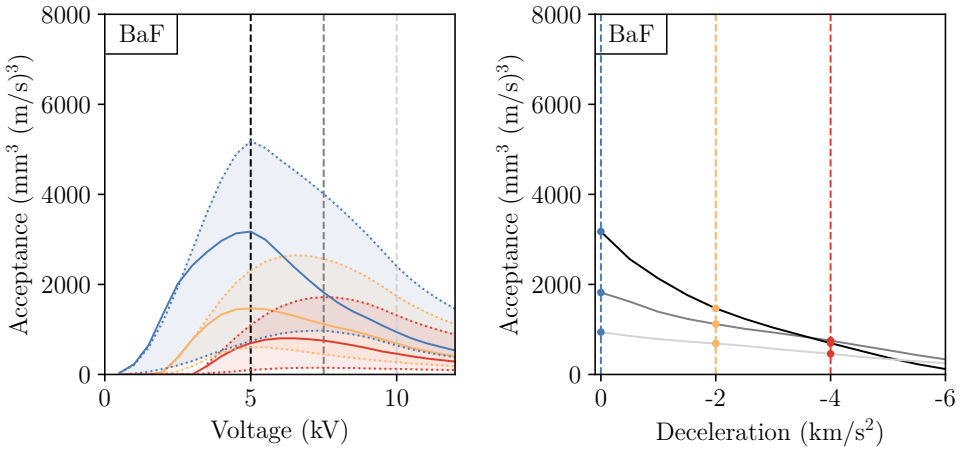

***Figure 4.13** | Three-dimensional phase-space acceptance for BaF in the $N = 1, M_N = 0$ state in a single trap of the decelerator. See caption of Figure 4.12 for details.*

4.4.4. Transversely confined molecules

Molecules which are not captured in the longitudinal velocity acceptance of the decelerator can still be transversely confined and thereby reach the end of the decelerator without being decelerated. As a result, non-decelerated molecules have been observed in the time-of-flight profiles measured at the end of the decelerator.
These molecules are moving between multiple traps in the decelerator, but are not captured by any of them. In this case the molecules experience an effective radial potential given by the average over longitudinal structure of the a trap. The average electric field experienced by these molecules is expected to be as shown in the black dashed lines in Figure 4.5d. For molecules traversing the decelerator at a longitudinal velocity slightly above the acceptance, the relative velocity to the traps is low. As a result the averaging to this field is long relative to the transverse oscillation rate. Consequently, the molecules may experience an electric field amplitude above the turning point field E_{tp} for long enough to be extracted from the decelerator, towards the electrodes. The phase-space acceptance for these molecules does therefore strongly depend on the relative velocity compared to synchronous molecule and is beyond the scope of this work. Molecules have been observed to traverse the decelerator in this transversely confined manor in trajectory simulation as well as in measurements.

4.4.5. Oscillation frequency

Thus far, the boundaries of the three-dimensional traps within the decelerator have been considered, that determine the phase-space distribution accepted in the decelerator. To understand the motion of the molecules within the decelerator the shape of the traps has to be considered.
The electric field around the trap center increases linearly in each direction, as can be seen in Figure 4.5. The Stark shift for the lowest rotational levels of SrF and BaF in low fields is

quadratic. As a result, the effective potential around the trap center is also expected to be quadratic. This is confirmed by Figure 4.8d and Figure 4.9d, where a quadratic potential, $W_q = k_q q^2/2$ for $q = x, z$, is fitted to the effective potential up to half of the maximum trap depth energy, shown in the blue dashed line. The resulting spring constants k_q provide the angular oscillation frequency of molecules close to the trap center in the transverse and longitudinal direction,

$$\omega_q = \sqrt{\frac{k_q}{m}}, \tag{4.11}$$

where m is the mass of the molecule. Table 4.4 shows the oscillation frequencies for different voltages amplitudes applied to the decelerator for multiple states of SrF and BaF. In the appendix in section D.2, the oscillation frequencies are compared to the predicted values from the ideal decelerator field. Note that for motion in a harmonic potential the oscillation frequency provides the ratio between the maximum displacement and velocity.

***Table 4.4** | Longitudinal (ω_z) and transverse (ω_x) oscillation frequency for SrF and BaF molecules in the low-field seeking components of the lowest rotational states, for different voltage amplitudes applied to the decelerator (V_0). The angular oscillation frequency is obtained via harmonic fit to the cut-through of the potential up to half of the maximum trap depth as illustrated in Figure 4.8 and Figure 4.9.*

Molecule	$\lvert N, M_N\rangle$	V_0 (kV)	ω_z (krad/s)	ω_x (krad/s)
$^{88}Sr^{19}F$	$\lvert 1,0\rangle$	3	2.82	1.66
	$\lvert 1,0\rangle$	5	4.51	2.61
	$\lvert 2,0\rangle$	5	2.35	1.23
	$\lvert 2,0\rangle$	8	3.97	2.11
	$\lvert 2,0\rangle$	10	5.04	2.71
$^{138}Ba^{19}F$	$\lvert 1,0\rangle$	5	3.77	2.17
	$\lvert 2,0\rangle$	5	1.95	1.03
	$\lvert 2,0\rangle$	8	3.24	1.75
	$\lvert 2,0\rangle$	10	4.13	2.24

For SrF molecules in the $X^2\Sigma^+(v = 0, N = 1, M_N = 0)$ state traversing the 4.5 m long decelerator with a voltage amplitude of 5 kV at a typical guiding velocity of 200 m/s, this corresponds to approximately 17 longitudinal and 10 transverse oscillations over the length of the decelerator.

4.5. Filling of the phase-space acceptance

In the previous sections the phase-space acceptance of the decelerator in different operation modes has been considered. However, the phase-space acceptance only results in an increase in

the number of decelerated molecules if it is filled. In this section the filling of the phase-space acceptance is discussed.
Properties of the molecular beam will be discussed in chapter 5 and chapter 6, and in more detail in Esajas [46] for SrF and Mooij [47] for BaF. Here some typical values for the beam emittance are summarised, in order to investigate the filling of the phase-space acceptance. The cryogenic source produces a molecular pulse with a length of over 100 mm at a longitudinal velocity around 200 m/s, with a spread of tens of m/s. The initial molecular beam diameter is of the order of the aperture of the cell exit of 4.5 mm. The transverse velocity spread is again tens of m/s.
The length of the molecular pulse results in a distribution over multiple traps in the decelerator. The longitudinal velocity spread is far above the longitudinal velocity acceptance, resulting in a capture of only a fraction of the molecules in the distribution. The initial beam diameter matches the transverse position acceptance of the decelerator quite well. However, over the necessary free-flight between the source and the decelerator, the molecular beam diverges. As will be discussed in subsection 4.5.1, this reduces the transverse phase-space matching between the source and the decelerator, which is (partially) compensated by the hexapole lens.
The phase-space evolution of SrF molecules traversing the decelerator is illustrated in Figure 4.14. For clarity, only a two-dimensional simulation is considered, by putting $y = 0$ for all molecules. The longitudinal and transverse phase-space distribution of molecules is shown both for molecules that are in the three-dimensional acceptance of the decelerator (red) and only transversely confined (blue).
The latter is due to the large longitudinal velocity spread, between 150 and 250 m/s, and molecules entering the decelerator between the traps. These molecules are guided through the decelerator without being decelerated. The transverse velocity distribution of these molecules is observed to be smaller than that of the decelerated molecules, which is understood by the reduced transverse trap depth for an electric field averaged over multiple traps. At 25 ms after the experiment-trigger these molecules are seen to have left the decelerator, which spans from $z = 0$ to 4.5 m, shown by the black dashed line in the top figure. When the molecules have left the decelerator the distribution starts to expand freely.
The decelerated molecules follow the red line in the top figure, corresponding to the synchronous molecule for which the waveform is designed. The zoom-in of the longitudinal phase-space distribution at 45 ms illustrates the filling of some of the traps. The length of the pulse of decelerated molecules can be seen to span tens of decelerator traps at a separation of 6 mm. At 55 ms after the experiment-trigger the decelerated molecules have exited the decelerator and are transversely dispersed.
The dashed black lines in the zoom-in of the longitudinal phase-space, and the transverse phase-space, correspond to the phase-space separatrix in each of these directions. The simulated molecules are contained in these acceptance boundaries as expected. The inhomogeneous filling is understood from the projection of the molecule distribution contained in the three-dimensional trap.

4.5.1. Transverse phase-space matching

Ideally, there would be no distance between the source exit and decelerator entrance, as the initial transverse distribution encompasses the full transverse acceptance. Due to practical

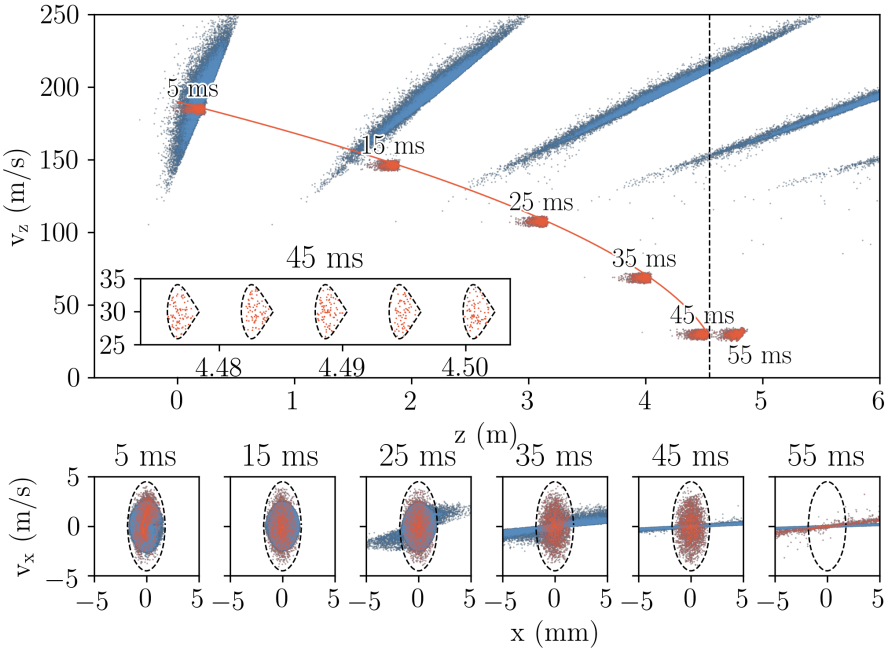

Figure 4.14 | *Simulated phase-space distribution of SrF molecules in the $N = 1, M_N = 0$ while being decelerated from 190 to 30 m/s at a voltage amplitude of 5 kV, corresponding to a = -4 km/s^2, at different times since the experiment-trigger, both in the (top) longitudinal and (bottom) a transverse direction. The red dots correspond to decelerated molecules. The red line in the top figure illustrates the trajectory of the synchronous molecule. The blue dots correspond to molecules that are transversely confined to the decelerator, but do not fall inside the longitudinal acceptance. The zoom-in at the top figure shows the distribution of the decelerated molecules over some of the traps at 45 ms. The black dashed lines in the zoom-in and in the transverse plots correspond to the phase-space separatrices found from the effective potential. This simulation is performed in two dimensions, with $y = 0$ for all molecules.*

limitations however this is not possible, and a free-flight distance of hundreds of millimeters has to be introduced.

This distance has to be included for a combination of reasons. First of all, the cryogenic source is enclosed by two layers of heat shields, limiting the heat load on the cell. Secondly, the cryogenic source has to be heated regularly, for maintenance and to unfreeze the neon buffer gas from the heat shield. To ensure the vacuum in the decelerator is not broken, after which the decelerator would have to be conditioned to high voltages, a vacuum valve is installed in the molecular beam line. Lastly, having the source exit and decelerator too close together would result in a high buffer gas density in the decelerator, which by collisions results in losses from the decelerator traps. Also, the high voltage applied to the decelerator would be difficult to maintain at this pressure.

The free-flight does however result in transverse dispersion of the molecular beam, resulting

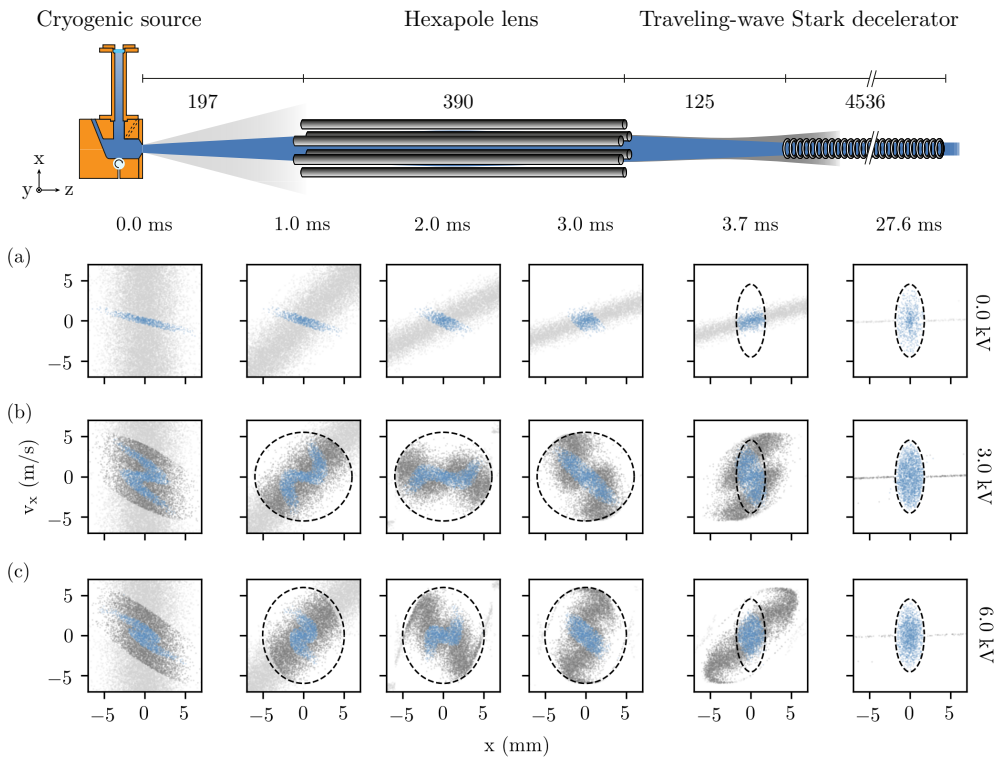

Figure 4.15 | *Transverse phase-space distribution of SrF molecules traversing the hexapole lens and decelerator, at different times after exiting the source. When molecules are within the hexapole lens (1.0 to 3.0 ms), its acceptance is shown as a dashed line. When molecules are in the decelerator (start 3.7 ms, end 27.6 ms) the acceptance thereof is shown as a dashed line, for guiding at a voltage amplitude of 5 kV. Molecules accepted transversely in the decelerator are shown in blue, molecules accepted in the hexapole lens in dark grey and molecules outside of the acceptance in light grey. Rows (a) to (c) correspond to voltage magnitudes applied to the hexapole lens from 0 to 6 kV. This simulation is performed in two dimensions, with $y = 0$ for all molecules. The longitudinal velocity spread is minimised for clarity, minimising chromatic aberrations. For reference the setup diagram is repeated with dimensions in mm.*

in under-filling of the transverse acceptance. This can be mitigated by a hexapole lens focusing molecules back to the beam axis as discussed in section 4.2.

Figure 4.15 demonstrates the impact of the hexapole lens on the transverse phase-space distribution of the molecular beam for multiple applied voltages based on the trajectory simulations. For clarity, the simulation is performed for a reduced longitudinal velocity spread with mean velocity of 190 m/s and Gaussian FWHM of 2 m/s. This minimises chromatic abortions of the lens, that would otherwise blur the focus of the molecular beam. Molecules with a different forward velocity are not accepted in the longitudinal acceptance of the decelerator and do not contribute to the number of decelerated molecules anyway. The

longitudinal position spread is set to zero. As a result, all molecules enter the hexapole lens and the decelerator at approximately the same time, at 1.0 and 3.7 ms, respectively.
The transverse distribution of the molecular beam at the exit of the source is simulated by a Gaussian transverse position distribution with FWHM of 5 mm. The transverse velocity distribution in the order of tens of m/s, is assumed to be uniform in the velocity range accepted by the hexapole lens and decelerator.
When no voltage is applied to the hexapole lens, the transverse phase-space distribution performs its typical free-flight stretching. At the entrance of the decelerator the distribution fills a fraction of the transverse acceptance. During the traversal of the decelerator molecules within the acceptance perform multiple oscillations, thereby being distributed over the full acceptance. As however the outer regions of the acceptance are under-filled the phase-space density is diluted.
Note that, because of the large position spread of the beam originating from the cryogenic source, the transverse acceptance is partially being filled even without hexapole lens.
As the Stark shift of SrF is not linear, the radial motion in the hexapole lens is anharmonic, with a stronger restoring force at larger displacement. As a result the rotation in phase-space is larger, further from the center of the distribution, resulting in the typical zigzag shape appearing in Figure 4.15. As a result the hexapole lens does not make a perfect image in mapping the molecular beam, analogous to spherical aberrations in an optical system. Nevertheless, a significant increase in transverse phase-space matching is achieved with the hexapole lens, resulting in a significant increase in number of decelerated molecules.
In introducing a hexapole lens, the distance between the source and the decelerator had to be increased from 370 to 712 mm, making the transverse dispersion worse in the case of free-flight, when no voltage is applied to the hexapole. The reduction of the transverse phase-space filling compared to no distance between the source and decelerator is estimated assuming a molecular beam with a Gaussian transverse position spread (FWHM) of 5 mm and a uniform transverse velocity spread. For a transverse position acceptance x^{acc} of 1.8 mm and velocity acceptance v_x^{acc} of 4.54 m/s for SrF, corresponding to a voltage amplitude of 5 kV applied to the decelerator (see Table 4.3), the intensity of the accepted beam is estimated to be reduced by a factor 3.9 due to a free-flight distance of 370 mm at a longitudinal velocity of 190 m/s. In free-flight over 712 mm a factor of 13 in intensity is estimated to be lost, a further reduction by a factor of 3.2.
For BaF the transverse velocity acceptance is $v_x^{acc} = 3.66$ m/s. In that case the estimated intensity reduction factor due to a free-flight over 370 mm at a longitudinal velocity of 200 m/s is 2.6. Over 712 mm the reduction factor is 7.7, a factor of 3.0 lower than before increasing the distance.

4.5.2. Longitudinal phase-space matching

By increasing the distance between the source and the decelerator the longitudinal velocity matching between the arriving molecules and the velocity of the waveform applied to the decelerator can be improved [78]. The longitudinal velocity for molecules arriving at a time t at the entrance of the decelerator, a distance d from the source exit, is $v = d/t$. For the synchronous molecule traveling at an initial velocity v_i, this is by definition equal to the velocity of the waveform when entering the decelerator, given in Equation 4.6. Therefore, molecules traveling at this velocity have optimal matching to the longitudinal phase-space

acceptance of the decelerator. The distance between the source and decelerator can be adjusted so that molecules velocity dependent free-flight time results in a matching between the velocity of the molecules and the waveform when these molecules arrive at the decelerator. This sets the condition,

$$\frac{dv}{dt}(t = d/v_i) = -\frac{v_i^2}{d} = a. \tag{4.12}$$

This shows that the optimal distance is $d = -v_i^2/a$ for a given deceleration and initial velocity. For a constant deceleration from initial velocity v_i to standstill ($v_f = 0$) over a decelerator length L, following Equation 4.7, the optimal distance would be $d = 2L$. Figure 4.16 illustrates that the optimal match for a typical initial velocity of the synchronous molecule $v_i = 200$ m/s and deceleration strength of $a = -4$ km/s^2 occurs at a distance $d = 10$ m.
To ensure the transverse confinement of the molecular beam over this longitudinal free-flight distance a hexapole can be installed. However, for a hexapole of this length the correlation between transverse velocity and position is lost due to longitudinal velocity spread and anharmonicity of the radial potential. In this regime the hexapole acts more analogous to a guide than a lens.

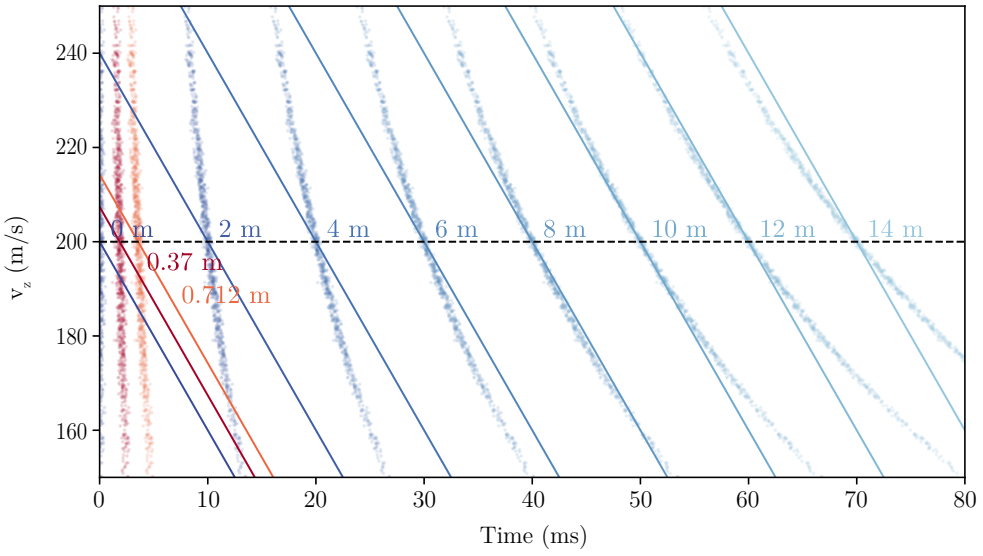

Figure 4.16 | *Matching between the longitudinal velocity of the molecular beam and the velocity of the applied waveform when these molecules arrive at the decelerator for different distances between the source exit and this decelerator. The solid lines show the velocity of the waveform corresponding to a deceleration $a = -4$ km/s^2, and matching the arrival time at the entrance of the decelerator of the synchronous molecule with an initial velocity v_i of 200 m/s. The arrival velocity and time at the decelerator are shown by the scatter. The distance from the source to decelerator are shown for the case before installation of the hexapole lens (red) and after (orange).*

The gain in number of molecules that fall in the acceptance of the decelerator, corresponding to intensity gain of the decelerated molecular beam, strongly depends on the longitudinal

velocity spread and the temporal spread of molecules exiting the source. However, from Figure 4.16 it is clear that the improvement of the longitudinal phase-space matching by the increase in distance from 370 mm to 712 mm due to the installation of the hexapole lens is minimal. From trajectory calculations this effect is estimated to have increased the beam intensity by ~5% for the typical values used in this example. When decelerating at a lower deceleration strength to a larger final velocity the effect is even smaller.
Next to practical limitations of implementing a 10 m long hexapole guide the flexibility of the setup would be greatly reduced as the optimal matching only holds for this ratio of initial velocity and deceleration. Nevertheless, for lighter molecules, that do not require such a long decelerator, it may be a viable option to consider. Also, for molecular beams with a significantly lower average longitudinal velocity this could become a feasible method to improve the longitudinal matching between the source and the decelerator.

4.6. Conclusion and outlook

In this chapter the working principle of the traveling-wave Stark decelerator and hexapole lens has been reviewed. The phase-space acceptance for SrF and BaF molecules has been characterised, firstly using the one-dimension separatrix found from the effective potential, then using Monte-Carlo trajectory simulations. The phase-space acceptance for BaF has been shown to be significantly smaller than for SrF due to the higher mass. This higher mass reduces the velocity acceptance for these molecules, but also increases the reduction of the phase-space acceptance when decelerating.
The filling of this phase-space acceptance has been investigated, demonstrating the improvements to the phase-space matching between the source and the decelerator by installing a hexapole lens between these.
In chapter 5 the experimental results for the improvements to deceleration of SrF are shown. The first Stark deceleration of BaF is demonstrated in chapter 6.
To further improve the phase-space matching between the source and the decelerator, transverse laser-cooling can be applied, as is under active development by our collaboration at the time of writing. By cooling the molecular beam, its transverse energy can be reduced, which is impossible with the conservative forces within the electrostatic hexapole lens. In particular the combination of transverse laser-cooling and a hexapole lens is promising in achieving small and collimated molecular beams suitable for being decelerated in a traveling-wave Stark decelerator.
In this chapter, we have mainly focused on molecules in the $N = 1, M_N = 0$ state. However, because of the significantly larger Stark shift of molecules in the $N = 2, M_N = 0$ state for high electric field amplitudes, the phase-space acceptance could be strongly increased by decelerating molecules in this state instead. As the Stark shift is only larger for high electric field however, this would only be beneficial when higher voltages can be applied to the decelerator than are currently feasible. At the time of writing, the use of transformers to generate the required rapidly oscillating high-voltages is being investigated in our group, as well as improvements to the decelerator modules to allow for the use of these higher voltage amplitudes. The effective potential for BaF in the $X^2\Sigma^+(v = 0, N = 2, M_N = 0)$ state in the decelerator with an applied voltage amplitude of 10 kV is shown in Figure 4.17, illustrating the significant phase-space acceptance increase possible for molecules in this state.

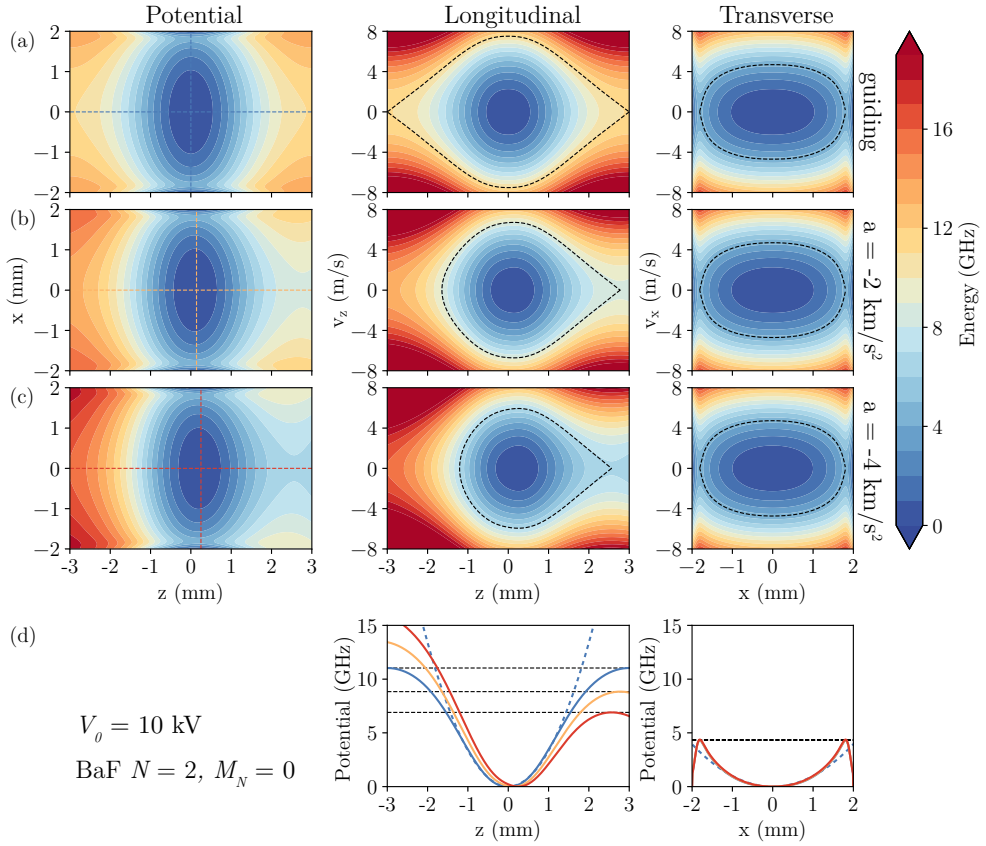

Figure 4.17 | *(left) Effective potential W_{eff} for BaF in $N = 2, M_N = 0$ in the decelerator at a voltage amplitude of 10 kV. The rows correspond to different operation modes of the decelerator, being (a) AC guiding (b) deceleration of a = -2 km/s^2 and (c) a = -4 km/s^2. The colored dashed lines show the effective potential minimum. The total energy is shown for (middle) longitudinal and (right) transverse displacement and velocity relative to the effective potential minimum. The black dashed lines indicate the separatrix, corresponding to the boundary of the trap. Row (d) shows a cut-through of the effective potential at the effective potential minimum for the deceleration of a = 0, -2 and -4 km/s^2 in blue, orange and red, respectively. Here the black dashed lines demonstrate the energy corresponding to the maximum trap depth. The blue dashed line shows the harmonic fit to the potential for AC guiding used to estimate the oscillation frequency within the trap.*



5

Deceleration of strontium fluoride

In this chapter the efforts to increase the number of decelerated molecules are described based on continued measurements on strontium fluoride (SrF), the specimen used during the development of the setup. These improvements are categorised as follows: (1) The source reliability and ease of maintenance have been improved by the replacing the target rotation mechanism. (2) The data acquisition system has been updated to have synchronisation between data-streams and provide access to background data on the state of the setup. (3) The intensity of the decelerated molecular beam has been increased by improved phase-space matching between the source and the decelerator using a hexapole lens. (4) The deceleration approach has been altered to mitigate losses of slow molecules exiting the decelerator.
The transition to barium fluoride (BaF), the molecule of choice for the NL-eEDM experiment, is described in chapter 6. This molecule is 1.5 times as heavy as SrF, making deceleration considerably more challenging, which is a good reason to optimise the decelerator setup using SrF first.

The chapter image shows the decelerator setup implemented in its environment, with the vacuum chamber and module partially opened to show what is inside.

5.1. Introduction

In previous work, presented in Aggarwal *et al.* [62], the deceleration of a pulsed beam of strontium fluoride ($^{88}Sr^{19}F$) molecules has been demonstrated. Starting from an initial velocity of 190 m/s, corresponding to the average longitudinal velocity of the beam, the molecules were decelerated to various final velocities, including standstill. Furthermore, trapping of the molecules for several tens of milliseconds was demonstrated. As part of that effort deceleration to a molecular beam velocity to 30 m/s was shown, which is the target velocity for the NL-eEDM experiment. This result is reviewed in Figure 5.1 as a starting point for this work.

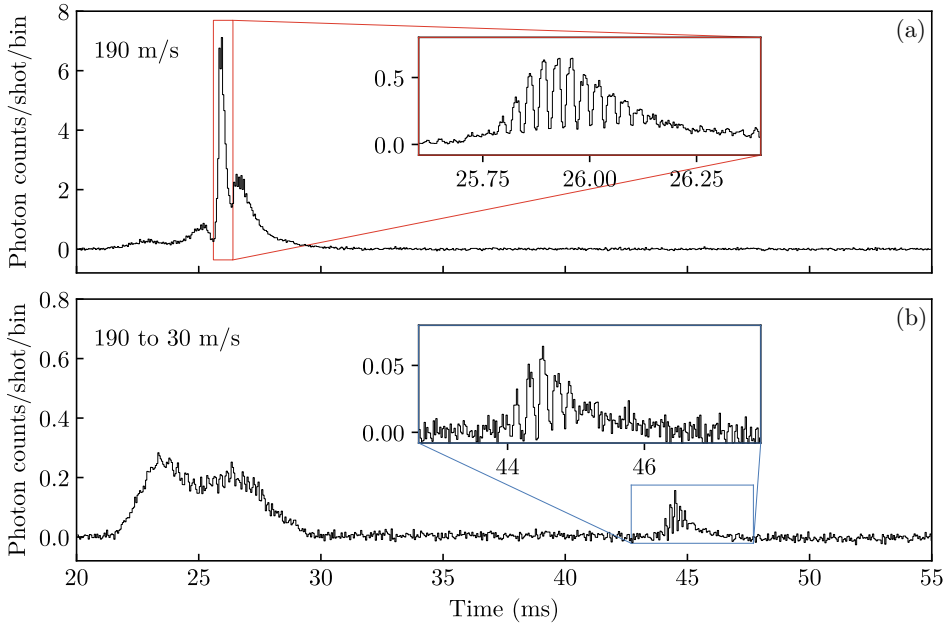

***Figure 5.1** | Time-of-flight profile of SrF molecules traversing the traveling-wave Stark decelerator based on data from Aggarwal* et al. *[62]. The binsize of the long timescale plots is 50 µs. (a) AC guiding at 190 m/s with an applied voltage amplitude of 3 kV. The zoom-in around the guided peak marked in red shows molecular packages filling multiple field minima, at a binsize of 3 µs. (b) Deceleration from 190 to 30 m/s with an applied voltage amplitude of 5 kV. Again a zoom-in is shown with the decelerated molecules at a binsize of 19 µs to compensate for the velocity difference.*

In Figure 5.1, time-of-flight profiles are shown measured by laser-induced fluorescence from SrF molecules at the end of the decelerator, 4.9 m from the source exit. The zero point for the time axis is given by the experiment-trigger, corresponding to the Q-switch trigger of the ablation laser, that initiates the production of the pulsed molecular beam. In Figure 5.1a the signal is shown in the case where molecules are guided through the decelerator at a constant velocity of 190 m/s. The molecules arrive at the fluorescence detection area between 20 to

30 ms after the experiment-trigger, and can be categorised in a guided and non-guided peak. The guided peak, marked by the red box, corresponds to molecules traversing the decelerator within its three-dimensional acceptance. The zoom-in around the guided peak shows substructure, corresponding to molecules occupying multiple electric field minima, to which the molecules in low-field seeking states are attracted. These electric field minima occur at a separation of 6 mm, which combined with the velocity of the molecules explains the spacing of the peaks in the time-of-flight. From the peaks in this substructure it is seen that more than ten of these traps are occupied during guiding. The broader distribution around this guided peak is referred to as the non-guided peak, which corresponds to molecules that are only confined transversely, as the longitudinal velocity of these molecules is too far from the guiding velocity. These molecules fall only in the transverse, not in the longitudinal acceptance of the decelerator.

Figure 5.1b shows the time-of-flight for the first Stark deceleration result of SrF from 190 to 30 m/s. The decelerated molecules arrive between 43 and 47 ms after the experiment-trigger and are marked by the blue box. Again a significant fraction of the signal corresponds to molecules that fall inside the transverse, but outside the longitudinal acceptance of the decelerator. These molecules are not decelerated and appear between 20 and 30 ms after the experiment-trigger. The zoom-in shows that the decelerated molecules occupy multiple field minima. However, the number of occupied traps seems much lower than for the guiding case, although the pulse entering the decelerator is not altered. This is understood to be due to transverse dispersion of the molecular beam once the voltage on the decelerator is turned off. In these measurements the decelerator was switched off at 43.1 ms after the experiment-trigger, corresponding to the moment the first decelerated molecules reach the end of the decelerator. These molecules traverse a free-flight distance of 10 mm between the end of the decelerator and the detection area. For molecules decelerated in later traps this free-flight distance is increased, by 6 mm per trap. At the longitudinal velocity of 30 m/s, even the transverse velocity of up to a few meter per second is enough for the molecules to diverge away from the detection area.

Apart from limitations to the detected signal, the divergence of the molecular beam would also cause a problem for a downstream (eEDM) measurement, which requires a significantly longer free flight distance of approximately 2 m. To reduce the transverse velocity, a region of transverse laser cooling is planned to be used after the decelerator. For effective laser cooling as well as detection, it is important therefore to guide molecules out of the decelerator after deceleration, which will be shown here.

5.2. Experimental setup

A schematic overview of the setup used in this work is shown in Figure 5.2. Molecules are produced in a cryogenic cell by the reaction between the ablation product from a strontium (Sr) metal target and (SF_6) reactor gas. They are thermalised to and transported out of the cell by the (neon) buffer gas. The molecules are detected 5 mm from the cell exit by resonant absorption of a double-pass transverse laser beam. An electrostatic hexapole lens focuses the molecules into the traveling-wave Stark decelerator, in which their longitudinal velocity is reduced. After exiting the decelerator the molecules are detected using laser-induced fluorescence (LIF) on a photomultiplier tube (PMT).

This setup has been developed over the past decade. Details on the cryogenic source can be found in Esajas [46] and details on the decelerator in van den Berg [48], Meinema [49], Zapara [50], Aggarwal [51], and Mathavan [52].

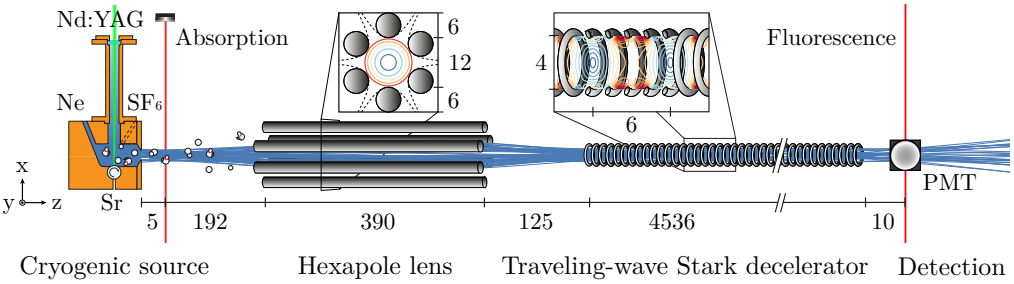

Figure 5.2 | *Schematic overview of the decelerator setup, with molecules traveling from left to right. Blue lines illustrate simulated trajectories of molecules through the setup. Molecules are produced in the cryogenic source, monitored by absorption detection, focused into the traveling-wave Stark decelerator using a hexapole lens and detected using laser-induced fluorescence. Fluorescence is induced by a laser beam crossing the molecular beam at 10 mm after the last ring of the decelerator. The insets show the transverse electric field in the hexapole lens and the longitudinal electric field in the decelerator. Dimensions are indicated in mm, but not drawn to scale.*

The improvements to the decelerator setup presented in this chapter can be grouped in four categories. Firstly, the improvement to the reliability of the source is discussed in section 5.3, based on a redesign of the target rotation mechanism in the cryogenic source.
Secondly, the updates to the data acquisition and control system are discussed in section 5.4. This includes the laser system used to produce the laser light necessary for the absorption and fluorescence detection of the molecules at the start and end of the setup, respectively.
Thirdly, the improved use of the transverse phase-space acceptance of the decelerator using a hexapole lens is shown in section 5.5.
Fourthly, in section 5.6 the improved operation of the decelerator is discussed, in which the long molecular pulse is actively guided out of the decelerator. This is demonstrated by the improved result for the deceleration of SrF to 30 m/s.

5.3. Source reliability and ease of maintenance

To optimise the downstream setup, the reliable production of a molecular pulse is of great importance. Despite normalisation to the molecular yield of the source monitored by the absorption signal, having a stable signal is extremely beneficial. Furthermore, reproducibility of source performance between different measurement days is crucial, especially when interrupted by regular maintenance runs. Upgrades to the cryogenic buffer gas source to improve this reliability are discussed here.

5.3.1. Cryogenic source

The cryogenic source used in this work has been developed by Esajas [46] and has been shown to produce a cold and intense molecular beam of SrF molecules. In a cryogenic cell a plasma of atoms is formed by ablating a Sr metal target with a 532 nm wavelength Nd:YAG laserpulse (Continuum Inlite II) of 5 ns at an intensity of 3-5 mJ in a surface spotsize of < 1 mm. The cell design is based on Truppe *et al.* [79]. The cell is thermally stabilised to a temperature of typically 17 K by a feedback loop based on silicon temperature diodes (Cryocon s950-BB) and a temperature controller (Cryocon model 26). Controlled heating is performed using a resistive cartridge heater (Cryocon CC-3039-001). The cell is continuously cooled via a two-stage pulse tube cryocooler (SHI RP-082B2S), with typical temperature during operation of 27 K for the warm stage and 4 K for the cold stage to which the cell is connected. A copper inner and aluminum outer shield around the cell, connected to the cold and warm stages of the cryocooler, respectively, shield the cell from thermal radiation. The inner shield is cooled below the freezing point of neon, which makes this an effective pump for the buffer gas. Together with the turbo pump (Pfeiffer TC 400) this maintains the vacuum condition in the source chamber during operation measured to $\leq 10^{-6}$ mbar. However, the pressure is expected to be higher directly around the molecular beam due to the presence of the neon buffer gas.
The ablation product reacts with fluorine (F) in the SF_6 gas, which is inserted to the cell at a flow rate of 0.01 to 0.05 sccm, regulated by a flow controller (Bronkhorst M18202321A). As the freezing point of the SF_6 gas is far above the cryogenic temperatures of the cell, a thermally insulated (PEEK) supply tube is heated by a constantan wire to avoid clogging.
The produced hot plasma, which includes SrF molecules, is cooled by collisions with neon buffer gas. This buffer gas is cooled via the supply tube and the cell itself. The neon flow is regulated by a flow controller (Bronkhorst M19201817A) and is typically between 8 and 50 sccm. The significant impact of this and other parameters on the phase-space distribution and intensity of the molecular beam is discussed for a similar source producing BaF molecules in Mooij *et al.* [80].

5.3.2. Target rotation

The Sr atoms used to produce the molecules are ablated from a cylindrical metal target (15 mm height, 5 mm diameter) with an intense laser pulse that is focused to a spotsize of < 1 mm diameter. To avoid the constant ablation of the same spot, the target it is rotated continuously with a typical rotation period of 20 seconds/rotation. As the axle holding the target is allowed to freely slide relative to the motor and is passed through a threaded hole, the rotational motion induces a vertical displacement as well, resulting in a helix-shaped ablation pattern over the target surface.
In previous work the rotation was performed by a motor mounted to the vacuum chamber, with the target thermally insulated from the motor using a PEEK axle. The plate with threaded hole was mounted below the cryogenic cell to the 4 K stage, through which the ablated target was cooled. As the target had to be installed through this hole during maintenance, the inner diameter of the threaded hole had to be > 5 mm, and was chosen as ISO M8 with a pitch of 1.25 mm, which is larger than the ablation laser-spot diameter.
With this setup the target had to be replaced weekly. During this target replacement the

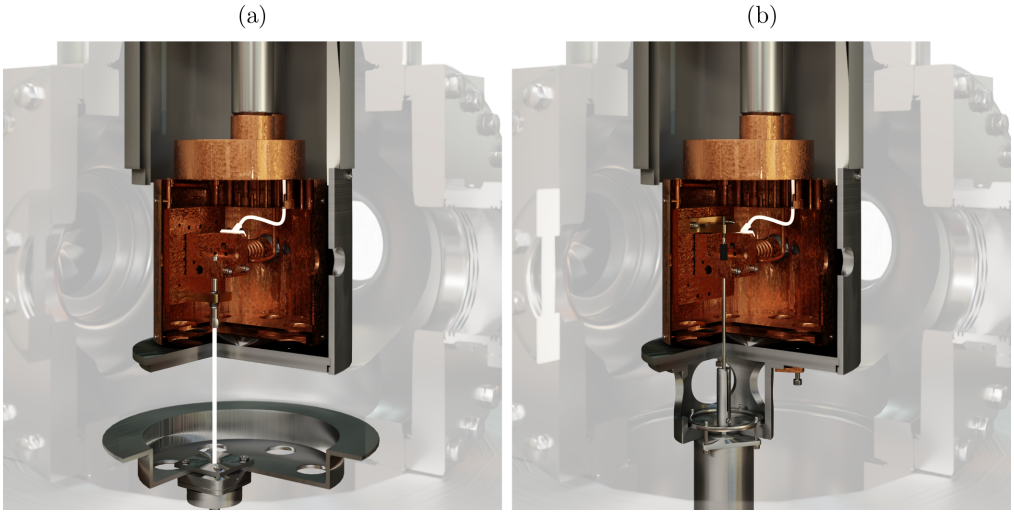

Figure 5.3 | *(a) Previous target rotation design with the motor attached to the vacuum chamber, and using a threaded hole below the cell with a pitch of 1.25 mm. (b) Current target rotation design with motor being attached to the outer cooling shield, and using a threaded hole above the cell with a pitch of 0.5 mm.*

target would easily get stuck by misalignment between the target motor mounted to the vacuum chamber and the plate with threaded hole connected to the cooling stages. Often this problem only occurred after cooling the setup to cryogenic temperatures which takes multiple hours.
Based on positive experience of our collaborators in Amsterdam [47], the target rotation mechanism was replaced based on a motor suitable for operation at cryogenic temperatures (Phytron VSS 42.200.1.2) directly mounted to the outer cooling shield and with a ISO M3 threaded hole above the cell with a pitch of 0.5 mm. The design and installation is discussed in detail in Boulsnane [81]. The design before and after the change are illustrated in Figure 5.3. By the installation of guiding pins the alignment of the target has become notably more reliable. The target gets stuck significantly less often and can be used for over a month before replacement. The source maintenance is thereby reduced to (daily) heating of the shields to unfreeze the collected neon, which is to be automated overnight to minimise dead-time.

5.4. Data collection and control system

The state-selective detection of the molecules is performed by the interaction of the molecular beam with laser light. Just after exiting the cryogenic buffer gas cell the molecules are detected using absorption detection. At the end of the decelerator the molecules are detected using laser-induced fluorescence.
The data acquisition system had to be revised due to the breakdown of the time-to-digital converter that was previously used for digitising the timestamps from the detected photons in fluorescence detection. In the revised data acquisition system, the datastreams from the absorption and fluorescence detection are combined. It also includes environmental measurements such as temperatures in the source and pressures in vacuum chambers. The control and readout of the lasers are also incorporated in this system.

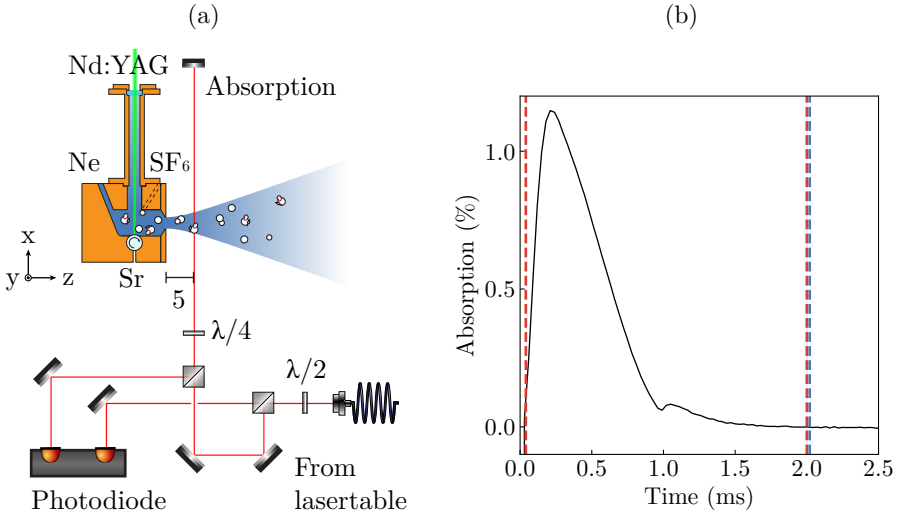

Figure 5.4 *| (a) Optical setup for absorption detection 5 mm from the source exit. Not to scale. Circularly polarized light passes through the molecular beam twice. The non-absorbed light is collected on the photo-diode. (b) Typical time-of-flight double-pass absorption signal. The region between the dashed red lines show the signal region of 2 ms. The blue dashed line shows the starting point of the region used to determine the base level, typically taken to be 10 ms long.*

5.4.1. Absorption detection

The molecules produced in the cryogenic source are probed by a retro-reflected laser beam traversing the pulsed molecular beam at 5 mm from the cell exit as demonstrated in Figure 5.4a. This absorption signal is used to monitor the source performance while data-taking, and as a normalisation between different measurements. The laser light at 663 nm is tuned to be in resonance to the $X^2\Sigma^+(v = 0, N = 1)$ to $A^2\Pi_{1/2}(v' = 0, J' = 1/2)$ transition. Due to the large transverse velocity spread of the molecular beam the transition is strongly Doppler broadened and only a fraction of the molecular is resonant with the laserlight. The returning

laser light is captured on a photo-diode (Thorlabs PDB210A/M).
The absorption fraction is integrated over the pulse, relative to a time region where there is no molecular signal. A typical absorption signal is shown in Figure 5.4b. Averaged over the signal region of 2 ms, a typical integrated absorption signal of 0.5% to 3% is observed, dependent on the operation parameters of the source. In Esajas [46] this signal was estimated to correspond to 10^9 molecules per pulse in the $X^2\Sigma^+(v = 0, N = 1)$ state. From the 1 ms duration of the molecular pulse traversing the absorption laser beam at an average forward velocity of 190 m/s the molecular pulse at the exit of the source is found to be approximately 190 mm long.

5.4.2. Fluorescence detection

Behind the decelerator the molecules are detected using fluorescence, induced by laser light resonant to the $X^2\Sigma^+(v = 0, N = 1)$ to $A^2\Pi_{1/2}(v' = 0, J' = 1/2)$ transition. The fluorescence signal is captured on a photon counting tube (PMT, Hamamatsu H7422-P40). The quantum efficiency $\eta = \frac{hc}{\lambda e} Sk$ [82] at the detection wavelength λ of 663 nm and radiant sensitivity Sk of 0.16 A/W [83] is 0.3 for this PMT.

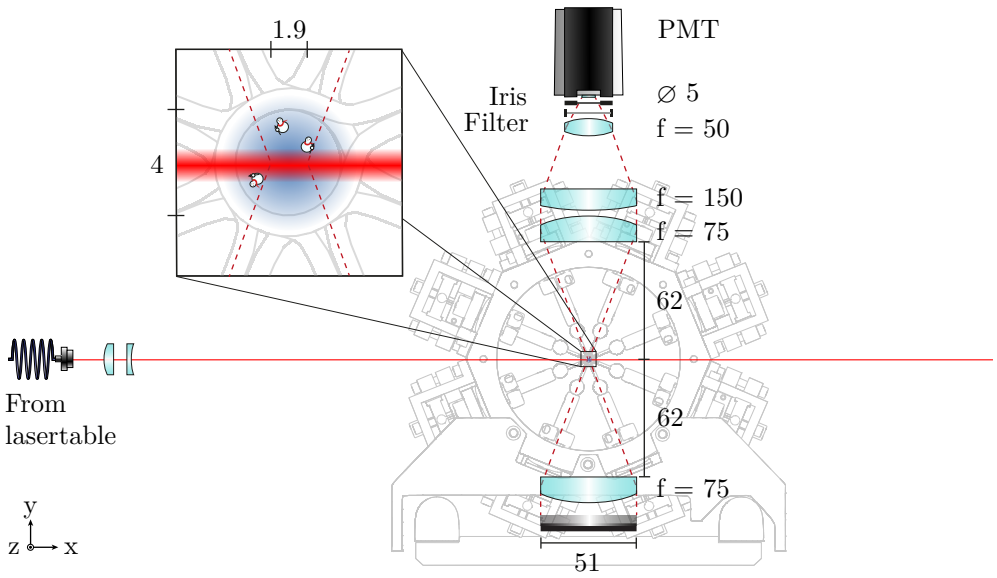

***Figure 5.5** | Optical setup for fluorescence detection 10 mm from the last ring of the decelerator, viewed from the back of the molecular beam setup. Not to scale, dimensions and focal lengths are given in mm. The zoom-in illustrates the limited detection area of 1.9 mm wide.*

The photon capture lens system is illustrated in Figure 5.5. The solid angle of the system is set by the two 2-inch lenses ($r = 25.4$ mm) at a distance h of 62 mm above and below the laser beam, resulting in a solid angle $\Omega = 2\pi\left(1 - \frac{h}{\sqrt{h^2+r^2}}\right)$ of 0.94 steradian, corresponding to a collected fraction of 0.075.

To minimise environmental background light, a 20 nm bandwidth filter centered at 661 nm (Semrock FF01-661/20-25) is placed in front of the detector, which has a transmission of < 0.02 for wavelength outside of the bandwidth, specified for parallel light rays. The total transmission T at the detection wavelength of the full lens system is estimated to be 0.75.
To address all four hyperfine components of the $X^2\Sigma^+(v = 0, N = 1)$ ground state, an electro-optic modulator (EOM) is used to create sideband frequencies at a separation of 42 MHz, with a modulation index of 2.6 to have approximately equal power in the first and second order sidebands from the carrier frequency [49]. Note that molecules that have traversed the decelerator are in a low-field seeking state, the distribution of molecules at the end of the decelerator will be over the two hyperfine component with these components. The hyperfine structure of this $X^2\Sigma^+(v = 0, N = 1)$ ground state and the Stark shift of the hyperfine components is shown in Figure 4.1c.
At high laser intensity, multiple photon scattering per molecule should occur at the rotationally closed transition probed in this experiment, which has an excited state lifetime of 24.1 ns [84]. With sufficient interaction time, the limiting factor would be loss to hyperfine components labeled by m_F, dark to the laser light at the set polarisation. This is estimated in Aggarwal [51] based on the hyperfine branching rations from Barry [85] to result in 5 photons scattered per molecule on average, referred to as n.
By introducing a magnetic field during detection, remixing of these hyperfine components should occur at suitable polarisation. However, this could not be demonstrated in this work. A possible disruption could be due to the presence of a significant varying electric field at the detection area 10 mm from the end of the decelerator. The number of photons scattered per molecule is therefore uncertain. The conservative estimate from Aggarwal [51] will be followed here.
As a result, the estimated ratio of molecules in the $X^2\Sigma^+(v = 0, N = 1)$ ground state N_{det} corresponding to a detected photon S is given by,

$$\frac{N_{det}}{S} = \frac{1}{\eta \times \Omega/(4\pi) \times T \times n} = \frac{59}{n}. \tag{5.1}$$

The estimate for the total number of molecules in the beam also depends on the detection area, limited by the cross-section of the molecular beam with the laser beam, and the imaging of this interaction region onto the 5 mm diameter active area of the PMT. As the lens system projects the fluorescence signal on the PMT with a magnification $M = 2.7$ [62], the maximum horizontal transverse region where molecules are expected to be detected is 1.9 mm. In practice this region might be even smaller due to imperfect lens adjustments and blockage due to mounting systems.
The fluorescence signal is measured close to the end of the decelerator, which has highly reflective surfaces from the polished electrodes. Especially for larger laser beams, this produces a significant background to the signal from the molecules. Therefore, it was chosen to use a laser beam of typically 1 mm FWHM, with a Gaussian profile and at a power of 0.5 mW distributed over the sidebands. In that case the background scattering rate is limited to 10 kHz at most, corresponding to a typical signal to background ratio at the arrival of the molecular pulse of between 0.1 and 10. The background could be further reduced by partial closing the iris in front of the PMT, but this further reduces the detection area for fluorescence signal.

With this limited detection area of 1.9 × 1 mm it is expected that for most measurements only the center of the molecular beam is detected. In general however, the molecular beam profile is difficult to predict. It depends on the phase-space acceptance of the decelerator and the filling thereof, discussed in chapter 4. In this work significant effort was put into the improved filling of the transverse phase-space acceptance of the decelerator by the implementation of a hexapole lens. As the improved filling is mostly expected in the outer regions of the transverse phase-space acceptance, see Figure 5.8, detecting only the middle of the molecular beam may underestimate the gain in total increase in number of captured molecules. Uncertainty in the detection area, as well as in the initial distribution of molecules complicate the quantitative simulation of improvements to the molecular beam properties. To enable the direct measurement of the molecular beam distribution detection with an EMCCD camera was considered as demonstrated in chapter 7, but did not yet produce reliable results during this part of the work.

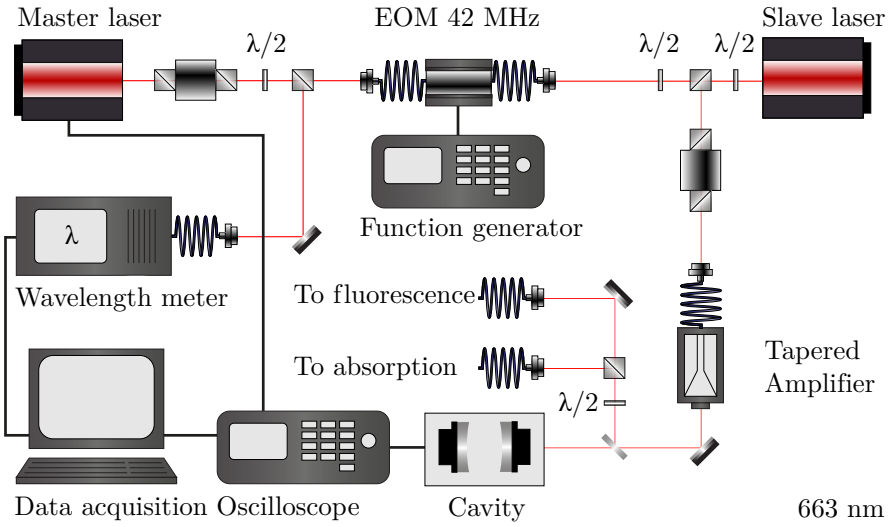

Figure 5.6 | *Setup overview of the optics system providing laser light at a wavelength of 663 nm for detection of SrF molecules. The master laser is locked to a wavelength meter via a digital PID loop. An EOM is used to create side-bands, after which the light is amplified in a slave laser and tapered amplifier. A Fabry–Pérot cavity is used to monitor the intensity distribution over the side-bands before the light is brought to the detection setups via optical fibers. Adapted from van Hofslot [86].*

5.4.3. Laser system

The setup for producing the detection laser light driving the $X^2\Sigma^+(v = 0, N = 1)$ to $A^2\Pi_{1/2}(v' = 0, J' = 1/2)$ transition in SrF is largely a compacted version of the one described in section 3.2 of Aggarwal [51], and is therefore only briefly discussed here. The main difference is that the master laser, a home-built external cavity diode laser (Opnext HL6545MG) is now locked to the wavelength meter (HighFinesse WS8-2) via a digital differen-

tial feedback loop. The arbitrary waveform generator in the digital scope (PicoScope 5444D), also used in the data acquisition, sets the voltage applied to the piezo element controlling the angle of the grating which determines the length of the external cavity based on the readout of the wavelength meter. This new lock serves as a replacement for the external cavity lock which was referenced to a 663 nm helium–neon laser used previously [46], as this laser stopped working.
The light from the master laser is divided over side-bands using an electro-optical modulator (EOM, Jenoptik PM660) at 42 MHz to target all four hyperfine levels of the $X^2\Sigma^+(v = 0, N = 1)$ ground state. This light is then amplified using another external cavity diode laser and Tapered Amplifier (Toptica Photonics BoosTA). The laser light is split and brought to the setup using optical fibres where it is used for both absorption and laser-induced fluorescence detection.

5.4.4. Data acquisition and control

The absorption data from the photo-diode and the fluorescence data from the PMT are both collected on a digital oscilloscope (PicoScope 5444D). In addition to the raw digitised data, interpreted data is stored for each shot. For example, for the absorption signal, the averaged intensity over the signal region defined in subsection 5.4.1 is saved for each shot.
The data acquisition for the fluorescence is more involved. The TTL pulses from the photon counting PMT are sent through a gate generator (U. Heidelberg G43) to extend the short pulse, to make it detectable at the time resolution at which the digitiser is operated. As the gate generator is based on NIM electronics, a pegel convertor (U. Heidelberg L49A) is used to invert the signal. In this pulse manipulation the signal is delayed by 70 ns as shown in Figure 5.7, which is insignificant to our experiment.

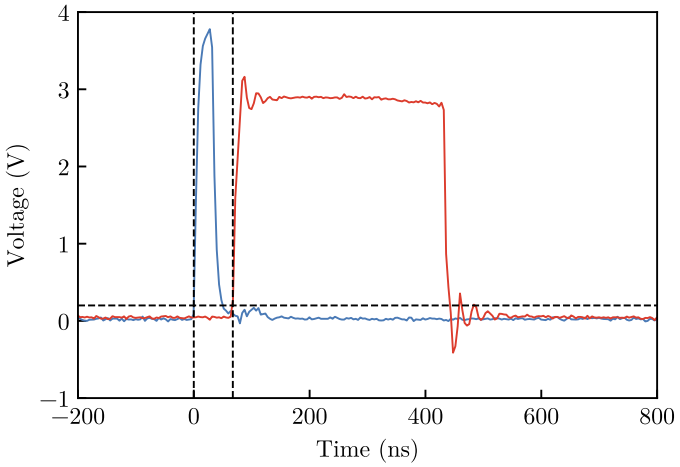

***Figure 5.7** | Original pulse from the PMT in blue and after manipulation in red. The resulting pulse of 350 ns is delayed by 70 ns relative to the original.*

The fluorescence signal is digitized over 60 ms at a typical time resolution of 1.2 μs. A

software algorithm has been developed to translate the voltage signal to arrival times of photons at every time the signal rises above a 200 mV threshold. By binning these arrival times of the photons in a histogram, the time-of-flight figures are obtained.
It has been observed that this algorithm can be too slow to keep up with the data stream in real-time, resulting in missed shots in the live plots. This is resolved in the analysis by performing the peak detection algorithm again on the raw data, to generate a complete processed dataset. To resolve this also in the real-time analysis, replacement by a system based on a frequency counter (Keysight 53230A) or Analog I/O (Moku:Pro) is investigated at the time of writing.
The maximum observed peak photon rate during experiments in this work is 80 kHz. With a typical sampling rate of 833 kHz, the chances of overlapping pulses is limited. In future experiments this may become a limiting factor of this data acquisition approach and should be taken into account in the transition to the frequency counter system.
The fluorescence signal per shot is defined to be the photon counts in a signal region, subtracted by the photon counts in a background region, compensating for the length ratio of these windows. The definition of these signal and background regions depends on the operation mode of the decelerator. Typically the background region is taken from 5 to 20 ms after the experiment-trigger. The signal region is anywhere between 20 and 55 ms, dependent on the arrival time of the molecules.
The monitoring and control of pressures in the vacuum chambers, source temperatures and gas flows is performed by a Labjack based system as described in Esajas [46]. The data from this system, recorded at a second timescale, is send over the local network to the data acquisition. Here it is displayed and stored in the same structure as the molecule signals. The frequency of the detection lasers is collected over a Caddie [57] based socket connection, similar to the structure described in chapter 3, and added to the data.
The control of the ablation laser and motor to rotate the metal target is done using the software provided by the supplier. The motor that controls the target rotation is programmed to rotate 26 to 32 turns back and forth to form an ablation helix of 13 to 16 mm dependent on the length of the target. Monitoring of the intensity of the ablation laser, expected to contribute significantly to the fluctuations in number of molecules produced in the cell, is not implemented at this point, but would be a useful future upgrade.

5.5. Intensity increase using a hexapole lens

By mapping more molecules in the transverse acceptance of the decelerator the intensity of the molecular beam at the end of the decelerator is increased. A radial restoring force for molecules in the low-field seeking states is applied using an electrostatic hexapole lens, as discussed in section 4.2. The magnitude of the radial restoring force can be tuned by the electric field strength, determined by the voltage amplitude which is applied to the rod electrodes of the hexapole lens, alternating between positive and negative for adjacent rods.

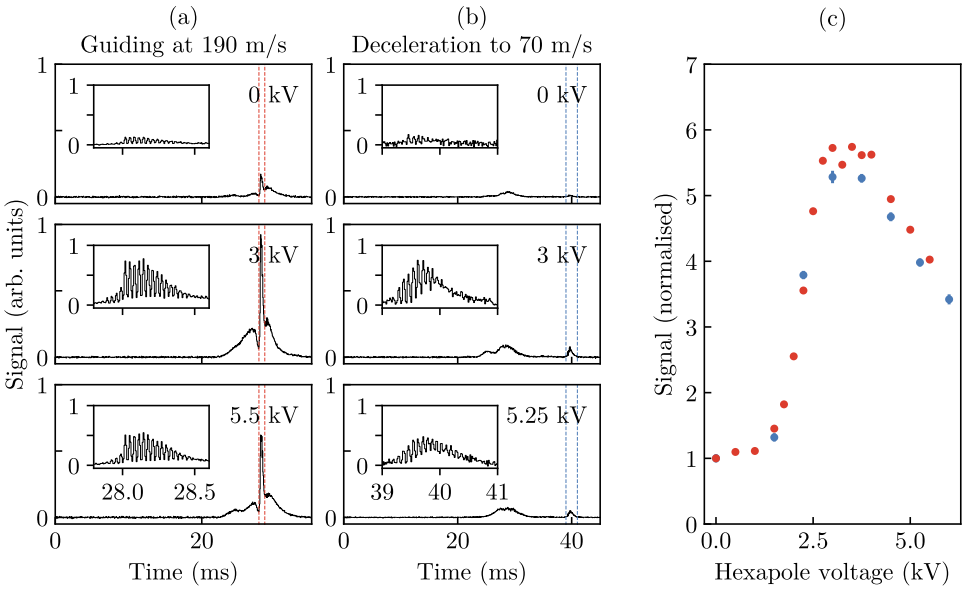

Figure 5.8 *| Intensity of the molecular beam of SrF at the end of the decelerator, for different voltages applied to the hexapole lens. (a) Time-of-flight for AC guiding at 190 m/s with voltage amplitude of 3 kV. The guided peak is marked by the red dashed lines. (b) Time-of-flight for deceleration from 190 to 70 m/s with voltage amplitude of 5 kV. The decelerated peak is marked by the blue dashed lines. (c) Integrated signal increase over the guided (red) and decelerated peak (blue) for different voltages applied to the hexapole lens.*

In Figure 5.8, the intensity of the molecular beam at the end of the decelerator is shown for different voltages applied to the hexapole lens. In Figure 5.8c the integrated intensity of the signal is shown for the case of guiding at 190 m/s at a decelerator voltage amplitude of 3 kV and for deceleration from 190 to 70 m/s, corresponding to a deceleration $a = -3.5$ km/s^2 at a voltage of 5 kV. The measurement for different hexapole voltages is normalised to the measured absorption signal to compensate for source fluctuations. Guiding is performed at a voltage amplitude of 3 kV as this has previously been observed to yield a stronger signal than for higher voltages [50]. Although not completely understood, it was theorised to be due to non-adiabatic losses occurring at the traversal of the electric field minimum at the center of the trap, which have been observed in earlier experiments on ND_3 [87], CO [88] and CaF [89]. The integrated intensity signal is normalised to the signal when the hexapole lens

is switched off.
As observed, the molecular beam intensity increases with the voltage applied to the hexapole lens, up to a maximum at a voltage amplitude between 3 and 4 kV. The increase in signal may be understood by considering the phase-space plots shown in Figure 4.15. When a voltage of 3 to 4 kV is applied to the hexapole, the transverse phase-space distribution of the molecules is rotated such that it matches with the acceptance of the decelerator, resulting in more molecules being guided or decelerated. When even higher voltages are applied to the hexapole, the phase-space distribution is rotated too far and the number of guided or decelerated molecules decreases.
Note that the increase in number of decelerated molecules as function of hexapole voltage shows a steeper increase than focusing curves where the full molecular pulse is considered, as shown for instance for BaF in Figure 7.12. This is partly because of the relatively small transverse velocity acceptance of the decelerator; only molecules that pass the hexapole close to the molecular beam axis are accepted. In addition, only molecules within the longitudinal velocity acceptance, traveling at a forward velocity close to 190 m/s are accepted. Hereby, the variations in traversal times of the hexapole lens are small, and the chromatic aberrations, which smooth out the focusing curve for the full molecular pulse, are of limited impact here.
If the position and velocity distribution of the molecular beam from the source and the detection area are well known, the measurement in Figure 5.8 could be used to determine the acceptance of the decelerator by comparison to simulations. Unfortunately, the detection was poorly defined when the measurements were performed, and a quantitative analysis was deemed ineffectual. The observed increase of a factor of 5.5 seems reasonable given that the maximum increase, assuming perfect phase-space matching and a detection area sufficiently large to detect all guided or decelerated molecules, is a factor of 13, as estimated in subsection 4.5.1.
Note that a larger gain was expected for decelerating at a voltage of 5 kV than for guiding at 3 kV, because of the larger transverse acceptance of the former. That this is not observed maybe explained from the limited detection area, discussed in subsection 5.4.2 to be due to the optimisation to signal to background. The molecules in the phase-space volume contributing to the signal detected by the PMT is expected to be accepted in both cases, explaining the similar gain by improved filling thereof. The gain in total molecular beam intensity is therefore expected to be larger than the signal gain measured here.
Thus far, the signal gain compared to the case where the hexapole was switched off, corresponding to 0 kV in Figure 5.8. In installing the hexapole lens the distance between the source and the decelerator had to be approximately doubled, increasing the transverse losses to begin with. For a more realistic estimate to the gain in signal with the hexapole lens this has to be taken into account. The loss depends on the phase-space acceptance of the decelerator and the beam diameter originating from the source. From the trajectory simulations the transverse losses due to the increased distance have been estimated to have halved the signal, leaving still a significant gain achieved with the installation of the hexapole lens.

5.5.1. Alignment into the decelerator

The hexapole lens is also used to optimise the alignment of the molecular beam into the decelerator, which previously had to be done by rotation of the full source. To facilitate this, the hexapole lens is mounted in a vacuum system which can be oriented using a XY-

manipulator (Hositrad HMC1000), as discussed in section 4.2. The manipulator is a vacuum bellow, where the end flanges can be displaced with respect to each other by translators along two orthogonal transverse axes, controlled by micrometer screws outside of the vacuum system. With the hexapole lens mounted between a freely moving vacuum bellow on one side and the manipulator on the other its orientation can be fine-tuned.

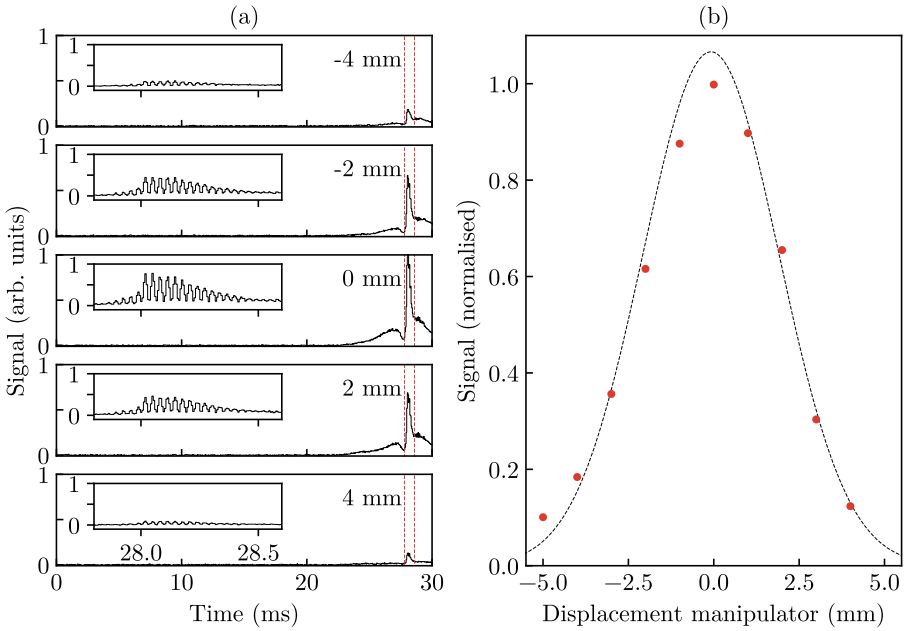

Figure 5.9 | *Intensity of the molecular beam of SrF at the end of the decelerator,* AC *guided at 190 m/s and voltage amplitude of 3 kV, with horizontal displacements of the hexapole lens using the manipulator. The signal in (b) corresponds to the integrated signal over the guided peak, enclosed by the red dashed lines in (a). The fitted Gaussian has a* FWHM *corresponding to a molecular beam displacement of 4.4(3) mm, comparable to the inner diameter of the decelerator of 4 mm and the 4.5 mm aperture of the source.*

Figure 5.9 shows how the intensity of the molecular beam at the end of the decelerator is maximised by the orientation of the hexapole lens. The signal clearly disappears for a displacement of the manipulator by a couple of millimeters, demonstrating the importance of the alignment. The displacement is only shown in the horizontal direction here, but similar results have been achieved for the displacement in the vertical direction.
In section 7.7 the displacement of a beam of BaF molecules with the hexapole lens will be studied. In these experiments, the molecular beam is imaged using an EMCCD camera. It is found that the transverse displacement of the center of the molecular beam at the position of the decelerator entrance, scales linearly with the manipulator displacement, with a scaling coefficient of 0.93(2). The falloff of the signal intensity with the displacement of the hexapole lens is therefore in accordance with the inner diameter of the decelerator and the aperture of the source.

5.6. Improvement to the deceleration of SrF

In previous work [62], it was observed that the number of molecular packages, corresponding to filled electric field traps, detected at the end of the decelerator is much lower for deceleration compared to guiding, as discussed in section 5.1. This is attributed to transverse losses in the free-flight between release and detection, which are more dominant for lower longitudinal velocities of the molecular beam leaving the decelerator. As the voltages on all ring electrodes in the decelerator is switched off simultaneously, molecules in later traps have an over ten times longer free-flight time than those in the first trap, resulting in a molecular density drop of two orders of magnitude. This can be solved by guiding molecules out of the decelerator after deceleration instead of switching of directly after deceleration.

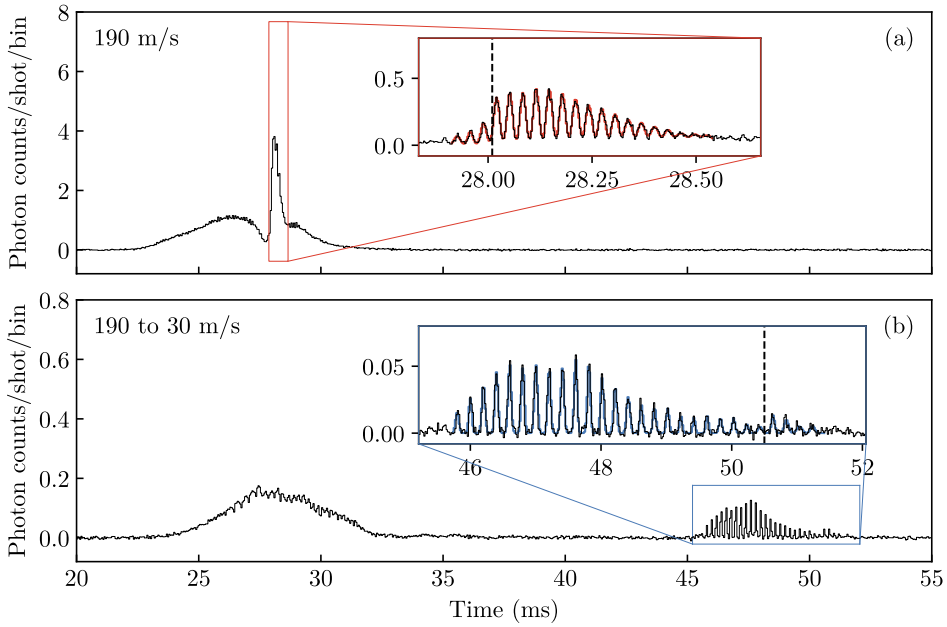

Figure 5.10 | *Time-of-flight profile of SrF molecules traversing the traveling-wave Stark decelerator. (a) AC guiding at 190 m/s with an applied voltage amplitude of 3 kV, with a zoom-in around the guided peak. (b) Deceleration from 190 to 30 m/s with an applied voltage amplitude of 5 kV, with a zoom-in around the decelerated peak. To the guided and decelerated peak substructure a sequence of equally spaced Gaussians are fitted. The black dashed lines show the moment the decelerator voltage is being switched off.*

Figure 5.10a shows the time-of-flight profile for SrF molecules that have traversed the decelerator when guided at 190 m/s. The waveform is ended after 28 ms, as indicated by the dashed line in the zoom-in. Molecules arriving later in the detection area have been in free-flight for a longer time, resulting in fewer molecules traversing the small detection area described in subsection 5.4.2.
In the zoom-in of the guided peak, a fit of a sequence of Gaussians is fitted to the substructure,

corresponding to molecules in the electric field traps in the decelerator. These do therefore have an equal time-offset of $l/(2v_z)$, where $l/2$ is the separation between the traps of 6 mm. The signal from 20 consecutive traps corresponds therefore to a molecular pulse of 120 mm, shorter than the estimated pulse length from the absorption signal, due to the density losses during free-flight.
For a lower longitudinal velocity the molecular beam expands during a longer time, increasing the effect of transverse losses. To avoid this, the waveform of decelerator voltages applied to the decelerator is extended to guide the decelerated molecules out of the decelerator. For the measurement shown in Figure 5.10b after 44.5 ms, when the first decelerated molecules reach the end of the decelerator, the waveform is transitioned from deceleration to guiding at 30 m/s. As it was observed previously that the signal for guiding at 190 m/s was higher at a voltage amplitude of 3 kV [50], the same was applied here. The time-of-flight profile shows filling of many more electric field traps in this operation mode.
The guiding waveform is applied up to 50.5 ms, after which the voltage on the decelerator is switched off. This is shown in the zoom-in by a dashed line. Directly after, the fluorescence signal seems to increase. Apparently, the fluorescence signal is suppressed due to the (alternating) electric field in the detection area, which is situated 10 mm from the last ring electrode. The electric field at the detection area must be so strong that the induced Stark shift shifts the transition out of resonance. A similar jump in signal is seen for guiding at 190 m/s. To reduce the electric field, a grounded electrode is installed between the decelerator and the detection area for the experiments on BaF presented in chapter 6.
Again, a sequence of Gaussians is fitted to the substructure of the decelerated peak. The blue line in the zoom-in of Figure 5.10b shows the fit to the signal from molecules occupying 28 traps in the decelerator, corresponding to a pulse length of 168 mm. This is more in line with the predicted length from the absorption signal.

5.6.1. Phase-space analysis

The substructure in the guided and decelerated peaks in the time-of-flight profile corresponding to the electric field traps within the decelerator provides valuable information on the phase-space distribution of the molecular pulse.
In the previous section the transverse losses due to free-flight, reducing the intensity of the beam were discussed. To investigate the transverse distribution of the molecular beam, the drop of the signal strength could be deduced from varying the end time of the guiding waveform. As the detection area is limited and not well known for this setup, this is not done here, instead aiming for direct imaging of the transverse dimensions of the molecular beam using an EMCCD camera.
The longitudinal phase-space acceptance of the traps in the decelerator appears in the width of the peaks in the time-of-flight profile. The widths dt of the sequence of Gaussian distributions fitted to the guided and decelerated peaks in Figure 5.10 are shown at the arrival time of the corresponding trap in Figure 5.11. The width in the time-of-flight is multiplied by the longitudinal velocity v_z, which is confirmed by the separation of the peaks, to convert it to the longitudinal width of the pulse.
The (longitudinal) width of the molecules in a trap is expected to be constant while in the decelerator, and is given by the phase-space acceptance of the decelerator dz. Once it leaves the decelerator, the distribution of molecules starts to expand due to the velocity distribution

of the molecules dv_z. In the case where the decelerator is still on when the molecules leave the setup, the time of free-flight is determined by the distance from the end of the decelerator to the detection area d_0 of 10 mm. In the case where the decelerator is switched off before, the free-flight time is extended. The width of the distribution of molecules contained in a trap is expected to be,

$$v_z\, dt = \begin{cases} \sqrt{dz^2 + \left(\frac{d_0}{v_z} dv_z\right)^2} & \text{if } t \leq t_0 + \frac{d_0}{v_z}, \\ \sqrt{dz^2 + \left((t - t_0)\, dv_z\right)^2} & \text{if } t > t_0 + \frac{d_0}{v_z}. \end{cases} \tag{5.2}$$

Here t is the mean arrival time of the molecules at the detection area and t_0 the time the decelerator voltage is switched off. This model is an extension to the model used in Aggerwal *et al.* [62], which did not include the description of molecules guided out of the decelerator.

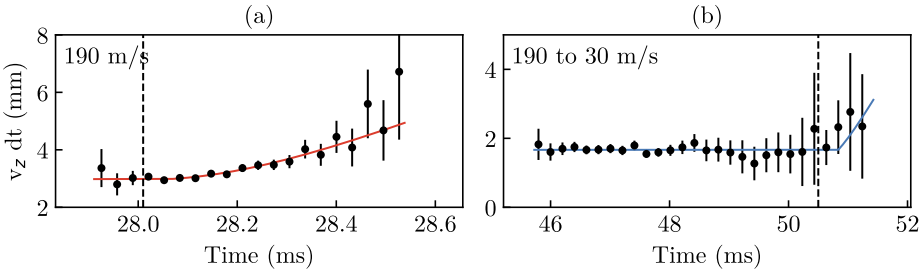

***Figure 5.11** | Fitted Gaussian width (FWHM) of the peaks in the time-of-flight profile in Figure 5.10 demonstrating the longitudinal position and velocity spread captured in the traps. (a) AC guiding at 190 m/s with an applied voltage amplitude of 3 kV. (b) Deceleration from 190 to 30 m/s with an applied voltage amplitude of 5 kV. The black dashed lines show the moment the decelerator voltage is being switched off.*

To find the longitudinal position and velocity spread of the molecules, Equation 5.2 is fitted to the width of the distributions for different free-flights times. For guiding at 3 kV the FWHM longitudinal positions spread dz is found to be 2.95(3) mm, and the FWHM velocity spread dv_z is 7.5(3) m/s. These values are in accordance with the expectation from the width of the distribution of the accepted molecules in the Monte-Carlo simulation in Figure 4.10. For the decelerated molecules the width of the peaks in the time-of-flight is significantly smaller, as expected from the reduced longitudinal phase-space acceptance. From the fit the position spread dz is 1.3(3) mm, and the velocity spread dv_z is 3.1(12) m/s. The uncertainty is large in this case due to the velocity spread, which is determined from the very last peaks of the signal. The spread of the molecular packages seems to be lower than expected, which is likely due to the transfer between deceleration and guiding in which the most energetic molecules are lost from the trap. By matching the voltage amplitude, and possibly adding a phase-jump to adjust for the position in the trap center when decelerating [62], this is expected to be recovered.

5.6.2. Number of molecules

The guided peak in Figure 5.10 corresponds to 22.3(2) photons per pulse. The decelerated peak has an intensity of 1.64(2) photons per pulse. This loss in intensity is significantly larger than the expected loss from the reduction in phase-space acceptance between these operation modes, which from Figure 4.12 is found to be a factor of 2 to 3.
There are a number of effects that may explain this discrepancy, mostly to do with the detection area. The varying electric field present during detection of most of the pulse when guiding the decelerated molecules out is seen in the time-of-flight to reduce the detection efficiency by approximately a factor of 2. The limited detection area, shown in subsection 5.4.2, results in detection of the transverse center of the molecular beam. Despite the effort to limit the free-flight for decelerated molecules, the transverse losses at the final velocities may have impact on the detected fraction of the molecular beam.
On top of that the mismatch between the voltage amplitude used during deceleration and guiding, and the lack of a phase-jump to adjust for the effective trap center are also expected to result in losses for this more complicated operation mode.
Out of the 10^9 SrF molecules per pulse in the $X^2\Sigma^+(v = 0, N = 1, M_N = 0)$ created in the cryogenic source, 10^5 are expected to be captured in the decelerator, according to the phase-space acceptance of the decelerator and the characteristics of the molecular pulse. From the estimate on the number of detected photon per molecule in subsection 5.4.2, the number of decelerated molecules is 2 to 3 orders of magnitude lower than this expectation. Part of this is expected to be due to the limited detection area used in this work. Another explanation for the high losses might be a too high pressure from the buffer gas in the decelerator, as will be discussed in chapter 6.

5.7. Conclusion and outlook

In this chapter the improvement to the traveling-wave Stark decelerator setup have been presented, as a step towards creating a slow and intense molecular beam to use in the NL-eEDM experiment. The source reliability and ease of maintenance have been improved by the replacement of the target rotation mechanism, resulting in lower down-time in the experiment. The data acquisition system has been updated to include absorption and fluorescence signals from the molecular pulse, as well as many experimental parameters such as the conditions of the source and the frequency of the detection laser. The intensity of the molecular beam accepted in the decelerator was increased by the implementation of a hexapole lens between the source and the decelerator entrance. This hexapole lens improves the transverse phase-space matching between the source and the decelerator. By guiding decelerated molecules out of the decelerator the transverse losses are mitigated.
Characterisation of the molecular beam is complicated by the limited detection area in this setup, as had to be implemented to reach a reasonable signal to background ratio. The varying electric field present in the detection area further complicates the measurements. The improvements to the detection area were made in the transition to BaF, for which a more flexible laser system was available. The transition to this molecule of interest for NL-eEDM experiment is discussed in chapter 6. The full characterisation of the hexapole lens is done by imaging fluorescence from the molecular beam on an EMCCD camera in chapter 7.

6

Guiding and deceleration of barium fluoride

The NL-eEDM collaboration aims for an EDM measurement on a beam of barium fluoride (^{138}Ba^{19}F) molecules traveling at 30 m/s [44]. To achieve this, a traveling-wave Stark decelerator is used for decelerating molecules produced in a cryogenic buffer gas source from a mean longitudinal velocity of 200 m/s.
In this chapter the changes to the setup are discussed that are necessary in the transition from SrF to BaF. The molecular structure of these molecules are largely the same, but the 1.5 times higher mass makes deceleration of BaF significantly more challenging, as demonstrated in chapter 4 based on the phase-space acceptance of the decelerator for both of these molecules.
The pulsed molecular beam from the buffer gas source is characterised, to demonstrate the parameter relevant for deceleration. The improved phase-space matching between the molecular pulse from the source and the acceptance of the decelerator by a hexapole lens is demonstrated. To analyse the transverse dimensions of the beam, imaging of guided molecules using an EMCCD camera at the end of the decelerator is demonstrated. The first results for Stark deceleration of BaF are shown. Molecules are decelerated from 200 to 150 m/s, corresponding to a deceleration a = -2 km/s^2, as a first step towards the goal of 30 m/s, which requires a deceleration of a = -4 km/s^2.
At this point, due to a breakdown of the electronics, the research in this work was interrupted. An outlook is given on the continuation of Stark deceleration in future work.

The chapter image shows the last module of the decelerator sticking into the laser cooling chamber, used in this work as a fluorescence detection area.

6.1. Setup changes for transition to BaF

The setup used for the deceleration is largely the same as the setup described in chapter 5 used for decelerating SrF. Therefore, only the changes necessary for the deceleration of BaF are discussed here.

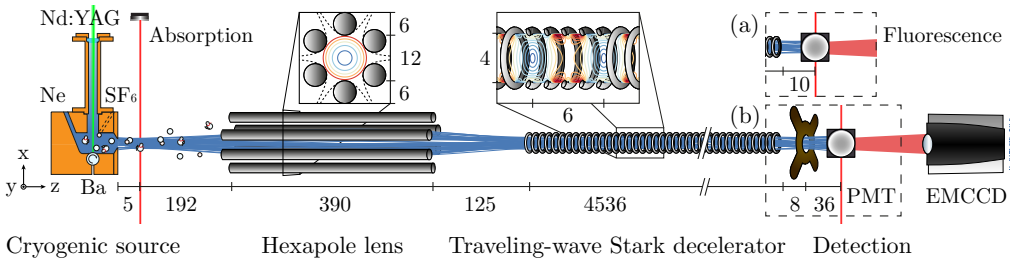

***Figure 6.1** | Schematic overview of the decelerator setup, with molecules traveling from left to right. Blue lines illustrate simulated trajectories of molecules through the setup. Molecules are produced in the cryogenic source, monitored by absorption detection, projected into the traveling-wave Stark decelerator using a hexapole lens and detected using laser-induced fluorescence. The insets show the transverse electric field in the hexapole lens and the longitudinal electric field in the decelerator. (a) For most measurements the fluorescence detection geometry was the same as in chapter 5, (b) but for later experiments a field shield was implemented and the detection area was moved backwards. An EMCCD camera was installed to image the transverse distribution of the molecular beam exiting the decelerator. Dimensions are indicated in mm, but not drawn to scale.*

The production mechanism in the cryogenic source has remained the same, except for using a barium metal target instead of strontium.
The differences in the molecular constants in SrF and BaF are covered in section 4.1. The turning point field E_{tp} for both molecules is similar, as the ratio between the electric dipole moment and rotational constant μ_e/B is approximately equal. The hexapole and decelerator are therefore operated at the same voltage amplitudes as before. The maximum energy shift W_{tp} at the turning point is 0.86 times lower for BaF due to the rotational constant, that is lower by the same amount. The 1.5 times higher mass of BaF results in a further reduction of the capture velocity relative to SrF, as shown in Table 4.2. The mass difference also results in a stronger longitudinal phase-space acceptance reduction for deceleration, overall complicating the deceleration of this heavier molecule.
The electronic energy level splitting for BaF is significantly different from SrF, which required a replacement of the optical setup used for the detection of the molecules. The 663 nm diode laser system used for SrF has been substituted by a Titanium-Sapphire laser system (MSquared SolsTiS 233800). This laser has a widely tunable (700 to 1000 nm) operation range, which includes the 860 nm light used for probing the $X^2\Sigma^+(v = 0)$ to $A^2\Pi_{1/2}(v' = 0)$ transition in BaF, and a specified linewidth of < 100 kHz. The laser is pumped by a continuous 532 nm laser (MSquared Equinox, later replaced by Lighthouse Photonics Sprout-G). The frequency is controlled by a built-in feedback referenced to the wavelength meter (HighFinesse WS8-2), where the readout of the latter is also saved by the data acquisition. Differently from the SrF measurements presented in the previous chapter the system used in this work does not

include sideband production and thereby probes only one hyperfine transition in fluorescence detection. The optical setup is shown in Figure 6.2.

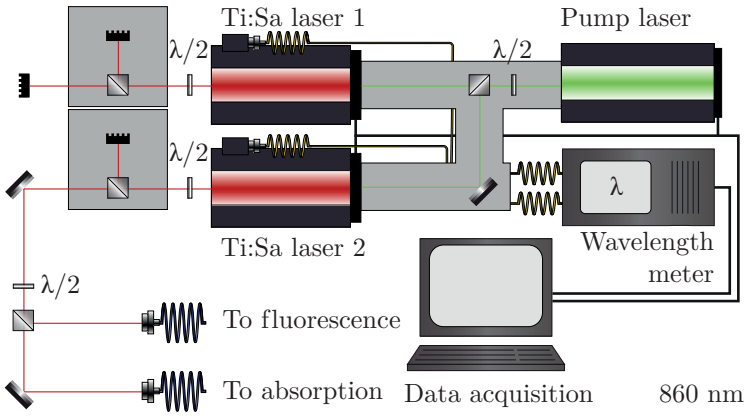

***Figure 6.2** | Simplified setup overview of the optics system providing laser light at a wavelength of 860 nm for detection of BaF molecules. Two Titanium-Sapphire lasers are pumped by the same pump-laser. In grey the shielding boxes are illustrated that contain the high power laser light. Ti:Sa laser 1 is not used in this work. The lasers are locked to the wavelength meter, which is also used in the data acquisition system. The light is brought to the setup via optical fibers.*

The photomultiplier tube used to capture fluorescence (Hamamatsu, HS7421-50) has a quantum efficiency of 8.5% at 860 nm. To reduce background light on this PMT and the EMCCD camera used to image the transverse distribution of the beam, a single-band bandpass filter (Semrock, FF01-860/11-25) was installed in front of both detectors.
During most of the measurements presented in this work, the fluorescence detection lens system was the same as shown in Figure 5.5. Later a grounded electrode was installed between the decelerator and the detection area, acting as a field shield to negate the resonance shifts for detecting the molecules due to the (varying) electric field. At the same time the vacuum chamber where fluorescence detection takes place was replaced. The new chamber is designed to enable transverse laser cooling in two orthogonal directions through large windows in the horizontal and vertical directions.
In the first iteration, shown in Figure 6.3a, the field shield was made from a copper plate mounted to the last module of the decelerator. The side facing the detection area was painted black to reduce the background in fluorescence detection. This field shield did however not leave space for the detection optics, which was replaced by a lens system outside the vacuum chamber. The resulting solid angle Ω of the lens system for the PMT dropped from 0.94 to 0.08 steradian. No reasonable signal was observed with this setup, but it may become relevant again in future work on transverse laser cooling of the beam as it allows for interaction with laser light in a region with minimal electric field close to the decelerator exit.
To improve the solid angle, a new lens system was installed inside the vacuum chamber, mounted to an aluminium slab acting as a field shield hanging from the last module of the decelerator. This system is shown in Figure 6.3b during the installation. The slight angle relative to the vacuum chamber, at which it seems to be hanging here, was still adjusted

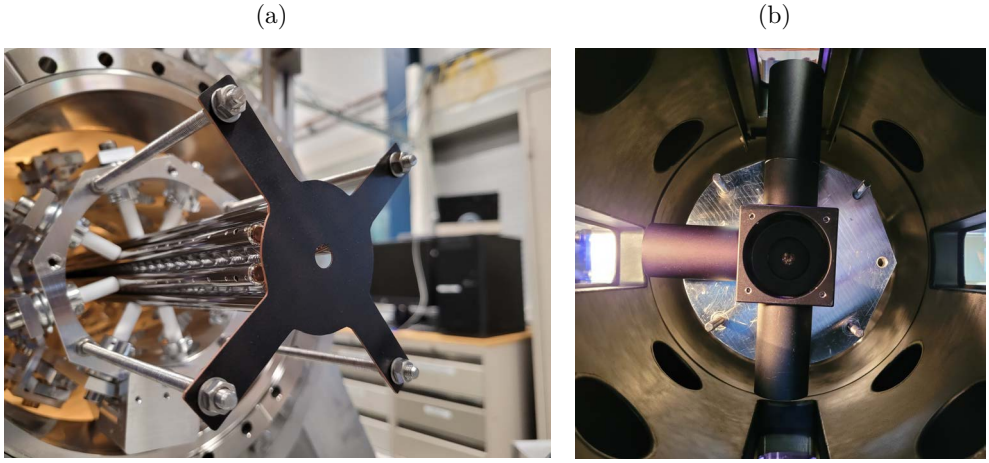

***Figure 6.3** | Two iterations of the electric field shield at the end of the decelerator. (a) With minimal distance from the end of the decelerator to the detection area, and (b) with a lens system attached to improve solid angle. Pictures taken by J.W.F. van Hofslot [86].*

before fixing it in place. Lenses were mounted above and below the detection area at a distance of 30 mm, with a mirror below and the PMT above the setup, resulting in a solid angle of 0.90 steradian. In the implementation of such a lens system, the detection area had to be moved to 44 mm behind the last ring of the decelerator as shown in Figure 6.1b. This lens system has a magnification of one, contrary to the setup used for SrF discussed in subsection 5.4.2, that limited the detection area probed by the PMT. The reflections from the polished electrodes causing a significant background to the fluorescence signal in the SrF setup were minimised due to the shielding, allowing for the use of a laser sheet of multiple millimeters tall, which enables detection of a larger fraction of the molecular beam at a reasonable signal to background ratio.

As there are no sidebands in the detection laser light, the scattering of multiple photons per molecule is unlikely. Following the reasoning in subsection 5.4.2, the estimated ratio of molecules in the detection area to a detected photon is, $N_{det}/S = 200$, for this fluorescence detection system.

6.1.1. Fluorescence spectroscopy

Molecules in the $X^2\Sigma^+(v = 0, N = 1)$ are probed by laser-induced fluorescence, driving the transition to $A^2\Pi_{1/2}(v' = 0, J' = 3/2)$. Note this is different from the transition to $A^2\Pi_{1/2}(v' = 0, J' = 1/2)$ probed for SrF.

In Figure 6.4a the spectrum for transitions from the $X^2\Sigma^+(v = 0, N = 1, J = 3/2)$ components of the ground state is shown, for molecules traversing the decelerator in a DC guiding mode with voltage amplitude of 2 kV. The voltage on the last ring is set to zero to minimise the electric field and corresponding Stark shift at the detection area.

At the end of the decelerator, only molecules occupying low-field seeking state are expected, as these are guided through the decelerator. In the energy level diagram in Figure 6.4b the low-field seeking components are marked in blue. The allowed transitions induced by

linearly polarised light from these low-field seeking components are shown as solid red arrows. The spectrum for these transitions is simulated in PGOPHER with a natural linewidth of 2.78 MHz from the lifetime of the exited state [90] and a Gaussian FWHM of 5 MHz, as shown in the solid blue line in Figure 6.4a. The spectrum is also simulated for the case where all hyperfine components are populated, shown in the solid black line. A full scale inset is shown to illustrate the relative intensities of these spectra.

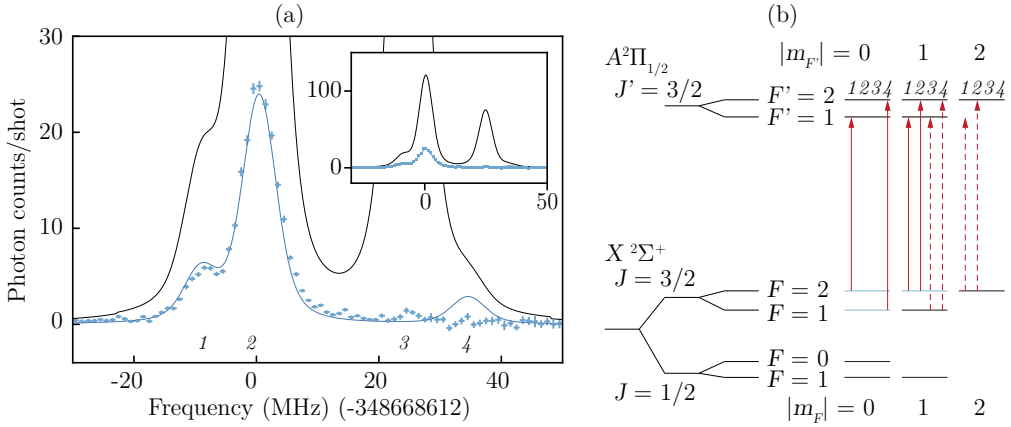

Figure 6.4 *| (a) Spectrum of $X^2\Sigma^+(v = 0, N = 1, J = 3/2)$ to $A^2\Pi_{1/2}(v' = 0, J' = 3/2)$ transitions measured after DC guiding at a voltage amplitude of 2 kV. The spectrum simulated in PGOPHER is shown in black for transitions from all hyperfine components, and in blue for only the low-field seeking ones. The zoom-out shows the contribution of the low-field seeking components to the full simulated spectrum. (b) Corresponding energy level diagram, with low-field seeking groundstate components marked in blue.*

In the measured spectrum, no strong signal from molecules in the $X^2\Sigma^+(v = 0, N = 1, J = 3/2, F = 1, m_F = 0)$ is observed. Initially, this was thought to be evidence for a significant loss channel for molecules in this state due to non-adiabatic transitions from this low-field seeking state to a high-field seeking state, in which molecules are not confined to the decelerator. The crossing with the high-field seeking $F = 2, m_F = 2$ state shown in Figure 4.2c was suspected to play a role in this.

However, it was realised later that no electric dipole transition can be made between $m_F = 0 \nleftrightarrow m_{F'} = 0$ when $\Delta F = 0$. Therefore, the population of the $X^2\Sigma^+(v = 0, N = 1, J = 3/2, F = 1, m_F = 0)$ is only probed via the transition to $A^2\Pi_{1/2}(v' = 0, J' = 3/2, F' = 2)$, marked as *4*, which is relatively weak. This measurement is therefore not conclusive on population of the low-field seeking component $F = 1, m_F = 0$ at the end of the decelerator and occurrence of non-adiabatic transitions. By performing the measurement with circularly polarised light instead, the population of this state should be more distinguishable.

6.2. Characterisation of the molecular beam

A characterisation of the molecular beam of SrF created in the cryogenic source can be found in Esajas [46]. In this chapter the characterisations relevant for this work are repeated for BaF. Further characterisation and optimisation of a similar cryogenic source can be found in Mooij [47].

6.2.1. Absorption spectroscopy

To characterise the molecular beam of BaF produced in the cryogenic buffer gas source the laser frequency is scanned over the rotational transitions in $X^2\Sigma^+$ ($v = 0$) to $A^2\Pi_{1/2}$ ($v' = 0$), recording a double-pass absorption spectrum 5 mm downstream from the cell exit. The central 180 GHz of the transitions is shown in Figure 6.5. The measurement consists of consecutive scans over approximately 35 GHz taken over 15 minutes each.
A summary of the energy level structure and naming convention of states and transitions can be found in Appendix A. The (rotational) temperature and velocity distribution of the molecular beam are known to strongly depend on the operation parameters of the source [80]. In this measurement the source cell temperature was stabilized to 17 K, which was also used for the simulation of the spectra in PGOPHER [68]. From the relative intensity of the transitions, it can be seen that the distribution over the states is not well described by one rotational temperature. This is expected as the molecular beam is cooled in the supersonic expansion from the cell, but during the expansion the collision rate is insufficient for full thermalisation of the beam.
The spectrum is simulated for a mixture of isotopologues $^{134}Ba^{19}F$ to $^{138}Ba^{19}F$ at a ratio corresponding to their natural abundance of the isotopes of Ba[1]. As $^{138}Ba^{19}F$ is the specimen of interest for this work, for this isotopologue the four branches of transitions are labelled explicitly. The branches correspond to the four sets of transitions from $X^2\Sigma^+(v = 0, N)$ to $A^2\Pi_{1/2}(v' = 0, J' = N \pm 3/2, N \pm 1/2)$, which are each marked in a different color in the simulated spectrum.
In fluorescence detection, molecules that have traversed the decelerator in the $X^2\Sigma^+(v = 0, N = 1)$ are typically probed at the transition to $A^2\Pi_{1/2}(v' = 0, J' = 3/2)$, corresponding to the second transition in the qQ/qR-branch marked by * in the spectrum.
The Gaussian FWHM of the transitions in the absorption spectrum is found to be 211(2) MHz, which is therefore also used in the simulated spectra. This width is expected to be dominated by the Doppler width from the transverse velocity spread of the molecular beam, which is thereby estimated to be 182(2) m/s. The width is significantly higher than the 135 MHz found by Mooij [47]. It could be that other broadening effects such as power or pressure broadening contribute to the measured width of the transitions, but this is not further studied here.
The spectrum has been taken at a relatively large neon buffer gas flow of 30 sccm. This is known to produce a molecular beam with a large forward velocity as demonstrated in Figure 6.6. For deceleration a beam with smaller initial velocity is favourable, which is achieved at a lower buffer gas flowrate of typically 10-15 sccm.

[1] Abundances ^{134}Ba: 2.4%, ^{135}Ba: 6.6%, ^{136}Ba: 7.9%, ^{137}Ba: 11.2%, ^{138}Ba: 71.7% [91]

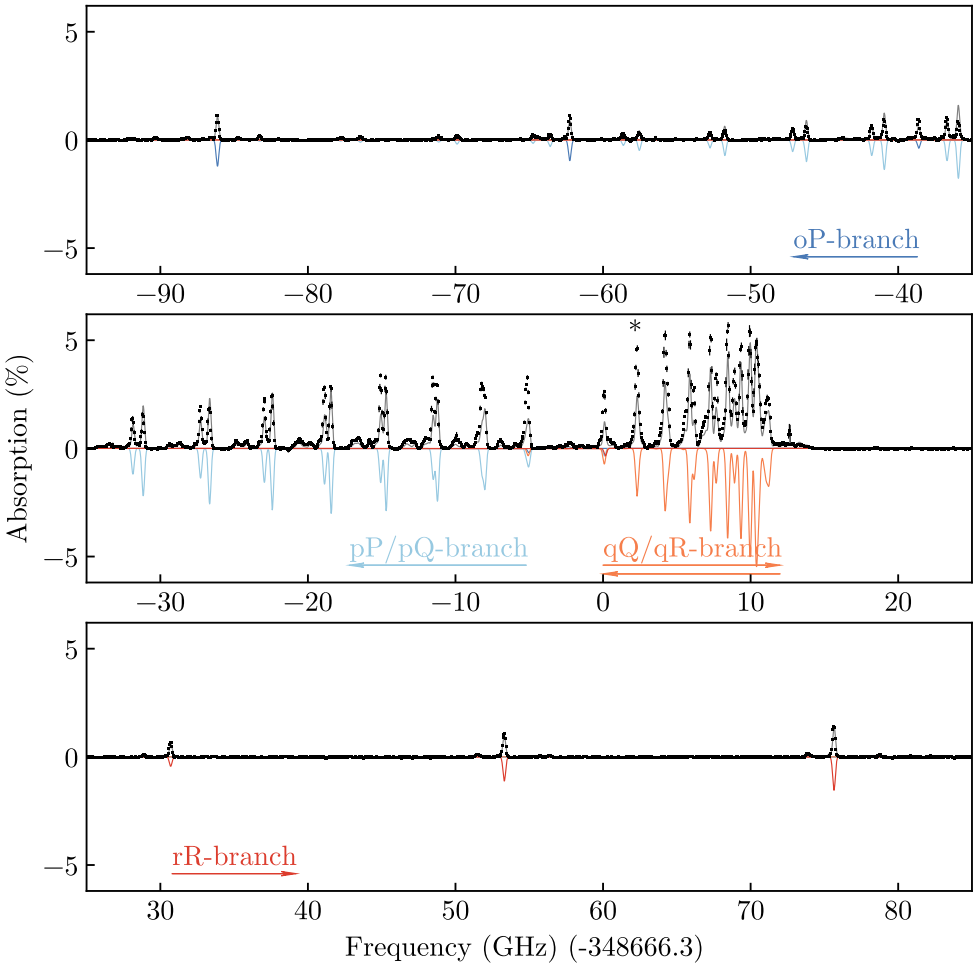

Figure 6.5 *| Rotational spectrum of $X^2\Sigma^+(v = 0)$ to $A^2\Pi_{1/2}(v' = 0)$ transitions for BaF measured using double-pass absorption detection 5 mm behind the cell exit. For comparison the spectrum simulated in* PGOPHER *[68] is shown in the solid grey line, at a rotational temperature of 17 K and Gaussian* FWHM *of 211 MHz. The simulated spectrum contains isotopes of $^{134}Ba^{19}F$ to $^{138}Ba^{19}F$ at their natural abundance [47]. The different branches of transitions for $^{138}Ba^{19}F$ are shown separately, mirrored to negative absorption. The direction of increasing N of the ground state for these branches is shown by the arrows. Note the qQ/qR-branch turns from increasing to decreasing energy splitting for transitions from state with $N > 7$. The zero point of the frequency axis corresponds to the $X^2\Sigma^+(v = 0, N = 0)$ to $A^2\Pi_{1/2}(v' = 0, J' = 1/2)$ transition, for which the frequency is confirmed by Doppler free spectroscopy referenced to a frequency comb in Mooij* et al. *[92]. The $X^2\Sigma^+(v = 0, N = 1)$ to $A^2\Pi_{1/2}(v' = 0, J' = 3/2)$ transition used to probe molecules that have traversed the decelerator is marked *.*

6.2.2. Neon flow

A parameter with significant impact on the characteristics of the molecular beam is the neon buffer gas flowrate. The effect of this flowrate on the intensity of the different longitudinal velocity components of the molecular beam of BaF in the $X^2\Sigma^+(v = 0, N = 0)$ state was investigated in detail in Mooij *et al.* [80] based on a velocity selective detection scheme 780 mm downstream from a cryogenic buffer gas source comparable to the one in this work. In that work it is shown that increasing the neon flowrate increases both the intensity and mean longitudinal velocity of the molecular beam. Despite the increase in longitudinal velocity, the increase in beam intensity shows an increasing molecular yield in the velocity range around 200 m/s up to a flowrate of 30 sccm.

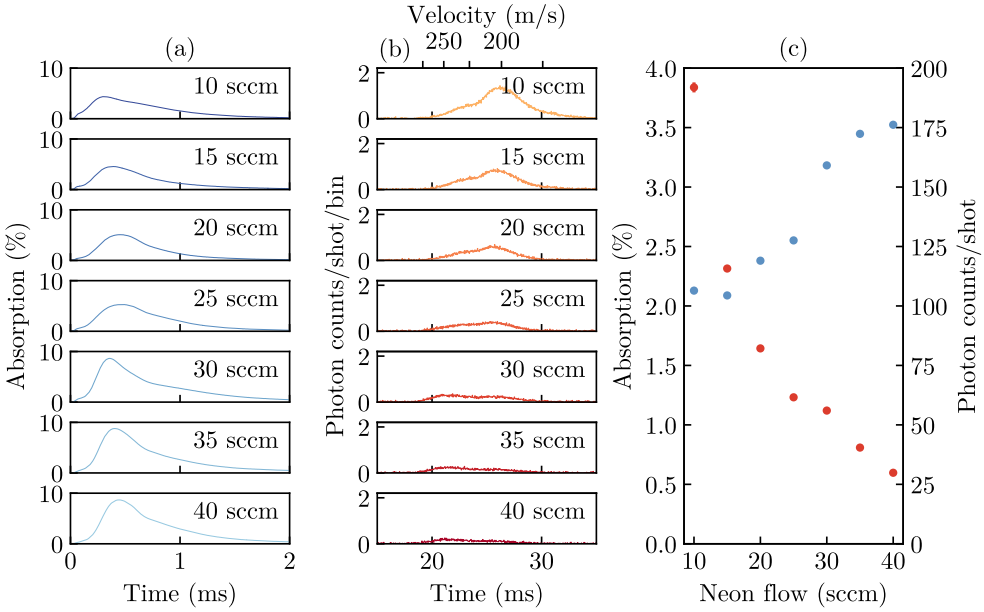

Figure 6.6 | *Characteristics of the molecular pulse for different neon buffer gas flowrates. Time-of-flight profiles are shown measured by (a) absorption 5 mm from the cell exit and (b) laser-induced fluorescence 10 mm from the last ring of the decelerator. The decelerator is operated in a DC guiding mode at a voltage amplitude of 2 kV. The signals integrated over the time-of-flight are shown for different neon flowrates on the (c), with the absorption signal in blue and the fluorescence signal in red.*

Figure 6.6a shows the time-of-flight profile based on a double-pass absorption signal measured 5 mm from the cell exit for different neon flowrates. The time integrated signal over the pulse is shown in blue in Figure 6.6c. The total intensity of the molecular beam is observed to increase with neon flowrate, in line with the observations from Mooij *et al.*[80]. This is understood from the increased extraction efficiency from the cell.
Figure 6.6b shows the time-of-flight profile based on laser-induced fluorescence 10 mm downstream from the last ring of the decelerator for different neon flowrates. Molecules are guided through the decelerator in a DC guiding mode at a voltage amplitude of 2 kV to

accept a large range of longitudinal velocities. The estimate for the longitudinal velocity of the molecules is shown at the top, based on the arrival time and the traversed distance. The distribution consists of a fast and a slow part, corresponding to the parts of the molecular beam extracted before and after reaching thermal equilibrium with the buffer gas respectively. It can be seen how the mean velocity of the thermalised part of the beam increases with neon flow which is explained in Mooij *et al.* [80] to be due to the more supersonic behaviour of the beam with the increased pressure in the cell. There it is also suggested that the cell may be lengthened to reduce the temperature and the longitudinal velocity of the beam.
The time integrated fluorescence signal is shown in red in Figure 6.6c. Here it is shown that the total number of molecules detected at the end of the decelerator decreases with neon flowrate, contrasting with the absorption signal directly after the cell exit and the measurements in Mooij *et al.* [80]. The reduction in signal downstream is likely caused by the high pressure in the setup, resulting from the abundance of buffer gas which increases with the neon flowrate. Collisions between the BaF molecules and neon would result in losses from traps in the decelerator by transitions out of the low-field seeking states or by momentum transfer kicking the molecules out of the decelerator altogether. In experiments performed after this work with the same source, an increase in fluorescence signal is observed by over an order of magnitude when an extra vacuum pump is installed to reduce the pressure. The pressure in the decelerator could be reduced in future experiments by using a skimmer between the source and the downstream part of the setup.
In the experiments shown in the remainder of this chapter, the source is operated at a neon flowrate of 10-15 sccm as this seems to give the best balance between a stable signal from the source and high intensity of slow part of the molecular beam, showing the strongest signal at the end of the decelerator.

6.2.3. Longitudinal velocity

To probe the longitudinal velocity distribution of the molecular pulse produced in the cryogenic source, the AC guiding signal is measured at multiple longitudinal velocities.

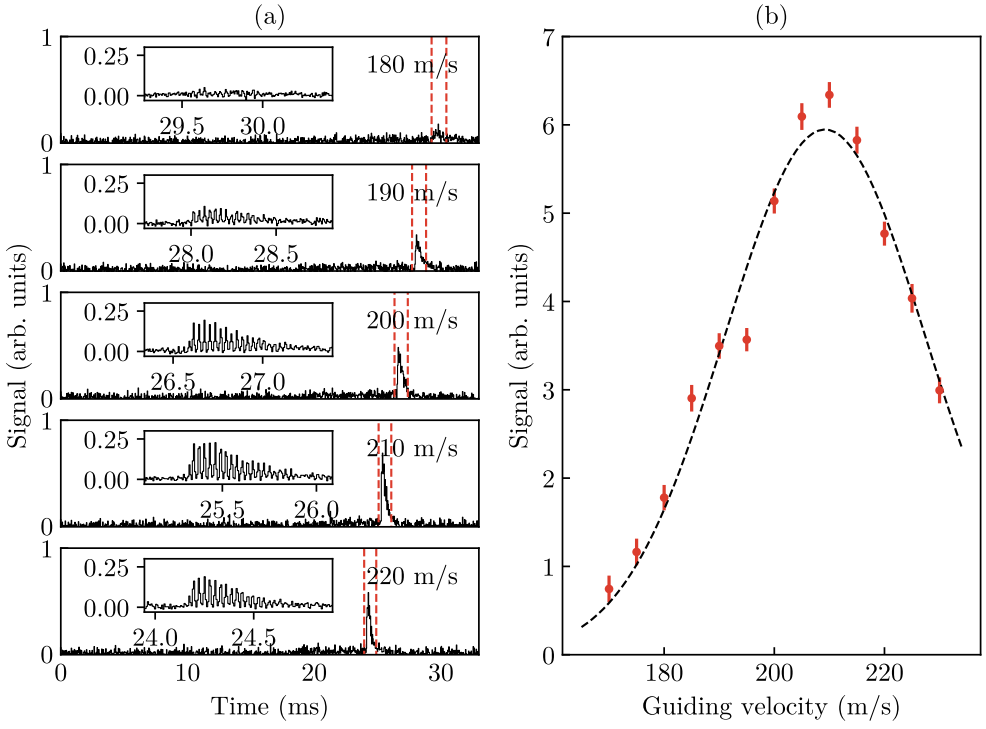

Figure 6.7 | *Signal strength for different longitudinal velocity components of the molecular beam, probed by AC guiding at a voltage amplitude of 5 kV for different velocities. (a) Time-of-flight profiles, with a zoom-in around the guided peak marked by the red dashed lines. (b) Integrated signal over the guided peak at each guiding velocity. The black dashed line shows a fitted Gaussian velocity distribution.*

In Figure 6.7 the time-of-flight profile is shown for a selection of longitudinal velocities. The starting point and length of the zoom-in is adjusted to the guiding velocity and corresponds to a window of 210 mm consistently. The time-integrated signal over the corresponding time windows are shown on the right side of Figure 6.7 for different guiding velocities. A Gaussian distribution is fitted to the longitudinal velocity profile, showing a 43(9) m/s FWHM velocity distribution centered at 209.2(6) m/s.

6.3. Guiding at different voltage amplitudes

The phase-space acceptance of the decelerator strongly depends on the voltage amplitude at which it is operated, as discussed in detail in chapter 4. In Figure 6.8 the signal for AC guiding at 200 m/s is shown for different voltage amplitudes.

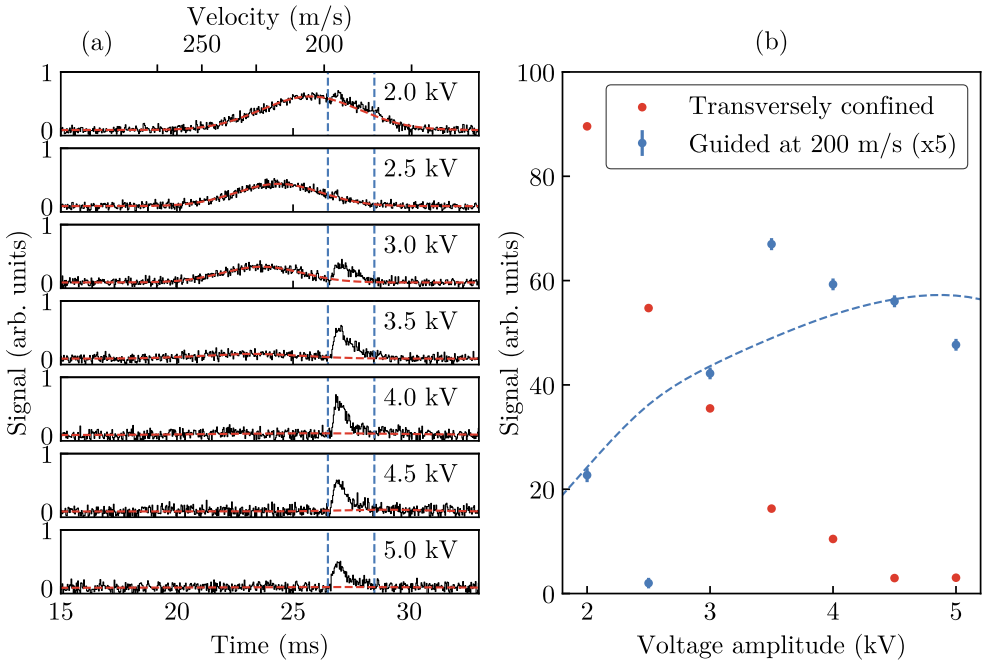

Figure 6.8 | *Signal strength for BaF molecules guided at 200 m/s for different voltage amplitudes applied to the decelerator. (a) Time-of-flight profiles with the arrival time for molecules guided at 200 m/s marked in blue dashed lines. To the signal from the transversely confined molecules a Gaussian profile is fitted shown in the red dashed lines. (b) Integrated signal over the transversely confined molecules from the fit in red, and from the molecules guided at 200 m/s in blue (multiplied by 5). The blue dashed line shows the simulated acceptance for guiding (see section 4.4).*

The signal from the transversely confined molecules, which are not contained longitudinally, strongly decreases at higher voltage amplitudes. This is understood from the traversal of these molecules through regions of electric field strength above the turning point field E_{tp}. With increasing voltage amplitude these regions of electric field strength for which the Stark shift is high-field seeking increases, resulting in increasing repulsion of these molecules from the decelerator. For voltage amplitudes above 4 kV the signal from the transverse confined BaF molecules is negligible. This is different from SrF, for which also at higher voltage amplitude signal from transversely confined molecules was observed, despite the similar turning point field. This difference may be due to the oscillation frequency of BaF due to the higher mass, resulting in a longer occupation of a region of high field. The limited detection volume for SrF may also play a role, as molecules at a higher transverse displacement are

closer to expulsion from the decelerator.
The signal from the guided signal increases with voltage amplitude as expected from the increasing phase-space acceptance as demonstrated in Figure 4.13. The simulated phase-space acceptance for guiding is repeated in Figure 6.8b, scaled to match the measured signal. The simulated phase-space acceptance is maximum for a voltage amplitude of 5 kV, understood from the turning point field occurring on the longitudinal axis for this voltage.
The simulated acceptance does not match the signal from the guided molecules perfectly. An optimum in the guided signal strength is found for voltage amplitudes below 5 kV, as previously also observed for SrF [51]. This in not yet fully understood. The dip in the signal from molecules that have been contained in the same trap within the decelerator is not observed in these measurement. This dip suggested the non-adiabatic losses to high-field seeking states at the low field in trap centers for the measurement for SrF with a molecular beam at 345 m/s from a supersonic source [50].
The outliers in integrated signal from the guided molecules could suggest some systematic biases in this measurement. The partial overlapping of the signal from the guided molecules with the signal from the transversely confined molecules complicate this study and additional measurements will be necessary to fully understand the implications for the decelerator acceptance.

6.4. Hexapole lens

A hexapole lens is used to improve the phase-space matching between molecular pulse from the cryogenic source and the acceptance of the decelerator. The design and operating principle are discussed in section 4.2. The full characterisation of the hexapole lens for BaF is given in chapter 7, based on direct imaging of the molecular signal at the position of entrance of the decelerator.

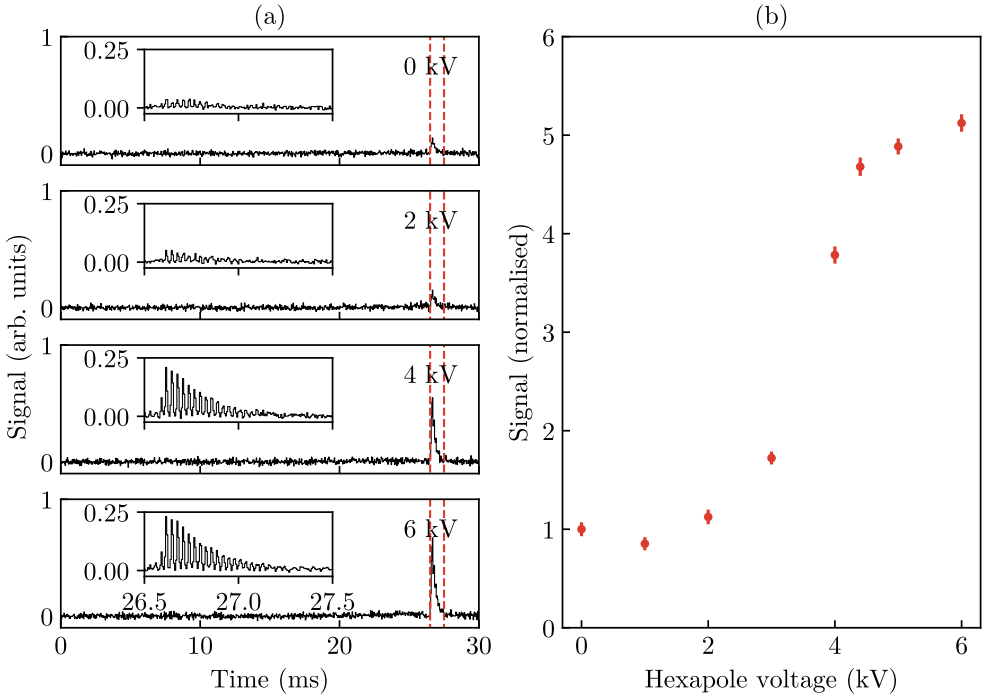

Figure 6.9 *| Intensity of the molecular beam of BaF at the end of the decelerator, for different voltages applied to the hexapole lens. (a) Time-of-flight for* AC *guiding at 200 m/s with voltage amplitude of 5 kV. The guided peak is marked by the red dashed lines. (b) Integrated signal over the guided peak for different voltages applied to the hexapole lens.*

In Figure 6.9 the fluorescence signal at the end of the decelerator is shown for different voltage applied to the hexapole lens. The molecules are AC guided at a velocity of 200 m/s through the decelerator with a voltage amplitude of 5 kV. The sharp increase in intensity of the signal over the first packages of the guided peak correspond to the signal increase when the electric field from the decelerator is switched off. This measurement was performed before the installation of the electric field shield.
In Figure 7.12, the maximum signal strength at the position of the entrance of the decelerator occurs for voltage of 4 kV applied to the hexapole lens from direct imaging of the molecular beam on an EMCCD camera. This difference shows the role of phase-space acceptance, projecting molecules into the decelerator does not guarantee them to be captured. At a

voltage of 6 kV, the phase-space distribution of the beam is rotated such that it is well matched to the acceptance of the decelerator.
As discussed in section 5.5, the steep increase in the signal intensity from the guided molecules is due to the longitudinal velocity selection, reducing the effect of chromatic aberrations compared to the measurements on the full molecular pulse presented in chapter 7. The higher voltage at which the optimal phase-space matching occurs is higher than for SrF because of the 1.5 times higher mass of BaF, which requires a higher force to achieve the same phase-space rotation or effective focal length of the hexapole lens.
The guided signal is observed to be more than five times stronger at the end of the decelerator when a voltage of 6 kV is applied to the hexapole lens than without a voltage applied. In chapter 7 the hexapole lens is further investigated and its performance is compared to simulations.

6.5. Camera imaging of molecular beam

To characterise the transverse properties of the molecular beam exiting the decelerator, significant effort has been put in imaging laser-induced fluorescence on an electro-multiplying charged-coupled device (EMCCD camera, Andor iXon DU897). As shown in Figure 6.1, the camera is mounted facing opposite to the molecular beam, into the exit of decelerator.

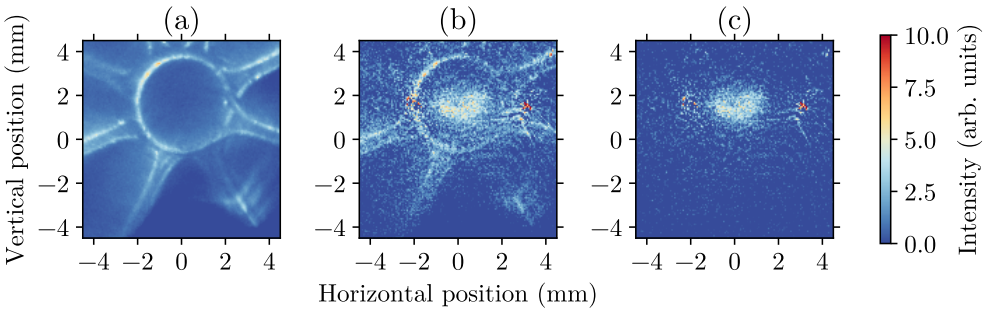

Figure 6.10 | *Camera image looking back into the decelerator exit. (a) Reflections from the last ring electrodes. (b) Ring electrodes and molecular signal overlapped at arbitrary scale. (c) Fluorescence signal from molecules surrounded by reflections. The origin of the axis is chosen to the center of images.*

The image in Figure 6.10a shows the reflection of the 4 mm inner diameter ring electrodes of the decelerator. The image was taken with a single exposure without electron multiplying while illuminating the electrodes with a flashlight.
The image in Figure 6.10c is taken with a laser sheet at 10 mm from the last ring, in this image traversing the molecular beam from left to right. The decelerator is operated in a DC guiding mode at a voltage amplitude of 2 kV. The vertical width of the imaged molecular beam is constrained by the size of the laser sheet.
This image is the result of averaging over 4000 shots, corresponding to 400 seconds of measurement time. In each shot the signal it taken with an exposure from 18 to 33 ms after the experiment-trigger, as this is when the molecules are expected to arrive in the detection

area, as confirmed by the time-of-flight measured with the PMT. Another image is taken with exposure over a period of equal length, from 68 to 83 ms after the experiment-trigger, when the molecular pulse has passed the detection area. This background image is subtracted from the signal image in the analysis, which significantly reduces the inhomogeneous background signal due to photon scatters and pixel dependent number of dark counts.

Despite this background subtraction method there are two significant noise sources which do not seem to average out, of approximately twice the intensity of the molecular signal. Fortunately these are spatially distinguishable on the camera image, falling to the left and right of the molecular beam. When overlapped with the image of the ring electrode reflections, as done in Figure 6.10b, it can be seen that the noise source on the left originates from the reflection of the laser sheet from the last ring electrode. The noise source on the right does not coincide with the position of the electrodes and was found to originate from a fibre stuck to the electrodes, possibly a hair that was lost during installation. Next to a noise source in these images, it may have caused a significant contribution to the background counts in the PMT signal. It has been removed during the installation of the electric field shield.

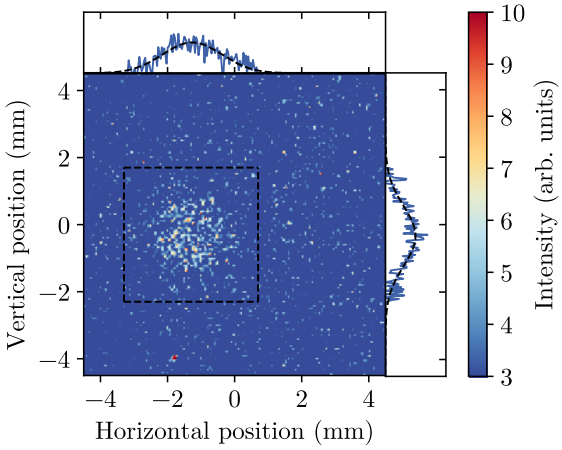

Figure 6.11 | *Camera image looking back into the decelerator exit showing the fluorescence signal of molecules DC guided at a voltage amplitude of 2 kV. Projections along each axis are shown in blue, obtained by integration over the black dashed box. A Gaussian fit to each of the projections is shown as a black dashed line, corresponding to a 2.1(1) mm FWHM beam width in each direction*

After the installation of the electric field shield, the molecular beam was again imaged on the EMCCD camera by laser-induced fluorescence from the traversal of a laser sheet of 5 mm height at 44 mm from the last ring electrode of the decelerator. Figure 6.11 shows the image of the molecular beam from the decelerator when DC guiding at a voltage amplitude of 2 kV, with the same background subtraction method as described above. The signal is integrated in each direction over a square region of 4×4 mm around the center of the molecular beam to obtain the beam projection along and orthogonal to the laser sheet. A Gaussian beam profile was fitted to these projections, providing a molecular beam width (FWHM) of 2.1(1) mm in

each direction.
To obtain this image the signal was averaged over 10000 shots, corresponding to 1000 seconds of data taking for the relatively strong signal of DC guiding, in which the decelerator accepts molecules with a large range of longitudinal velocities. Therefore, it had to be concluded that a full characterisation of the transverse phase-space distribution of the molecular beam at different deceleration modes by direct imaging was not feasible at the current molecular signal strength.

6.6. First deceleration of BaF

In this section the first deceleration results for BaF using a traveling-wave Stark decelerator are presented. Molecules in the $N = 1, M_N = 0$ has been decelerated from 200 to 150 m/s, corresponding to a deceleration a of -2 km/s^2. Hereby, almost half of the kinetic energy from the longitudinal velocity of these molecules is removed.

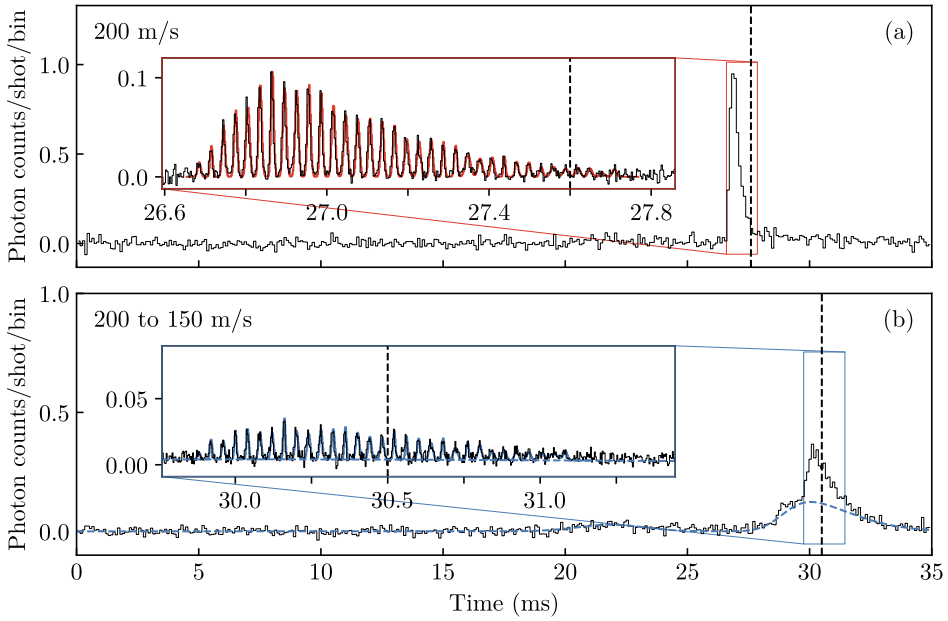

Figure 6.12 | *Time-of-flight profile of BaF molecules traversing the traveling-wave Stark decelerator. (a) AC guiding at 200 m/s, with a zoom-in around the guided peak. (b) Deceleration from 200 to 150 m/s, with a zoom-in around the decelerated peak. In both cases a voltage amplitude of 5 kV is applied to the decelerator. To the guided and decelerated peak substructure a sequence of equally spaced Gaussians are fitted. The black dashed lines show the moment the decelerator voltage is switched off.*

In Figure 6.12 the time-of-flight profile for the deceleration from 200 to 150 m/s is shown together with the signal for AC guiding at 200 m/s, both for a voltage amplitude applied to the decelerator of 5 kV. Both datasets have been taken on the same day and under similar

source operation condition, resulting in similar absorption signals. The mean peak absorption for these measurements is 9.5%, with a mean integrated absorption over the pulse length of 1 ms of 5.2%.
The time-of-flight profiles have not been normalised to the absorption signal to illustrate the number of photons detected on the PMT. The scale of the histograms and the time span of the zoom-in region are adjusted to the longitudinal velocity of the molecular beam.
In Figure 6.12b, in addition to the signal from the decelerated molecules, a broad distribution of signal from transversely confined molecules that have not been captured longitudinally can be observed. The overlap between these signals complicates the distinction of the origin of the detected photons. The contribution from the non-decelerated molecules is estimated by fitting a skewed Gaussian to the part of the signal that does not overlap in arrival time with the signal from the decelerated molecules. Another skewed Gaussian is fitted to the signal from the faster non-decelerated molecules arriving between 18 and 25 ms after the experiment-trigger. The combination of these fits is shown in the blue dashed line in Figure 6.12b. This fit to the signal from the non-decelerated molecules is used as an offset for the sequence of equally spaced Gaussians, fitted to the signal from the decelerated molecules. The overlap of the signal from the decelerated and non-decelerated molecules poses a large uncertainty on the width of the distributions of decelerated molecules contained in a single trap in the decelerator. As a result, an analysis of the longitudinal phase-space distribution as presented for SrF in subsection 5.6.1 did not yield reliable results. The intensity of the signal from molecular packages that are still contained within the decelerator once the voltage is switched off is not enough to clearly distinguish them from the background, for both the guiding and deceleration signal. For molecular packages arriving earlier at the detection area a Gaussian FWHM of approximately 1.8 and 1.6 mm are observed for guiding and deceleration respectively. The contribution from the position spread in the decelerator and the velocity spread expanding the package over the free-flight of 44 mm can not be distinguished. From the phase-space acceptance simulation in Figure 4.11 a larger FWHM is expected at the detection point, of 2.3 and 2.0 mm for guiding and deceleration at $a = -2$ km/s^2 respectively.

6.6.1. Number of molecules

To quantify the performance of the decelerator, the number of molecules at different positions in the setup is estimated based on the detected signal there.

Cryogenic source - The number of molecules extracted from the cryogenic source is monitored by the absorption signal measured 5 mm after the cell exit. Over the measurements presented in Figure 6.12, an average double-pass peak absorption of 9.5% was measured. In Mooij [47] this is estimated to correspond to 10^{10} molecules per pulse in the $X^2\Sigma^+(v = 0, N = 1)$ state.

Decelerator - The number of molecules at the end of the decelerator strongly depends on the operation mode thereof, as analysed by the phase-space acceptance in chapter 4. The molecules are probed by the fluorescence signal at 44 mm from the last ring of the decelerator for the measurements presented here. In section 6.1 it is estimated that on average one photon is be detected on the PMT for every 200 molecules traversing the detection area.

On the day of the measurement of the signal for deceleration from 200 to 150 m/s presented in section 6.6 also a DC guiding signal at voltage amplitude of 2 kV was measured, with an average time integrated signal of 240 photons counts/shot, corresponding to 5×10^4 molecules per pulse. This corresponds to molecules that have been transversely guided through the decelerator with a transverse velocity acceptance of 3.68 m/s and transverse position acceptance of 1.8 mm as demonstrated in subsection 4.3.1. The longitudinal acceptance in this operation mode is not limiting.

In Figure 6.12a, a signal for AC guiding at 200 m/s was demonstrated with an average signal strength of 5.1 photon counts/shot, corresponding to 1×10^3 molecules per pulse. According to the skewed Gaussian fit to the signal from the non-decelerated molecules in Figure 6.12b, 1.9 out of the 4.1 photon counts/shot detected in the time window marked in blue correspond to non-decelerated molecules. This implies 2.2 photon counts/shot originate from the molecules to 150 m/s, corresponding to 4×10^2 molecules per pulse. This decrease in signal from guiding to deceleration at $a=-2$ km/s^2 by just over half is in line with the expectation from the phase-space acceptance in Figure 4.13.

The transverse acceptance for the decelerator is similar in an operation of DC guiding at a voltage amplitude of 2 kV and for trapped molecules in AC guiding or deceleration at a voltage amplitude of 5 kV. The transverse velocity acceptance v_x^{acc} is 3.68 m/s and 3.66 m/s for DC and AC modes respectively, for BaF in the low-field seeking components of the $X^2\Sigma^+(v=0,N=1)$ state. The difference in the fluorescence signal is from the phase-space acceptance. The FWHM longitudinal velocity distribution of the molecular pulse is shown in subsection 6.2.3 to be 43(9) m/s. The HWHM longitudinal velocity distribution of the accepted molecules for AC guiding at 5 kV is found from simulation in Figure 4.11 to be 3.2 m/s. This gives an estimate for the relative velocity with respect to the electric field minima of molecules which are accepted, corresponding to an accepted fraction of 0.14. The HWHM longitudinal position distribution for each trap is estimated to be 1.0 mm, reducing the accepted fraction by another 0.33, resulting in a total reduction of the longitudinal acceptance of 0.046. The coupling between the longitudinal and transverse acceptance is only partially taken into account in this analysis, and would increase the total acceptance reduction further. The measured signal strength is a factor of 0.02 lower for AC guiding at 5 kV than for DC guiding at 2 kV.

The reduction of molecules detected just behind the source and after the decelerator is less well understood. The largest loss is due to the transverse velocity distribution of the molecular pulse of approximately 40 m/s FWHM, of which a small fraction is accepted. Velocities of up to 3.6 m/s can be accepted, but the simulated HWHM transverse velocity of the accepted molecules is shown in Figure 4.11 to be 1.9 m/s. Assuming a Gaussian distribution in both transverse directions, this corresponds to an accepted fraction of the velocities of 4.1×10^{-3}. With the hexapole lens the molecular beam is focused to a FWHM of 6 mm at the position of the first ring of the decelerator, as shown in Figure 7.11, resulting in another reduction in accepted signal of 0.22.

This suggests an expected reduction in number of molecules in the pulse just outside of the source, to the pulse at the end of the decelerator for DC guiding at a voltage amplitude of 2 kV of 9.1×10^{-4}. However, the estimated reduction in number of molecules based on the

measured signal of 5×10^{-6} is much larger. This difference is attributed to the pressure in the setup, especially between the source and the decelerator. In subsection 6.2.2 the detrimental effect of increasing the flow of the neon buffer gas to the fluorescence signal at the end of the decelerator is discussed, despite the increasing signal strength just after the source. Even for lower flow rates the pressure buildup could be significant, resulting in losses in signal due to collisions of BaF with the background gas. If the pressure in the setup is reduced, a significant gain in decelerated signal is expected. A signal increase of over an order of magnitude has been observed in the setup without the decelerator used at the time of writing, after installation of another turbo pump.

6.7. Outlook

In this chapter the deceleration from 200 to 150 m/s has been demonstrated, corresponding to a deceleration strength a of -2 km/s^2, and a reduction of the half the kinetic energy from the forward velocity of these molecules. For the NL-eEDM experiment the target velocity is 30 m/s [44], which requires a deceleration strength a of -4 km/s^2 when decelerating from 200 m/s. This limits the phase-space acceptance for BaF in the low-field seeking components of the $X^2\Sigma^+(v = 0, N = 1)$, which reduces the intensity of the decelerated beam. Thus far, signal from molecules at this deceleration has not been observed. Further efforts were interrupted by a sudden increase of pressure within vacuum chambers of the decelerator, due to unfreezing of the neon gas while heating the cryogenic source without closing the valve to separate these chambers. This cause discharges between electrodes in the decelerator, resulting in the irreparable breakdown of multiple amplifiers.
Fortunately, effort was already being put into the development of transformers to enable an upgrade to voltage amplitudes above 5 kV to be applied to the decelerator, showing promising results at the time of writing. The electric field within the decelerator is already close to the turning point field for BaF molecules in the $N = 1$ and increasing the voltage amplitude above 5 kV would not be beneficial to the phase-space acceptance of the decelerator for these. For BaF molecules in the $N = 2$, for which the Stark shift at electric field strength within the decelerator at a voltage amplitude of 5 kV is lower, a significantly larger phase-space acceptance of the decelerator would be achievable. In Figure 4.17 the effective potential is shown for a voltage amplitude of 10 kV, but if this would not be feasible the acceptance would also increase drastically at a voltage amplitude of 8 kV as demonstrated in Table 4.3. In addition, the transverse laser cooling of BaF can be used to increase the number of molecules mapped into the phase-space acceptance of the decelerator. Implications for laser cooling of BaF laser cooling have been investigated theoretically [93] and Doppler cooling has been demonstrated on a molecular beam produced in a cryogenic buffer gas source [94]. At the time of writing, a setup is being developed where laser cooling on a molecular beam focused by the hexapole lens is pursued, which could be used as an input for the decelerator. The laser light for re-pumping excited vibrational states and addressing multiple hyperfine components of the ground state can also be used to optically pump molecules into states which can be focused in the hexapole lens and decelerated in the traveling-wave Stark decelerator.

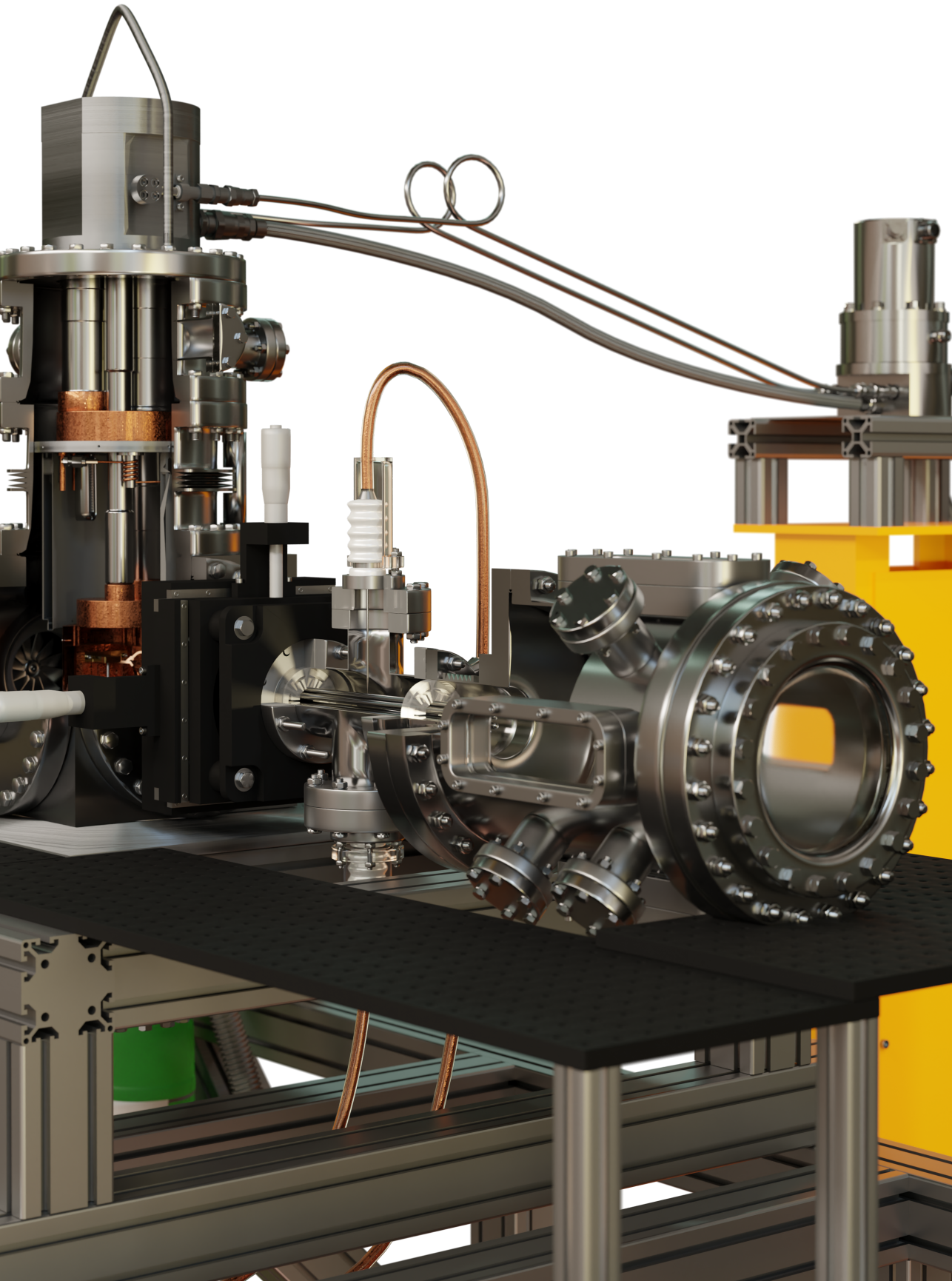

7

Electrostatic hexapole lens

An electrostatic hexapole lens is used to manipulate the transverse properties of a beam of barium fluoride molecules from a cryogenic buffer gas source. The spatial distribution of the beam is measured by recording state-selective laser-induced fluorescence on an EMCCD camera, providing insight into the intensity and transverse position spread of the molecular beam. Although the high mass and unfavorable Stark shift of barium fluoride pose a considerable challenge, the number of molecules in the low-field seeking component of the $N = 1$ state that pass a 4 mm diameter aperture 712 mm behind the source is increased by a factor of 12. Furthermore, it is demonstrated that the molecular beam can be displaced by up to ± 5 mm by moving the hexapole lens. Our measurements agree well with numerical trajectory simulations. We discuss how electrostatic lenses may be used to increase the sensitivity of beam experiments such as the search for the electric dipole moment of the electron.

Chapter based on Anno Touwen *et al.* "Manipulating a beam of barium fluoride molecules using an electrostatic hexapole", *New J. Phys.* **26** 073054, July 2024.
The chapter image shows the partially opened hexapole lens setup showing the cryogenic source, hexapole lens electrodes and laser cooling chamber used for molecule detection.

7.1. Introduction

Heavy polar molecules are uniquely suitable as probes for symmetry violation beyond what is incorporated in the Standard Model of particle physics [95]. Currently, the most precise limits on the electric dipole moment of the electron (eEDM) are set by experiments on HfF^+ [42], ThO [96] and YbF [97]. A non-zero value of the eEDM would constitute a violation of time-reversal (T)-symmetry and CP-symmetry, where C denotes charge conjugation and P parity. The current bounds for the eEDM already put tight constraints on theories that extend the Standard Model [36, 98].

The NL-eEDM collaboration aims to measure the eEDM in a beam of barium fluoride (BaF) molecules. Compared to molecules used in other studies, BaF is relatively light and has a somewhat smaller enhancement factor for the electron electric dipole moment. However, a competitive measurement is possible by exploiting the long interaction times offered by Stark deceleration and laser-cooling of an intense cryogenic buffer gas cooled beam [44]. Here, we present experiments on manipulating a beam of BaF molecules using an electrostatic hexapole lens.

The main motivation for this work is to increase the number of molecules that enters our traveling-wave Stark decelerator. In previous experiments on deceleration of SrF molecules [62], there was a 370 mm gap between the cryogenic source and the decelerator to allow for separation of the source and decelerator chambers by a vacuum valve[1], resulting in a transverse loss of molecules. This loss can be avoided by mapping the emittance of the beam at the exit of the source onto the *transverse* acceptance of the decelerator using an electrostatic lens [69]. By mounting the lens on a manipulator, the alignment of the beam into the decelerator can be optimised. In principle, the *longitudinal* phase-space matching of the beam with the acceptance of the decelerator is also improved by increasing the distance between the beam source and decelerator [78], but for realistic lengths of the lens this increase is limited.

Electrostatic multipole lenses were first introduced in the 1960s by Gordon *et al.* [99] and Bennewitz *et al.* [100] to perform microwave spectroscopy on state-selected molecular beams and are used for collision studies between state-selected oriented molecules [69, 101, 102]. Many studies have targeted relatively light and simple molecules such as OH, CH, CH_3F and NH_3 in low-field seeking states that have a large electric dipole moment to mass ratio and a Stark shift that is either predominantly linear or quadratic. In contrast, BaF is both much heavier and has a much less favourable Stark shift over the relevant range of electric field strength, changing from quadratic into linear and ultimately becoming high-field seeking. Nevertheless, it is shown here that the beam intensity down stream from the source can be increased significantly by using a properly designed hexapole lens. The hexapole lens was developed for BaF molecules in the first excited rotational level ($N = 1$) of the electronic and vibrational ground state and has also been tested with molecules in the second excited rotational state ($N = 2$) state, that may be used as an upgrade to the experiment in the future. In a related study, Wu *et al.* used a hexapole lens to enhance the molecular flux of ThO molecules for the ACME experiment [103]. Two-dimensional imaging was previously

[1] Such a valve is necessary, as the source is heated up every night and the target is replaced every few weeks. Breaking the vacuum of the decelerator chamber requires high voltage conditioning of the electrodes which typically takes many hours.

used to study the performance of a hexapole lens for beams of metastable CO [104].

7.2. The force on barium fluoride in an electrostatic multipole lens

The electrostatic potential Φ for a charge free region of space fulfills Laplace's equation $\nabla^2\Phi = 0$. In the case where it is constant along an axis z it can be written as a multipole expansion in cylindrical coordinates as [69],

$$\Phi(r,\theta,z) = \Phi_0 \sum_{n=1}^{\infty} a_n \left(\frac{r}{r_0}\right)^n \cos(n\theta + \theta_n). \tag{7.1}$$

The electrostatic potential Φ for a charge free region of space fulfills Laplace's equation $\nabla^2\Phi = 0$. In the case where it is constant along an axis z it can be written as a multipole expansion in cylindrical coordinates as [69],

$$\Phi(r,\theta,z) = \Phi_0 \sum_{n=1}^{\infty} a_n \left(\frac{r}{r_0}\right)^n \cos(n\theta + \theta_n). \tag{7.2}$$

The field is parameterised by voltage magnitude Φ_0, coefficient a_n, inner radius r_0 and offset angle θ_n. When considering a single multipole term the resulting electric field strength is,

$$E_{(n)}(r,\theta,z) = |-\vec{\nabla}\Phi_n| = n\Phi_0 \frac{r^{n-1}}{r_0^n}, \tag{7.3}$$

representing the dipole, quadrupole and hexapole fields for $n = 1, 2, 3$, respectively.
The radial force on a polar molecule within an electric field E is given by $F_r = -\partial W(E)/\partial r$, with $W(E)$ being the potential energy of a molecule in an electric field, also known as the Stark shift. For an ideal lens, this restoring force is linear, $F_r = -kr$, where k is the spring constant of the system.
For a molecule in a state with predominantly quadratic Stark effect $W(E) = \frac{1}{2}\alpha E^2$, such as NH_3 in the upper inversion level of the $J = 1, K = 1$ state, a linear restoring force can be established by a quadrupole field $E_{(2)}(r) = 2\Phi_0\, r/r_0^2$ [99, 105]. In a state with a linear Stark shift $W(E) = -\mu_{eff}E$, such as OH in the upper level of the Λ-doublet in the $J = 1, \Omega = 3/2$ state [106] or ND_3 in the upper inversion level of the $J = 1, K = 1$ state [107], a linear restoring force can be established with a hexapole field $E_{(3)}(r) = 3\Phi_0\, r^2/r_0^3$ instead.
Let us now turn to barium fluoride. The solid lines in Figure 7.1 show the Stark effect of the lowest rotational states of BaF in the lowest vibrational state ($v = 0$) of the electronic ground state ($X^2\Sigma^+$) found by diagonalisation of the Stark Hamiltonian using PGOPHER [68]. Here the electric dipole moment, μ_e = 3.1702(15) D, and the hyperfine constants are taken from Ernst *et al.* [67] and other molecular constants, including the rotational constant, B = 6.47395465(11) GHz, from Ryzlewicz *et al.* [66].
The rotational levels, labeled by N, are split due to the spin-rotation interaction with the spin of the molecules, ($S = 1/2$), due to the unpaired valence electron, resulting in fine structure states labeled by J. These fine structure states are further split due to spin-spin

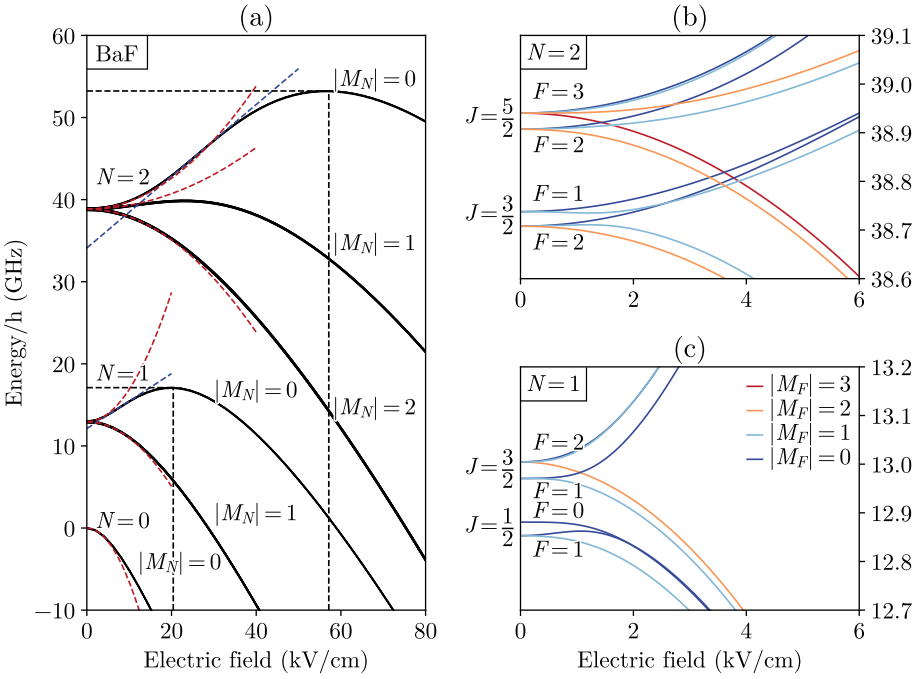

Figure 7.1 | *(a) Stark effect in $^{138}Ba^{19}F$ for the lowest rotational states ($N \leq 2$) of $X^2\Sigma^+(v = 0)$ calculated using PGOPHER [68] based on molecular constants from Ryslewicz* et al. *[66] and Ernst* et al. *[67]. The red and blue dashed lines show the quadratic extrapolation at zero and a linear extrapolation at intermediate field strengths to illustrate Stark curves ideal for quadrupole and hexapole lenses, respectively. The dashed black lines indicate the electric field strength and energy when these low-field seeking components become high-field seeking. (b) and (c) show the low electric field regime for $N = 2$ and $N = 1$ respectively, demonstrating their hyperfine structure.*

and spin-rotation interaction with the nuclear spin of the fluorine ($I = 1/2$) atom, resulting in four hyperfine states labeled by the total angular momentum F. The Stark shift of these hyperfine states is shown in Figure 7.1(b) and (c). At higher electric field, different M_F levels group together and shift collectively depending on M_N.
To describe the motion of the molecules within the multipole lens, we will neglect the hyperfine splittings and only consider the shift of the rotational level $N, |M_N|$ as a whole. At low field strength, the Stark shift of these levels can be well approximated by perturbation of the Stark Hamiltonian up to second-order [63], as,

$$W_{lf}(E) = W^{(0)}(N) + W^{(2)}(N, M_N)\frac{\mu_e^2 E^2}{B}. \tag{7.4}$$

The odd power terms vanish (for a negligible eEDM) because of the odd parity of the field [108]. This quadratic expansion is shown as red dashed lines in Figure 7.1(a). Note

the splitting into low and high-field seeking states, curving up and down for increasing field strength.

When the electric field is increased further the contribution of higher rotational levels increases and the low-field seeking Stark curves follow a linear trend. The blue dashed lines in Figure 7.1(a) show this trend at the maximum slope, which happens at a field of 7.1 kV/cm for the $N = 1$ state and 25.4 kV/cm for the $N = 2$ state. The effective dipole moments, $\mu_{eff} = -\partial W(E)/\partial E$, at these points are found to be −0.665 D and −0.867 D for the $|M_N| = 0$ substates of $N = 1$ and $N = 2$, respectively.

At even higher electric field strength, the Stark shift becomes comparable to the rotational splittings and the rotational states become high-field seeking. The states with $|M_N| = 0$, which start as low-field seeking at low electric field strengths, turn into high-field seeking at turning point field strengths E_{tp} of 20.4 kV/cm and 57.1 kV/cm for $N = 1$ and $N = 2$, respectively.

The energy shift at these turning point fields provide the maximum potential energy for molecules in these states in an electric field. From relating this to kinetic energy, the resulting maximum transverse capture velocity of any electrostatic multipole lens for the heavy BaF molecules ($m = 157$ amu) in these states is equal to 4.6 m/s and 8.6 m/s, corresponding to a maximum trap depth of 32 mK and 110 mK, respectively.

7.3. Design of the hexapole lens

Due to the shape of the low-field seeking Stark shift described above, molecules in a quadrupole field experience a linear restoring force in a regime of low field close to the molecular beam axis and thereby perform a harmonic oscillation. Molecules in higher fields further away from the axis will experience a reduced restoring force and will oscillate with a lower frequency that depends on the amplitude of their motion. In principle, a perfect lens can be constructed by using a large quadrupole and low voltage, however, the capture velocity of such a lens would be very small, making it ineffective.

As the orifice of the source and the spatial acceptance of the decelerator are both significant compared to a typical size of a multipole lens, some image distortion is acceptable for our purpose. To maximise the mapping into the acceptance region the ideal lensing for intermediate displacements is more important than for molecules close to the axis. Therefore, we have chosen to use a hexapole lens, which generates a linear restoring force for molecules in higher electric field occurring at larger displacements from the beam axis.

To maximise the velocity of the molecules that will be refocused by the lens, the electric field strength at the electrodes should be equal to the turning point field $E_{(n)}(r_0) = E_{tp}$. A higher maximum electric field strength would reduce the effective hexapole diameter. For a hexapole with inner radius of 6 mm, this optimal field strength for molecules in the $N = 1, |M_N| = 0$ is achieved at a voltage magnitude of 4 kV.

Figure 7.2 shows the electric field that is created by a hexapole formed by six hyperbolic electrodes to which alternating voltages of plus or minus 4 kV are applied. For ease of manufacturing, we use cylindrical rods which have a diameter of 6 mm and are placed with a minimal distance to the center of 6 mm. These rods are indicated by the grey circles in the figure. The use of cylindrical electrodes instead of hyperbolic electrodes introduces small

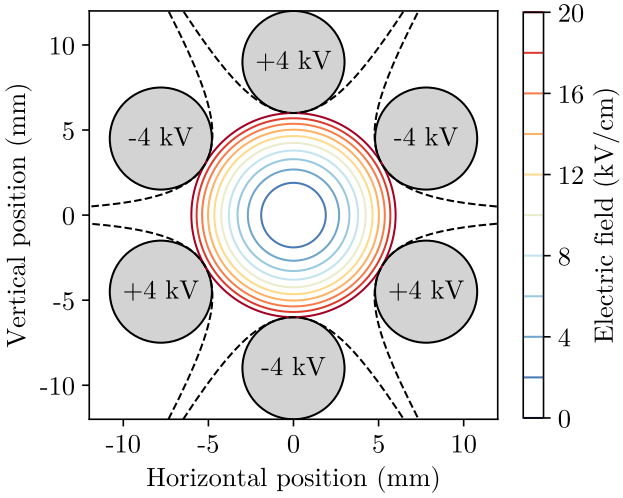

Figure 7.2 | *Electric field in an ideal hexapole with inner radius of $r_0 = 6\,\text{mm}$ and applied voltage magnitude of $\Phi_0 = 4\,\text{kV}$. The ideal hyperbolic electrodes are shown as black dashed lines, the grey circles show the practical implementation using cylindrical electrodes with a 6 mm diameter.*

deviations from the ideal field [69] with limited impact on our results[1].
An analytic description of the dynamics of particles in a hexapole lens system and the relations to properties known from optics can be found in Cho *et al.* [109]. To estimate the length scale of the system, the oscillation length can be considered,

$$l = 2\pi \frac{v_l}{\omega} = 2\pi\, v_l \sqrt{-\frac{m\, r_0^3}{6\mu_{eff}\Phi_0}}, \tag{7.5}$$

where v_l is the longitudinal velocity of the molecules. Here the linear fit to the Stark curve at maximum slope is used as was described before. For a molecule in the $N = 1, |M_N| = 0$ state in a hexapole with inner radius r_0 of 6 mm and applied voltage Φ_0 of 4 kV and longitudinal velocity of 184 m/s this corresponds to a half oscillation length of $l/2 = 594\,\text{mm}$. In the lower and higher field regimes the restoring force is smaller, resulting in a longer effective oscillation length.
The non-linearity of the Stark curve results in a spread of the molecular beam at the focus point of the hexapole lens, analogous to spherical aberrations in optical systems. These aberrations can in principle be compensated for by introducing a sequence of quadrupole and hexapole lenses as demonstrated by Everdij *et al.* [110], but this comes at a cost of increased complexity and reduced flexibility. The focus is further softened by the large velocity spread of our cryogenic buffer gas cooled molecular beam, analogous to chromatic aberrations in optical systems. Chromatic aberrations can be reduced by applying pulsed voltages to the hexapole rods as discussed by Ke *et al.* [111] (see also Crompvoets *et al.* [112]).

[1]The deviation from the ideal field is discussed in the appendix in section D.1

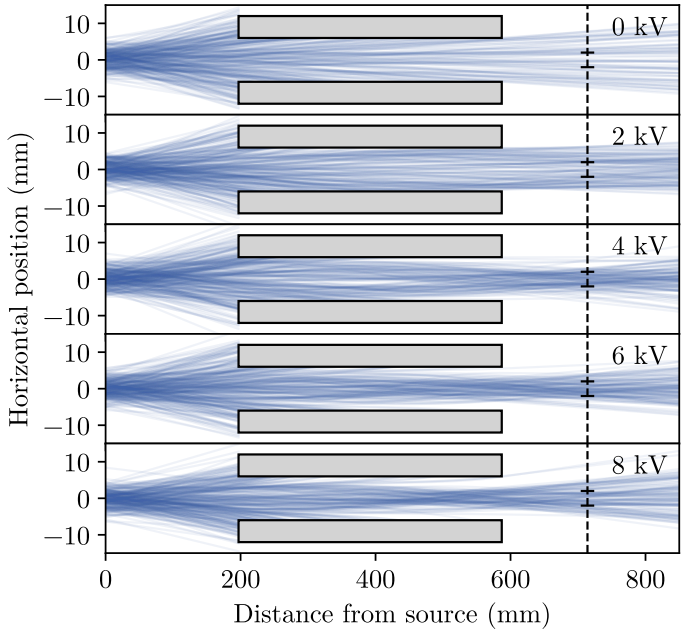

***Figure 7.3** | Simulated trajectories of barium fluoride molecules in the $N = 1, |M_N| = 0$ state for five different voltages applied to the hexapole electrodes as indicated. The position of the hexapole lens is indicated by the grey rectangles. The dashed black line shows the position of the detection zone aimed for in this experiment. The markings show the target region of 4 mm corresponding to the inner diameter of the decelerator. The initial distribution of the molecular beam is chosen to be only in the shown transverse direction for clarity. The transverse velocity spread is limited as molecules with higher velocity do not make it to the target region.*

To optimise the design and understand the behaviour of the hexapole lens a Monte Carlo trajectory simulation package has been developed. Figure 7.3 shows simulated trajectories for different applied voltage magnitudes to the hexapole lens, demonstrating the oscillation length of the system and the transverse spread of the molecular beam at the detection zone. In the simulated trajectories the previously described motion of the molecules through the lens can be seen. As understood from (7.5), the focal length decreases for increasing voltage. For voltages above 4 kV, molecules close to the electrodes experience an electric field that is beyond the turning point of the Stark curve and are being defocused. As a result, the effective inner diameter of the hexapole lens is reduced.

7.4. Methods

An overview of the setup consisting of a cryogenic source, hexapole lens and detection zone is shown in Figure 7.4. A render of the practical implementation of the setup can be found in Figure 7.5. The pulsed beam of barium fluoride molecules is produced in the cryogenic

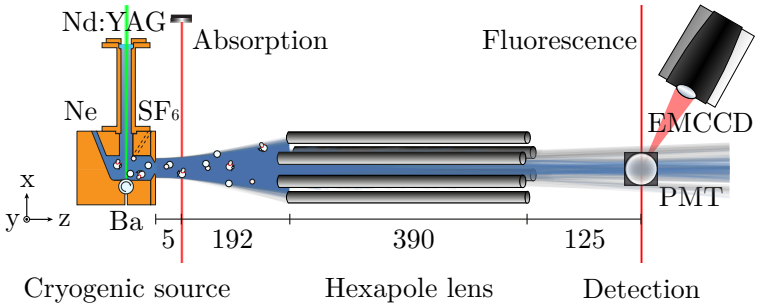

Figure 7.4 | *Experimental setup as seen from above with molecules traversing from left to right. Longitudinal distances are given in mm (not to scale). The pulsed molecular beam is produced in the cryogenic source, monitored with absorption, focused transversely by the hexapole lens and imaged using laser-induced fluorescence on a* PMT *above the molecular beam and on an* EMCCD *camera at a 60 degree angle from the molecular beam. The grey and blue lines show trajectories for molecules traversing the hexapole at an applied voltage of 0 and 4 kV, respectively.*

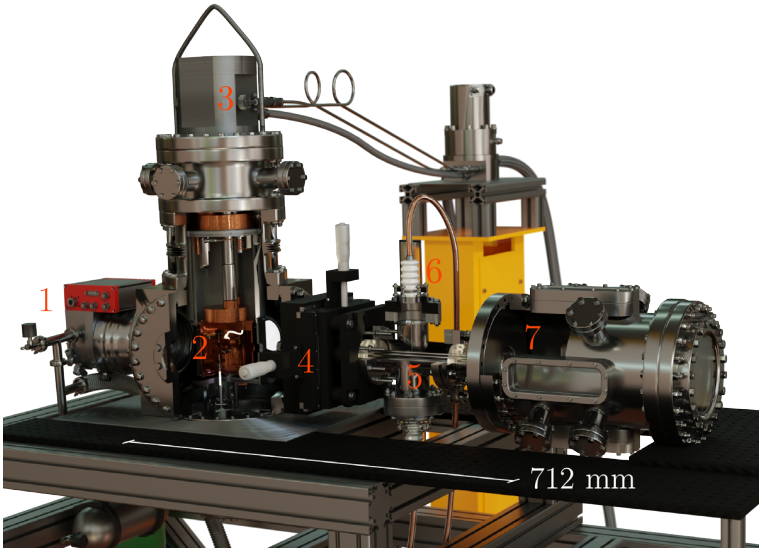

Figure 7.5 | *Render of the implementation of the setup described in Figure 7.4 with partial removal of vacuum chambers. The tube that holds the hexapole lens shown in the middle can be displaced using a manipulator, shown in black. The chamber used for fluorescence detection has been designed to enable transverse laser-cooling of the molecular beam close to the hexapole lens exit. The main components of the setup are labelled: (1) Turbopump, (2) copper cell, (3) cryo-cooler, (4) manipulator, (5) hexapole lens, (6)* HV *feed-through, (7) fluorescence detection chamber.*

source, in a copper cell cooled to 17 K. A rotating Ba metal target is ablated with a 5 ns pulse of 3-5 mJ in a 1 mm diameter focus from an Nd:YAG laser at a wavelength of 532 nm. The ablation product forms BaF molecules in a chemical process involving SF_6 gas. The molecules are cooled by collisions with a neon buffer gas and expand through the 4.5 mm diameter cell exit to form a molecular beam.

The molecular beam is monitored by absorption detection at 5 mm from the cell exit by passing through a retro-reflected 860 nm laserbeam probing the $X^2\Sigma^+(v = 0, N = 1)$ or $(N = 2)$ to $A^2\Pi_{1/2}(v' = 0, J' = 3/2)$ or $(J' = 5/2)$ transitions. The returning laserlight is captured on a photo-diode (Thorlabs PDB210A) and digitised on an analog-to-digital converter (Picoscope 5444D) with a time resolution of 400 ns. A typical time of flight profile is shown as the blue curve in Figure 7.6. The laserlight for detection is produced by a Ti:Sapphire laser (MSquared SolsTiS PSX-XF) pumped by a diode-pumped solid-state laser (Lighthouse Photonics Sprout-D) and locked to a wavelength meter (HighFinesse WS8-2). The wavelength meter data is also read out and stored with the molecule signal to be used in spectroscopy measurements.

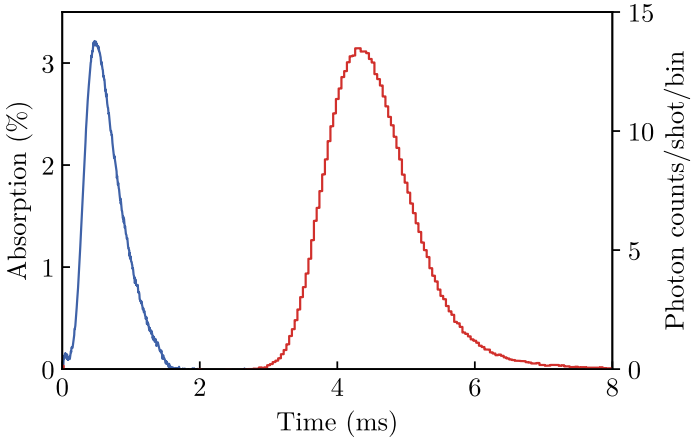

Figure 7.6 | *Time of flight profiles of the pulsed molecular beam at 5 and 712 mm from the cell exit measured by absorption (blue curve) and fluorescence (red curve) detection respectively. The double-pass absorption percentage is averaged over 40 μs, the fluorescence photon arrival times are presented in 40 μs bins. In total this corresponds to ~500 photons per shot captured on the* PMT.

After a total free-flight of 197 mm the molecules enter a hexapole lens with an inner diameter of 12 mm, consisting of six cylindrical rods of 6 mm diameter and 390 mm length connected in an alternating pattern to a positive and negative high voltage supply, as is shown in Figure 7.2. The hexapole rods are made from stainless steel. The hardness of this material allows its surface to be highly polished which minimises discharges. The electrodes are suspended by acrylic glass discs with increased path length along the surface, again to minimise discharges [101]

After another 125 mm of free-flight the molecular beam intersects the perpendicular probe laser sheet and laser-induced fluorescence is detected at the same transition as absorption.

The laser sheet has a 22 mm height with flat-top intensity profile, and a 0.3 mm Gaussian full width at half maximum (FWHM). For time sensitive measurements, the fluorescence light is captured on a photomultiplier tube (PMT, Hamamatsu HS7421-50) mounted orthogonally to both the molecular beam axis and the laser beam. The PMT has an effective solid angle $\Omega/4\pi = 2.2 \times 10^{-3}$ and quantum efficiency of 8.5%. Single photon pulses captured on the PMT are extended and recorded on the same analog-to-digital converter as used for absorption. Pulse detection software records the arrival time of these photons with a 400 ns time resolution resulting in a time of flight profile as shown as the red curve in Figure 7.6. From these time sensitive measurements the longitudinal velocity is deduced to be 184 m/s with a Gaussian FWHM spread of 64 m/s, which is used as an input for the simulations.

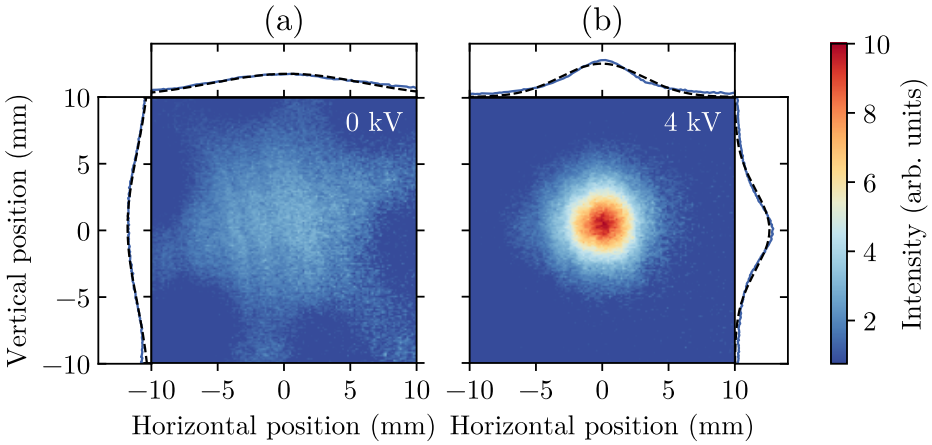

Figure 7.7 | *Images of the cross section of the molecular beam at the detection zone (a) without voltage and (b) with near optimal voltage applied to the hexapole lens (4 kV). The molecules are imaged by laser-induced fluorescence captured on an EMCCD camera, probing molecules in the $N = 1, J = 3/2$ ground state. The projections along each orthogonal axis (blue curves) are shown together with Gaussian fits (black dashed-line). In (a) the free-flight of the molecular beam is only obstructed by the electrodes, resulting in the six shadows. From these shadows it follows that the hexapole is mounted at a ~10 degree angle compared to Figure 7.2. Note that the hexapole lens was unintentionally rotated by ~10 degrees while moving the setup, which is clearly visible in the image. Due to the symmetry of the lens, this rotation does not affect the measurements.*

Fluorescence light is also captured on an electro-multiplying charged-coupled device (EMCCD camera, Andor iXon DU897) in the plane of the molecular and laser beam at an angle of 60 degrees from the molecular beam axis. This angle was chosen to avoid the background radiation originating from the afterglow of the barium target, which could not be sufficiently suppressed by using narrow-band filters (Semrock FF01-860/11-25). The angle is compensated for by scaling the horizontal axis in post processing. A slight trapezoidal distortion of the image is neglected. To verify this simplification the horizontal and vertical projections are considered separately in the analysis presented in this paper showing equivalent results.
To capture a signal image on the camera, a time window from 2 to 8 ms after the ablation

pulse is used, as this is when the molecules traverse the laser sheet as shown in the time of flight in Figure 7.6. To compensate for the significant readout background counts in the camera, a background image is taken when no molecules are present and subtracted from the signal image. The timing is incorporated in the measurement sequence controlled by the delay generator (Berkeley Nucleonics Model 575). Typically an image presented here consists of the average over 1000 shots, which corresponds to 100 seconds of data taking. An example of a molecular beam image is shown in Figure 7.7.

7.5. Spectra with and without hexapole lens

In Figure 7.8, spectra recorded using the PMT are shown of the transitions from the $X^2\Sigma^+(v = 0, N = 1)$ to the $A^2\Pi_{1/2}(v' = 0, J' = 3/2)$ with the hexapole lens off (blue data points) and at a voltage magnitude near the optimal focus (red data points). In these measurements, the laser power in the sheet is 35 μW and the linewidths of the observed transitions are limited by residual Doppler broadening. Four main peaks, corresponding to transitions originating from the four hyperfine components in the ground state, are easily distinguishable. Three of these peaks are further split due to hyperfine structure in the excited state. The dashed blue and red lines are the result of a fit using multiple Voigt profiles. The position and intensity of the lines correspond well to those predicted by PGOPHER using the molecular constants from Ernst *et al.* [67], Ryzlewicz *et al.* [66], Steimle *et al.* [113] and Marshall *et al.*[114]. The transitions are labelled 1 to 7 for ease of reference. The zero point of the frequency axis is set at the $X^2\Sigma^+(v = 0, N = 1, J = 3/2, F = 2)$ to the $A^2\Pi_{1/2}(v' = 0, J' = 3/2, F' = 2)$ transition at 348668610 MHz[2], labelled 2 in the figure.

When a voltage is applied to the hexapole, molecules in a low-field seeking state are focused into the detection zone, while molecules in a high-field seeking state are defocused. As a result, the intensity increases or decreases based on the distribution of low- and high-field seeking components of the ground state that is probed in the transition.

We will now discuss the effect of the hexapole lens on the different transitions. Transitions 5 to 7 originate from the $N = 1, J = 1/2, F = 0, 1$ states which are high-field seeking. Consequently, when voltage is applied to the hexapole, the intensity of these transitions decrease as expected. Transition 1 probes the $|M_F| = 0, 1$ components of the $N = 1, J = 3/2, F = 2$ which are low-field seeking. Consequently, when voltage is applied to the hexapole, the intensity increases. Transition 2, 3 and 4 probe a mix of low-field and high-field seeking states. The intensities depends strongly on the angle between polarisation of the light and the magnetic field.

Besides being more intense, the width (FWHM) of transition 1 and 2 is also increased, from 6.1 MHz to 7.7 MHz, as a result of the increased velocity spread of the focused molecules. The observed linewidths correspond to velocity spreads of 5.2 m/s and 6.6 m/s, respectively.

In Figure 7.9 similar spectra are shown of the transitions from the $X^2\Sigma^+(v = 0, N = 2)$ to $A^2\Pi_{1/2}(v' = 0, J' = 5/2)$, both with the hexapole lens off (blue data points) and at a voltage magnitude near the optimal focus (red data points). Again four main peaks, corresponding to transitions originating from the four hyperfine components in the ground state, are easily distinguishable. The hyperfine structure in the excited state is unresolved in this measurement.

[2]The offset of these spectra are determined based on PGOPHER simulations of the molecule based on literature and the absolute frequencies from Mooij *et al.* [92]

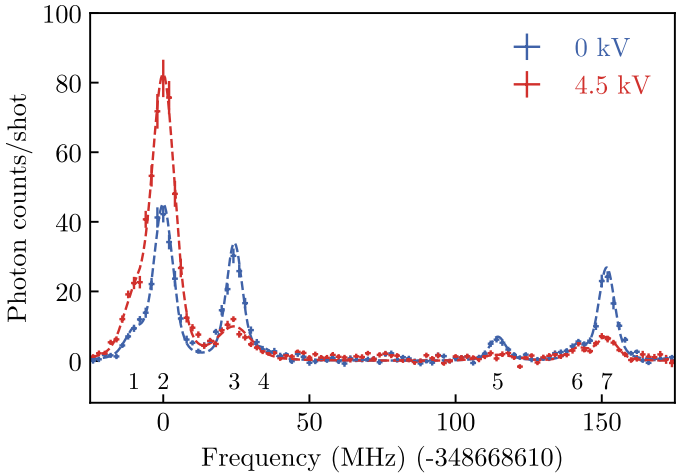

***Figure 7.8** | Spectra of the $X^2\Sigma^+(v = 0, N = 1)$ to $A^2\Pi_{1/2}(v' = 0, J' = 3/2)$ transition at a binsize of 1 MHz with the hexapole lens off (blue datapoints) and at a voltage magnitude near optimal focus (red datapoints). The dashed blue and red lines result from a fit using multiple Voigt profiles. Seven transitions are expected in this frequency range, which are labeled for ease of reference.*

The transitions are labelled 8 to 14 for ease of reference. The zero point of the frequency axis is set at the $X^2\Sigma^+(v = 0, N = 2, J = 5/2, F = 2)$ to the $A^2\Pi_{1/2}(v' = 0, J' = 5/2, F = 3)$ transition at 348670640 MHz^2, labelled 9 in the figure.
The $N = 2$ state contains components that increase in energy ($|M_N| = 0$), stay approximately constant ($|M_N| = 1$) or decrease in energy ($|M_N| = 2$) when the electric field is increased. Transitions 8 and 9 originate mainly from low-field seeking states, transitions 10-12 originate mainly from $|M_N| = 1$ states, while transitions 13 and 14 mainly target high-field seeking states. Indeed, when applying voltages to the hexapole, peaks 8 and 9 are broadened and become more intense compared to the situation when no voltage is applied. The intensity of peaks 13 and 14 is reduced when voltage is applied, while the intensity of 10-12 remains approximately the same.

7.6. Molecular beam widths and intensities

To examine the performance of the hexapole lens the beam characteristics have been measured at 712 mm from the cell exit, at the position where the molecular beam will enter the traveling-wave Stark decelerator [44]. For these measurements, the laser frequency was kept fixed at transition 2 or 8, while the power of the laser sheet was increased to 700 μW. At this intensity, the lines are broadened to about 25 MHz, which is sufficiently large to detect molecules independent of their transverse velocity. In this case several transitions are addressed simultaneously. For $N = 1$, transition 1-4 contribute, which implies that all 8 components of the $N = 1, J = 3/2$ are detected, of which 4 are low-field seeking ($|M_N| = 0$) and 4 are high-field seeking ($|M_N| = 1$). For $N = 2$, transition 8-12 contribute, which implies that all 12

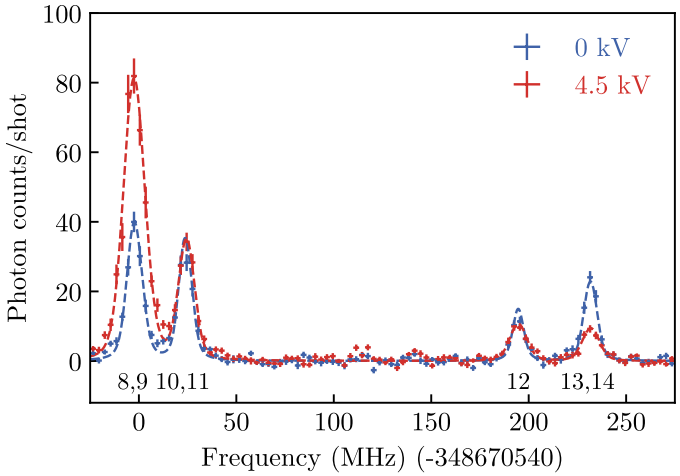

Figure 7.9 *| Spectra of the $X^2\Sigma^+(v = 0, N = 2)$ to $A^2\Pi_{1/2}(v' = 0, J' = 5/2)$ transition at a binsize of 2 MHz with the hexapole lens off (blue datapoints) and at a voltage magnitude near the optimal focus (red datapoints). The dashed blue and red lines result from a fit using multiple Voigt profiles. Seven transitions are expected in this frequency range, which are labeled 8 to 14 for ease of reference. The hyperfine structure in the excited state is unresolved in our measurement. The unassigned peaks correspond to transitions in $^{137}Ba^{19}F$.*

components of the $N = 2, J = 5/2$ are detected, of which 4 are low-field seeking ($|M_N| = 0$), 4 are high-field seeking ($|M_N| = 2$) and 4 are in between ($|M_N| = 1$).

Figure 7.10 shows the effect of variation of the hexapole voltage on the molecular beam both from simulations (a) and imaging on the EMCCD camera (b). It shows an increasing focusing effect up to 4 kV, after which the intensity starts decreasing and the beam starts to expand. As discussed in section 7.2, this corresponds to under- and overfocusing with a soft-focus behind or in front of the detection point, respectively. When a voltage of 2 kV is applied, the molecular beam is collimated. At this voltage, a vague donut shape can be observed in the recorded image caused by spherical aberration of the lens. The donut is washed out by the longitudinal velocity spread in the molecular beam.

Figure 7.11 shows the Gaussian FWHM beam width of the molecular beam projections as well as the prediction from the simulation for both the (a) $N = 1, J = 3/2$ and (b) $N = 2, J = 5/2$ states. The beam projections are found by integrating the images over the horizontal or vertical axis, corresponding to the axis along the laser sheet and orthogonal to it respectively. Examples of these projections and the corresponding Gaussian fits are shown in Figure 7.7. The beam projection along the horizontal (blue data points) and vertical axis (red data points) are presented separately. The error bars represent the uncertainty in the least squares fit. As the widths along both directions are the same within the error, the method used for compensating the camera angle is validated. Furthermore, this confirms that the intensity of the laser sheet is sufficiently homogeneous and that all Doppler components of the molecular beam are detected equally.

The solid lines also shown in Figure 7.11 result from trajectory calculations, using as input

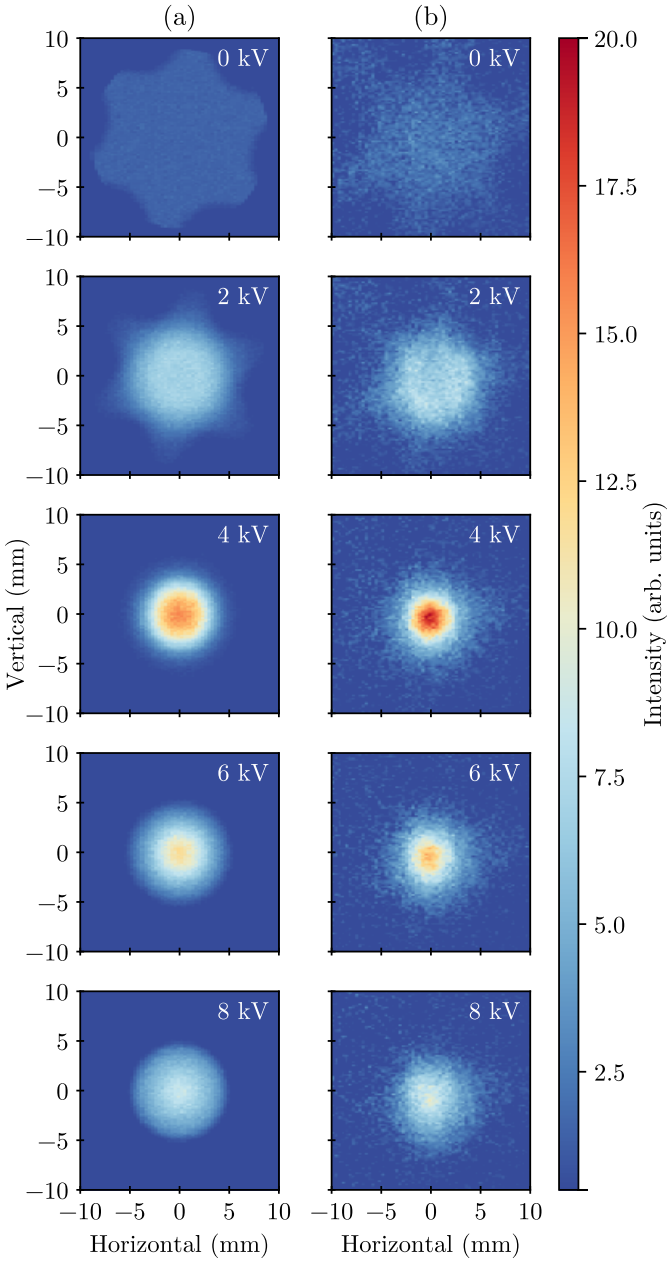

Figure 7.10 | *Transverse spread of molecular beam in the $N = 1, J = 3/2$ at the detection zone for different voltages applied to the hexapole electrodes from simulations (a) and measurements (b). All images are converted to the same color scale.*

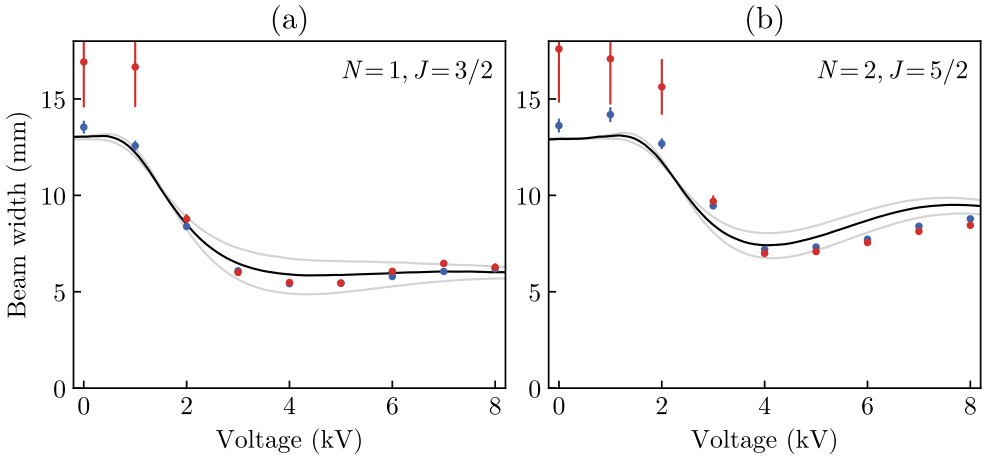

Figure 7.11 *| Gaussian FWHM of the molecular beam at the detection zone for molecules in the $N = 1, J = 3/2$ (a) and $N = 2, J = 5/2$ (b) states as function of the voltage magnitude applied to the hexapole. The beam projection along the horizontal (blue) and vertical axis (red) are presented separately. The solid lines show the prediction from trajectory calculations, for an initial FWHM beam width of 6 mm (black), 4.5 and 7.5 mm (grey).*

the longitudinal velocity distribution from the measured time-of-flight profiles shown in Figure 7.6 and the transverse velocity spread taken from the absorption spectrum measured directly behind the source. The initial transverse spread, corresponding to the size of the molecular beam at the so-called freezing plane, from where collisions in the molecular beam are negligible [115], is a priori not known and is a free parameter. The black line is simulated using a Gaussian FWHM position spread of 6 mm (black) while the grey curves are calculated using a spread of 4.5 and 7.5 mm. As our cryogenic buffer gas source is operated in the regime between supersonic and effusive expansion, an effective beam diameter slightly larger than the 4.5 mm cell aperture seems reasonable [116].

Figure 7.12 shows the beam intensities integrated over a 4 mm diameter circular area around the center of the molecular beam for different voltage magnitudes applied to the hexapole lens, for molecules in (a) the $N = 1, J = 3/2$ and (b) the $N = 2, J = 5/2$ states. Again the result for trajectory simulations is shown as a solid line, with the same initial beam widths at the freezing plane as in Figure 7.11. The contributions of the $|M_N|$ components are simulated separately and shown for the 6 mm initial beam width as colored dashed lines in Figure 7.12. The detected transitions probe ground states with equal contributions of each of the $|M_N|$ components, corresponding to equal contributions to the integrated intensity when the hexapole lens is off. The maximum intensity gain for molecules in the low-field seeking $N = 1, |M_N| = 0$ component is 12, reached at an applied voltage magnitude of 3.7 kV, close to where the electric field strength at the electrodes is equal to the turning point field E_{tp}. Note that the signal is normalized to the observed signal at zero voltage with equal contribution from all $|M_N|$ levels, while the signal observed at the optimal voltage originates predominately from molecules in the $|M_N| = 0$ level.

For molecules in the low-field seeking $N = 2, |M_N| = 0$ component, a similar maximum gain

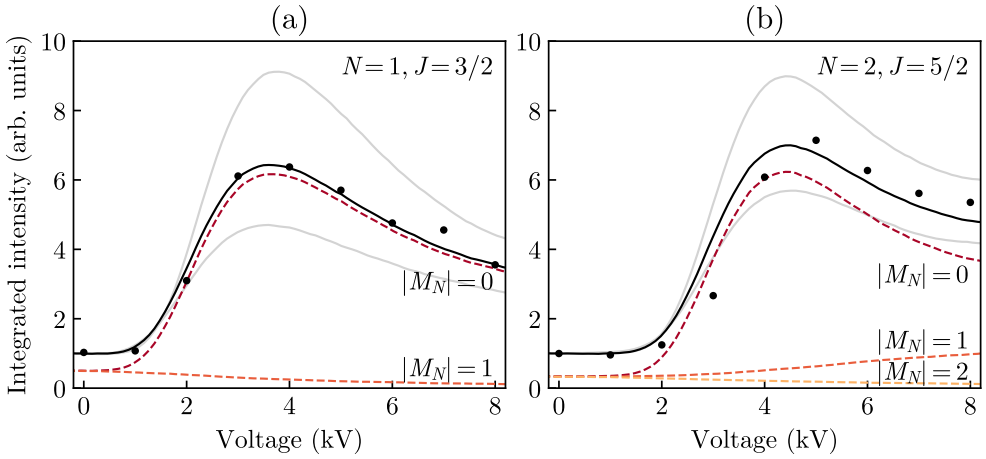

Figure 7.12 | *Intensity of a beam of molecules in (a) the $N = 1, J = 3/2$ and (b) the $N = 2, J = 5/2$ state integrated over a 4 mm diameter circular area as function of the voltage applied to the hexapole lens. The solid lines result from trajectory calculations for an initial beam with a FWHM transverse position spread of 6 mm (black), 4.5 and 7.5 mm (grey). The dashed lines correspond to the contributions of the different M_N components to the simulation shown in black.*

factor is found, despite the ∼2 times larger capture velocity which should result in a ∼4 times larger gain factor. At the voltage at which the maximum gain is obtained, the electric field at the electrodes is well below the turning point field E, for which a voltage of 11.4 kV has to be applied. However, in this case, the focal point for this hexapole lens lies before the detection zone. A hexapole lens aimed for molecules in the $N = 2$ should have a shorter length than the current one, designed for molecules in the $N = 1$. Alternatively, the effective hexapole length could be adjusted with pulsed voltages as for example is done in [105].

7.7. Beam deflection and alignment

The tube that holds the hexapole lens can be moved relative to the source chamber by a XY-manipulator (Hositrad HMC1000). In this way the hexapole lens can be moved in both transverse directions separately, orthogonal to the molecular beam axis. Figure 7.13(a) shows the horizontal distribution of the molecular beam at the detection zone after traversal of the hexapole lens for different displacements of the manipulator along the horizontal axis. In these measurements a voltage of 4 kV was applied to the hexapole. The displacement of the center of the beam is found from a Gaussian fit to these projections and is plotted in Figure 7.13(b).

As observed and expected, the beam displacement is linear with the displacement of the manipulator, with a translation factor of 0.93(2). The beam can be displaced by several millimeter without severe intensity loss. The intensity decrease at increasing displacement is consistent with the diameter of the molecular beam determined from the measurements

shown in Figure 7.11. Similar results have been obtained for the vertical displacement. The ability to move the beam can be used to fine-tune the alignment between the source and the downstream setup, such as a traveling-wave Stark decelerator.

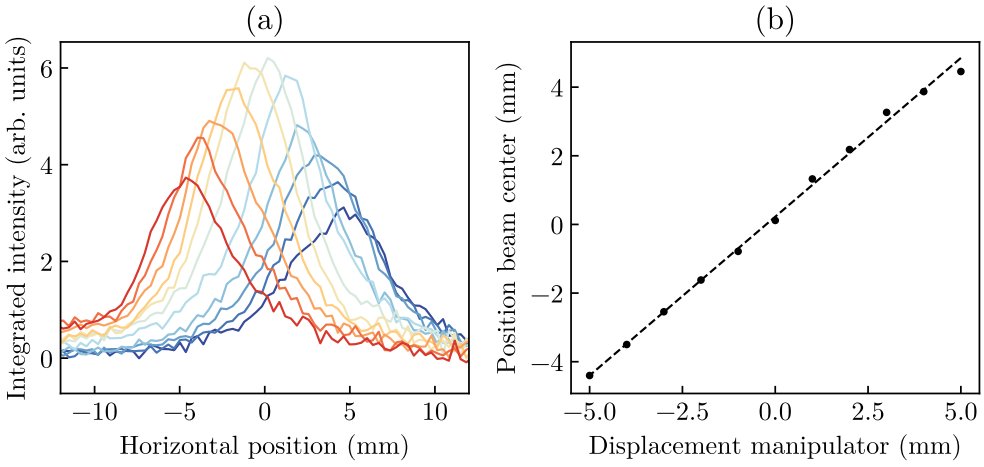

Figure 7.13 | *Horizontal translation of the molecular beam when the hexapole lens is moved using a manipulator. (a) The projection of the full beam onto the horizontal axis with the hexapole lens being displaced in steps of 1 mm. (b) The resulting center position of the beam found from a Gaussian fit to the projections (data points). The linear fit (dashed line) shows a translation factor of 0.93(2) over a range of 10 mm.*

7.8. Conclusions and outlook

We demonstrate that beams of barium fluoride molecules can be focused using a hexapole lens. State selective imaging based on laser-induced fluorescence captured on an EMCCD camera is used to record the spatial distribution of the molecules. It is shown that the number of molecules in the $N = 1, |M_N| = 0$ state reaching a 4 mm diameter target area at a distance of 712 mm from the source is increased by a factor of 12, limited by spherical aberrations caused by the non-linearity of the Stark curves and the low capture velocity. In addition, we demonstrate that the molecular beam can be displaced by up to ±5 mm by moving the hexapole lens.

The main motivation for this work is to increase the number of molecules that enters our traveling-wave Stark decelerator. In previous experiments [62], there was a 370 mm gap between the cryogenic source and the decelerator to allow for separation of the source and decelerator chambers by a vacuum valve. By free-flight propagation of the initial beam distribution, it can be calculated that, for BaF in the $N = 1, |M_N| = 0$ state, this gap results in a factor of 2.6 loss in number of molecules in the transverse phase-space acceptance of the decelerator. For molecules with a larger Stark shift and lower mass, the decelerator has a larger acceptance resulting in a greater loss at the same distance. By implementing a hexapole the gap was increased to 712 mm, resulting in a loss factor of 7.7 when no voltages

are applied. From our trajectory calculations we find that, at the optimal voltage, the number of molecules that fall on the transverse phase-space of the acceptance is increased by a factor of 6.5. Consequently, with a hexapole, the loss factor is only 1.2. Or equivalently, 84% of the maximum molecular beam intensity, that would occur for zero separation between the source and decelerator, is regained by the hexapole lens. Compared to the minimal distance of 370 mm given by practical limitations a factor of 2.5 is gained.
Increasing the distance between the beam source and decelerator from 370 mm to 720 mm results in an increase of the longitudinal phase-space matching by 5% in experiments where molecules are decelerated from 200 m/s to 30 m/s in 4.5 m. For a more significant increase, the distance would need to be increased to several meters [78].
The level structure of BaF allows for laser-cooling [93, 94, 117]. An exciting prospect is to combine electrostatic lenses, that provide a force that depends only on the transverse position of the molecules, with laser-cooling techniques, that provide a force that depends only on the transverse velocity of the molecules. In this way, beams are both cooled and focused. The resulting dense and cold beam of molecules can be used for precision tests directly, or as input for a Stark decelerator.

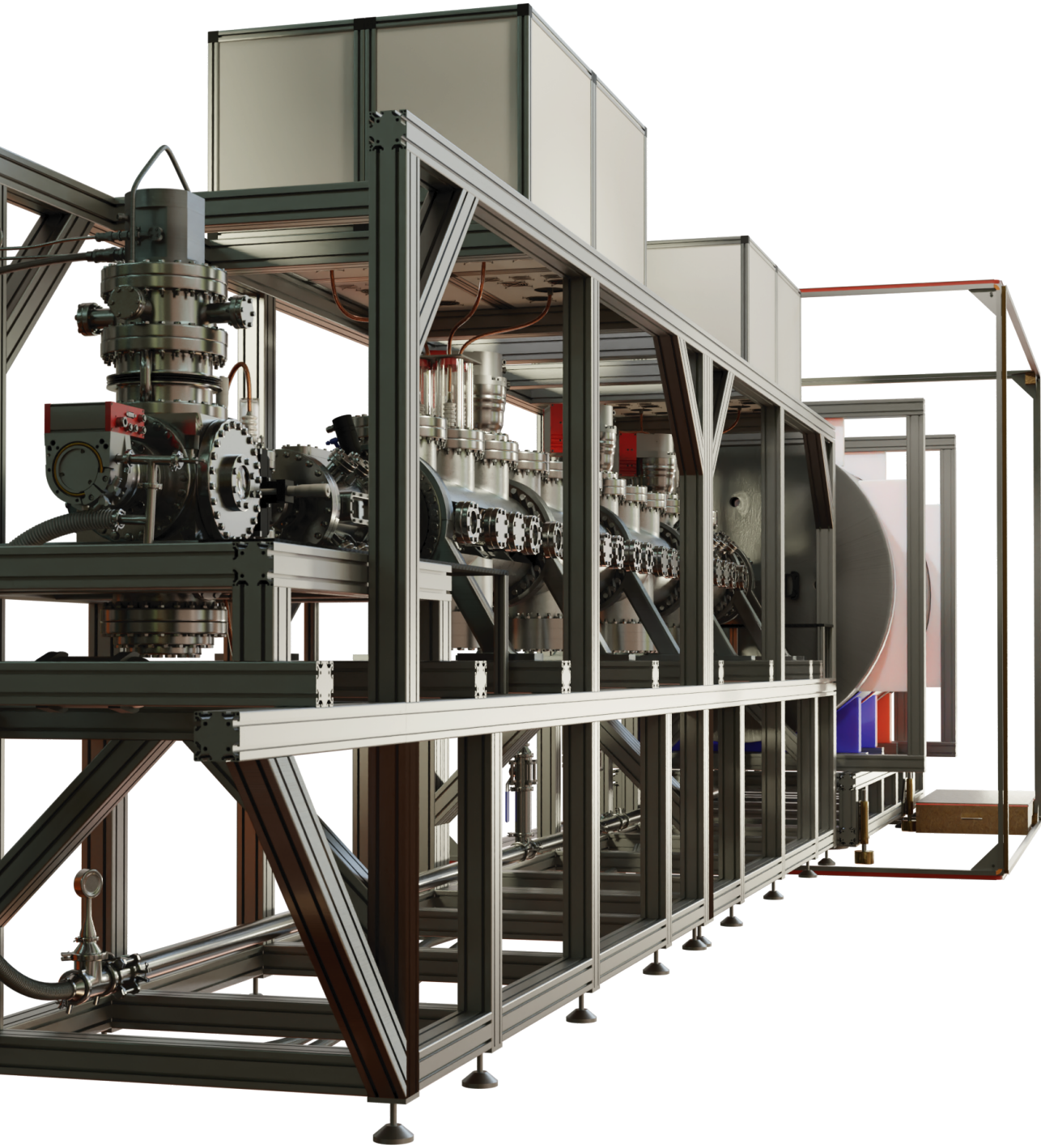

8

Summary and outlook

In this thesis contributions to many aspects of the NL-eEDM project have been discussed. In this chapter these will be summarised, linked together and the lessons learned are revisited in an outlook for possible future improvements to the experiment.

8.1. Summary

Precision measurement on molecules form a sensitive probe for beyond the Standard model physics. In particular, measurements on the electric dipole moment (EDM) of fundamental particles provide a limit on processes violating parity (P) and time-reversal (T) symmetry. Typically, the combined symmetry of parity with charge conjugation (C) is considered, which is also violated by these electric dipole moments.
These limits on electric dipole moments restrict the parameter space for extension of the CP violating sector of Standard model. This despite the cosmological observations of imbalance between matter and anti-matter in the universe, which requires sources of CP violation beyond the ones currently known.
Molecules such as barium monofluoride (BaF) provide an enhanced sensitivity to the CP violating interactions of the electron electric dipole moment (d_e) and the scalar-pseudoscalar electron-nucleon interaction (C_S). In **chapter 1** the relation between electric dipole moment searches and CP violating physics is reviewed. The double-differential measurement of the energy difference between magnetic hyperfine-sublevels via a Ramsey interference method is discussed. The measurement is performed in parallel and anti-parallel magnetic and electric field, where the difference in accumulated phase after exclusion of systematic biases is attributed to the CP violating electric dipole moment.
The context of the NL-eEDM experiment in the active field of electron electric dipole moment searches is discussed, illustrating its approach of a measurement on a intense and slow

The chapter image shows the proposed setup for the NL-eEDM experiment, with the decelerator setup combined with the spin-precession setup to measure the electron electric dipole moment on a slow and intense molecular beam.

molecular beam to be able to reach a competitive statistical uncertainty.
In **chapter 2** a more detailed description of the measurement sequence is given based on the experiment performed on a pulsed supersonic beam of BaF molecules. An analytic model for the spin-precession spectrum is derived showing the dependence on many experimental parameters. This demonstrates the many parameters that have to be measured or controlled to achieve an accurate measurement of the electric dipole moment.
The data acquisition and control system developed for this experiment is discussed in **chapter 3**. The system is designed to be adaptable and robust based on its modular nature in a network of devices and software. This modular framework follows the shot-based time structure of the experiment.
The control system is designed around a switch sequence of different states of the setup. The switching procedure is demonstrated by the switching between electric field orientations.
To reach a meaningful statistical sensitivity to the electron electric dipole moment within a reasonable measurement time the NL-eEDM experiment is proposed to be performed on a slow and intense beam of BaF molecules. This beam is to be produced in a combination of a cryogenic buffer gas source and a traveling-wave Stark decelerator. By the increase in molecular flux and interaction time this is expected to increase the statistical sensitivity of the experiment by orders of magnitude compared to the currently used supersonic beam.
In **chapter 4** the phase-space acceptance of the traveling-wave Stark decelerator is reviewed for guiding and deceleration of SrF and BaF molecules in the lowest rotational states of the $X^2\Sigma^+(v = 0)$ electronic and vibrational groundstate. The limitations to the acceptence are shown, especially how it is reduced by the higher mass of BaF. It has been shown how the transverse phase-space matching between the cryogenic source and decelerator is improved by installation of a hexapole lens.
In **chapter 5** improvements to the decelerator setup have been demonstrated by the continuation of measurements on strontium monofluoride (SrF) molecules. The improvements can be divided in four main categories:

(1) The source reliability and ease of maintenance have been improved by the replacing the target rotation mechanism.
(2) The data acquisition system has been updated to have synchronisation between data-streams and to provide access to background data on the state of the setup.
(3) The intensity of the decelerated molecular beam has been increased by improved phase-space matching between the source and the decelerator using a hexapole lens.
(4) The waveform applied to the decelerator has been altered to mitigate losses of slow molecules exiting the decelerator.

The transition to the heavier barium monofluoride (BaF) is demonstrated in **chapter 6**. A characterisation of the molecular beam produced in the cryogenic buffer gas source is presented, regarding the relevant parameters for the combination with the traveling-wave Stark decelerator. The first results for the Stark deceleration of BaF are presented.
A hexapole lens is used to improve the phase-space matching between the cryogenic buffer gas source and traveling-wave Stark decelerator. This hexapole lens is characterised in **chapter 7** by imaging of the molecular beam on an EMCCD camera. The achieved focusing of the molecular beam and associated beam intensity increase are explained using numerical trajectory simulations.

8.2. Discussion and outlook

To increase the sensitivity of the NL-eEDM experiment multiple improvements can be considered, many of which are under active investigation by the NL-eEDM team at the time of writing.

8.2.1. Spin-precession setup with supersonic source

In this and related work [23, 37, 45] the development of a spin-precession experiment sensitive to the CP violating electric dipole moment, has been discussed based a pulsed beam om BaF molecules at a mean longitudinal velocity of 600 m/s, produced in a supersonic source. The interaction time T between the electric field plates of 750 mm long is on the order of 1 ms. Systematic effects that play a role in such an experiment are investigated. The systematic error on the EDM results from an asymmetry of the experiment performed in each of the relative field orientations, between which is switched in the measurement.
The first results for switching between opposite electric field configurations are shown in this work, showing the RC time constant of the switching between these configurations. This sets a lower-bound on the switching rate within a measurement run. To translate the systematic effects into a systematic uncertainty the stability of a variety of parameters at this timescale is to be investigated, for example using an Allan variance analysis.

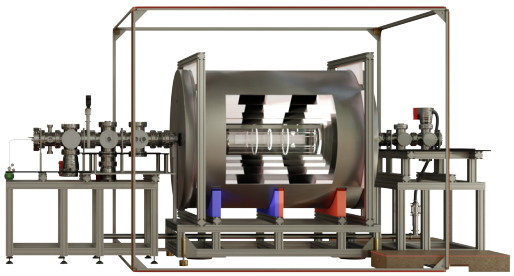

***Figure 8.1** | Illustration of the current spin-precession experiment setup for a molecular beam at 600 m/s from a supersonic source.*

By probing the molecules on a cycling transition and thereby detecting multiple photons per molecule, the sensitivity of the experiment can also be improved, as discussed in Boeschoten [23]. Also, an increase of the efficiency of the detection system is demonstrated to be beneficial. The excess noise factor $\sqrt{F}$ (Equation 1.9) is estimated for the current experiment to be 45. This reduces the statistical sensitivity significantly from the quantum projection limit (Equation 1.8), demonstrating a clear direction for future improvement.
The statistical sensitivity of the current experiment is estimated in Boeschoten [23] to be,

$$\sigma_{d_e} \approx 1.4 \times 10^{-25}\ e\ \mathrm{cm}\sqrt{\mathrm{day}}, \tag{8.1}$$

based on typical fluorescence signal of 100 photons per shot, corresponding to $N = 10^5$ molecules per pulse, and a polarization $P(E) = 0.35$ for an electric field strength of 5 kV/cm, the maximum currently achievable with the field plates at 4 cm separation. The estimate

for the number of molecules per pulse contributing to the spin-precession experiment is slightly higher than the estimate based on Aggerwal *et al.*, which states a molecular yield of 6×10^8 molecules per sr per pulse in the $X^2\Sigma^+(v = 0, N = 1)$ state and a rotational temperature of 3.5 K. The solid angle of the pulse contributing to the measurement is assumed to be limited in this experiment by the detection lasersheet of 10 mm tall, positioned 3820 mm from the gas nozzle in the source [37], resulting in a solid angle of $5{\times}10^{-6}$ sr.

At the time of writing, the distance between the electric field plates in the interaction zone has been reduced from 4 to 2 cm, doubling the electric field amplitude. By applying a voltage amplitude of 10 kV on each plate an electric field of 10 kV/cm should be achieved, corresponding to a polarisation of the molecules $P(E)$ of 0.5 [34].
Thus far, the readout of the spin-precession experiments has been based on molecules projected back from the superposition into the $X^2\Sigma^+(v = 0, N = 0, F = 0)$, or remaining in the orthogonal superposition in the $X^2\Sigma^+(v = 0, N = 0, F = 1)$. By probing both states in the same shot the asymmetry $A = (S_{F=0} - S_{F=1})/(S_{F=0} + S_{F=1})$ is measured in each shot, instead of being deduced via the contrast involving the average over the interference spectrum. This reduces the sensitivity to instabilities over the measurement run.
To find a limit on the EDM, a longer measurement run should be performed and analysed, to quantify both the systematic and statistical uncertainty. The experiment and incorporated data acquisition and control system have been demonstrated to be suitable for multi-day continuous measurement runs.
By improving the detection to reduce the excess noise factor to $\sqrt{F} \approx 1$, and increasing the electric field strength in the interaction zone such that $P(E) = 0.5$, the statistical sensitivity of this setup could be improved to,

$$\sigma_{d_e} \approx 2.2 \times 10^{-27}\ e\ \mathrm{cm}\sqrt{\mathrm{day}}. \tag{8.2}$$

8.2.2. Cryogenic source and transverse laser cooling

To improve both the molecular beam intensity and interaction time the supersonic source used in the spin-precession experiment can be replaced by a cryogenic buffer gas source. This source has been demonstrated to produce a molecular pulse containing $1.3(5){\times}10^{11}$ molecules per sr per pulse in the $X^2\Sigma^+(v = 0, N = 0)$ state [80].
Assuming again a constraint to molecules traversing a detection area of 10 mm tall at 3820 mm from the source exit, the solid angle of the molecular pulse contributing to the measurement remains 5×10^{-6} sr. The estimate for number of molecules per pulse partaking in the spin-precession experiment N is 7×10^5.
The molecular beam has a typical longitudinal velocity of 200 m/s, with a FWHM spread of 40 m/s. The pulse is approximately 0.2 m long when exiting the source and expands to 0.5 m after 2.5 m of free-flight to the end of the interaction zone.
When the superposition is created and projected back by counter-propagating laser pulses once the full molecular beam is within the interaction zone, the length of the pulse will reduce the effective interaction zone length to approximately 0.25 m. The resulting interaction time will again be approximately 1 ms.
To increase the interaction time and thereby the statistical sensitivity of the experiment, two spatially separated, transversely crossing laser beams can be used instead, as also used in the

EDM experiment on ThO by the ACME collaboration [41]. In this way the interaction time can be increased to 3 ms. Assuming a polarisation $P(E) = 0.5$ and detection with $\sqrt{F} \approx 1$, the statistical sensitivity such a setup is estimated to be,

$$\sigma_{d_e} \approx 2.7 \times 10^{-28}\ e\ \mathrm{cm}\sqrt{\mathrm{day}}. \tag{8.3}$$

The spatially separated superposition pulses change quite some of the interference signal characteristics relative to the timing-based pulses, which results in different systematic effects. In this case the molecules will traverse the same longitudinal region, reducing field homogeneity requirements. This comes at a cost of a variety of interaction times and traversal times of the superposition creation beams due to the significant relative longitudinal velocity spread of 0.2 of the molecules, resulting in a variety of accumulated phases $\omega_{EB}T$ and population transfers $\Omega_{PS}t$ respectively. These different systematics may even provide useful insights, especially when time selective detection is used to distinguish the signals from different velocity regimes.

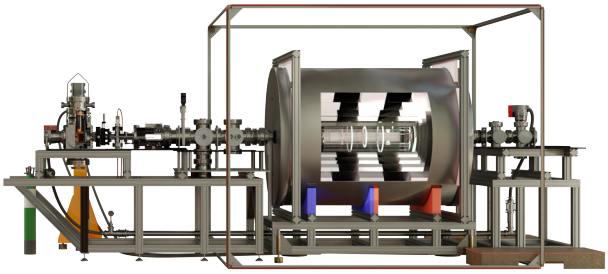

***Figure 8.2** | Concept sketch of a spin-precession experiment setup for a molecular beam at 200 m/s from a cryogenic buffer gas source, combined with a hexapole lens and transverse laser cooling.*

To increase the intensity of the molecular pulse contributing to the EDM experiment a hexapole lens and transverse laser cooling can be used to focus and then collimate the molecular beam. Laser cooling of BaF has been studied theoretically by Hao *et al.* [93] and demonstrated experimentally by Zhang *et al.* [94] and Rockenhäuser *et al.* [118].

Transverse laser cooling has been part of the proposed NL-eEDM experiment [44] to reduce the divergence of the decelerated molecular beam while traversing the interaction zone. It can also be used to collimate the converging beam focused in a hexapole lens.

In Figure 7.11 it was shown that the molecular beam can be focussed to a Gaussian FWHM of 6 mm. Molecules with a transverse velocity below 2 m/s are expected to be laser coolable to transverse velocities close to the Doppler limit in a reasonable interaction time of 1 ms, corresponding to >1000 photon scatters. As this transverse velocity is significantly below the hexapole acceptance v_{max} of BaF in the $X^2\Sigma^+(v = 0, N = 1)$ of 4.59 m/s, these molecules are expected to be focussed into a beam of width <10 mm, as can be used in the spin-precession setup. With a transverse velocity spread (FWHM) of 40 m/s in each direction this corresponds to 7×10^{-3} of the $1.9(6) \times 10^{10}$ molecules in the total pulse. Here the estimate for the number of molecules in the $X^2\Sigma^+(v = 0, N = 0)$ from Mooij *et al.* [80] is used, from the rotational

temperature the population in the $N = 1$ is expected to be similar. Half of the molecules are in a low-field seeking component of this state and therefore focussed by the hexapole lens. Based on the resulting number of molecules expected to contribute to the EDM experiment $N = 7 \times 10^7$, an interaction time $T = 3$ ms, polarisation $P(E) = 0.5$ and detection efficiency $\sqrt{F} \approx 1$, the statistical sensitivity of this setup is expected to be,

$$\sigma_{d_e} \approx 2.7 \times 10^{-29}\ e\ \mathrm{cm}\sqrt{\mathrm{day}}. \tag{8.4}$$

8.2.3. Longitudinal deceleration

To increase the interaction time further the traveling-wave Stark decelerator can be used to reduce the longitudinal velocity of the molecular pulse. In this work the first results for Stark deceleration of BaF has been presented. The proposed longitudinal velocity of 30 m/s for the NL-eEDM experiment [44] has not yet been achieved. However, deceleration from 200 m/s to 150 m/s, corresponding to half the kinetic energy, has been demonstrated in chapter 6, before the electronics broke down.
To enable the operation of the decelerator again, transformers are under development at the time of writing. These had already been planned as a replacement for the HV amplifiers used in this work, to be able to reach higher voltage amplitudes even up to 10 kV.
As an alternative, deceleration in a pulsed mode instead of a traveling-wave mode may be considered, as presented in Shyur *et al.* [77], which is significantly less demanding on the electronics.
The higher voltage amplitude is beneficial to the phase-space acceptance of the decelerator for BaF molecules in a higher rotational state $X^2\Sigma^+(v = 0, N = 2)$, as demonstrated in Figure 4.17. These molecules can be decelerated at higher electric field strength due to the higher turning point in the Stark curve.

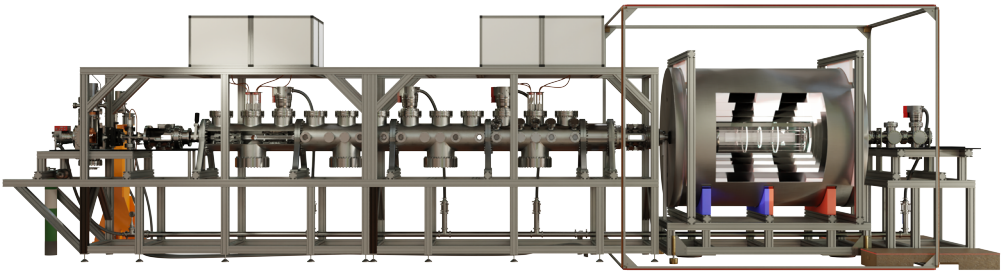

Figure 8.3 | *Concept sketch of a spin-precession experiment setup for a molecular beam at 30 m/s achieved by deceleration of a beam from a cryogenic buffer gas source, combined with a hexapole lens and transverse laser cooling.*

A hexapole lens has been demonstrated to improve the phase-space matching between the source and the decelerator, improving the efficiency of the latter. Possibly, transverse laser cooling can be used to reduce the transverse velocity spread, to get more molecules in the decelerator.
By longitudinal deceleration from 200 to 30 m/s the interaction time can increased by about an order of magnitude. The statistical sensitivity of the EDM experiment Equation 1.8

increases by doing so if in the process less than two orders of magnitude are lost in molecular beam intensity. From the phase-space acceptance of the decelerator discussed in chapter 5, reaching this efficiency may be challenging, even when molecules are decelerated in the $N = 2$ at a voltage amplitude of 10 kV. For a molecular beam experiment the decelerator may not turn out to be beneficial. To reach still longer interaction times, performing an EDM experiment on molecules in a fountain or a trap is considered. The decelerator can be used to prepare a slow molecular beam reflected into a fountain or loaded into a trap. In these experiments precession times can be reached far beyond that of beam experiments. As these experiments introduce completely different systematic effects however, an estimate for the sensitivity of these is beyond this outlook, but is in preparation in Bause *et al.* [119].

8.2.4. Polyatomic molecules

Another direction of improvement which is under investigation, is the transition to polyatomic molecules in the search for CP violating physics. These molecules that can be laser cooled, also allow for the existence of internal comagnetometer states, through the opposite parity states with small energy splitting in the bending mode [120]. These internal comagnetometer states provide sensitivity to the EDM within one field configuration, removing many systematic biases which play a role in an experiment based on field direction switching.
For the NL-eEDM experiment a barium based system would make sense because of the similarities to the currently used BaF molecules. The enhancement factor to the electron Electric Dipole Moment has been calculated for BaOH by Denis *et al.* [121] to be comparable to the enhancement for BaF. The Stark shift for BaOH enables full polarization of this molecule ($P(E) = 1$), at much lower electric field strengths than BaF. This increases the sensitivity to the EDM and reduces the experimental complications in achieving and switching this field strength. Steinebach [122] has demonstrated that this Stark shift makes BaOH also suitable for deceleration in the traveling-wave Stark decelerator. The linearity of the Stark shift makes it particular compatible with the hexapole lens and asymmetries between transverse and longitudinal trap field in the decelerator. The preliminary results for production of these molecules in a cryogenic buffer gas source obtained at the time of writing are promising [123].

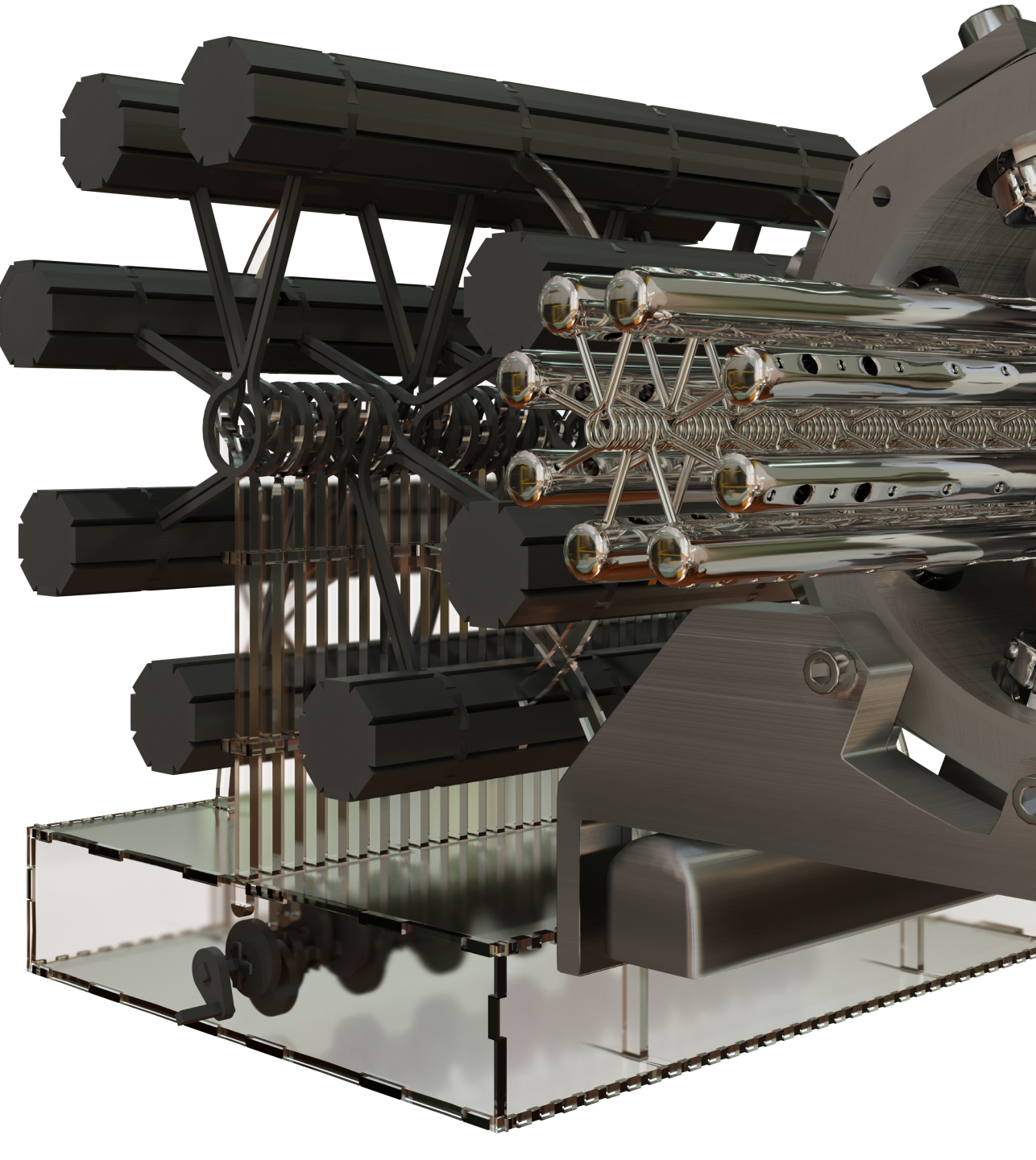

9

Nederlandse samenvattingen

Aangezien de auteur grote waarde hecht aan de toegankelijkheid van wetenschappelijke kennis voor iedereen, onafhankelijk van diens deskundigheid, is de Nederlandse samenvatting van dit proefschrift gesplitst in twee delen; een niet-deskundigen samenvatting en een wetenschappelijke samenvatting. In de eerste worden de basis principes die aan de grondslag liggen van dit werk demonstreert, voor in de tweede de resultaten van dit werk besproken worden.

9.1. Niet-deskundigen samenvatting

De vraag naar waar we vandaan komen is al eeuwen oud. Er zijn over de millennia vele antwoorden op gegeven, waarbij de meeste antwoorden het probleem alleen doorschuiven naar de volgende vraag. Als je het een natuurkundige vraagt, eventueel indirect door in diens proefschrift te lezen, dan krijg je waarschijnlijk een antwoord als dit:
Wij zijn, net als de wereld om ons heen, opgebouwd uit moleculen. Die moleculen zijn dan weer opgebouwd uit atomen, die op diens plaats weer opgebouwd zijn uit protonen, neutronen en elektronen. Protonen en neutronen zijn dan weer opgebouwd uit quarks, en dat is hoe ver we materie uit elkaar kunnen pluizen. Daarom noemen we deze deeltjes ook wel fundamentele deeltjes, de kleinste bouwstenen die we kennen. Hoe elke grotere structuur is opgebouwd uit de kleinere elementen wordt gegeven door de interacties tussen de elementen. Die interacties zijn te groeperen in vier krachten, de sterke en zwakke kernkracht, de elektromagnetische kracht en de zwaartekracht. Voeg hier nog een paar meer exotische vormen van materie aan toe, en negeer de zwaartekracht die nauwelijks een rol speelt op kleine schaal en je komt uit bij het Standaardmodel van deeltjesfysica. Dit model is erg succesvol in het beschrijven en voorspellen van bijna alle fenomenen die we tegenkomen. Toch is de theorie niet compleet, er zijn fenomenen die niet verklaard worden door het Standaardmodel. Het grootste teken dat

---

De afbeelding ter illustratie bij dit hoofdstuk toont het schaalmodel dat gebruikt wordt om de werking van de lopendegolf-Starkafremmer te demonstreren aan de hand van knikkers, naast een module van de afremmer zelf.

het incompleet is, is misschien wel dat de vierde kracht, de zwaartekracht, niet beschreven wordt door het model.
Ook geeft het Standaardmodel geen antwoord op de vraag waar de materie op grotere schaal vandaan komt. Op de grotere schaal, zo groot als het universum, speelt de zwaartekracht juist een dominante rol. Uit kosmologische observaties blijkt dat het universum aan het uitdijen is. Als je terug redeneert in de tijd kom je bij het moment dat het universum een punt was. Dit moment van het ontstaan van het universum noemen we de oerknal, en lijkt een logisch moment voor het ontstaan van materie.

Materie-antimaterie asymmetrie
Dat brengt ons bij het probleem waar het onderzoek waar dit proefschrift deel van is zich mee bezig houdt. De vraag lijkt misschien, hoe kan materie uit het niets ontstaan? Maar die vraag wordt juist goed beantwoord door het Standaardmodel. Het blijkt mogelijk om materie te doen ontstaan, als je maar genoeg energie hebt. Het probleem is dat in dit proces tegelijkertijd evenveel antimaterie ontstaat. En die antimaterie lijkt nergens te vinden.
Antimaterie komt zo weinig voor in onze directe omgeving dat je er mogelijk nog nooit van gehoord hebt. Het is opgebouwd uit antideeltjes, die erg vergelijkbaar zijn met hun deeltjes tegenhangers. Vele eigenschappen van deze tegenhangers zijn gelijk (zoals hun massa), maar andere zijn juist tegengesteld (zoals de elektrische lading).
Er zijn dus processen bekend waarbij materie ontstaat, maar daarbij ontstaat tegelijkertijd antimaterie. Er zijn ook tegengestelde processen, waarbij antimaterie verdwijnt, maar daarbij verdwijnt tegelijkertijd materie. Als de antimaterie zich niet ergens anders in het universum schuilhoudt, een theorie die weer nieuwe vragen met zich mee brengt, moet er een proces zijn dat de voorkeur geeft aan materie.

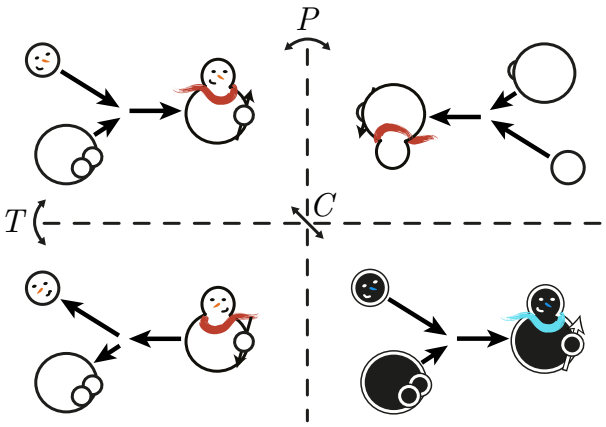

***Figuur 9.1** | Discrete transformaties van fundamentele interacties geïllustreerd aan de hand van de vorming van een sneeuwpop. De pariteittransformatie (P), tijdsinversie (T) en ladingconjugatie (C) zijn afzonderlijk afgebeeld. Als een interactie equivalent is aan de getransformeerde interactie noemen we deze symmetrisch.*

Een voorwaarde voor een dergelijk proces is de schending van CP-symmetrie. Deze symmetrie die de inversie van lading en van ruimtelijke coördinaten beschrijft is in veel gevallen behouden.

Dit betekent dat een proces en het getransformeerde proces zich hetzelfde gedragen. Een derde, gerelateerde symmetrie T, die tijdsinversie beschrijft, blijkt voor veel processen neer te komen op de combinatie van de andere twee.
Het Standaardmodel beschrijft, naast vele processen waarbij de CP-symmetrie behouden is, ook een proces dat deze symmetrie schendt. Dit proces is alleen onvoldoende om de grote disbalans tussen materie en antimaterie in het universum te verklaren. Daarom zijn we op zoek naar meer processen die de symmetrie schenden, die ons daarmee meer leren over de interacties van de materie om ons heen.

Meetmethoden voor symmetrie schendende processen
Er zijn verschillende, complementerende benaderingen voor het onderzoeken van de asymmetrie tussen materie en antimaterie. Het is mogelijk om materie en antimaterie te maken in hoog energetische processen, zoals wordt gedaan in grote deeltjesversnellers. Door bestuderen van de restproducten van een botsing van deeltjes met hoge snelheid wordt gezocht naar CP-schendende processen. Daarnaast wordt er gekeken naar hoog energetische processen van deeltjes die uit het universum de atmosfeer binnen vliegen.
Een derde benadering, zoals onder anderen gebruikt wordt door de NL-eEDM collaboratie, is minder direct gebaseerd op hoog energetische processen. Het blijkt dat een precisie meeting aan eigenschappen van fundamentele deeltjes dezelfde CP-schendende processen op de proef stelt.
Hierbij gaat het in dit werk specifiek over het elektrisch dipool moment van het elektron, afgekort eEDM. Deze eigenschap is analoog aan de magnetische dipool, met een noord- en een zuidpool. Dit dipool moment heeft naast een sterkte ook een richting, zoals een magnetisch kompas die een richting op wijst. Voor fundamentele deeltjes zoals het elektron moet deze richting wijzen langs de spin-as. Spin is een kwantummechanisch fenomeen vergelijkbaar met de klassieke draaiing, vandaar de naam.

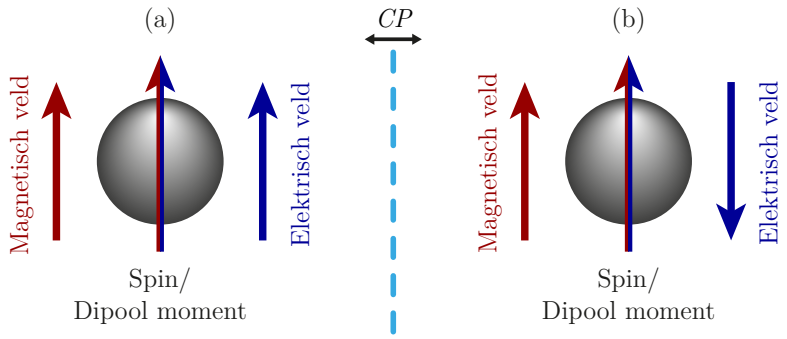

***Figuur 9.2** | Voor fundamentele deeltjes is de koppeling tussen een magnetisch veld en magnetisch dipool moment symmetrisch onder CP-transformaties. De koppeling tussen een elektrisch veld en elektrisch dipool moment is dat niet.*

Uit de symmetrie transformaties van de spin, en het magnetisch en elektrisch veld, blijkt de koppeling tussen het magnetisch veld en dipool moment van een fundamenteel deeltje CP-symmetrie te behouden, terwijl de koppeling tussen het elektrische veld en dipool moment

van een fundamenteel deeltje *CP*-symmetrie schendt. Doordat *CP*-symmetrie grotendeels behouden lijkt, moet het elektrisch dipool moment van fundamentele deeltjes erg klein zijn. De aanwezigheid van antimaterie bij dit *CP*-schendende proces is minder duidelijk dan in de hoog energetische processen waarbij het direct gemaakt wordt. Toch speelt antimaterie ook een rol bij het elektrisch dipool moment. Volgens de onzekerheidsrelatie in kwantummechanica is het namelijk toegestaan energie te lenen voor korte tijd. Hierbij kan deze energie een zogenaamd paar van een virtueel deeltje en antideeltje creëren, dat ook snel daarna weer annihileert. Het fundamentele deeltje en het elektrisch veld kunnen in dit proces koppelen via het virtuele paar, en dus via antimaterie.

Precisiemeetingen aan moleculen

In het NL-*e*EDM project proberen we het erg kleine elektrisch dipool moment van het elektron te meten via bariummonofluoride (BaF) moleculen. Dit molecuul bestaat uit een barium en een fluor atoom, die als twee ballen van een sneeuwpop inspiratie boden voor het logo van de collaboratie. Het fluor atoom heeft een sterke aantrekkingskracht op een van de elektronen van het barium atoom waardoor beide atomen aan elkaar gebonden worden. Dit laat een ander elektron van het barium atoom alleen in een schil achter. Daarmee zijn er toestanden van het molecuul die gevoelig zijn voor effecten van het elektrisch dipool moment van het elektron. Deze effecten zijn in dit zware molecuul erg versterkt. De sterke aantrekking van het fluor atoom op het gedeelde elektron zorgt ook voor een elektrische dipool moment in het molecuul. Aangezien het hier gaat om een daadwerkelijke ladingsverdeling en deze niet gekoppeld is aan de spin-as, schendt dit dipool moment de *CP*-symmetrie niet.

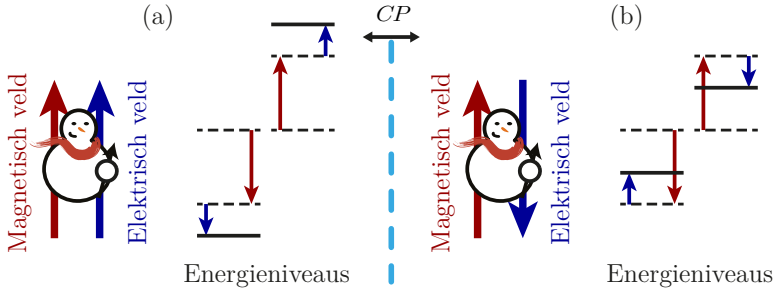

***Figuur 9.3** | Verschuiving van twee energieniveaus van een molecuul in een magnetisch en elektrisch veld, voor de gevallen dat deze velden parallel, dan wel tegengesteld zijn. De transformatie tussen beide gevallen correspondeert met een CP-transformatie.*

Het elektrisch dipool moment van het elektron resulteert in een kleine verschuiving van energieniveaus van de moleculen als deze zich in een elektrisch veld bevinden. Een vergelijkbare, maar veel grotere verschuiving van de energieniveaus vindt plaats door het magnetisch dipool moment in de aanwezigheid van een magnetisch veld. In aanwezigheid van zowel een magnetisch als een elektrisch veld vindt een verschuiving van de energieniveaus plaats door beide velden in gelijke of tegengesteld richting, afhankelijk van of beide velden in gelijke of tegengestelde richting wijzen.

In het experiment vliegt een wolk moleculen door een interactiezone met een elektrisch en magnetisch veld. Hierbij worden de moleculen met behulp van laserlicht in een kwantumsuperpositie gebracht die erg gevoelig is voor de verschuiving van de energieniveaus door deze

velden. Door de interactie met de elektrische en magnetische velden verandert namelijk de fase van de superpositie, afhankelijk van de interactietijd. Door te meten welk deel van de moleculen door een volgende puls laserlicht terug te brengen is uit de superpositie kan de verschuiving van de energieniveaus erg nauwkeurig bepaald worden.
Door het experiment te herhalen voor een volgende wolk moleculen, maar nu met de richting van het elektrisch veld ten opzichte van het magnetisch veld omgedraaid, kan de verandering in de verschuiving van de energieniveaus worden bepaald. Dit geeft een maat voor het elektrisch dipool moment van het elektron, en test daarmee CP-schendende interacties die ons meer kunnen leren over de disbalans tussen materie en antimaterie in het universum.
We maken dus als het ware een CP-spiegel, waarbij we heel nauwkeurig zoeken naar verschillen tussen het beeld en het spiegelbeeld. Dit is ook wat de voorkant van dit proefschrift illustreert. De spiegel is gegeven door het omkeren van het elektrisch veld ten opzichte van het magnetisch veld. Dat geeft dan ook meteen de grootste uitdaging van dit onderzoek; we kunnen niet tegelijkertijd naar het beeld en het spiegelbeeld kijken. Daarom moeten we zorgen dat het beeld zo constant mogelijk is, en begrijpen of een gemeten afwijking van het spiegelbeeld ten opzichte van het eerder gemeten beeld daadwerkelijk komt door een asymmetrie, of komt doordat het beeld ook veranderd is.
De eerste helft van dit proefschrift beschrijft hoe het gemeten signaal van de moleculen kan veranderen door verschillende experimentele parameters die kunnen fluctueren. Daarnaast beschrijft het het computersysteem dat we ontwikkeld hebben om vele van deze parameters te monitoren en te besturen. Deel daarvan is hoe we de asymmetrie waar we in geïnteresseerd zijn introduceren door de richting van het elektrisch veld te schakelen.

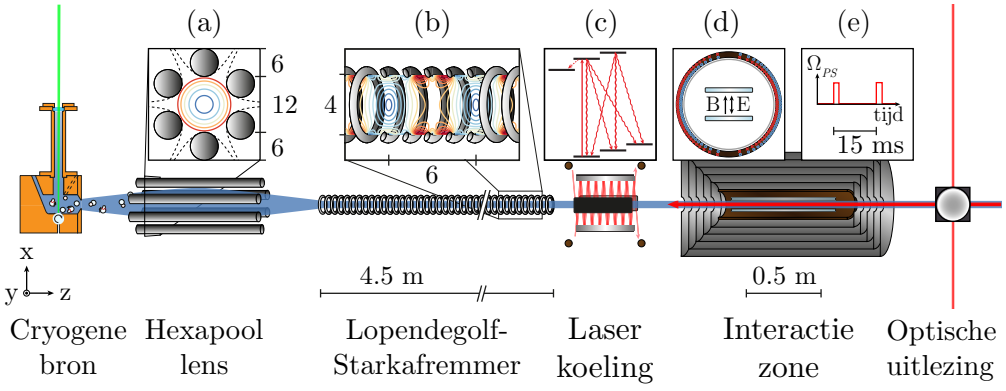

Figuur 9.4 | *Schematische weergave van de voorgestelde proefopstelling voor het NL-eEDM experiment. Bariummonofluoride moleculen worden gemaakt in de cryogene bron, gefocusserd in de hexapool lens, afgeremd in de lopendegolf-Starkafremmer en transversaal gekoeld met laserkoeling. Daarna wordt de meeting gedaan in de interactiezone, afgesloten door optische uitlezing.*

Meer en langzamere moleculen

In de beschrijving van de meetprocedure hierboven vertelde ik al hoe we de verschuiving van de energieniveaus van de moleculen meten na een tijd van interactie met het elektrisch en magnetisch veld. We kunnen de gevoeligheid van deze meeting verbeteren door aan meer

moleculen te meten, en door deze moleculen een langere interactietijd te geven met de velden. De tweede helft van het proefschrift beschrijft de proefopstelling die we ontwikkeld hebben om dit te kunnen bereiken.
Typisch vliegen moleculen die gebruikt worden voor dit soort experimenten met een snelheid van duizenden kilometer per uur, door de energie die ze hebben bij normale temperaturen. Met deze snelheid vliegen ze door de interactiezone met elektrisch en magnetisch veld van een halve meter in een duizendste van een seconde. Om deze interactietijd te verlengen remmen we de moleculen af.
Om te beginnen maken we gebruik van een cryogene bron, waarbij de moleculen bij productie gekoeld worden naar een paar graden boven het absoluut nulpunt. Hierdoor hebben ze al een relatief lage snelheid van honderden kilometer per uur.

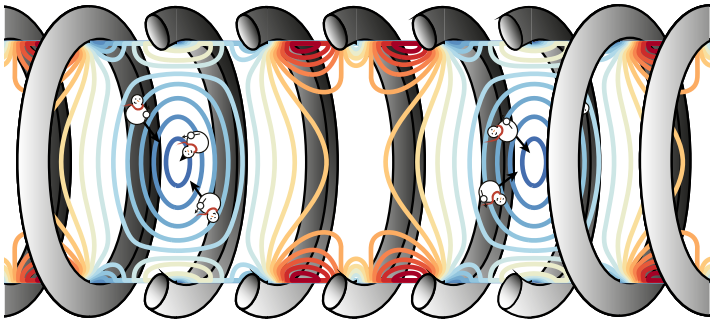

***Figuur 9.5** | Moleculen worden aangetrokken door de elektrisch veld minima in de lopendegolf-Starkafremmer.*

Om ze verder af te remmen gebruiken we de moleculen in toestanden die afgestoten worden door sterke elektrische velden. In de lopendegolf-Starkafremmer schakelen we spanningen op ringelektroden zodat er kommetjes ontstaan van elektrisch veld minima waar de moleculen in worden gevangen. Door het patroon van spanningen op de elektroden op de juiste snelheid te schakelen bewegen we deze kommetjes mee met de moleculen die door de afremmer heen vliegen. Door geleidelijk de snelheid van de kommetjes te verlagen remmen we ook de moleculen af, zoals je ook met een bal die je vangt meebeweegt terwijl je deze tot stilstand brengt.
De kracht die we op deze manier op de moleculen kunnen uitoefenen is echter vele malen kleiner dan bij het vangen van een bal. Zeker voor de relatief zware bariummonofluoride moleculen die we afremmen moeten we over een lang stuk meebewegen om ze succesvol op te vangen. Daarom is de afremmer die we gebruiken vier en een halve meter lang, bestaande uit meer dan drieduizend ringelektroden.
In de tweede helft van dit proefschrift wordt de effectiviteit van de afremmer geschat aan de hand van simulaties en getest aan de hand van metingen. Verbeteringen aan de opstelling worden besproken, eerst aan de hand van het lichtere molecuul strontiummonofluoride (SrF) dat eenvoudiger af te remmen is, voor we overstappen op bariummonofluoride waarin we vooral geïnteresseerd zijn.
Een belangrijke uitbreiding van de proefopstelling is in de implementatie van een hexapool lens. Deze lens van zes elektroden gebruikt dezelfde afstotende werking van elektrische velden

op de moleculen, maar nu door een naar buiten toenemend veld, waardoor de uitdijende wolk van moleculen worden gefocusseerd in de afremmer. Hierdoor kunnen meer van de moleculen die geproduceerd worden in de bron worden afgeremd om bij te dragen aan de gevoeligheid van de meeting. Aan het einde van dit proefschrift wordt de werking van deze lens gekarakteriseerd door middel van direct afbeelding van het licht dat de molecuulbundel uitzendt op een camera.

De toekomst van het NL-*e*EDM project

In dit proefschrift en voorgaand werk is de ontwikkeling van een proefopstelling die gevoelig is voor het *CP*-schendende elektrisch dipool moment van het elektron besproken. Ook is de doorontwikkeling van de molecuulafremmer besproken die in de geplande opstelling van het NL-*e*EDM experiment gebruikt wordt om de interactietijd met het elektrisch en magnetisch veld te verlengen. Om deze opstelling compleet te maken wordt op het moment van schrijven het transversaal laserkoelen ontwikkeld, dat de transversale uitspreiding van de molecuulbundel tijdens de vlucht door de interactiezone moet verminderen. De volgende uitdagingen zullen liggen in het combineren van de onderdelen van de proefopstelling en het verzamelen en analyseren van de data om tot een meeting te komen van het elektrisch dipool moment van het elektron.

Met de ervaring van de ontwikkeling van deze opstelling komen ook alternatieven voor een nog gevoeliger experiment in beeld. Zo wordt overwogen of een opstelling zonder de afremmer niet gevoeliger zou zijn, doordat de winst in interactietijd niet opweegt tegen de verliezen in aantal deelnemende moleculen tijdens het afremproces. Daarnaast wordt het gebruik van andere moleculen overwogen, veelal moleculen die bestaan uit meer dan twee atomen. Ook wordt er gewerkt aan een opstelling waarbij moleculen zullen worden ingevangen, in plaats van het vliegen door een interactiezone, waardoor de interactietijd aanzienlijk verlengd kan worden. In dat laatste kan de lopendegolf-Starkafremmer opnieuw een grote rol spelen.

9.2. Wetenschappelijke samenvatting

Precisie-metingen aan moleculen vormen een gevoelige test van fysica voorbij het Standaardmodel. In het bijzonder bieden metingen aan het elektrisch dipoolmoment (EDM) van fundamentele deeltjes limieten op processen die de pariteit (P) en tijdsomkeersymmetrie (T) schenden. Gewoonlijk wordt de gecombineerde symmetrie van pariteit met ladingsconjugatie (C) beschouwd. Deze combinatie wordt eveneens geschonden door deze elektrisch dipoolmomenten.

De limieten aan elektrisch dipoolmomenten beperken de parameterruimte voor uitbreiding van de CP-schendende sector van het Standaardmodel. Dit ondanks de kosmologische waarnemingen van disbalans tussen materie en antimaterie in het universum, welke bronnen van CP-schending vereisen bovenop de reeds bekende.

Moleculen zoals bariummonofluoride (BaF) bieden een verhoogde gevoeligheid voor de CP-schendende interacties van het elektrisch dipoolmoment van het elektron (d_e) en de scalaire-pseudoscalaire elektron-nucleoninteractie (C_S).

In **hoofdstuk 1** is de relatie tussen zoektochten naar elektrisch dipoolmomenten en CP-schendende fysica besproken. Het principe van de dubbel differentiële meting van het energieverschil tussen magnetische hyperfijnsubniveaus via een Ramsey-interferentiemethode is behandeld. De meting wordt uitgevoerd in parallelle en antiparallelle magnetische en elektrische velden, waarbij het verschil in opgebouwde fase na uitsluiting van systematische afwijkingen wordt toegeschreven aan het CP-schendende elektrisch dipoolmoment.

De context van het NL-eEDM-experiment in het actieve veld van zoektochten naar het elektrisch dipoolmoment van het elektron is besproken, waarbij de aanpak om een meting te doen aan een intense en langzame moleculenbundel om een competitieve statistische onzekerheid te bereiken behandeld is.

In **hoofdstuk 2** is een gedetailleerdere beschrijving gegeven van de meet-procedure aan de hand van het experiment uitgevoerd op een supersone, gepulste bundel van BaF-moleculen. Een analytisch model voor het spin-precessiespectrum is afgeleid dat de afhankelijkheid laat zien van experimentele parameters, wat de vele parameters laat zien die moeten worden gemeten of aangestuurd om een nauwkeurige meting van het elektrisch dipoolmoment te bereiken.

Het data-acquisitie- en aansturingssysteem ontwikkeld voor dit experiment is besproken in **hoofdstuk 3**. Het systeem is ontworpen om uitbreidbaar en robuust te zijn op basis van zijn modulaire aard zowel in het netwerk van meetapparaten als in de software. Dit modulaire raamwerk volgt de schot-gebaseerde tijdsstructuur van het experiment.

Het aansturingssysteem is ontworpen rond een schakelreeks van verschillende toestanden van de proefopstelling. De schakelprocedure is gedemonstreerd door het schakelen tussen elektrisch veld-oriëntaties.

Om een betekenisvolle statistische gevoeligheid voor het elektron elektrisch dipoolmoment te bereiken binnen een redelijke meettijd, is gepland om het NL-eEDM-experiment uit te voeren op een langzame en intense bundel van BaF-moleculen. Deze bundel moet worden geproduceerd in een combinatie van een cryogene buffergasbron en een lopendegolf-Starkafremmer. Door de toename van de moleculaire flux en de interactietijd wordt verwacht dat dit de statistische gevoeligheid van het experiment met meerdere ordes van grootte verhoogt in vergelijking met de momenteel gebruikte supersone bundel.

In **hoofdstuk 4** wordt de faseruimte-acceptatie van de lopendegolf-Starkafremmer besproken voor het gidsen en afremmen van SrF en BaF moleculen in de laagste rotationele toestanden van de $X^2\Sigma^+(v = 0)$ elektronische en vibrationele grondtoestand. De beperkingen van de acceptatie worden getoond; voornamelijk hoe deze wordt verminderd door de hoge massa van BaF. Er wordt getoond hoe de transversale fase-ruimte-koppeling van de cryogene bron in de afremmer verbetert door de installatie van een hexapool-lens tussen beide.
In **hoofdstuk 5** zijn verbeteringen aan de afremmer-opstelling gedemonstreerd aan de hand van voortgezette metingen met strontiummonofluoride (SrF) moleculen. De verbeteringen kunnen worden onderverdeeld in vier categorieën:

(1) De betrouwbaarheid van de bron en het gebruiksgemak zijn verbeterd door het vervangen van het rotatie-mechanisme van het ablatie-doelwit.
(2) Het data-acquisitie systeem is herzien om synchronisatie tussen verschillende datastromen te hebben en toegang te bieden tot data over de status van de opstelling.
(3) De intensiteit van de afgeremde molecuulbundel is verhoogd door een verbeterde faseruimte-koppeling tussen de bron en de decelerator met behulp van een hexapool-lens.
(4) De afrem-procedure is gewijzigd om verliezen van langzame moleculen die de afremmer verlaten te minimaliseren.

De overgang naar het zwaardere bariummonofluoride (BaF) is gedemonstreerd in **hoofdstuk 6**. Een karakterisering van de molecuulbundel geproduceerd in de cryogene buffergasbron is gepresenteerd, gericht op de relevante parameters voor de combinatie met de lopendegolf-Starkafremmer.
Een hexapool-lens is gebruikt om de faseruimte overeenkomst tussen de cryogene buffergasbron en de lopendegolf-Starkafremmer te verbeteren. Deze hexapool-lens is gekarakteriseerd in **hoofdstuk 7** door afbeelding van de molecuulbundel op een EMCCD-camera. Het bereikte focusseren van de molecuulbundel en de bijbehorende toename van de bundelintensiteit worden verklaard aan de hand van numerieke simulaties van molecuulbanen.



Acknowledgements

In this thesis I have been describing my contributions to the research that is being conducted by the NL-*e*EDM collaboration. To anyone who has not directly skipped through the thesis looking for the acknowledgements, it should be clear from the interwoven nature of the work described in this thesis that it would not have been possible for me to have done this alone. Therefore, I would like to take this opportunity to finish this thesis with some personal notes.

Rick, I am extremely grateful for all your supervision. Thank you for daring to start this endeavour with a theoretician with minimal programming experience. Thank you for giving me the space to find my own way and guiding me whenever I was lost. Thank you for always showing me the positive approach to every challenge I brought to you, even when I was not always overexcited in presenting it. Thank you for providing me with the secure feeling of always having someone on my side, especially in all my refusals to pick a side myself. Thank you for making sure I left all of our meetings with a smile on my face.
Steven, I would like to express my deepest appreciation for your support to my work. I am greatly inspired by your significant skill in bringing people together, helping them find a good position to contribute to the project and keeping them involved in the work and the appreciation thereof. I am highly thankful for the opportunities you have given me with the place in your lab; I have fond memories of the conversations we have had there, and during many group activities.
Lorenz and ***Klaus***, thank you for involving me in what developed into the fast beam effort. Thank you for all the challenges, directions and explanations you have given me over the years. I will remember forever your drive towards the core of any problem and perpetual focus on finding its solution.
I would like to thank the ***Snelle bundel bende*** for all of their support. The significant number of references to your theses shows the interconnected nature of our work, which I enjoyed a lot. ***Alexander***, thank you for always having great insights on how to approach a problem, in the unusual cases you had not solved it before. ***Ginny***, thank you for all the great energy you brought both to our work and the social environment we conducted this in. I also appreciate your efforts in making sure I went home on time, even after your move to Geneva. ***Thomas***, thank you for always being up for conversation, sharing your ideas on many different topics. You managed to lift the spirits of many a meeting by your underrated puns.
I am grateful for all the mentoring I got from my predecessors in the *Cold molecules lab*, ***Artem, Kevin, Yanning*** and ***Parul***. The work I did on the cryogenic source and decelerator setup would not have been possible without your achievement as well as the valuable lessons

The chapter image shows the team effort that has been crucial to this research project, and the support I have experienced in conducting my work from both people within and outside of the NL-eEDM collaboration.

you taught me on the practical problem solving required in experimental work. I have fond memories of our outings which always managed to involve ice cream.
I also had great pleasure of working with ***Mina***. You have an extraordinary skill in finding something fun in every job to be done and have shown me the power of a motivational message on a sticky note many times.
Maarten, I very much appreciate your availability to collaborate. The many exchanges both in visiting each other's labs and during countless conference calls ensured my feeling of you as a close colleague, despite the physical distance. I also cherish fond memories from our travels to Durham and the last-minute lab visit in London on the way back.
Most of the measurements in the second half of this work have been performed together with ***Joost***, and I consider them therefore just as much his achievement as mine. I cannot begin to express my thanks to you, for the energy you brought to our lab, your enthusiasm for every plot I showed you, and for hiding the tape you loved using on our setup. I have been trying to replace myself by an analysis script, but for you I will always be glad to fulfill the role of data manager.
Many thanks to ***Mark***, for teaching me how to be a programmer, helping me set up our *Barry* system, and humiliating me at table tennis.
I am also grateful to ***Richard***, for getting the camera system to work for direct imaging of the molecular beam, and his disgusting naming convention in analysis scripts.
I appreciate ***Thijs*** for finishing the work of the previously mentioned. And also together with him entertaining me at board game nights, which I hope will continue far into the future.
I would also like to thank all the other bachelor, master and engineering students I greatly enjoyed working with.
Leo, I am greatly inspired by your unprecedented skill in constructing, maintaining and repairing anything which is not a laser (because they *never work*). If ours is the *lab where the future is made*, with yours the future is in great hands.
Thank you, ***Arif***, for all your support in the last stages of finishing this thesis. Proudly, I hand over the responsibility of being the next to submit a thesis to you.
I would also like to thank all further members of the NL-*e*EDM collaboration and Van Swinderen Institute I had the pleasure of working with, ***Agustin, Anastasia, Andrej, Ann-Kathrin, Bart, Briain, Eifion, Elwin, Heleen, Hilde, Jelmer, Jennifer, Jordy, Julia, Kristof, Lisa, Lucas, Lukas, Malika, Martijn, Gerco, MD, Mick, Nikos, Nithesh, Oliver, Pi, Rob, Roman, Steve, Ties, Wim, Yongliang, Yuly,*** and many more.
Julia Even, Patrick Decowski and ***Gerard Meijer***, thank you for your willingness to form my reading committee and the value feedback you provided on my manuscript.

This scientific work would also have been impossible without the support I got from my friends and family.
I would like to express my gratitude to the green, blue and yellow to my red. ***Martine***, thank you for all the games of squash and *War of the Ring* we played. ***Sophie***, thank you for letting me share in your unlimited love for cats. ***Kwintijn***, thank you for owning every tool I could ever need and your willingness to deliver them at the shortest notice.
I appreciate ***Bas*** and ***Syb*** for demonstrating that challenging times of working from home also provide opportunities in having lunch together despite being hundreds of kilometers

apart. You have shown me how nothing stops us from saving the world from an international spy network, as long as the tape used to stick the camera to my dining room lamps holds.
I have fond memories of the late-night Minecraft sessions with ***Jesper***. Thank you for the creative inspiration you gave me there and in many other projects.
Thank you, ***Daan W***, for all the times you let me win at squash and boardgames, and the ample supply of cake you presented me with.
I cannot begin to express my thanks to ***Daan M***, who has never once failed to see right through me and always managed to provide me with the support and friendship I needed.
Thank you, ***Just***, for the great hikes we went on together, crossing many mountain ranges and even national borders.
Thanks also to ***Hidde***, for the many games we have played, both on a tabletop and online.
Thank you, ***Dineke***, for all the times you made sure I spend enough time on the me-part of my work, the museums visits we did together and the many cups of tea in your beautiful garden.
I am grateful to ***Arjen, Robert, Michele*** and the rest of the ***Spellenmakersgilde***, who provided me monthly with challenging puzzles associated with board game design.
I appreciate all the members of ***Scouting Titus Brandsma Deventer***, especially those of the ***Zaterdagscouts, Dreamteam*** and ***Verenigingsbestuur*** for all the great adventures you took me on and making sure I never had time to get bored.
Most of all, I would like to express my deepest gratitude to my family, who has been there for me every step of the way. ***Pietro***, thank you for pretending to be sporty with me. Your words have been crucial many times in encouraging me to push just a bit further to finish what I was working on, or even more importantly, to let go of what was not worth worrying about. ***Brommie***, thank you for demonstrating weekly how phone providers assume no-one will ever want to have a phone call longer than two hours, and continuously proving them wrong. ***Mr Tou***, thank you for your unwavering interest in my work, demonstrated by multiple *surprises* involving snowmen.

List of Publications

A. Touwen, J. W. F. van Hofslot, T. Qualm, R. Borchers, R. Bause, H. L. Bethlem, A. Boeschoten, A. Borschevsky, T. H. Fikkers, S. Hoekstra, K. Jungmann, V. R. Marshall, T. B. Meijknecht, M. C. Mooij, R. G. E. Timmermans, W. Ubachs and L. Willmann, "Manipulating a beam of barium fluoride molecules using an electrostatic hexapole," *New Journal of Physics*, **26** 073054, July 2024.
Contributions: Design of the experiment, performing simulations, data taking and analysis, writing first draft of the manuscript.

A. Boeschoten, V. R. Marshall, T. B. Meijknecht, A. Touwen, H. L. Bethlem, A. Borschevsky, S. Hoekstra, J. W. F. van Hofslot, K. Jungmann, M. C. Mooij, R. G. E. Timmermans, W. Ubachs and L. Willmann, "Spin-precession method for sensitive electric dipole moment searches", *Physical Review A*, **110** L010801, July 2024.
Contributions: Development of the experiment and data acquisition and control system, discussion of measurement approach and interpretation, data taking, assisted in writing first draft of the manuscript.

M. C. Mooij, H. L. Bethlem, A. Boeschoten, A. Borschevsky, K. Esajas, T. H. Fikkers, S. Hoekstra, J. W.F. van Hofslot, K. Jungmann, V. R. Marshall, T. B. Meijknecht, R. G. E. Timmermans, A. Touwen, W. Ubachs, L. Willmann and Y. Yin, "Influence of source parameters on the longitudinal phase-space distribution of a pulsed cryogenic beam of barium fluoride molecules," *New Journal of Physics*, **26** 053009, May 2024.
Contributions: Development of data acquisition system, discussion of results, proofreading of the manuscript.

M. C. Mooij, H. L. Bethlem, A. Boeschoten, A. Borschevsky, T. H. Fikkers, S. Hoekstra, J. W.F. van Hofslot, K. Jungmann, V. R. Marshall, T. B. Meijknecht, R. G. E. Timmermans, A. Touwen, W. Ubachs and L. Willmann, "A novel method to determine the phase-space distribution of a pulsed molecular beam," arXiv:2401.16588, January 2024 (submitted).
Contributions: Development of data acquisition system, proofreading of the manuscript.

M. Denis, P. A. B. Haase, M. C. Mooij, Y. Chamorro, P. Aggarwal, H. L. Bethlem, A. Boeschoten, A. Borschevsky, K. Esajas, Y. Hao, S. Hoekstra, J. W. F. van Hofslot, V. R. Marshall, T. B. Meijknecht, R. G. E. Timmermans, A. Touwen, W. Ubachs, L. Willmann and Y. Yin, "Benchmarking of the Fock-space coupled-cluster method and uncertainty estimation: Magnetic hyperfine interaction in the excited state of BaF", *Physical Review A*, **105** 052811, May 2022.
Contributions: Discussion of results, proofreading of the manuscript.

P. Aggarwal, Y. Yin, K. Esajas, H. L. Bethlem, A. Boeschoten, A. Borschevsky, S. Hoekstra, K.

Jungmann, V. R. Marshall, T. B. Meijknecht, M. C. Mooij, R. G. E. Timmermans, A. Touwen, W. Ubachs, and L. Willmann, "Deceleration and Trapping of SrF Molecules," *Physical Review Letters*, **127** 173201, October 2021.
Contributions: Assisted in data taking, discussion of analysis approach and interpretation, proofreading of the manuscript.

P. A. B. Haase, D. J. Doeglas, A. Boeschoten, E. Eliav, M. Iliaš, P. Aggarwal, H. L. Bethlem, A. Borschevsky, K. Esajas, Y. Hao, S. Hoekstra, V. R. Marshall, T. B. Meijknecht, M. C. Mooij, K. Steinebach, R. G. E. Timmermans, A. Touwen, W. Ubachs, L. Willmann, and Y. Yin, "Systematic study and uncertainty evaluation of P, T-odd molecular enhancement factors in BaF," *The Journal of Chemical Physics*, **155** 034309, July 2021.
Contributions: Discussion of results, proofreading of the manuscript.

P. Aggarwal, H. Bethlem, A. Boeschoten, A. Borschevsky, K. Esajas, Y. Hao, S. Hoekstra, K. Jungmann, V. Marshall, T. Meijknecht, M. Mooij, R. Timmermans, A. Touwen, W. Ubachs, L. Willmann, Y. Yin, and A. Zapara, "A supersonic laser ablation beam source with narrow velocity spreads," *The Review of scientific instruments*, **92** 033202, March 2021.
Contributions: Discussion of results, proofreading of the manuscript.

P. Aggarwal, V. R. Marshall, H. L. Bethlem, A. Boeschoten, A. Borschevsky, M. Denis, K. Esajas, Y. Hao, S. Hoekstra, K. Jungmann, T. B. Meijknecht, M. C. Mooij, R. G. E. Timmermans, A. Touwen, W. Ubachs, S. M. Vermeulen, L. Willmann, Y. Yin, and A. Zapara, "Lifetime measurements of the $A^2\Pi_{1/2}$ and $^2\Pi_{3/2}$ states in BaF," *Physical Review A*, **100** 052503, November 2019.
Contributions: Discussion of results, proofreading of the manuscript.

Y. Hao, L. F. Pašteka, L. Visscher, P. Aggarwal, H. L. Bethlem, A. Boeschoten, A. Borschevsky, M. Denis, K. Esajas, S. Hoekstra, K. Jungmann, V. R. Marshall, T. B. Meijknecht, M. C. Mooij, R. G. E. Timmermans, A. Touwen, W. Ubachs, L. Willmann, Y. Yin, A. Zapara, "High accuracy theoretical investigations of CaF, SrF, and BaF and implications for laser-cooling," *The Journal of Chemical Physics*, **151** 034302, July 2019.
Contributions: Discussion of results, proofreading of the manuscript.

A

Molecular structure and labeling

The energy level structure of states in diatomic molecules such as $^{88}Sr^{19}F$ and $^{138}Ba^{19}F$ is discussed in great detail in textbooks, such as [63, 124]. It has been worked out for the molecules of interest in [23, 51]. Structure constants can be found for SrF in [64, 125–127] and for BaF in [65, 67, 128, 129] as well as more recent work in [114, 130]. In this appendix the relevant labeling and states of transitions used in this work are reviewed.
The labeling of states is based on the extreme cases for which a certain coupling of angular momenta in the molecule is dominant over others in a given energy regime. In practice however, molecules often do not follow one extreme case, and mixtures of states are encountered instead. An effective field theory description of BaF describing mixing of states can be found in Boeschoten [23].

A.1. State labeling

The largest splittings between molecular states is given by the electronic states, similar to atomic systems, and is typically of the order of 100 THz. The electronic states are given by the electrons orbital (L) and spin (S) angular momentum, which couple to a total electronic angular momentum $J_a = L + S$. The projection on the inter-nuclear axis of these quantum numbers are labeled Λ, Σ and Ω respectively. Together with the reflection symmetry ($\pm$), these are used in the term symbol to label the electronic states,

$$^{2S+1}\Lambda^{\pm}_{\Omega}, \tag{A.1}$$

where the projected electronic orbital angular momentum is given in the spectroscopic notation, with $\Sigma, \Pi, \Delta, \Phi, ...$ for $\Lambda = 0, 1, 2, 3, ...$ After a X for the groundstate an alphabetical labeling of the excited electronic states is used.
As the molecules of interest for this research have one valence electron, the electronic ground

state is $X^2\Sigma^+$ and the first[1] excited state is $A^2\Pi_{1/2}$.
The vibrational motion of the nuclei splits the electronic states in vibrational states labeled by the vibrational quantum number v, with a typical splitting of order THz. Unless stated otherwise, the work in this thesis concerns molecules in the vibrational ground state $v = 0$. The rotation of the molecule add another angular momentum, labeled by R. The corresponding rotational energy level splitting is in the order of GHz. The rotational level structure is given by a combination of angular momentum coupling mechanisms, which are categorised in Hund's cases [131] based on dominating coupling strengths. The lowest electronic states of the molecules of interest follow Hund's cases (a) and (b), which are illustrated in Figure A.1, for which the coupling of the electrons angular momenta to the inter-nuclear axis is strong.

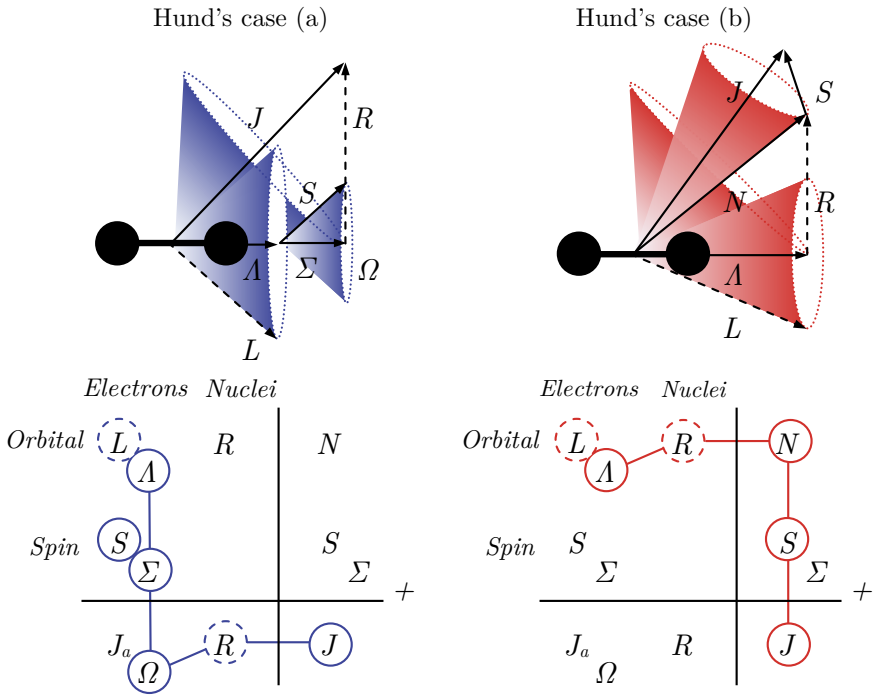

Figure A.1 *| Coupling schemes and (encircled) good quantum numbers for labeling of states in Hund's case (a) and (b).*

As the electronic groundstate $X^2\Sigma^+$ has $\Lambda = 0$, the spin-orbit coupling vanishes and therefore the rotational structure follows Hund's case (b). The total angular momentum excluding spin $N = \Lambda + R$ is equal to the rotational angular momentum of the molecule $N = R$. This couples to the electrons spin S to form the total angular momentum $J = N + S$, known as finestructure. The typical splitting of these finestructure levels is of the order 10-100 MHz. The electronic excited state $A^2\Pi_{1/2}$ has $\Lambda = 1$ and a strong spin-orbit coupling. This state is therefore best described by Hund's case (a). The Ω-doublet with the $A^2\Pi_{3/2}$ has a splitting

[1] Actually the $A'^2\Delta_{3/2}$ has lower energy, but as it does not play a role in this work it is omitted in this discussion.

of tens of THz. The splittings between the finestructure levels labeled by the total angular momentum $J = \Omega + R$ is again of the order of 10-100 MHz.
The rotational states (J) split under the nuclear spin (I) to hyperfine states with quantum number $F = J + I$. As the nuclear spin of both ^{88}Sr and ^{138}Ba is zero, only the nuclear spin of the ^{19}F ($I = 1/2$) plays a role. Typically the hyperfinesplitting is of the order of MHz.

A.2. Transitions and branches

Electronic dipole transitions between states follow strict selection rules, limiting the transitions observed in molecular spectra. In addition to a change of parity the difference in total angular momentum between ground and excited state in an electronic dipole transition is constraint to $\Delta J = \pm 1$. As a result three branches of transitions are observed, labeled $P(\Delta J = -1)$, $Q(\Delta J = 0)$ and $R(\Delta J = +1)$.

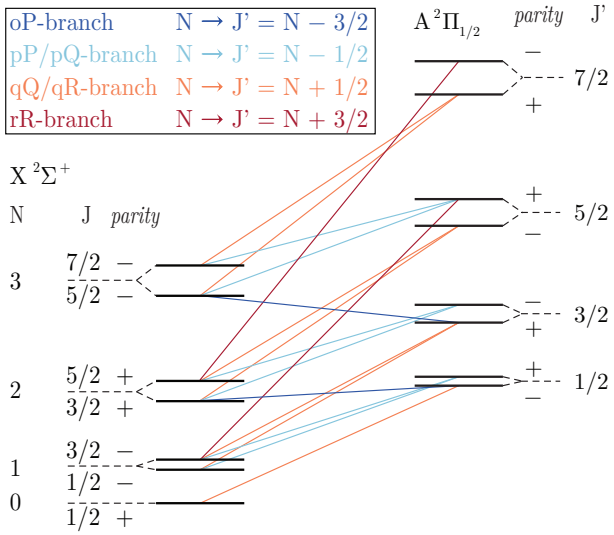

***Figure A.2** | Transitions between rotational states in a $X^2\Sigma^+$ to $A^2\Pi_{1/2}$ manifold such as the ground state and electronically excited state of $^{88}Sr^{19}F$ or $^{138}Ba^{19}F$. The transitions are grouped in four branches.*

However, as the coupling to rotational states ($N = \Lambda + R$) in the electronic groundstate of ^{88}Sr^{19}F and ^{138}Ba^{19}F is dominant over the coupling to the electron spin $J = N + S$ the transitions are better grouped in four branches as shown in Figure A.2. The lowercase letter in this branch shows the change in rotational quantum number ΔR following the same alphabetical naming convention as for ΔJ.

B

(Re)booting the DAQ system - Full manual

Operator manual for data acquisition and control system of the NL-eEDM experiment. Next to a starting procedure of the system, it includes common issues and debugging strategies.

(Re)Booting the DAQ system – Full manual

[AT, 2022-10-31]

General advice

Restart the whole system if something is malfunctioning, there might be more interconnected than you think.

Table of Contents

General advice 1
General procedure 2
Caddie 2
Alcatraz-vme012 2
Laserlab-vme011 4
Laserlab-wlm3 4
Laserlab-comb 5
DAQ PC (Laserlab-flash) 6
Function generators (Laserlab-WG01 and Laserlab-WG02) and HV supply (Alcatraz-HV00) 6
Barry 7
DAQ PC (Laserlab-flash) 7
Control 8
Bitpattern Controller 8
Controlled devices 9
Function generators (Laserlab-WG01 and Laserlab-WG02) 9
HV supply (Alcatraz-HV00) 10
Common issues and debugging strategies 11

General procedure

First start Caddie, which controls the readout from the hardware modules, on all devices relevant for the measurement. At least Caddie should be running on Alcatraz-vme012, as it is used as a trigger for data flushing and controlling devices.

Then Barry is started, which does the first analysis and data storage.

Then start the control programs which switch the state of the setup and possibly are also involved in the readout of the controlling devices.

Then live plotting scripts can be started.

At the end of the document there is a collection of common issues and debug strategies.

Caddie

Alcatraz-vme012

First start the DAQ PC (Laserlab-flash) with the power button on the PC under the standing table to the right in the laserlab, ubuntu will boot

1. Start the vme-cpu by booting the crate
2. Connect to vme012 via ssh from the DAQ PC
    1. Open a terminal (ctrl+alt+T)
    2. Connect via ssh: *ssh datacq2@192.168.25.59*
    3. Password: serendipity
3. Stop Caddie if it is still running
    1. To see whether another instance of Caddie is still running run the following command in the terminal
    ps aux|grep Caddie
    2. If it returns a process of ./Caddie.exeDebugLinux86 find the 4 digit process number at the start of that line.
    3. Kill the process by
    kill -9 4-digit_process_number
4. Start Caddie
    1. Change to directory (cd) /Caddie

2. Run Caddie by ./Caddie.exeDebugLinux86 (version 1.6 built Aug 17 2021 11:39:32)
3. Start a run by 0 (Caddie actions), then 5 (Start run). To show options use ?, to confirm us &, to cancel use !
4. It could be that caddie starts in the setup menu. If so it will probably tell you what is wrong. Sometimes it is just that settings have to be confirmed with &, after which the run can be stared normally as described in the previous step. An example of what is done if it is in a submenu is found as a text document in the caddie folder

5. Set the delay generator
    1. With the buttons on the Delay generator module set the delay on the top channel (ch0) to 7 ms and the bottom (ch1) to 10 microseconds
    2. Press Loc for each channel to activate manual control
    3. Press + and - on Dig sel (bottom) to change the selected digit
    4. Press + and - on Fig sel (top) to change the value of the selected digit
    5. Change the switch to change the channel (Ch0 <-> Ch1)

Backup if ssh is not working/ something went wrong

1. Connect the monitor found on top of the cabinets along the windows in the laserlab to the CPU module in the VME-crate, situated in the rack in the back of the alcatraz lab (alcatraz-vme012) and a wall outlet. This computer has a virtual screen configured, but it only works after booting has completed. Then the physical screen can be removed again)
2. Connect to the alcatraz-vme012 via a VNC connection from laserlab-flash by starting Remmina and selecting alcatraz-vme012, the password is edmvnc



Laserlab-vme011

1. Start the computer by booting the crate, situated in the rack to the right of the first lasertable when entering the laserlab
2. Start Caddie
    1. Open a terminal (ctrl+alt+T)
    2. Change to directory (cd) Caddie
    3. Run Caddie by ./CaddieIO.exeDebugLinux86 (version 1.6 built Aug 17 2021)
    4. Start a run by 0 (Caddie actions), then 5 (Start run). To show options use ?, to confirm us &, to cancel use !
3. Set the delay generator
    1. With the buttons on the Delay generator module set the delay on the bottom channel (CH1) to 5900 microseconds and the bottom (CH2) to 7 ms
    2. Press Loc for each channel to activate manual control
    3. Press + and - on Dig sel (bottom) to change the selected digit
    4. Press + and - on Fig sel (top) to change the value of the selected digit
    5. Change the switch to change the channel (Ch0 <-> Ch1)



Laserlab-wlm3

1. Start the computer with the power button on the PC standing on top of the first laser table when entering the laserlab. One might need the key to open the front cap first
2. Both the wavelength meter software and caddie should start automatically, but it is good to check. Note that both a normal PC screen and the TV in the laserlab are connected to this PC. It is

controlled via a wireless keyboard including mouse labeled laserlab-wlm2

3. If the wavelength meter software is running a window should be open where it shows the current readouts of the wavelength meter, if not it can be started by Start Wavelength Meter WS8 4061 on the desktop
4. If caddie is running a terminal should show-up with the caddie interface, including a boot message which includes the version. The current version is 1.6 built June 21 2021 14:47:18. If caddie is not running it can be by double clicking wlmCaddieNoDebug.exe in the WavelengthCaddie folder on the Desktop.
5. Start a run by 0 (Caddie actions), then 5 (Start run). To show options use ?, to confirm us &, to cancel use !

Note that the caddie software can only provide data on the wavelength meter if the wavelength meter software is also running

Laserlab-comb

1. Start the computer in the bottom of the rack to the right of the lasertable in the back of the laserlab (laserlab-comb)
2. Run the lasercomb software Fibre Comb Control 0.6.5
3. Start caddie from My Documents/CombCaddie by running CombCaddie.exe
4. If caddie is running a terminal should show up with the caddie interface, including a boot message which includes the version. The current version is 1.6 built on Apr 10 2014. No run has to be started as it is controlled by the laserlab-vme011. Note that the caddie software can only provide data on the frequency comb if the frequency comb software is also running

DAQ PC (Laserlab-flash)

Make sure Caddie is started on at least Alcatraz-vme012 as this Caddie is only a feedthrough of other Caddie datastreams

1. Start Caddie
    1. Open a terminal (ctrl+alt+T)
    2. Change to directory (cd) /Projects/Caddie
    3. Run Caddie by ./Caddie.exeDebugLx86_64 (version 1.6 built May 17 2021 16:11:35)
    4. Start a run by 0 (Caddie actions), then 5 (Start run). To show options use ?, to confirm use &, to cancel use !
    5. It could be that caddie starts in the setup menu. If so it will probably tell you what is wrong. Sometimes it is just that settings have to be confirmed with &, after which the run can be stared normally as described in the previous step

Function generators (Laserlab-WG01 and Laserlab-WG02) and HV supply (Alcatraz-HV00)

Although these devices are sending out data over Caddie this happens via the control program, the startup procedure is therefore described in the Control section of this document.

Barry

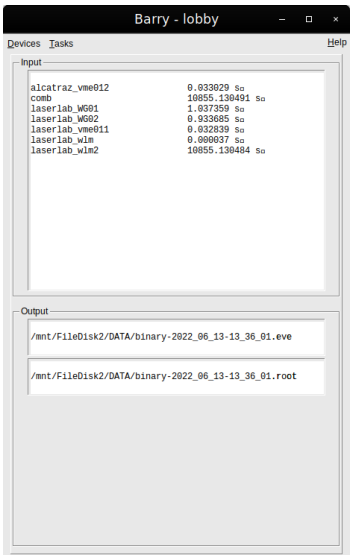

DAQ PC (Laserlab-flash)

1. Start Barry
    1. Open a terminal (ctrl+alt+T)
    2. Change to directory
    cd /Projects/Barry
    3. Run Barry ./bin/Barry
    4. A UI (Barry – Connect) should show up. Connect to Caddie datastream (which was started in the previous step) by selecting host: localhost and port: 1115 (should be default)
    5. Another UI (Barry – Lobby) should show up with when data has come in from the other connected PCs where caddie is running (if any).
    6. NOTE: Data is only saved when at least the Alcatraz-vme012 is connected, make sure the latest update time in the input box is recent (< 1 second).
    7. Check whether data from all device of which Caddie has been started is coming in, make sure the latest update time in the input box is recent (< 1 second) for all these devices. If not, check Caddie is indeed running.
2. The connection to the NAS where the datafiles are updated to should be automatically restored, this can be checked by running the Synology Drive Client, if it says Backup completed with a recent last backup time it is running

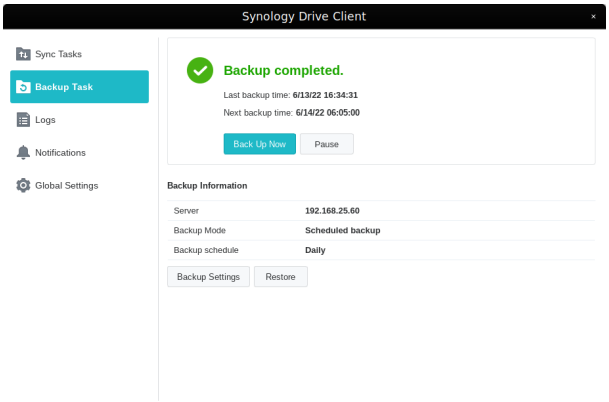

Control20,18 cm

Bitpattern Controller

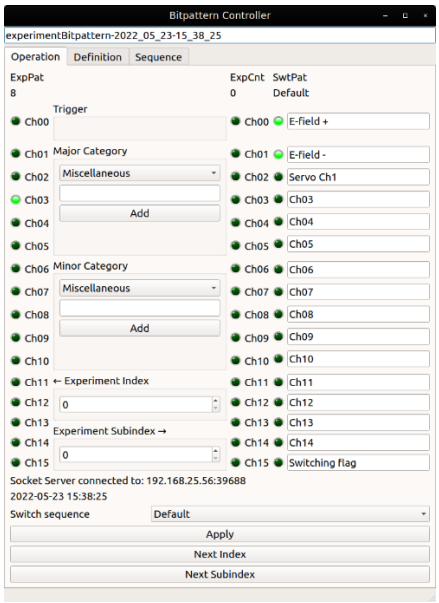

1. NOTE: This controller connects to Caddie modules in Laserlab-vme011 and Alcatraz-vme012, therefore first make sure both of these Caddies are active (don't have to be running)
2. Open a terminal (ctrl+alt+T) at the DAQ PC (Laserlab-flash)
3. Change to directory (cd) /Projects/Control/BitpatternSequence
4. Run the BitpatternController in python by
   python3 BitpatternController.py
5. A user interface should appear which sets the state of three Caen V977 IO modules.
6. Select a Switch sequency to be used for the experiment to be run. The Default sequence does not switch anything, but sets all control parameters to each default.
7. The settings are applied when Apply is pressed, after which the state of the output LEDs on the relevant modules should be the same as in the UI

For further details on how to work with the Bitpattern Controller and how to make a new Switch sequence see the manual in /Projects/Control/BitpatternSequence.

Controlled devices

1. To control the E-field inside the interaction zone make sure the HV-power supplies are providing the necessary voltage.
2. To control the blocking of the pump beams make sure the Servo box is set to remote control.
3. To control the Function generators make sure these are connected as described in the section Function generators (Laserlab-WG01 and Laserlab-WG02)

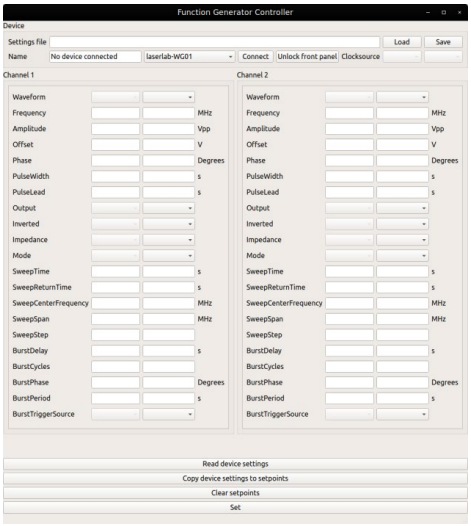

Function generators (Laserlab-WG01 and Laserlab-WG02)

1. NOTE: This controller connects both to the Caddie on the DAQ PC (Laserlab-flash) as the Bitpattern Controller (To be used in the switching sequence). Make sure both programs are running.
2. Open a terminal (ctrl+alt+T) at the DAQ PC (Laserlab-flash)
3. Change to directory (cd) /Projects/Control/RigolDG4062
4. Run the Function generator controller in python by *python3 RigolDG4062Controller.py*
5. A user interface should appear which can be used to manually control the function generators remotely as well as define new settings files for switching.
6. Check in the terminal whether a connection has been established to Caddie and the BitpatternController for each of the to be controlled devices. Check in Barry whether data is coming in from both function generators.

For further details on how to work with the Function generator Controller and how to make a new settings file for switching see the manual in /Projects/Control/ RigolDG4062.

HV supply (Alcatraz-HV00)

1. NOTE: This controller connects both to the Caddie on the DAQ PC (Laserlab-flash) as the Bitpattern Controller (To be used in the switching sequence). Make sure both programs are running.
2. Open a terminal (ctrl+alt+T) at the DAQ PC (Laserlab-flash)
3. Change to directory (cd) /Projects/Control/iseg \HPpn300106
4. Run the controller in python by *python3 IsegHVController.py*
5. A user interface should appear which can be used to manually control the function generators remotely as well as define new settings files for switching.
6. Check in the terminal whether a connection has been established to Caddie and the BitpatternControlle. Check in Barry whether data is coming in from the device (Alcatraz-HV00)

Common issues and debugging strategies

Caddie does not start

- Try the (No)Debug version instead. In the Debug version it does some extra safety checks, but it can also be hanging on these although there is no big issue.

Caddie menu does not show the standard EventProcessing menu when started

- If you are in a *Global options* menu it has probably not read in the parameter files (.par) correctly. Check whether the parameter files are still there in the same folder as the executable. Also check the filename start with Caddie, without any prefix, otherwise it will not be read correct.
- If you are in any other settings menu, for example the general *Caddie* menu with as a first option the *Event Buffer Size* there was some issue in starting Caddie.
    - If there is no Error message for any of the settings, try to confirm the settings with &, which should then bring you back to the standard EventProcessing menu.
    - If there is an Error message, try to trace it back to the submenus and see whether it can be solved there. A common issue is that the wavelenghtmeter Caddie is running without the wavelengthmeter software itself. Make sure Wavelength Meter WS8 4061 is running before starting Caddie.

Caddie does not want to start or stop the run

EveProc-E-WrongState-System is in a wrong state for this operation

- One can check the current state of Caddie by running the Caddie monitor which can be opened by the first option in the Caddie Actions menu called "Toggle monitor". In the terminal Caddie this is toggled by 0 0, in the UI Caddie it is the first option in the top-left menu dropdown.
    - If it is in a rundown state, but does not switch to Idle it is probably because there are still events in the buffer. To empty the buffer run the receiving program of the socket, which is either the Caddie or Barry running on the DAQ PC (Laserlab-

flash). If it remains hanging Caddie can always be closed by ctrl+C, but any data in the buffer is then lost and Caddie has to be restarted.

Caddie Monitor

State — Current state of this Caddie: Running - if Run is started, Idle - if no run is started, RunDown - if stopping a run

EveInMethod — Input source for events: ModularEveIn - From modules, SocketEveIn - Via socket connection to other device, MergeEveIn - A combination of other EveInMethods

EveOutMethod — Out method: SocketEveOut - Send via socket to other devices (or Bogey or Barry)

List of Clients — A list of all Caddies that are controlled from this one, including their state

Barry does not connect to the datastream

- If after connecting to the datastream no Barry – Lobby appears or Barry crashes immediately after check the Caddie on the DAQ PC (Laserlab-flash) is running, as well as the one on Alcatraz-vme012, then try again.
- If Caddie is running make sure it is triggered. In both the Laserlab-vme011 and Alcatraz-vme012 lights should be blinking at the trigger rate (probably 10 or 25 Hz). If this is not the case although Caddie is running there is probably an issue in the hardware between the BNC Triggerbox and the zeroth channel of the Caen V977 IO module, responsible for triggering the readout. Trace back the bath and make sure all NIM electronics is running.

Barry does not create a dataTree(file)

- If there is no Tree->Print() structure shown in the terminal in which Barry has been started there is no dataTree being made. Check in the folder Projects/Barry/config what the most recent config file is and whether this is in accordance with your expectations. If a new (empty) config file has been made some wrong buttons have been pressed,

move the config file to somewhere else as a backup and try starting Barry again.

- If no data file is saved, check the file location specified in the Output box in the Barry- Lobby. Check the file location /mnt/FileDisk2/DATA is available and the current file is updating.

Data of some source is not coming in, latest update time keeps increasing

- In the Barry – Lobby it is shown how many seconds ago the last event from each Caddie device is received. If this number is increasing and a couple of hundred seconds or more the device is not connected to the datastream.
    - Check for the network connection of the device. Ping the fisnet IP address of the device running Caddie from the DAQ PC (Laserlab-flash). The IP address can be found on the list hanging to the right of the DAQ PC (Laserlab-flash). *Ping <IP>*
    - If there is a network connection check both the sening and the receiving Caddie are running. The receiving Caddie on the DAQ PC (Laserlab-flash) has to be started first. After restarting the run on the sending Caddie the time since last event should update, however this may take about two minutes. It should also reconnect in itself, but this can take a while (minutes). It is known that the Caddie on Laserlab-vme011 can be difficult to connect, sometimes restarting the Caddie helps.
    - One can also manually look for events in the datastream with the eventPrinter, which shows the raw data in hexadecimal form of each 32bit word in the stream. It can be started from the Barry – Lobby from the Tasks dropdown menu by pressing EventPrinter. It shows the datastream in the terminal from which Barry has been started.

Caddie datastream

The Caddie datastream is based on events, clusters of data from the same readout. These events consist of 32 bit words. The general structure of these events is always the same, every event consists of a 7 word header and either subEvent(s) or data.

Header

Size	Number of words in the event.
Version	0x03020100 to check compatibility in endianness between device.
MoreEventsNum	? Never used in current software.
Tag	Number of the event, increases by one for every event from this source.
CreationTime	Computer time in second since when event was created.
ID	Identifier for device, first 16 bits for device type, last number of device.
NumSubEvents	Number of subEvents contained in this event. Zero if datablock follows.

SubEvents

If the NumSubEvents is larger than zero there will follow this many subEvents. These subEvents are of the same form as events, again starting with the same header structure. They can therefore be treated as events themselves and can contain more subEvents.

Subevents are used for modules is a VME crate, where one event corresponds to one readout of the crate. But also to structure data from the same event, like in for example the wavelengthmeter, where frequency, wavelength and other data like the temperature are in separate subEvents

Data

If the NumSubEvents is zero datawords will follow, in total Size - 7 words for the header. By Caddie these words are treated as 32 bit integers, but that does not mean data consists of only integers of this size, the bites can be interpreted as any structure. Often multiple smaller readouts are combined into one word, for instance four 8bit datapoints can be in one word for Caddie to minimise datasize. The datastructure is dependent on the device it is coming from, there are no general rules there.

List of known IDs, base addresses and ports

Caddie ID	Name	Base address or TCP/IP Port
None	Laserlab-flash	1115
0x00470000	Laserlab-vme011	1111
0x00060001	SIS3820_0* / scaler	0x3800
0x000c0002	Caen V1290N TDC*	0x2222
0x00290003	IO01 (ExpPat)	0x0000 / 2112
0x00290000	IO02 (ExpCnt)	0x5321 / 3112
0x00020000	laserlab-wlm2**	1112
0x00020001	empty extra laserlab-wlm2 event**	
0x00030000	laserlab-wlm3	1112
0x00030001	empty extra laserlab-wlm3 event	
0x00440000	laserlab-comb	1116
0x00450000	alcatraz-vme012 ***	1114
0x00060001	SIS3820_1*	0x4300
0x00060002	SIS3820_2	0x8300
0x00290003	IO04 (ExpPat)*, ****	0x2234 / 2111
	IO03 (SwtPat)	0x2235 / 3111
0x000a0004	SIS3300 ADC*	0x2500
0x00500000	laserlab-WG01	1118 / 4111
0x00510000	laserlab-WG02	1119 / 4111
0x00600000	alcatraz-HV00	1120 / 4111

* Not saved to dataTree and/or event file

** Currently used in ColdMol lab and disconnected from the datastream

*** Trigger dataTree flushing to file

**** Copy of Laserlab-vme011 - IO01

C

Data Acquisition channels

List of channels in the data analysis software for the NL-eEDM experiment. A summary and connection to the devices used to perform the data acquisition is given in Figure 3.2.

Names	Description	Definition
PMT signals		
PMTCn0 [18]	Number of counts in section D for each bin.	Scaler buffer channel 16 and up, divided by 10 for counts per shot
SignB0	Fluorescence signal in B (Used for normalisation)	Scaler buffer channel 31, divided by 10 for counts per shot
SignD0	Fluorescence signal in D (BackD0 subtracted)	Scaler buffer channel 20 to 26, divided by 10 for counts per shot, take away BackD0
BackD0	Background fluorescence signal in D	Scaler buffer channel 30 compensated for time window length, divided by 10 for counts per shot
NormD0	Fluorescence signal in D normalised to fluorescence signal in B (SignD0/SignB0)	SignD0/SignB0

Names	Description	Definition
Time		
Index0	Index of the shot according to the scaler counter.	anaBuffer->i
TiUnS0	Unix time in seconds (Unix Epoch on January 1st, 1970 at UTC).	anaBuffer->UnixTime
TiSta0	Unix time as timestamp.	TiUnS0 in timestamp format
TiStr0	Local time as String.	TiUnS0 in string format
TimeS0	Time since measurement start in seconds (ana.Time)	anaBuffer->Time
Lasers / Frequency, intensities, pulses		
PulPD0[2][6]	Superposition pulses, intensity and timing from photo diodes PulPD0[0, 1 for polarization][parameter], with intensity in $V \cdot \mu s$ and times in μs parameter: 0: start time first pulse (T_0) 1: pulse length first pulse (t) 2: time between pulses (T) 3: pulse length second pulse (t) 4: integrated intensity first pulse 5: integrated intensity second pulse	ADCP branch
PulFG0[3]	Superposition pulses, timing from function generator PulPD0[parameter], with times in μs parameter: 0: start time first pulse (T_0) 1: pulse length (t) 2: time between pulses (T)	laserlab_WG01
Det2P0	Detuning, two photon detuning from groundstate hyperfine splitting (65.85 MHz) in kHz	Scaler buffer channel 15 over Scaler buffer channel 1 with hard codded calibation
DetSc0[5]	Scan parameters for two photon detuning DetSc0[parameter] parameter: 0: Start frequency, in kHz 1: End frequency, in kHz 2: Time of it takes to do one scan, in seconds 3: Number of steps in the detuning scan, up or down 4: Center frequency including HFS, in kHz	laserlab_WG01 branch

Names	Description	Definition
Lasers / Frequency, intensities, pulses, continued		
Inten0[4]	Laser intensity Inten0[parameter] 0: Optical pumping 1: Detection at B 2: Detection at D	
Frequ0[12]	Frequ0[0 to 11 for laser number] in THz, frequency of the laser	laserlab_wlm, laserlab_wlm2
Wavel0 [12]	Wavel0[0 to 11 for laser number] in nm, wavelength of the laser	laserlab_wlm, laserlab_wlm2
WLMVo0[12]	WLMVo0[0 to 11 for laser number] in volt, locking voltage from the wavelengthmeter	laserlab_wlm, laserlab_wlm2
WLMTe0	WLMTe0 in Celsius, temperature as measured in the wavelengthmeter	laserlab_wlm2
WLMPr0	WLMPr0 in mbar, pressure as measured in the wavelengthmeter	laserlab_wlm2
E-field		
EFiel0	E-field in interaction zone (in kV/cm) based on the HV supplies and Switch state.	Not implemented
HVMon0[2][2]	HV Switch box monitoring HVMon0[Polarity, plus = 0, minus = 1][Field configuration, A = 0, B = 1], in kV corresponding to the applied voltage from the supply	SIS3820_2 rate channels [55] to [58] with hard coded calibration
HVSup0[2][3]	HV supply readout HVSup0[Polarity, plus = 0, minus = 1][Voltage, Current, State]	alcatraz_HV00

Names	Description	Definition
B-field		
BCurr0[2]	BCurr0[axis, x=0. y=1], Current through cosine coil generating a field along the axis, in mA.	SIS3820_2 rate ch [49] and [50] with hard codded calibration
FluxG0[8][3]	FluxG0[0 to numFluxGates][Bx, By, Bz, Bnorm] in microT	FG[8] branch, which are based on fixed calibration in Barry
Switch state		
ExpPa0	ExpPa0, Bitpattern describing type of experiment	IO01
ExpCn0	ExpCn0, Bitpattern with experiment counter	IO02
SwtPa0	SwtPa0, Bitpattern describing the switch state	IO03
SwtTi0	Time since last change of the switch pattern in seconds	TimeSwtPat, generated by AddTimeSinceSwtPatChange function based on TimeS0
SwtBl0	Index of the switch block, where the block started SwtTi0 seconds before	SwtBl0, generated by AddTimeSinceSwtPatChange function
SwtSt0[ ]	Switch state of the experiment, Booleans for the state of the experiment SwtSt0[parameter] parameter: "HVA": Switch box is in switch state A "HVB": Switch box is in switch state B "HVGrou": Switch box is in switch state Grounded (Switches connect field plates to ground) "HVFloa": Switch box is in switch state Floating (Switches open) "Pump": Pump laser unblocked	Interpretation of specific bits in SwtPa0

D

Electric field configurations

In this work different electric field configurations are considered to manipulate trajectories of molecules in low-field seeking states. In this appendix the different field configurations are discussed, demonstrating their use and limitations.
In a region without charges, the electric potential follows Laplace's equation $\nabla^2\Phi = 0$, which in cylindrical coordinates reads,

$$\nabla^2\Phi(r,z,\theta) = \frac{1}{r}\frac{\partial}{\partial r}\left(r\frac{\partial\Phi}{\partial r}\right) + \frac{\partial^2\Phi}{\partial z^2} + \frac{1}{r^2}\frac{\partial^2\Phi}{\partial\theta^2} = 0. \tag{D.1}$$

For a beam experiment, considering cylindrical coordinates is particularly useful as the symmetry of the setup includes a longitudinal axis along the molecular beam, fixing the z axis of the coordinate system. The electric field is given by the gradient of the potential. As the Stark shift depends on the amplitude of the electric field, this is usually what is considered in this work, $E = |-\vec{\nabla}\Phi|$.
In particular two regimes of solutions to Laplace's solution are of interest for this work, which are treated in the following sections separately. Firstly, the multipole radial field expansion is considered, used in electrostatic multipole lenses for focussing the molecular beam. Secondly, a longitudinal train of field three dimensional field minima is discussed, forming the basis of the traveling-wave Stark decelerator.

D.1. Radial multipole field

In this section electric field configurations are considered without longitudinal component, for which $\frac{\partial\Phi}{\partial z} = 0$. These fields can be used to transversely confine a beam of molecules in a low-field seeking state, in the form of a multipole guide. Dependent of the Stark shift these field configuarions can also be used as a multipole lens as discussed at the end of this section and in chapter 7.
By separation of variables the potential can be written as $\Phi(r,\theta) = \Phi_r(r)\Phi_\theta(\theta)$, which splits

Laplace's equation in two decoupled differential equations,

$$\frac{\partial^2 \Phi_r}{\partial r^2} + \frac{1}{r}\frac{\partial \Phi_r}{\partial r} - \frac{n^2}{r^2}\Phi_r = 0, \tag{D.2}$$

$$\frac{\partial^2 \Phi_\theta}{\partial \theta^2} + n^2 \Phi_\theta = 0, \tag{D.3}$$

where n is a constant. The general solution to these equations for the potential is of the form,

$$\Phi(r,\theta) = \frac{A_n}{n} r^n \cos(n\theta - \theta_0). \tag{D.4}$$

As Laplace's equation is linear, any linear combination of solutions provides a solution as well. Here each multipole field are considered separately.
The $2n$-pole field solution can be found from the boundary condition of electrodes to which a positive voltage Φ_0 at an inner radius r_0 at $n\theta - \theta_0 = 2\pi$. From this boundary condition the potential is found to be,

$$\Phi_{(n)}(r,\theta) = \Phi_0 \left(\frac{r}{r_0}\right)^n \cos(n\theta - \theta_0). \tag{D.5}$$

The corresponding electric field is,

$$\vec{E}(r,\theta) = n\Phi_0 \frac{r^{n-1}}{r_0^n}\left[-\cos(n\theta - \theta_0)\hat{r} + \sin(n\theta - \theta_0)\hat{\theta}\right]. \tag{D.6}$$

The electric field strength $E(r) = |\vec{E}(r)|$, which is the relevant parameter for the Stark shift, is radially symmetric for the ideal multipole field.
The shape of the electrodes to which constant voltages $\pm\Phi_0$ have to be applied are given by the electric potential to be,

$$\cos(n\theta - \theta_0) = \left(\frac{r_0}{r}\right)^n. \tag{D.7}$$

These shapes[1] have asymptotes at $n\theta - \theta_0 = \pm\pi/2$. At these asymptotes, electrodes to which opposite voltages are applied are coming close together, which can result in discharges. In practice cylindrical electrodes are used instead, which also provide ease of manufacturing. This results in deformations of the electric field geometry near the electrodes, but this seems to be of limited impact on this work.
The radius of curvature of the ideal multipole electrodes at the point closed to the center is,

$$R = \frac{r_0}{n-1}. \tag{D.8}$$

Further away from the center the radius of curvature of the ideal electrodes increases, therefore the electric field deformation would be lower for cylindrical electrodes with a slightly larger radius. Indeed, Everdij *et al.* [110] has found a minimal deviation from the perfect quadrupole lens ($n = 2$) with cylindrical electrodes of radius $R = 1.148 r_0$. For a hexapole lens ($n = 3$) Anderson [132] has found an optimal cylindrical electrode radius of $R = 0.565 r_0$. In Figure D.1 the electric field for an ideal multipole and for a multipole with radius following Equation D.8 are shown.

[1] The shape is easily confused for a hyperbola, but strictly speaking is only hyperbolic for $n = 2$, and in the limiting case with a focus at infinity for $n = 1$.

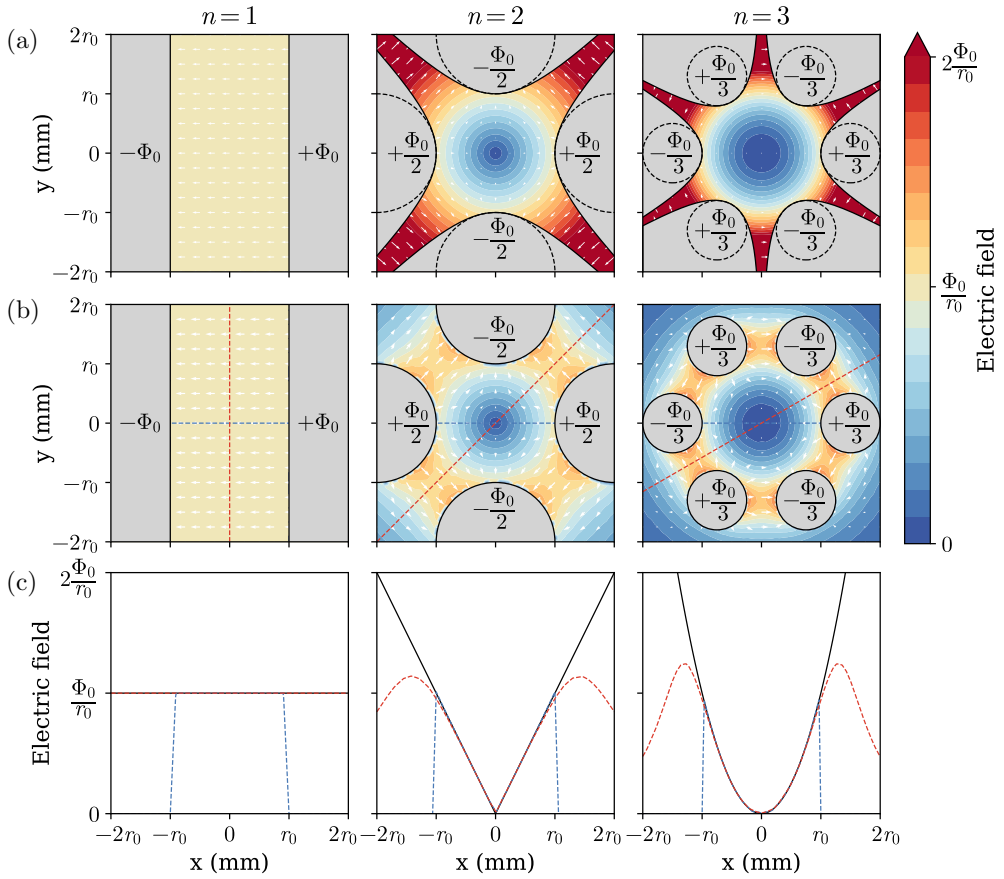

Figure D.1 *| Electric field in a dipole ($n = 1$), quadrupole ($n = 2$) and hexapole ($n = 3$). To the electrodes alternating positive and negative voltages are applied with an amplitude Φ_0/n, such that the field at the inner radius r_0 is approximately equal for each configuration. (a) Ideal electric field and electrode geometry. Grey surfaces with solid black borders show the electrodes. (b) Electric field for cylindrical electrodes with radius $R = r_0/(n-1)$ simulated in* COMSOL *[75]. The blue and red dashed lines show the positions of the electric field traces. (c) Electric field traces along (blue) and between (red) electrodes. The deviation from the ideal electric field shown in the black line show the imperfection of this electrode geometry.*

D.2. Traveling-wave Stark decelerator field

In this section the electric field configuration used in the traveling-wave Stark decelerator is described, first analysing the theoretical ideal configuration of an infinite longitudinal hollow cylinder, then the practical implementation by a series of ring electrodes. Finally, the implication of misaligned ring electrodes is discussed, which results in a reduction of phase-space acceptance. The electric field derivation is analogous to the one presented in Meerakker *et al.* [69].
The electrodes and the electric field in this configuration are cylindrically symmetric, therefore $\frac{\partial \Phi}{\partial \theta} = 0$, simplifying Laplace's equation to two dimensions. To solve this equation for the potential separation of variables, similar to the approach used for the radial multipole field. In this case the potential is written as $\Phi(r, z) = \Phi_r(r)\Phi_z(z)$, resulting in the coupled differential equations,

$$\frac{\partial^2 \Phi_r}{\partial r^2} + \frac{1}{r}\frac{\partial \Phi_r}{\partial r} - k^2 \Phi_r = 0, \tag{D.9}$$

$$\frac{\partial^2 \Phi_z}{\partial z^2} + k^2 \Phi_z = 0. \tag{D.10}$$

Note the difference in the last term of the radial equation compared to Equation D.2. Here the constant is labelled as k, not to confuse the solutions to the ones for the radial multipole field. The solution to these differential equations is,

$$\Phi(r, z) = A_k I_0(kr) \sin(kz - \phi), \tag{D.11}$$

where I_α is the modified Bessel function of the first kind with order α. In principle any linear combination of potentials of this form fulfill Laplace's equation, but here we are mainly interested in the one corresponding to a hollow cylinder electrode of inner diameter r_0 to which a longitudinally periodic voltage of amplitude V_0 is applied, i. e. $\Phi(r_0, z) = V_0 \sin(kz - \phi)$. The potential following this boundary condition is,

$$\Phi(r, z) = V_0 \frac{I_0(kr)}{I_0(kr_0)} \sin(kz - \phi). \tag{D.12}$$

The corresponding electric field is $\vec{E}(r, z) = -\vec{\nabla}\Phi(r, z)$,

$$\vec{E}(r, z) = \frac{V_0 k}{I_0(kr_0)} \left[I_1(kr) \sin(kz - \phi)\hat{r} + I_0(kr) \cos(kz - \phi)\hat{z} \right]. \tag{D.13}$$

For the Stark shift experienced by the molecules the magnitude of the electric field $E(r, z) = |\vec{E}(r, z)|$ is the relevant quantity, which is,

$$E(r, z) = \frac{V_0 k}{I_0(kr_0)} \sqrt{\left[I_1(kr) \cos(kz - \phi) \right]^2 + \left[I_0(kr) \sin(kz - \phi) \right]^2}. \tag{D.14}$$

This ideal electric field is shown in Figure D.2 for an inner radius r_0 of 2 mm and longitudinal period of $l = 2\pi/k$ of 12 mm. The electric field has minima at $r = 0, z = z_0 = (\phi + \pi m)/k$ for $m \in \mathbb{Z}$, at the radial center, longitudinally separated by π/k.
Molecules in a low-field seeking state are attracted to these field minima, which form three dimensional traps. The traps can be made to move by making the phase $\phi(t)$ time dependent, which can be used to guide or decelerate the molecules as discussed in section 4.3.

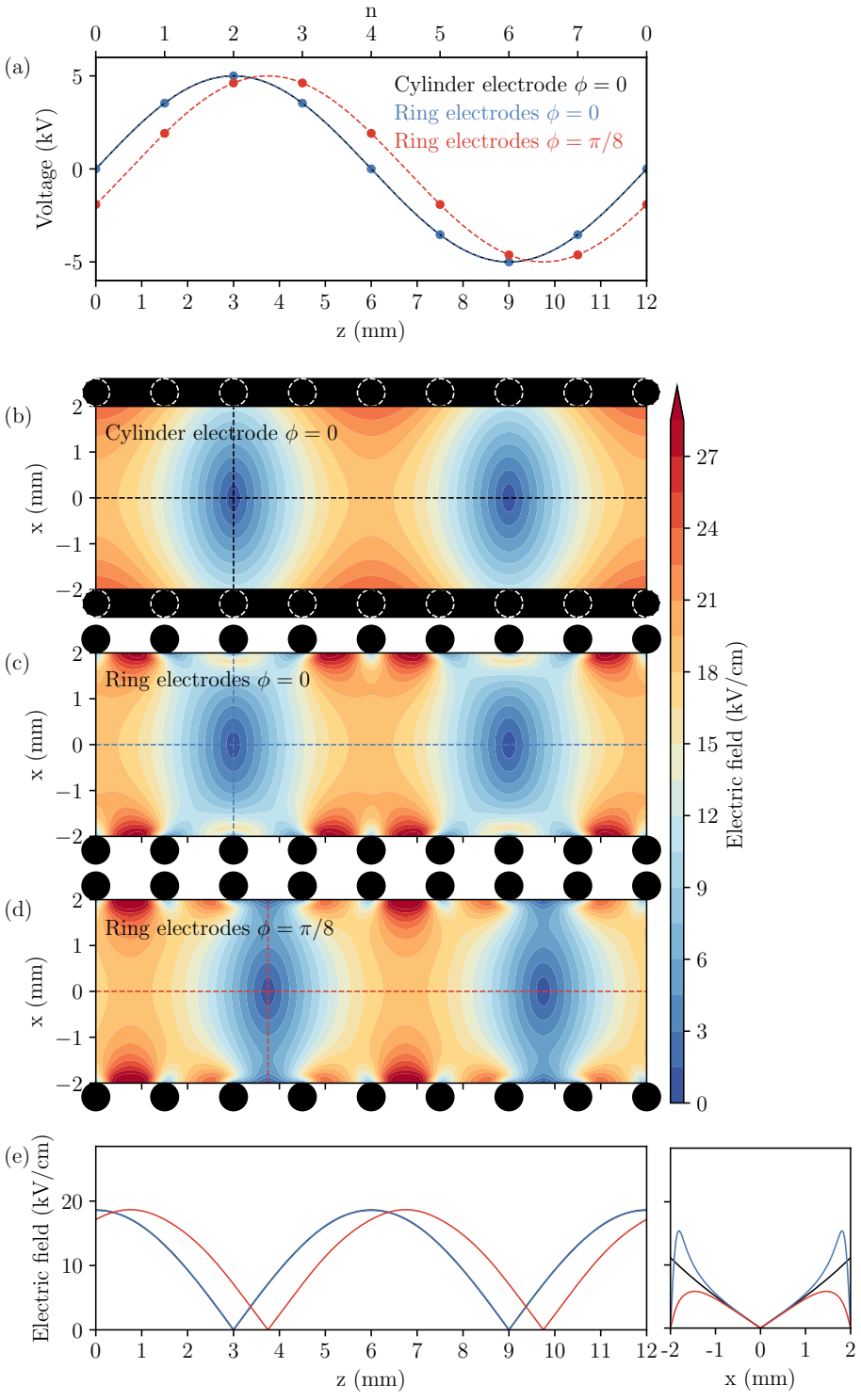

Figure D.2 | *Caption moved to footnote*[2].

D.2.1. Oscillation frequency

Along the longitudinal axis the electric field amplitude is $E(r=0,z) = V_0 k |\sin(kz-\phi)|/I_0(kr_0)$ as is shown in Figure D.2e. Around the field minima the field increases approximately linear and can be expanded up to first order to be,

$$E^{(1)}_{z=z_0}(r=0,z) = \frac{V_0 k^2 |z-z_0|}{I_0(kr_0)}. \tag{D.15}$$

In the radial direction, also shown in Figure D.2e, the electric field amplitude around each field minimum is given by $E(r, z=z_0) = V_0 k |I_1(kr)|/I_0(kr_0)$. The electric field magnitude around the minima also increases linearly and can be expanded up to first order to be,

$$E^{(1)}_{r=0}(r, z=z_0) = \frac{V_0 k^2 |r|}{2I_0(kr_0)}. \tag{D.16}$$

Here it can be seen that the electric field amplitude increases twice as fast in the longitudinal as in the transverse directions. Therefore, the decelerator traps correspond approximately to a three dimensional quadrupole trap which is twice as steep in the longitudinal as in the transverse directions.
From Equation 4.1, the Stark shift of the low-field seeking state with $N > 0, M_N = 0$ in the low field regime is quadratically increasing with field strength as,

$$\Delta W_{lf}(E) = \frac{1}{(2N-1)(2N+3)} \frac{\mu_e^2 E^2}{2B}. \tag{D.17}$$

From combining the low field Stark shift and the linear expansion of the electric field around the electric field minima the oscillation frequency around this minimum in each direction, $q = r, z$, can be found though,

$$\omega_q = \sqrt{\frac{2\Delta W_{lf}\left(E^{(1)}_{q=q_0}\right)}{mq^2}}, \tag{D.18}$$

to be,

$$\omega_z = 2\omega_r = \frac{V_0 k^2}{I_0(kr_0)} \sqrt{\frac{\mu_e^2}{m(2N-1)(2N+3)B}}. \tag{D.19}$$

In Table D.1 these analytic oscillation frequencies are compared to the result from the values found from the fit to the effective potential up to half the trap depth.

[2] ***Figure D.2 |*** *Comparison between ideal decelerator field generated by hollow cylinder electrode and a series of ring electrodes. (a) The voltage with amplitude V_0 of 5 kV applied to the decelerator; for the ring electrodes the discrete voltages applied for each electrode number (n), for the cylinder electrode the continuous longitudinally periodic voltage. The corresponding electric field within the decelerator along the longitudinal axis (z) and a transverse axis (x) in he case of a cylinder electrode (b) and ring electrodes (c) and (d). For the ring electrodes the field is given for a phase $\phi = 0$ (c) and $\phi = \pi/8$ as the shape is different. The black filled shapes show the geometry of the electrodes electrodes. (d) A longitudinal and transverse field slice at positions marked in (b) to (d) with dashed lines.*

Table D.1 | *Comparison between longitudinal (ω_z) and transverse (ω_r) oscillation frequencies obtained by harmonic fit to the cut through of the potential up to half of the maximum trap depth in each direction, and the analytic estimate in the low field regime. The fitted values are taken from Table 4.4.*

Molecule	$\lvert N, M_N\rangle$	V_0 (kV)	Fit		Analytic	
			ω_z (krad/s)	ω_r (krad/s)	ω_z (krad/s)	ω_r (krad/s)
$^{88}Sr^{19}F$	$\lvert 1,0\rangle$	3	2.82	1.66	3.50	1.75
	$\lvert 1,0\rangle$	5	4.51	2.61	5.84	2.92
	$\lvert 2,0\rangle$	5	2.35	1.23	2.85	1.41
	$\lvert 2,0\rangle$	8	3.97	2.11	4.56	2.28
	$\lvert 2,0\rangle$	10	5.04	2.71	5.70	2.85
$^{138}Ba^{19}F$	$\lvert 1,0\rangle$	5	3.77	2.17	4.74	2.37
	$\lvert 2,0\rangle$	5	1.95	1.03	2.31	1.16
	$\lvert 2,0\rangle$	8	3.24	1.75	3.70	1.85
	$\lvert 2,0\rangle$	10	4.13	2.24	4.63	2.31

There are two effects deforming the trap for increasing displacement from the center. Firstly, the electric field shape deviates from the linear gradient around the trap center, especially in the longitudinal direction. Secondly, the gradient of the Stark shift reduces, making it less quadratic. Both of these effects reduce the effective trap frequency experienced by molecules with a trajectory of higher displacement from the trap center.

D.2.2. Trap dimensions

The shape of the electric field within the traveling-wave Stark decelerator is clearly fixed by the solution of Laplace's equation, as shown in Equation D.14. The electric field consists of a series of quadrupole-like traps, which around the trap center increases twice as fast in the longitudinal as in the transverse direction, as discussed in the previous section. Nevertheless, there are two degrees of freedom to set the size of the traps, parameterised here by the (transverse) inner radius of the electrodes r_0 and the (longitudinal) separation between the trap centers π/k.

Instead, one could consider these two degrees of freedom as a overall scale and an aspect ratio. Typically, experiments are performed on molecular beams with a diameter in the order of millimeters, as is also the case in this work. This sets the scale of the voltages that have to be applied to the electrodes to achieved the fields necessary to capture these molecules to kilovolts, which, although challenging, can be achieved in the lab. Stark decelerators on a chip, with dimensions in the order of tens of micrometers have also been demonstrated to work, although based on a different field geometry [133].

The decelerator used in this work has an inner radius r_0 of 2 mm and trap center separation π/k of 6 mm, resulting in an aspect ratio $2kr_0/\pi$ of 2/3. As can be seen from Figure D.2 for this aspect ratio the transverse electric field boundary of the trap is lower than in the

longitudinal direction. For the ideal decelerator field this is understood by the ratio of the fields at the transverse $E(r = r_0, z = \phi/k)$ and longitudinal $E(r = 0, z = (\phi + \frac{\pi}{2})/k)$ trap boundary. From Equation D.14 this ratio is found to be $I_1(kr_0)$, which for these dimensions is 0.60.
In section 4.4 it was shown that the maximum phase-space acceptance of the decelerator for molecules in the $X^2\Sigma^+(v = 0, N = 1, M_N = 0)$ groundstate of SrF is achieved at a voltage amplitude of 5 kV, which results in a longitudinal electric field boundary close to the turning point field of the Stark shift E_{tp} at 21.0 kV/cm. For guiding, this voltage amplitude results for this aspect ratio to a transverse phase-space acceptance reduction, as the transverse trap depth is below the maximum trap depth possible from the Stark shift. For deceleration this is less of a limiting factor as in this case the longitudinal trap depth is reduced.
An equal electric field boundary in each direction could be achieved with electrode dimensions such that $I_1(kr_0) = 1$, corresponding to an aspect ratio $2kr_0/\pi$ of 0.97. In Figure D.3 the electric field is shown for this aspect ratio as would be achieved by increasing the inner radius from 2 to 2.89 mm.

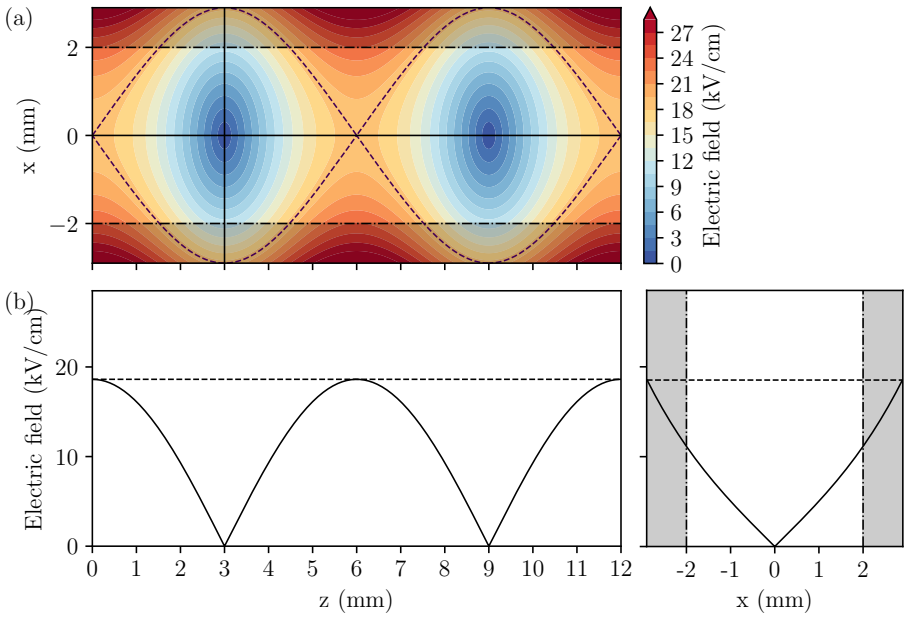

Figure D.3 | *Electric field for an ideal decelerator with an aspect ratio of transverse and longitudinal dimension of 0.97, such that electric field amplitudes on the transverse and longitudinal trap boundary are equal. The solid lines show (the position of) longitudinal and transverse field slices. The dashed lines show the electric field amplitude forming a boundary to the trap. The dashed-dotted lines and shaded areas show the region which is missed in the setup used in this work.*

Bibliography

The numbers behind each reference indicate on which pages it is used.

[1] C. N. Yang and R. L. Mills, "Conservation of Isotopic Spin and Isotopic Gauge Invariance," *Phys. Rev.*, vol. 96, pp. 191–195, Oct 1954. 1

[2] S. L. Glashow, "Partial-symmetries of weak interactions," *Nuclear Physics*, vol. 22, no. 4, pp. 579–588, 1961.

[3] S. Weinberg, "A Model of Leptons," *Phys. Rev. Lett.*, vol. 19, p. 1264, Nov 1967. 1

[4] G. Arnison *et al.*, "Experimental observation of lepton pairs of invariant mass around 95 GeV/c^2 at the CERN SPS collider," *Phys. Lett. B*, vol. 126, p. 398, Mar 1983. 1

[5] D. P. Barber *et al.*, "Discovery of Three-Jet Events and a test of Quantum Chromodynamics at PETRA," *Phys. Rev. Lett.*, vol. 43, p. 830, Sep 1979. 1

[6] G. Aad *et al.*, "Observation of a new particle in the search for the Standard Model Higgs boson with the ATLAS detector at the LHC," *Phys. Lett. B*, vol. 716, p. 1, Sep 2012. 1

[7] P. W. Higgs, "Broken Symmetries and the Masses of Gauge Bosons," *Phys. Rev. Lett.*, vol. 13, p. 508, Oct 1964. 1

[8] M. L. Perl *et al.*, "Evidence for Anomalous Lepton Production in $e^+ - e^-$ Annihilation," *Phys. Rev. Lett.*, vol. 35, p. 1489, Dec 1975. 1

[9] K. Kodama *et al.*, "Observation of tau neutrino interactions," *Phys. Lett. B*, vol. 504, p. 218, Apr 2001. 1

[10] J. E. Augustin *et al.*, "Discovery of a Narrow Resonance in e^+e^- Annihilation," *Phys. Rev. Lett.*, vol. 33, p. 1406, Dec 1974. 1

[11] J. J. Aubert, U. Becker, P. J. Biggs, J. Burger, M. Chen, G. Everhart, P. Goldhagen, J. Leong, T. McCorriston, T. G. Rhoades, M. Rohde, S. C. C. Ting, S. L. Wu, and Y. Y. Lee, "Experimental Observation of a Heavy Particle J," *Phys. Rev. Lett.*, vol. 33, p. 1404, Dec 1974. 1

[12] S. W. Herb *et al.*, "Observation of a Dimuon Resonance at 9.5 GeV in 400-GeV Proton-Nucleus Collisions," *Phys. Rev. Lett.*, vol. 39, p. 252, Aug 1977. 1

[13] S. Abachi *et al.*, "Observation of the Top Quark," *Phys. Rev. Lett.*, vol. 74, p. 2632, Apr 1995. 1

[14] F. Abe *et al.*, "Observation of Top Quark Production in $\overline{p}p$ collisions with the Collider Detector at Fermilab," *Phys. Rev. Lett.*, vol. 74, p. 2626, Apr 1995. 1

[15] H. Georgi and S. L. Glashow, "Unity of All Elementary-Particle Forces," *Phys. Rev. Lett.*, vol. 32, pp. 438–441, Feb 1974. 1

[16] J. C. Pati and A. Salam, "Lepton number as the fourth "color"," *Phys. Rev. D*, vol. 10, pp. 275–289, Jul 1974.

[17] H. Fritzsch and P. Minkowski, "Unified interactions of leptons and hadrons," *Annals of Physics*, vol. 93, no. 1, pp. 193–266, 1975.

[18] K. S. Babu, X.-G. He, and S. Pakvasa, "Neutrino masses and proton decay modes in SU(3)×SU(3)×SU(3) trinification," *Phys. Rev. D*, vol. 33, pp. 763–772, Feb 1986. 1

[19] P. Fayet and S. Ferrara, "Supersymmetry," *Physics Reports*, vol. 32, no. 5, pp. 249–334, 1977. 1

[20] I. P. Ivanov, "Building and testing models with extended Higgs sectors," *Progress in Particle and Nuclear Physics*, vol. 95, pp. 160–208, 2017. 1

[21] W. Buchmüller and D. Wyler, "Effective lagrangian analysis of new interactions and flavour conservation," *Nuclear Physics B*, vol. 268, no. 3, pp. 621–653, 1986. 1

[22] B. Grzadkowski, M. Iskrzyński, M. Misiak, and J. Rosiek, "Dimension-six terms in the Standard Model Lagrangian," *Journal of High Energy Physics*, vol. 2010, Oct. 2010. 1

[23] A. Boeschoten, *Precision measurements in diatomic molecules: a route to a permanent electric dipole moment*. PhD thesis, University of Groningen, 2023. 2, 4, 7, 9, 13, 15, 17, 18, 39, 41, 135, 156

[24] V. A. Kostelecky and N. Russell, "Data Tables for Lorentz and CPT Violation," *Rev. Mod. Phys.*, vol. 83, pp. 11–31, 2011. 2

[25] J. H. Christenson, J. W. Cronin, V. L. Fitch, and R. Turlay, "Evidence for the 2π Decay of the K_2^0 Meson," *Phys. Rev. Lett.*, vol. 13, pp. 138–140, Jul 1964. 2

[26] N. Cabibbo, "Unitary Symmetry and Leptonic Decays," *Phys. Rev. Lett.*, vol. 10, pp. 531–533, Jun 1963. 2

[27] M. Kobayashi and T. Maskawa, "CP-Violation in the Renormalizable Theory of Weak Interaction," *Progress of Theoretical Physics*, vol. 49, pp. 652–657, 02 1973. 2

[28] C. Callan, R. Dashen, and D. Gross, "The structure of the gauge theory vacuum," *Physics Letters B*, vol. 63, no. 3, pp. 334–340, 1976. 2

[29] R. Jackiw and C. Rebbi, "Vacuum Periodicity in a Yang-Mills Quantum Theory," *Phys. Rev. Lett.*, vol. 37, pp. 172–175, Jul 1976. 2

[30] C. Abel *et al.*, "Measurement of the Permanent Electric Dipole Moment of the Neutron," *Phys. Rev. Lett.*, vol. 124, p. 081803, Feb 2020. 2

[31] T. E. Chupp, P. Fierlinger, M. J. Ramsey-Musolf, and J. T. Singh, "Electric dipole moments of atoms, molecules, nuclei, and particles," *Rev. Mod. Phys.*, vol. 91, p. 015001, Jan 2019. 2

[32] A. D. Sakharov, "Violation of CP Invariance, C asymmetry, and baryon asymmetry of the Universe," *JETP Lett.*, vol. 5, p. 24, Jan 1967. 2

[33] P. Sandars, "Enhancement factor for the electric dipole moment of the valence electron in an alkali atom," *Physics Letters*, vol. 22, no. 3, pp. 290–291, 1966. 3

[34] P. A. B. Haase, D. J. Doeglas, A. Boeschoten, E. Eliav, M. Iliaš, P. Aggarwal, H. L. Bethlem, A. Borschevsky, K. Esajas, Y. Hao, S. Hoekstra, V. R. Marshall, T. B. Meijknecht, M. C. Mooij, K. Steinebach, R. G. E. Timmermans, A. Touwen, W. Ubachs, L. Willmann, and Y. Yin, "Systematic study and uncertainty evaluation of P, T-odd molecular enhancement factors in BaF," *The Journal of Chemical Physics*, vol. 155, no. 3, p. 034309, 2021. 3, 5, 41, 136

[35] Y. Yamaguchi and N. Yamanaka, "Large Long-Distance Contributions to the Electric Dipole Moments of Charged Leptons in the Standard Model," *Phys. Rev. Lett.*, vol. 125, p. 241802, Dec 2020. 4

[36] Y. Ema, T. Gao, and M. Pospelov, "Standard Model Prediction for Paramagnetic Electric Dipole Moments," *Phys. Rev. Lett.*, vol. 129, no. 23, p. 231801, 2022. 4, 114

[37] V. R. Marshall, *Spectroscopy and systematic effects: an eEDM experiment using BaF molecules*. PhD thesis, University of Groningen, 2024. 5, 7, 11, 12, 17, 18, 26, 29, 30, 41, 135, 136

[38] S. A. Murthy, D. Krause, Z. L. Li, and L. R. Hunter, "New limits on the electron electric dipole moment from cesium," *Phys. Rev. Lett.*, vol. 63, p. 965, Aug 1989. 5

[39] B. C. Regan, E. D. Commins, C. J. Schmidt, and D. DeMille, "New Limit on the Electron Electric Dipole Moment," *Phys. Rev. Lett.*, vol. 88, p. 071805, Feb 2002. 5

[40] J. J. Hudson, D. M. Kara, I. J. Smallman, B. E. Sauer, M. R. Tarbutt, and E. A. Hinds, "Improved measurement of the shape of the electron," *Nature*, vol. 473, p. 493, May 2011. 5

[41] ACME collaboration, "Improved limit on the electric dipole moment of the electron," *Nature*, vol. 562, p. 355, Oct 2018. 5, 137

[42] T. S. Roussy, L. Caldwell, T. Wright, W. B. Cairncross, Y. Shagam, K. B. Ng, N. Schlossberger, S. Y. Park, A. Wang, J. Ye, and E. A. Cornell, "An improved bound on the electron's electric dipole moment," *Science*, vol. 381, no. 6653, pp. 46–50, 2023. 5, 114

[43] J. Engel, M. J. Ramsey-Musolf, and U. van Kolck, "Electric dipole moments of nucleons, nuclei, and atoms: The Standard Model and beyond," *Prog. Part. Nucl. Phys.*, vol. 71, p. 21, Jul 2013. 5

[44] P. Aggarwal, H. L. Bethlem, A. Borschevsky, M. Denis, K. Esajas, P. A. Haase, Y. Hao, S. Hoekstra, K. Jungmann, T. B. Meijknecht, M. C. Mooij, R. G. Timmermans, W. Ubachs, L. Willmann, and A. Zapara, "Measuring the electric dipole moment of the electron in BaF," *European Physical Journal D*, vol. 72, no. 11, p. 197, 2018. 5, 6, 43, 93, 111, 114, 124, 137, 138

[45] T. B. Meijknecht, *Electric and Magnetic Field Control for Electric Dipole Moment Searches*. PhD thesis, University of Groningen, 2023. 7, 12, 13, 18, 28, 34, 39, 41, 135

[46] K. Esajas, *Intense slow beams of heavy molecules to test fundamental symmetries*. PhD thesis, University of Groningen, 2021. 7, 43, 64, 76, 77, 80, 83, 84, 98

[47] M. C. Mooij. PhD thesis, Vrije Universiteit Amsterdam, 2024. 7, 45, 64, 78, 98, 99, 109

[48] J. van den Berg, *Traveling-wave Stark deceleration of SrF molecules*. PhD thesis, University of Groningen, 2015. 7, 76

[49] J. Meinema, *Obtaining ultracold molecules through Stark deceleration and laser cooling*. PhD thesis, University of Groningen, 2016. 7, 76, 81

[50] A. Zapara, *Dynamics of molecular beams in a traveling-wave Stark decelerator*. PhD thesis, University of Groningen, 2019. 7, 60, 76, 85, 89, 104

[51] P. Aggarwal, *Production, deceleration and trapping of SrF molecules*. PhD thesis, University of Groningen, 2021. 7, 45, 76, 81, 82, 104, 156

[52] S. C. Mathavan, *Deceleration of a Supersonic Beam of SrF Molecules*. PhD thesis, University of Groningen, 2023. 7, 76

[53] A. Boeschoten, V. R. Marshall, T. B. Meijknecht, A. Touwen, H. L. Bethlem, A. Borschevsky, S. Hoekstra, J. W. F. van Hofslot, K. Jungmann, M. C. Mooij, R. G. E. Timmermans, W. Ubachs, and L. Willmann, "Spin-precession method for sensitive electric dipole moment searches," 2024. 9, 10, 19, 21, 27, 32, 40, 41

[54] D. M. Kara, I. J. Smallman, J. J. Hudson, B. E. Sauer, M. R. Tarbutt, and E. A. Hinds, "Measurement of the electron's electric dipole moment using YbF molecules: methods and data analysis," *New Journal of Physics*, vol. 14, p. 103051, oct 2012. 9, 13, 16, 17

[55] P. Aggarwal, H. Bethlem, A. Boeschoten, A. Borschevsky, K. Esajas, Y. Hao, S. Hoekstra, K. Jungmann, V. Marshall, T. Meijknecht, M. Mooij, R. Timmermans, A. Touwen, W. Ubachs, L. Willmann, Y. Yin, and A. Zapara, "A supersonic laser ablation beam source with narrow velocity spreads," *The Review of scientific instruments*, vol. 92, p. 033202, 03 2021. 11, 17, 43

[56] E. Bobrova Blyumin, *Counting Statistics of an Electron Electric Dipole Moment Experiment*. Bachelor thesis, University of Groningen, 2023. 18, 29

[57] F. Zwarts, *Caddie*. Kernfysisch Versneller Instituut, Groningen, 1.6 ed., 2006-2023. 23, 31, 84

[58] The ROOT Team, Cern, *ROOT*, 1995-2023. version 6.26. 23, 31

[59] U. Even, "The Even-Lavie valve as a source for high intensity supersonic beam," *EPJ Techn Instrum*, vol. 2, p. 17, 2015. 26

[60] L. Torvalds, *git*. https://git-scm.com/, 2005-2023. 32

[61] J. J. Hudson, *Measuring the electric dipole moment of the electron with YbF molecules*. PhD thesis, University of Sussex, 2001. 39

[62] P. Aggarwal, Y. Yin, K. Esajas, H. L. Bethlem, A. Boeschoten, A. Borschevsky, S. Hoekstra, K. Jungmann, V. R. Marshall, T. B. Meijknecht, M. C. Mooij, R. G. E. Timmermans, A. Touwen, W. Ubachs, and L. Willmann, "Deceleration and Trapping of SrF Molecules," *Physical Review Letters*, vol. 127, p. 173201, oct 2021. 43, 47, 49, 74, 81, 88, 90, 114, 129

[63] J. M. Brown and A. Carrington, *Rotational spectroscopy of diatomic molecules*. Cambridge Univ. Press, 2003. 44, 116, 156

[64] P. M. Sheridan, J.-G. Wang, M. J. Dick, and P. F. Bernath, "Optical-optical double resonance spectroscopy of the $C^2\Pi$-$A^2\Pi$ and $D^2\Sigma^+$-$A^2\Pi$ transitions of SrF," *J. Phys. Chem. A*, vol. 113, p. 13383, May 2009. 44, 156

[65] W. Ernst, J. Kändler, S. Kindt, and T. Törring, "Electric dipole moment of SrF $X^2\Sigma^+$ from high-precision stark effect measurements," *Chem. Phys. Lett.*, vol. 113, p. 351, Jan 1985. 44, 156

[66] C. Ryzlewicz and T. Törring, "Formation and microwave spectrum of the $^2\Sigma$-radical barium-monofluoride," *Chemical Physics*, vol. 51, no. 3, pp. 329–334, 1980. 44, 45, 115, 116, 123

[67] W. E. Ernst, J. Kändler, and T. Törring, "Hyperfine structure and electric dipole moment of BaF $X^2\Sigma^+$," *The Journal of Chemical Physics*, vol. 84, pp. 4769–4773, 05 1986. 44, 45, 115, 116, 123, 156

[68] C. M. Western, "PGOPHER: A program for simulating rotational, vibrational and electronic spectra," *Journal of Quantitative Spectroscopy and Radiative Transfer*, vol. 186, pp. 221–242, 2017. Satellite Remote Sensing and Spectroscopy: Joint ACE-Odin Meeting, October 2015. 45, 60, 98, 99, 115, 116

[69] S. Y. T. van de Meerakker, H. L. Bethlem, N. Vanhaecke, and G. Meijer, "Manipulation and control of molecular beams," *Chem. Rev.*, vol. 112, p. 4828, Mar 2012. 49, 114, 115, 118, 182

[70] J. E. van den Berg, S. H. Turkesteen, E. B. Prinsen, and S. Hoekstra, "Deceleration and trapping of heavy diatomic molecules using a ring-decelerator," *Eur. Phys. J. D*, vol. 66, p. 235, Sep 2012. 49

[71] J. E. van der Berg, S. C. Mathavan, C. Meinema, J. Nauta, T. H. Nijbroek, K. Jungmann, H. L. Bethlem, and S. Hoekstra, "Traveling-wave deceleration of SrF molecules," *J. Mol. Spec.*, vol. 300, p. 22, Jun 2014. 49

[72] H. L. Bethlem, G. Berden, and G. Meijer, "Decelerating Neutral Dipolar Molecules," *Physical Review Letters*, vol. 83, pp. 1558–1561, 8 1999. 49

[73] A. Osterwalder, S. A. Meek, G. Hammer, H. Haak, and G. Meijer, "Deceleration of neutral molecules in macroscopic traveling traps," *Phys. Rev. A*, vol. 81, p. 051401, May 2010. 49

[74] S. A. Meek, M. F. Parsons, G. Heyne, V. Platschkowski, H. Haak, G. Meijer, and A. Osterwalder, "A traveling wave decelerator for neutral polar molecules," *Review of Scientific Instruments*, vol. 82, p. 093108, 09 2011. 49

[75] COMSOL AB, Stockholm, "COMSOL Multiphysics v. 6.2." 51, 60, 181

[76] J. Muller, *Electric fields and molecule motion in a traveling-wave Stark decelerator*. Bachelor thesis, University of Groningen, 2017. 51, 60

[77] Y. Shyur, J. A. Bossert, and H. J. Lewandowski, "Pulsed operation of a ring Stark decelerator," *Journal of Physics B: Atomic, Molecular and Optical Physics*, vol. 51, p. 165101, jul 2018. 52, 138

[78] M. I. Fabrikant, T. Li, N. J. Fitch, N. Farrow, J. D. Weinstein, and H. J. Lewandowski, "Method for traveling-wave deceleration of buffer-gas beams of CH," *Physical Review A*, vol. 90, p. 033418, Sep 2014. 67, 114, 130

[79] S. Truppe, M. Hambach, S. M. Skoff, N. E. Bulleid, J. S. Bumby, R. J. Hendricks, E. A. Hinds, B. E. Sauer, and M. R. Tarbutt, "A buffer gas beam source for short, intense and slow molecular pulses," *Journal of Modern Optics*, vol. 65, no. 5-6, pp. 648–656, 2018. 77

[80] M. C. Mooij, H. L. Bethlem, A. Boeschoten, A. Borschevsky, K. Esajas, T. H. Fikkers, S. Hoekstra, J. W. F. van Hofslot, K. Jungmann, V. R. Marshall, T. B. Meijknecht, R. G. E. Timmermans, A. Touwen, W. Ubachs, L. Willmann, Y. Yin, and NL-*e*EDM collaboration, "Influence of source parameters on the longitudinal phase-space distribution of a pulsed cryogenic beam of barium fluoride molecules," *New Journal of Physics*, vol. 26, p. 053009, may 2024. 77, 98, 100, 101, 136, 137

[81] S. Boulsnane, *Engineering for cryogenic source improvement and laser cooling chamber implementation*. Internship report, University of Groningen, Institut National des sciences appliquées, 2022. 78

[82] Hamamatsu, *Photomultiplier tubes, Basics and Applications*. 80

[83] Hamamatsu, *Metal Package PMT with Cooler, Photosensor Modules H7422 Series Datasheet*. 80

[84] P. J. Dagdigian, H. W. Cruse, and R. N. Zare, "Radiative lifetimes of the alkaline earth monohalides," *J. Chem. Phys.*, vol. 60, p. 2330, Aug 1974. 81

[85] J. F. Barry, *Laser cooling and slowing of a diatomic molecule*. Ph.D. thesis, Yale University, 2013. 81

[86] J. W. F. van Hofslot, *Increasing the intensity of a slow molecular beam using an electrostatic hexapole*. Master thesis, University of Groningen, 2021. 82, 96

[87] M. Kirste, B. G. Sartakov, M. Schnell, and G. Meijer, "Nonadiabatic transitions in electrostatically trapped ammonia molecules," *Phys. Rev. A*, vol. 79, p. 051401, May 2009. 85

[88] S. A. Meek, G. Santambrogio, B. G. Sartakov, H. Conrad, and G. Meijer, "Suppression of nonadiabatic losses of molecules from chip-based microtraps," *Phys. Rev. A*, vol. 83, p. 033413, Mar 2011. 85

[89] T. E. Wall, S. K. Tokunaga, E. A. Hinds, and M. R. Tarbutt, "Nonadiabatic transitions in a Stark decelerator," *Physical Review A*, vol. 81, p. 033414, Mar 2010. 85

[90] P. Aggarwal, V. R. Marshall, H. L. Bethlem, A. Boeschoten, A. Borschevsky, M. Denis, K. Esajas, Y. Hao, S. Hoekstra, K. Jungmann, T. B. Meijknecht, M. C. Mooij, R. G. E. Timmermans, A. Touwen, W. Ubachs, S. M. Vermeulen, L. Willmann, Y. Yin, and A. Zapara, "Lifetime measurements of the $A\,^2\Pi_{1/2}$ and $A\,^2\Pi_{3/2}$ states in BaF," *Physical Review A*, vol. 100, p. 052503, Nov 2019. 97

[91] J. Emsley, *The Elements*. Oxford Univ. Press, 1995. 98

[92] M. C. Mooij, H. L. Bethlem, A. Boeschoten, A. Borschevsky, T. H. Fikkers, S. Hoekstra, J. W. F. van Hofslot, K. Jungmann, V. R. Marshall, T. B. Meijknecht, R. G. E. Timmermans, A. Touwen, W. Ubachs, and L. Willmann., "A novel method to determine the phase-space distribution of a pulsed molecular beam," 2024. 99, 123

[93] Y. Hao, L. F. Pašteka, L. Visscher, P. Aggarwal, H. L. Bethlem, A. Boeschoten, A. Borschevsky, M. Denis, K. Esajas, S. Hoekstra, K. Jungmann, V. R. Marshall, T. B. Meijknecht, M. C. Mooij, R. G. E. Timmermans, A. Touwen, W. Ubachs, L. Willmann, Y. Yin, A. Zapara, and NL-eEDM Collaboration, "High accuracy theoretical investigations of CaF, SrF, and BaF and implications for laser-cooling," *The Journal of Chemical Physics*, vol. 151, p. 034302, 07 2019. 111, 130, 137

[94] Y. Zhang, Z. Zeng, Q. Liang, W. Bu, and B. Yan, "Doppler cooling of buffer-gas-cooled barium monofluoride molecules," *Physical Review A*, vol. 105, mar 2022. 111, 130, 137

[95] M. S. Safronova, D. Budker, D. DeMille, D. F. J. Kimball, A. Derevianko, and C. W. Clark, "Search for new physics with atoms and molecules," *Rev. Mod. Phys.*, vol. 90, p. 025008, Jun 2018. 114

[96] V. Andreev, D. G. Ang, D. DeMille, J. M. Doyle, G. Gabrielse, J. Haefner, N. R. Hutzler, Z. Lasner, C. Meisenhelder, B. R. O'Leary, C. D. Panda, A. D. West, E. P. West, and X. Wu, "Improved limit on the electric dipole moment of the electron," *Nature*, vol. 562, no. 7727, pp. 355–360, 2018. 114

[97] J. Hudson, B. E. Sauer, M. R. Tarbutt, and E. A. Hinds, "Measurement of the electron electric dipole moment using YbF molecules.," *Physical Review Letters*, vol. 89 2, p. 023003, 2002. 114

[98] V. Cirigliano, W. Dekens, J. de Vries, and E. Mereghetti, "Is there room for CP violation in the top-Higgs sector?," *Physical Review D*, vol. 94, p. 016002, Jul 2016. 114

[99] J. P. Gordon, H. J. Zeiger, and C. H. Townes, "Molecular Microwave Oscillator and New Hyperfine Structure in the Microwave Spectrum of NH_3," *Physical Review*, vol. 95, pp. 282–284, Jul 1954. 114, 115

[100] H. G. Bennewitz, W. Paul, and C. Schlier, "Fokussierung polarer Moleküle," *Zeitschrift für Physik*, vol. 141, p. 6, Feb 1955. 114

[101] S. Stolte, "Aiming the molecular arrow," *Nature*, vol. 353, pp. 391–392, Oct 1991. 114, 121

[102] M. Brouard, D. H. Parker, and S. Y. T. van de Meerakker, "Taming molecular collisions using electric and magnetic fields," *Chem. Soc. Rev.*, vol. 43, pp. 7279–7294, 2014. 114

[103] X. Wu, P. Hu, Z. Han, D. G. Ang, C. Meisenhelder, G. Gabrielse, J. M. Doyle, and D. DeMille, "Electrostatic focusing of cold and heavy molecules for the ACME electron EDM search," *New Journal of Physics*, vol. 24, p. 073043, jul 2022. 114

[104] R. T. Jongma, T. Rasing, and G. Meijer, "Two-dimensional imaging of metastable CO molecules," *The Journal of Chemical Physics*, vol. 102, pp. 1925–1933, 02 1995. 115

[105] C. Cheng, A. P. P. van der Poel, P. Jansen, M. Quintero-Pérez, T. E. Wall, W. Ubachs, and H. L. Bethlem, "Molecular Fountain," *Physical Review Letters*, vol. 117, p. 253201, Dec 2016. 115, 128

[106] K. Schreel, J. Schleipen, A. Eppink, and J. J. t. Meulen, "State-to-state cross sections for rotational excitation of OH by collisions with He and Ar," *The Journal of Chemical Physics*, vol. 99, pp. 8713–8722, 12 1993. 115

[107] N. Butkovskaya, M. Larichev, I. Leipunskii, I. Morozov, and V. Tal'rose, "Mass-spectrometric analysis of the polar molecules beam.: I. Focusing in inhomogeneous electric field," *Chemical Physics*, vol. 12, no. 3, pp. 267–271, 1976. 115

[108] M. Cohen, T. Feldmann, and S. Kais, "Stark effect of a rigid rotor," *Journal of Physics B: Atomic and Molecular Physics*, vol. 17, p. 3535, sep 1984. 116

[109] V. A. Cho and R. B. Bernstein, "Tight focusing of beams of polar polyatomic molecules via the electrostatic hexapole lens," *The Journal of Physical Chemistry*, vol. 95, no. 21, pp. 8129–8136, 1991. 118

[110] J. J. Everdij, A. Huijser, and N. F. Verster, "Improved Space Focusing of Polar Diatomic Molecules in a System of Quadrupole and Hexapole Fields," *Review of Scientific Instruments*, vol. 44, pp. 721–725, 04 1973. 118, 180

[111] Y. Ke, X.-B. Deng, and Z.-K. Hu, "Low chromatic aberration hexapole for molecular state selection," *Journal of Physics B: Atomic, Molecular and Optical Physics*, vol. 49, p. 025101, dec 2015. 118

[112] F. M. H. Crompvoets, H. L. Bethlem, and G. Meijer, *A storage ring for neutral molecules*, pp. 209–287. Academic Press, 2005. 118

[113] T. C. Steimle, S. Frey, A. Le, D. Demille, D. A. Rahmlow, and C. Linton, "Molecular-beam optical Stark and Zeeman study of the A 2Π - X 2Σ+ (0,0) band system of BaF," *Physical Review A - Atomic, Molecular, and Optical Physics*, vol. 84, p. 012508, 7 2011. 123

[114] V. Marshall, P. Aggarwal, J. Joosten, L. Rozeboom, S. Venekamp, A. Boeschoten, A. Borschevsky, M. Denis, K. Esajas, P. Haase, Y. Hao, S. Hoekstra, K. Jungmann, T. Meijknecht, M. Mooij, R. Timmermans, A. Touwen, W. Ubachs, L. Willmann, and Y. Yin, "Resolved Hyperfine structure of ^{138}Ba^{19}F $X^2\Sigma+$ and $A^2\Pi$ states," *In preparation*, 2023. 123, 156

[115] H. Pauly, *Atom, Molecule, and Cluster Beams I*, vol. 28 of *Springer Series on Atomic, Optical, and Plasma Physics*. Berlin, Heidelberg: Springer Berlin Heidelberg, 2000. 127

[116] N. R. Hutzler, H. I. Lu, and J. M. Doyle, "The buffer gas beam: An intense, cold, and slow source for atoms and molecules," *Chemical Reviews*, vol. 112, pp. 4803–4827, 9 2012. 127

[117] N. J. Fitch and M. R. Tarbutt, "Laser-cooled molecules," in *Advances In Atomic, Molecular, and Optical Physics*, pp. 157–262, Elsevier, 2021. 130

[118] M. Rockenhäuser, F. Kogel, T. Garg, S. A. Morales-Ramírez, and T. Langen, "Laser cooling of barium monofluoride molecules using synthesized optical spectra," 2024. 137

[119] R. Bause and NL-*e*EDM Collaboration *in preparation*. 139

[120] I. Kozyryev and N. R. Hutzler, "Precision Measurement of Time-Reversal Symmetry Violation with Laser-Cooled Polyatomic Molecules," *Phys. Rev. Lett.*, vol. 119, p. 133002, Sep 2017. 139

[121] M. Denis, P. A. B. Haase, R. G. E. Timmermans, E. Eliav, N. R. Hutzler, and A. Borschevsky, "Enhancement factor for the electric dipole moment of the electron in the BaOH and YbOH molecules," *Phys. Rev. A*, vol. 99, p. 042512, Apr 2019. 139

[122] K. Steinebach, *Production of a cryogenic beam and prospects for traveling-wave Stark deceleration of BaOH*. Master thesis, University of Groningen, 2020. 139

[123] T. Fikkers and NL-*e*EDM Collaboration *in preparation*. 139

[124] H. Lefebvre-Brion and R. W. Field, *Perturbations in the spectra of diatomic molecules*. Academic Press, 1986. 156

[125] P. Colarusso, B. Guo, K. Q. Zhang, and P. F. Bernath, "High resolution infrared emission spectrum of strontium monofluoride," *J. Mol. Spectrosc.*, vol. 175, p. 158, Jan 1996. 156

[126] T. C. Steimle, P. J. Domaille, and D. O. Harris, "Rotational analysis of the $A^2\Pi$- $X^2\Sigma$ system of SrF using a CW tunable dye laser ," *J. Mol. Spectrosc.*, vol. 73, p. 441, Dec 1978.

[127] T. C. Steimle, D. A. Fletcher, and C. T. Scurlock, "A molecular beam study of the (0, 0) $A^2\Pi$- $X^2\Sigma$ band system of SrF," *J. Mol. Spectrosc.*, vol. 158, p. 487, Apr 1993. 156

[128] A. Bernard, C. Effantin, E. Andrianavalona, J. Vergès, and R. F. Barrow, "Laser-induced fluorescence of BaF: Further results for six electronic states," *J. Mol. Spectrosc.*, vol. 152, p. 174, Mar 1992. 156

[129] C. Effantin, A. Bernard, J. D'Incan, G. Wannous, J. Vergès, and R. F. Barrow, "Studies of the electronic states of the baf molecule part I: Effective constants for seven states below 30 000 cm^{-1}," *Molecular Physics*, vol. 70, no. 5, pp. 735–745, 1990. 156

[130] M. Denis, P. A. B. Haase, M. C. Mooij, Y. Chamorro, P. Aggarwal, H. L. Bethlem, A. Boeschoten, A. Borschevsky, K. Esajas, Y. Hao, S. Hoekstra, J. W. F. van Hofslot, V. R. Marshall, T. B. Meijknecht, R. G. E. Timmermans, A. Touwen, W. Ubachs, L. Willmann, and Y. Yin, "Benchmarking of the Fock-space coupled-cluster method and uncertainty estimation: Magnetic hyperfine interaction in the excited state of BaF," *Phys. Rev. A*, vol. 105, p. 052811, May 2022. 156

[131] F. Hund, "Zur Deutung einiger Erscheinungen in den Molekelspektren," *Zeitschrift für Physik*, vol. 36, p. 657, Sep 1926. 157

[132] R. W. Anderson, "Tracks of Symmetric Top Molecules in Hexapole Electric Fields," *The Journal of Physical Chemistry A*, vol. 101, pp. 7664–7673, Oct 1997. 180

[133] S. A. Meek, H. Conrad, and G. Meijer, "A Stark decelerator on a chip," *New Journal of Physics*, vol. 11, p. 055024, may 2009. 185

university of groningen

faculty of science and engineering



Nikhef

NWO